First-principles Fröhlich electron-phonon coupling and polarons in oxides and polar semiconductors

Carla Verdi

St Catherine's College
University of Oxford

A thesis submitted for the Degree of
Doctor of Philosophy

Trinity Term, 2017

Abstract

First-principles Fröhlich electron-phonon coupling and polarons in oxides and polar semiconductors

Carla Verdi
St Catherine's College, University of Oxford

A thesis submitted for the Degree of *Doctor of Philosophy*
Trinity Term, 2017

The Fröhlich coupling describes the interaction between electrons and infrared-active vibrations at long wavelength in polar semiconductors and insulators, and may result in the formation of polaronic quasiparticles. Polarons are electrons dressed by a phonon cloud, which can strongly affect the electronic properties of the crystal. Despite their ubiquitous role in a broad range of technologies, first-principles investigations of the electron-phonon interaction in polar materials are scarce. In this thesis we develop a general formalism for calculating the electron-phonon matrix element in polar semiconductors and insulators from first principles, which represents a generalization of the Fröhlich model and can be used to compute the polar electron-phonon coupling as a straightforward post-processing operation. We apply this procedure to explore an important material for photovoltaics, the hybrid lead halide perovskite $CH_3NH_3PbI_3$. In this case we show that the temperature dependence of emission line broadening is dominated by Fröhlich coupling. Our method is formulated in conjunction with an *ab initio* interpolation technique based on maximally localized Wannier functions, which allows to describe all forms of electron-phonon coupling on the same footing. We demonstrate the validity of this approach on the prototypical examples GaN and $SrTiO_3$. Focusing on anatase TiO_2, a transition metal oxide of wide technological interest, we establish quantitatively the effect of including the *ab initio* Fröhlich coupling in the calculation of electron lifetimes. The rest of the thesis is devoted to exploring the quasiparticle properties in doped oxides. In particular, we investigate angle-resolved photoemission spectra from first principles in doped anatase TiO_2 by proposing a novel framework that combines our *ab initio* matrix elements, including the dynamical screening arising from the added carriers, and the cumulant expansion approach. We compare our results with experimental data, and show that the transition from a polaronic to a Fermi liquid regime with increasing doping concentration originates from nonadiabatic polar electron-phonon coupling. We further validate this mechanism by calculating angle-resolved photoemission spectra in the ferromagnetic semiconductor EuO.

Contents

CHAPTER 1

Introduction

The electron-phonon interaction is a cornerstone of condensed matter physics, and plays important roles in a diverse array of phenomena including electrical resistivity, conventional superconductivity and temperature-dependent optical properties. In the framework of first-principles calculations, the investigation of electron-phonon interaction properties has been heavily hindered by the high computational effort. Aided by the advances in first-principles techniques and by the development of efficient computational tools, very recent years have witnessed an exciting progress in *ab initio* calculations of the electron-phonon coupling, trying to bridge the gap between the rich amount of theoretical progress from early years and the current state of *ab initio* investigations.

This has taken several directions, such as the analysis of zero-point renormalization and temperature-dependent effects in the band gap and in the optical spectra of semiconductors and insulators, the calculation of phonon-limited carrier lifetimes and mobilities, and the investigation of superconducting properties. Interestingly, this fast-paced progress has mainly focused on metals and nonpolar semiconductors and insulators. By contrast, in the case of polar materials where electrons can strongly couple to the macroscopic electric field induced by long-wavelength optical phonons, first-principles calcula-

tions have not gone far and have been widely relying on the model developed by Fröhlich in the 1950s.

In this thesis we are concerned with developing a method for calculating the electron-phonon coupling in polar materials from first principles, which opens the possibility to explore several interesting properties. One direct application of our formalism is the study of carrier linewidths and lifetimes. We choose to focus mainly on two fascinating materials for this topic: the hybrid lead halide perovskite $CH_3NH_3PbI_3$, which has seen a great success in the last five years in the context of photovoltaic systems, and anatase titanium dioxide (TiO_2), a prototypical transition metal oxide with several technological applications.

Moving further, we note that a prime issue in polar materials is the nature of the charge carriers. Indeed, this is a key element in determining the conduction properties in these materials, for example in doped oxides. There, the mobile charges are not free electrons in general; instead, they can be dressed by the interaction with the phonons, resulting in heavier quasiparticles known as *polarons*. Recently conspicuous attention has been drawn to the investigation of polaronic properties in paradigmatic doped oxides by means of angle-resolved photoemission spectroscopy (ARPES). The experiments also show a remarkable evolution of the carriers with doping concentration, from polarons to a Fermi liquid. In the second part of this thesis we concentrate on this exciting problem, by calculating ARPES spectra from first principles in doped oxides. In particular, we study the case of doped anatase TiO_2 and of the metal oxide EuO, and we examine the evolution of the charge-carrier properties with doping.

In this chapter we introduce the topic of the electron-phonon coupling in polar materials within the Fröhlich model, and we present an overview of the formation of polaronic quasiparticles, with a focus on recent experimental findings. The connection between ARPES spectra and first-principles calculations is also described. The aim of each section is to provide a general introduction and motivation for the work presented in this thesis. An outline of the content of the following chapters is given at the end.

1.1 Fröhlich electron-phonon coupling and polarons

In polar semiconductors and insulators the fluctuations of the ionic positions corresponding to longitudinal optical (LO) phonons at long wavelength generate macroscopic electric fields which can couple strongly to electrons (and holes). This is known as *Fröhlich interaction*. More precisely, the Fröhlich model describes the interaction of a conduction electron in a parabolic band with longitudinal optical phonons with constant energy $\hbar\omega_{\mathrm{LO}}$, in a medium that is assumed to be isotropic and uniform. The core ideas behind the Fröhlich model stem from the macroscopic treatment of the motion of an electron in a polar lattice of Landau and Pekar [1], where the lattice is described as a dielectric continuum. In addition, in the Fröhlich model the lattice polarization field is treated in a quantum mechanical way.

Following the theory of Fröhlich [2], let us start from the frequency-dependent electric displacement $\mathbf{D}$ associated with the electric field $\mathbf{E}$ (in Gaussian units):

$$\mathbf{D}(\omega) = \epsilon(\omega)\,\mathbf{E}(\omega) = \mathbf{E}(\omega) + 4\pi\mathbf{P}(\omega)\,, \tag{1.1}$$

where $\mathbf{P}$ is the macroscopic polarization in the material and ϵ is the permittivity. In general, the total polarization has a contribution from high-frequency (electronic) oscillations, $\mathbf{P}_{\mathrm{e}}$, and one from infrared (atomic) oscillations, $\mathbf{P}_{\mathrm{i}}$. In the static limit it is given by:

$$\mathbf{P}(0) = (4\pi)^{-1}(1-\epsilon_0^{-1})\,\mathbf{D}(0)\,, \tag{1.2}$$

with ϵ_0 the total static permittivity (or dielectric constant) that includes the nuclear response. In the high-frequency limit $\omega \gg \omega_{\mathrm{LO}}$, where the lattice polarization is not excited, one has:

$$\mathbf{P} = \mathbf{P}_{\mathrm{e}} = (4\pi)^{-1}(1-\epsilon_\infty^{-1})\,\mathbf{D}\,, \tag{1.3}$$

where ϵ_∞ is the contribution to the static permittivity coming from interband electronic transitions. In the static limit, for a field $\mathbf{D}$ of equal strength, $\mathbf{P}_{\mathrm{e}}$ would have approximately

the same value as in Eq. (1.3), hence combining Eqs. (1.2) and (1.3) we obtain:

$$\mathbf{P}_{\mathrm{i}} = \mathbf{P} - \mathbf{P}_{\mathrm{e}} = (4\pi)^{-1}(\epsilon_{\infty}^{-1} - \epsilon_{0}^{-1})\,\mathbf{D}\,. \tag{1.4}$$

The Fourier components $\mathbf{P}_{\mathrm{i},\mathbf{q}}$ can be expressed in terms of the atomic displacements in the unit cell corresponding to a LO phonon, which are parallel to the wavevector $\mathbf{q}$. In the second quantization formalism this is expressed using the phonon creation ($\hat{a}_{\mathbf{q}}^{\dagger}$) and destruction ($\hat{a}_{\mathbf{q}}$) operators as we will see in Sec. 3.1.1, therefore we have:

$$\mathbf{P}_{\mathrm{i},\mathbf{q}} = \sqrt{\hbar/(2N_{\mathrm{c}}\Omega\gamma\omega_{\mathrm{LO}})}\,\hat{q}\,(\hat{a}_{\mathbf{q}} + \hat{a}_{-\mathbf{q}}^{\dagger})\,, \tag{1.5}$$

where Ω is the volume of the unit cell and N_{c} is the number of cells in the unit volume of the crystal. The constant $1/\gamma = \omega_{\mathrm{LO}}^{2}/(4\pi)(\epsilon_{\infty}^{-1} - \epsilon_{0}^{-1})$ is obtained from the static limit of the equation of motion for the classic ionic polarization field in the presence of an electron [2, 3].

In the absence of free external charges we have $\boldsymbol{\nabla}\cdot\mathbf{D} = 0$, or $i\mathbf{q}\cdot\mathbf{D}_{\mathbf{q}} = 0$ for each Fourier component, hence $\mathbf{E}_{\mathbf{q}} = -4\pi\mathbf{P}_{\mathbf{q}}$. In describing the motion of an electron in the ionic lattice field, only the lattice polarization $\mathbf{P}_{\mathrm{i},\mathbf{q}}$ needs to be considered [2]. The potential associated to the electric field $\mathbf{E}$ generated by the longitudinal optical phonons ($\mathbf{E}_{\mathbf{q}} = -i\mathbf{q}\,\Phi_{\mathbf{q}}$) is then given by:

$$\Phi_{\mathbf{q}} = -i\frac{4\pi}{q}\left(\frac{\hbar}{2N_{\mathrm{c}}\Omega\gamma\omega_{\mathrm{LO}}}\right)^{1/2}(\hat{a}_{\mathbf{q}} + \hat{a}_{-\mathbf{q}}^{\dagger})\,, \tag{1.6}$$

with $q = |\mathbf{q}|$. After substituting $1/\gamma$ in Eq. (1.6), the Fröhlich Hamiltonian is readily found from $\hat{H}_{\mathrm{F},\mathbf{q}} = -e\Phi_{\mathbf{q}}$:

$$\hat{H}_{\mathrm{F}} = \frac{1}{\sqrt{N_{\mathrm{c}}}}\sum_{\mathbf{q}} g_{\mathrm{F}}(\mathbf{q})\,e^{i\mathbf{q}\cdot\mathbf{r}}\left(\hat{a}_{\mathbf{q}} + \hat{a}_{-\mathbf{q}}^{\dagger}\right), \tag{1.7}$$

with the Fröhlich matrix element $g_{\mathrm{F}}(\mathbf{q})$ defined as:

$$g_{\mathrm{F}}(\mathbf{q}) = \frac{i}{q}\left[\frac{4\pi e^{2}}{\Omega}\frac{\hbar\omega_{\mathrm{LO}}}{2}\left(\frac{1}{\epsilon_{\infty}} - \frac{1}{\epsilon_{0}}\right)\right]^{1/2}. \tag{1.8}$$

The matrix element is often expressed in terms of a dimensionless parameter α, also

called the *Fröhlich coupling constant*:

$$\alpha = \frac{e^2}{\hbar}\left(\frac{m_\mathrm{b}}{2\hbar\omega_\mathrm{LO}}\right)^{1/2}\left(\frac{1}{\epsilon_\infty}-\frac{1}{\epsilon_0}\right), \tag{1.9}$$

with m_b the band effective mass of the conduction electron. The square modulus of Eq. (1.8) then takes the form:

$$|g_\mathrm{F}(\mathbf{q})|^2 = \frac{4\pi\hbar\,\alpha\,(\hbar\omega_\mathrm{LO})^{3/2}}{\sqrt{2m_\mathrm{b}}\,\Omega\,q^2}\,. \tag{1.10}$$

The Fröhlich Hamiltonian is one of the most extensively studied problems in condensed matter theory, as it describes the general problem of a fermionic particle interacting with a scalar bosonic field (the phonon). Depending on the value of α, i.e. on the strength of the coupling, it is customary to distinguish between weak, intermediate and strong coupling regimes. The latter is often considered as a formal case not verified in actual solid state systems [4]. While weak coupling can be treated using perturbation theory, several formalisms have been developed to tackle also intermediate regimes, such as the Lee, Low and Pines canonical transformation technique [5] or the linked cluster theory [6]. The most accurate solution comes from Feynman's variational method based on the path integral approach [7] which is applicable for any value of α. Extensive reviews on the Fröhlich literature can be found for example in Refs. [3, 4, 8]; here we recall some fundamental results from Rayleigh-Schrödinger perturbation theory regarding the renormalization of the electronic energy and mass. In this approximation, the lowest energy for an electron with zero momentum is found to be $E_0 = -\alpha\hbar\omega_\mathrm{LO}$ [2]. For small momenta, the result is:

$$E_\mathbf{k} = -\alpha\hbar\omega_\mathrm{LO} + \varepsilon_\mathbf{k}(1-\alpha/6)\,, \tag{1.11}$$

with $\varepsilon_\mathbf{k} = k^2/(2m_\mathrm{b})$ the energy of the unperturbed electron in the effective mass approximation. From Eq. (1.11) it follows that the renormalized ('dressed') effective mass is then given by:

$$m^* = m_\mathrm{b}/(1-\alpha/6)\,. \tag{1.12}$$

Surprisingly, even if perturbation theory should apply only for small values of α ($\alpha \lesssim 1$),

it has been shown that it constitutes a good approximation for values of α up to $\alpha \lesssim 5$, so that the perturbative results are often used at weak and intermediate coupling regimes [4]. These results strictly apply to the interaction of a single electron with LO phonons under the assumptions of the Fröhlich model. In Chapter 4 we will present a generalization of the polar Fröhlich coupling in the presence of many electrons within the formalism of many-body perturbation theory.

An electron moving in a polar crystal together with the lattice distortion or, in the language of second quantization, with the phonon cloud, is generally referred to as a polaron. The term polaron was first introduced by Pekar and Landau while studying the possibility of self-trapping of an electron in a polarizable medium [1, 9]. The Fröhlich Hamiltonian describes what is generally called a large polaron. In fact, the underlying assumption of treating the lattice as a continuum holds if the size of a polaron is larger than the lattice parameter. The length scale at play can roughly be estimated with the following reasoning: the distance traveled by an electron within the period of an atomic vibration $\omega_{\mathrm{LO}}^{-1}$ is $\Delta r \sim \Delta v/\omega_{\mathrm{LO}}$, with Δv the quadratic mean square deviation of the electron velocity. The uncertainty principle tells us that $\Delta p \Delta r \geq \hbar/2$, hence $m_{\mathrm{b}} \Delta v^2/\omega_{\mathrm{LO}} \geq \hbar/2$. From this we obtain $\Delta r \geq \sqrt{\hbar/(2m_{\mathrm{b}}\omega_{\mathrm{LO}})}$, which can be used as an estimate for the validity of the Fröhlich continuum model. The renormalized energy and effective mass from the perturbative treatment of the Fröhlich Hamiltonian presented above are therefore often referred to as the large polaron binding energy and effective mass.

The formation of polarons has profound implications for the charge-carrier properties of the material. A large polaron can be thought of as moving in the crystal analogously to an electron in the conduction band, with a higher effective mass. Its mobility $\mu = e\tau/m^*$, with τ the scattering time, falls with temperature following approximately the inverse of the phonon occupation number, $n(\omega_{\mathrm{LO}}) = (e^{\hbar\omega_{\mathrm{LO}}/(k_{\mathrm{B}}T)} - 1)^{-1}$ [10]. On the other hand, for small polarons, that is polarons with a radius compatible with the size of the lattice, the conduction mechanism is widely different, with a generally low mobility dominated by thermally-activated hopping from site to site [11, 12].

1.2 Polarons in ARPES spectra

The interest in investigating the electron-phonon coupling, not least of the Fröhlich type, has been invigorated by the recent advances in experimental techniques such as high-resolution angle-resolved photoemission spectroscopy (ARPES) [13] and, even more recently, resonant inelastic X-ray scattering (RIXS) [14], which made it possible to resolve spectral features within a few meV. In ARPES experiments the energy and emission angle of the photoexcited electrons emitted from the sample after irradiating it with photons are measured. Using momentum and energy conservation it is then possible to map the electronic band structure of the sample. RIXS, on the other hand, is a resonant technique where the incident photon energy is tuned to coincide with an atomic X-ray transition of the material. Information about the excited states is provided by the change in energy, momentum and polarization of the scattered photons. While in the following we focus mainly on ARPES, we also mention interesting RIXS results.

A common effect of the electron-phonon interaction, combined with other scattering mechanisms, is the broadening of the spectral lines in ARPES experiments and in other spectroscopy techniques. As we will see in the next section, within many-body theory this is described by the imaginary part of an electron-phonon self-energy. In this thesis we will concentrate extensively on this effect; in particular, in Chapter 5 we will investigate it by looking at the broadening of the emission peak in photoluminescence experiments on hybrid lead halide perovskites.

Another well-known effect is the appearance of kinks in the band dispersions, as measured for example in high-temperature superconducting cuprates, bilayer manganites and graphene [15, 16, 17, 18]. An additional spectral feature, characteristic of the Fröhlich electron-phonon coupling, is the presence of a series of satellite replica below the conduction band bottom, spaced by integer multiples of a LO phonon energy. This is the signature of polarons in ARPES spectra. The satellite intensities decrease following

a Poisson's distribution, the nth satellite corresponding to the excitation of n phonons. Correspondingly, in RIXS experiments the signature of polaronic states is the appearance of an asymmetric tail on one side of the main elastic peak in the measured intensities, which can be resolved as separate satellites spaced by a LO phonon energy, as seen in Ref. [19].

Fröhlich physics has received a renewed interest fuelled by experimental evidence of polarons in materials such as doped (polar) oxides. A notable example, and the first clear-cut observation of polaronic satellite replica, is n-doped anatase TiO_2 [20]. The spectra measured at low and intermediate doping concentration reveal a series of up to three satellites with an energy separation compatible with the highest LO phonon of anatase, while at high doping a band structure kink near a phonon energy below the Fermi level appears. In subsequent works, evidence of Fröhlich polarons comes from the investigation of two-dimensional (2D) electronic states at the surfaces or interfaces of oxides [21]. The most interesting and thoroughly studied case is the 2D electron gas (2DEG) formed at the surface of $SrTiO_3$. For this system, polaronic features have been observed in Refs. [22, 23], but the most conspicuous findings come from Ref. [24], where the doping dependence of the ARPES spectra has been tracked. This shows a behavior similar to the case of bulk anatase TiO_2. The interface between $SrTiO_3$ and $LaAlO_3$ also offers a playground for the formation of polarons [25]. These studies of 2D surface states are nicely complemented by earlier experiments on bulk $SrTiO_3$ [26, 27]. Another interesting material is ZnO, which has provided evidence for intermediate Fröhlich coupling involving 2D surface states [28]. Surface states in TiO_2 have been somewhat less investigated, with a band structure kink observed in Ref. [29]. Theoretical studies of these spectral features fully from first principles are still missing, with calculations generally employing analytical models or fitted self-energies. We will explore this problem in Chapter 7 and 8.

At last, we comment that ARPES experiments seem to provide evidence for the existence of large Fröhlich polarons. These results have sparkled more debate on the question of whether polarons in real systems such as doped TiO_2, $SrTiO_3$ and ZnO are small or

large, and on the strength of the coupling. An interesting point is that the Fröhlich constant α is found to be in an intermediate regime for these materials, thus suggesting a scenario that may include an interplay of small and large polarons or some intermediate polaronic regime. We will touch on the question of the polaron size in Chapter 7.

1.3 ARPES spectra from first principles

ARPES spectra constitute an exceptional point of contact between theory and experiment. In fact, as we are going to show the ARPES photocurrent is directly linked to the one-particle spectral function that can be calculated using techniques based on many-body perturbation theory. Notably, the experimental accuracy reached in recent years [13, 30] enables unprecedented comparisons between theoretical calculations and ARPES experiments, thus allowing to gain a deep insight into the electronic properties of materials. Indeed, the current state of first-principles calculations of ARPES spectra is far behind the abundant volume of experimental results, and more advanced and accurate calculations are called for.

A schematic description of the ARPES process is given by the three-step model [31]: first, a single electron is excited due to the incident light; then, the photoexcited electron travels to the surface of the sample, and finally it is emitted from the surface and detected by the analyzer. The measured ARPES photocurrent depends on the transition probability w_{0m} for an optical excitation between the initial ground state of the N-electron system $\Psi_0(N)$ and a final state $\Psi_m(N)$. Using Fermi's golden rule, this is:

$$w_{0m} = \frac{2\pi}{\hbar} \left| \langle \Psi_m(N) \,|\, \hat{\Delta} \,|\, \Psi_0(N) \rangle \right|^2 \delta(E_{\text{kin}} + E_{N-1,m} - E_{N,0} - \hbar\omega), \tag{1.13}$$

where the many-body wavefunction $\Psi_m(N)$ describes an excited state of the $(N-1)$-electron system plus the photoexcited electron. The energy-conserving delta function contains the kinetic energy of the photoelectron E_{kin}, the total energy of the N and $(N-1)$-electron system and the energy of the photon $\hbar\omega$. $\hat{\Delta}$ is the dipole transition operator

that accounts for the photon absorption cross section. This can be written in second quantization as $\hat{\Delta} = \sum_{\mathbf{k}''\mathbf{k}} \Delta_{\mathbf{k}''\mathbf{k}} \hat{c}^{\dagger}_{\mathbf{k}''} \hat{c}_{\mathbf{k}}$, with $\Delta_{\mathbf{k}''\mathbf{k}}$ the dipole matrix element, and $\hat{c}^{\dagger}_{\mathbf{k}}$ ($\hat{c}_{\mathbf{k}}$) an operator that creates (destroys) an electron with momentum $\mathbf{k}$ (see Appendix A).

At this point it is customary to introduce the so-called sudden approximation, where the photoelectron is assumed to be emitted almost instantaneously from the sample, and hence it does not interact with the $(N-1)$-electron system. The many-body state $\Psi_m(N)$ can then be approximated as the product of the many-body wavefunction $\Psi_m(N-1)$ and the wavefunction of an excited electronic state with momentum $\mathbf{k}'$, $\psi_{\mathbf{k}'}$. This corresponds to neglecting the intermediate step in the three-step model. In practice, extrinsic losses coming from the interaction of the photoelectron with the system can play an important role in renormalizing the spectral weights [32, 33]. Within the sudden approximation, the transition probability then takes the form [13]:

$$\begin{aligned} w_{0m} &= \frac{2\pi}{\hbar} \Big| \langle \Psi_m(N-1) | \, \hat{c}_{\mathbf{k}'} \sum_{\mathbf{k}''\mathbf{k}} \Delta_{\mathbf{k}''\mathbf{k}} \hat{c}^{\dagger}_{\mathbf{k}''} \hat{c}_{\mathbf{k}} \, | \Psi_0(N) \rangle \Big|^2 \delta(E_{\mathrm{kin}} + E_{N-1,m} - E_{N,0} - \hbar\omega) \\ &= \frac{2\pi}{\hbar} \sum_{\mathbf{k}} |\Delta_{\mathbf{k}'\mathbf{k}}|^2 \Big| \langle \Psi_m(N-1) | \, \hat{c}_{\mathbf{k}} \, | \Psi_0(N) \rangle \Big|^2 \delta(E_{\mathrm{kin}} - E_m - \hbar\omega) \,, \end{aligned} \tag{1.14}$$

where we used the commutation relations of the ladder operators in Appendix A, and we introduced the definition of the electron removal energy $E_m = E_{N,0} - E_{N-1,m}$ which corresponds to the energy of the m-th excited state of the $(N-1)$-electron system. After summing over all possible final states and neglecting the effects of the photon absorption cross section, the ARPES intensity is found to be proportional to the one-electron spectral function defined as:

$$A(\mathbf{k}, \omega) = \sum_m \Big| \langle \Psi_m(N-1) | \, \hat{c}_{\mathbf{k}} \, | \Psi_0(N) \rangle \Big|^2 \delta(\hbar\omega - E_m) \,. \tag{1.15}$$

The braket in Eq. (1.15) has the meaning of probability amplitude that the removal of an electron from the initial system will leave the $(N-1)$-electron system in the excited state m. If temperature effects are included, this needs to be multiplied by the Fermi-Dirac distribution $f(\omega) = (e^{\hbar\omega/(k_{\mathrm{B}}T)} + 1)^{-1}$.

The spectral function in Eq. (1.15) is related to the imaginary part of the one-electron Green's function by:

$$A(\mathbf{k},\omega) = \frac{1}{\pi}|\mathrm{Im}G(\mathbf{k},\omega)|. \tag{1.16}$$

We will discuss Green's functions in Chapter 3, however we introduce a few useful concepts here. In Green's function theory the electrons are described in terms of weakly interacting *quasiparticles* with a finite lifetime. The interaction is described by a self-energy, which includes all interaction effects with other quasiparticles e.g. electrons and phonons. If the electrons were noninteracting, then the spectral function would simply be a sharp delta function peaked at the electronic energy $\varepsilon_{\mathbf{k}}$. In fact, the Green's function for noninteracting electrons of energy $\varepsilon_{\mathbf{k}}$ is $G^0(\mathbf{k},\omega) = [\hbar\omega - \varepsilon_{\mathbf{k}} + i\eta\,\mathrm{sgn}(\varepsilon_{\mathbf{k}})]^{-1}$, with η a positive infinitesimal. Using the relation $(x \pm i\eta)^{-1} = \mathrm{P}(1/x) \mp i\pi\delta(x)$, one obtains $A(\mathbf{k},\omega) = \delta(\hbar\omega - \varepsilon_{\mathbf{k}})$. If the denominator of the Green's function contained a finite imaginary part Γ instead, as for a decaying particle, the spectral function would assume a Lorentzian shape: $A(\mathbf{k},\omega) = \pi^{-1}\,\Gamma/[(\hbar\omega - \varepsilon_{\mathbf{k}})^2 + \Gamma^2]$. In a real interacting system, a Lorentzian peak identifies a quasiparticle, with the broadening given by the imaginary part of the self-energy, while the real part is responsible for the shift of the peak position with respect to the noninteracting energy.[1] Moreover, the strength of the peak can be renormalized, and additional structures called satellites can emerge at higher binding energy. This picture is summarized in Fig. 1.1.

In the case of polar electron-phonon coupling, satellite peaks at multiples of $\hbar\omega_{\mathrm{LO}}$ can be observed as outlined in the previous section. Interestingly, this scenario can be obtained theoretically within an independent boson model similar to the Fröhlich Hamiltonian. By making use of a canonical transformation, it is possible to show that the spectral function results in a series of delta functions spaced exactly by $\hbar\omega_{\mathrm{LO}}$, with the peak intensities following a Poisson's distribution [35, 4]. In Chapter 7 we will see how multiple satellites can emerge from a many-body theory.

[1] To be more rigorous, the quasiparticle peak has an asymmetric Breit-Wigner form in general [34].

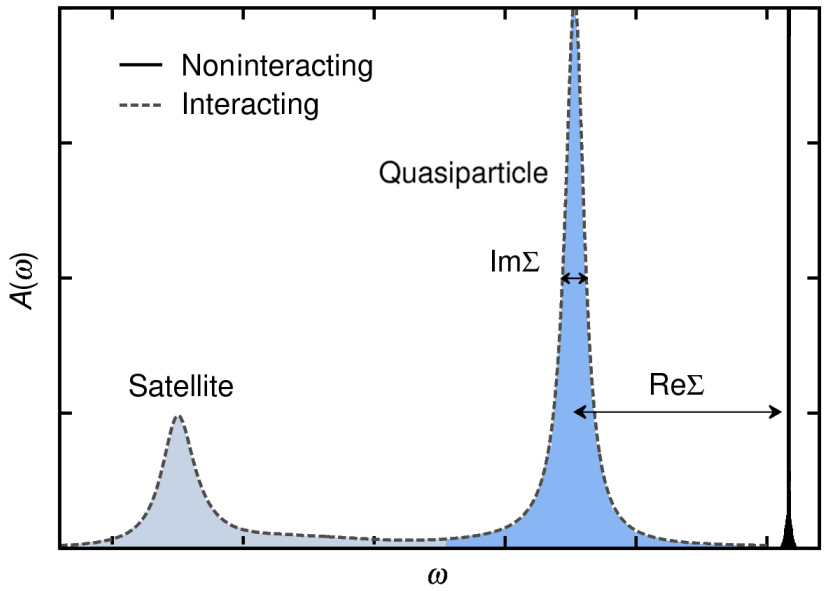

Figure 1.1: Schematic representation of the spectral function at fixed **k** showing the difference between a noninteracting and an interacting electronic system (the units are arbitrary in this example).

1.4 Overview of the thesis

In this chapter we provided an overview of some effects of the electron-phonon coupling that underlie and motivate the main topics of this thesis. In particular, we introduced the Fröhlich model for the polar electron-phonon coupling, and some experimental findings on polarons in doped oxides.

The rest of the thesis is organized as follows. In Chapter 2 we summarize the main theoretical framework for carrying out first-principles calculations of electronic and vibrational properties in solids, namely density-functional theory using a pseudopotential and plane-wave implementation, and density-functional perturbation theory, with additional focus on the treatment of polar materials. Chapter 3 covers the theory of the electron-phonon interactions within the second quantization and Green's function formalism. An overview of practical *ab initio* calculations and of the Wannier-Fourier interpolation technique of the `EPW` code is also given. In Chapter 4 we develop a formalism for calculating the electron-phonon matrix elements in polar semiconductors and insulators from first

principles, and we demonstrate its use in conjunction with Wannier-Fourier interpolation by performing calculations on GaN and $SrTiO_3$. Chapter 5 shows an application of the method whereby only the generalized Fröhlich matrix element is used in order to calculate electron and hole linewidths in a popular material for photovoltaic applications, the hybrid lead halide perovskite $CH_3NH_3PbI_3$. Chapter 6 and 7 deal with anatase TiO_2: in Chapter 6 we study the electron-phonon coupling and electron lifetimes, whereas in Chapter 7 we move to investigating the polaronic properties in doped anatase. In particular we present first-principles calculations of ARPES spectra using the cumulant expansion method and screened electron-phonon matrix elements, and we compute a polaron wavefunction using first-order perturbation theory. In Chapter 8 we use a similar approach to study the signature of polar electron-phonon coupling and the crossover from polarons to Fermi liquids in ARPES spectra of doped EuO. Finally, Chapter 9 contains the conclusions of this thesis and an outlook on interesting further work.

CHAPTER 2

First-principles methods: electrons and phonons

This chapter describes some of the fundamental theories underlying first-principles calculations of electronic and vibrational properties in solids, that is, density-functional theory and density-functional perturbation theory. The aim of the chapter is not to cover these topics in detail, but to introduce some of the main concepts and tools that constitute a starting point for the calculations presented in this thesis. First we briefly review density-functional theory in the Kohn-Sham and pseudopotential approximation, which is a common and successful choice for solving the electronic problem, and a seed for more sophisticated techniques based on many-body perturbation theory. We then describe how the lattice vibrations can be calculated using density-functional perturbation theory. In addition, the last section focuses on some properties specific to polar materials, namely the macroscopic electric field created by longitudinal optical vibrations and the LO-TO splitting induced by the dipole-dipole interactions.

2.1 Density-functional theory

2.1.1 The Born-Oppenheimer approximation

The evolution of a non-relativistic system of interacting electrons and nuclei (or ions) is governed by the Hamiltonian:[1]

$$\hat{H} = -\sum_i \frac{\hbar^2 \nabla_i^2}{2m_e} - \sum_I \frac{\hbar^2 \nabla_I^2}{2M_I} + \frac{1}{2}\sum_{i\neq j} \frac{e^2}{|\mathbf{r}_i - \mathbf{r}_j|} - \sum_{i,I} \frac{e^2 Z_I}{|\mathbf{r}_i - \mathbf{R}_I|} + \frac{1}{2}\sum_{I\neq J} \frac{e^2 Z_I Z_J}{|\mathbf{R}_I - \mathbf{R}_J|}, \quad (2.1)$$

where the index i runs over the N electrons with mass m_e and the index I over the M nuclei with mass M_I and atomic number Z_I; $\mathbf{r}_i, \mathbf{R}_I$ are the positions of electrons and nuclei respectively. The problem of solving the many-body Schrödinger equation associated to $\hat{H}$ and determining the energies and wavefunctions of the system $\Phi(\mathbf{r}_1, \ldots, \mathbf{r}_N, \mathbf{R}_1, \ldots, \mathbf{R}_M)$ is enormously complex because of the large number of interactions involved.

In order to simplify the problem, it is customary to apply the so-called adiabatic or Born-Oppenheimer approximation [36] which allows to decouple the nuclear and electronic degrees of motion, thanks to the fact that the nuclei are orders of magnitude more massive than the electrons. The nuclei can then be considered as fixed during the electronic motion, so that the wavefunction of the electrons $\Psi(\mathbf{r}_1, \ldots \mathbf{r}_N)$ depends only parametrically on the nuclear coordinates $\{\mathbf{R}_I\}$. The electronic Hamiltonian now reads:

$$\hat{H}_e = -\sum_i \frac{\hbar^2 \nabla_i^2}{2m_e} + \frac{1}{2}\sum_{i\neq j} \frac{e^2}{|\mathbf{r}_i - \mathbf{r}_j|} - \sum_{i,I} \frac{e^2 Z_I}{|\mathbf{r}_i - \mathbf{R}_I|}, \quad (2.2)$$

where the $\{\mathbf{R}_I\}$ are parameters: the nuclei produce a static external potential. Even with this simplification it is clear that finding the electronic many-body wavefunction is a formidable task, for which further approximations or different approaches are needed.

[1] We remind that Gaussian units are used throughout the thesis.

2.1.2 The Hohenberg–Kohn theorems

A breakthrough in the many-body problem came from the density-functional approach, which has its roots in the seminal work of Thomas [37] and Fermi [38] dated back in 1927, but relies on the theorems introduced by Hohenberg and Kohn in 1964 [39]. In density-functional theory (DFT) the N-body problem is exactly reformulated in terms of the electronic density associated with the full N-particle wavefunction $\Psi(\mathbf{r}_1, \mathbf{r}_2, \ldots, \mathbf{r}_N)$:

$$n(\mathbf{r}) = \langle \Psi | \sum_{i=1}^{N} \delta(\mathbf{r} - \mathbf{r}_i) | \Psi \rangle = N \int d\mathbf{r}_2 \cdots d\mathbf{r}_N \, |\Psi(\mathbf{r}, \mathbf{r}_2, \ldots, \mathbf{r}_N)|^2 \,. \tag{2.3}$$

This constitutes an important simplification at least in principle, as $n(\mathbf{r})$ depends only on one variable.

Let us consider an arbitrary system of N interacting fermions in an external potential V_{ext}, such as the electron-nuclei potential. Then:

Theorem I $V_{\text{ext}}(\mathbf{r})$ is uniquely determined (except for an additive constant) by the ground-state density $n_0(\mathbf{r})$.

Theorem II The energy of the system $E = \langle \Psi | \hat{H} | \Psi \rangle$ is a unique functional of $n(\mathbf{r})$, written in the form:

$$E[n] = F[n] + \int V_{\text{ext}}(\mathbf{r})\, n(\mathbf{r})\, d\mathbf{r} \,, \tag{2.4}$$

where $F[n]$ is a universal density functional (it does not depend on the external potential of the system). Moreover, the ground-state energy is the global minimum of this functional, and the density which minimizes $E[n]$ is the ground-state density $n_0(\mathbf{r})$.

These theorems thus guarantee that all ground-state properties of the system can be derived *exactly* from the density of the ground state; however, the complexity of the problem is hidden into the functional $F[n]$ which is unknown in general, so one has to rely on some approximations.

2.1.3 The Kohn-Sham equations

The scheme introduced by Kohn and Sham [40] enables a practical implementation of DFT. The main idea is to replace the interacting system with an auxiliary system of independent particles with the same ground-state density as the original one. Then, the universal functional $F[n]$ in Eq. (2.4) is rewritten as:

$$F[n] = T_0[n] + E_{\mathrm{H}}[n] + E_{\mathrm{xc}}[n], \tag{2.5}$$

where $T_0[n]$ is the kinetic energy of a system of noninteracting electrons with density $n(\mathbf{r})$, $E_{\mathrm{H}}[n]$ is the so-called Hartree energy:

$$E_{\mathrm{H}}[n] = \frac{e^2}{2}\int \frac{n(\mathbf{r})n(\mathbf{r}')}{|\mathbf{r}-\mathbf{r}'|}\,d\mathbf{r}d\mathbf{r}', \tag{2.6}$$

and $E_{\mathrm{xc}}[n]$ is defined as the exchange and correlation energy of an interacting system with density $n(\mathbf{r})$. After minimizing the total energy functional $E[n]$ with respect to the density, with the constraint that the number of electrons is fixed, the same equations that would hold for a system of noninteracting electrons in an effective potential $V_{\mathrm{KS}}(\mathbf{r})$ are formally obtained. Therefore, we are left to solve the one-particle Schrödinger equations:

$$\hat{H}_{\mathrm{KS}}\psi_i(\mathbf{r}) = \left(-\frac{\hbar^2\nabla^2}{2m_e} + V_{\mathrm{KS}}[n](\mathbf{r})\right)\psi_i(\mathbf{r}) = \varepsilon_i\psi_i(\mathbf{r}), \tag{2.7}$$

where $\psi_i(\mathbf{r})$ are the auxiliary single-particle Kohn-Sham orbitals. This set of equations must be solved self-consistently with the density of the interacting system:

$$n(\mathbf{r}) = \sum_{i=1}^{N} |\psi_i(\mathbf{r})|^2 . \tag{2.8}$$

The effective Kohn-Sham potential $V_{\mathrm{KS}}(\mathbf{r})$ is given by:

$$V_{\mathrm{KS}}[n](\mathbf{r}) = V_{\mathrm{ext}}(\mathbf{r}) + V_{\mathrm{H}}(\mathbf{r}) + V_{\mathrm{xc}}[n](\mathbf{r}), \tag{2.9}$$

where V_{H} is the Hartree potential:

$$V_{\mathrm{H}}(\mathbf{r}) = e^2\int \frac{n(\mathbf{r}')}{|\mathbf{r}-\mathbf{r}'|}d\mathbf{r}', \tag{2.10}$$

and $V_{\rm xc}$ is the so-called exchange-correlation potential (δ is a functional derivative [41]):

$$V_{\rm xc}[n](\mathbf{r}) = \frac{\delta E_{\rm xc}}{\delta n(\mathbf{r})}\,. \tag{2.11}$$

The total energy can now be expressed in terms of the Kohn-Sham eigenvalues:

$$E[n] = \sum_{i=1}^{N} \varepsilon_i - \frac{e^2}{2}\int \frac{n(\mathbf{r})n(\mathbf{r}')}{|\mathbf{r}-\mathbf{r}'|} d\mathbf{r}d\mathbf{r}' + E_{\rm xc}[n] - \int V_{\rm xc}(\mathbf{r})n(\mathbf{r})d\mathbf{r}\,. \tag{2.12}$$

The eigenenergies ε_i found by solving self-consistently the Kohn-Sham equations are used to describe the electronic band structure as a first approximation, even if this leads to well-known failures such as a systematic underestimation of the band gaps [42, 43].

2.1.4 Exchange-correlation functionals

As seen in the previous section, all the effects of exchange and correlation between electrons are transferred into the exchange-correlation energy functional, whose exact form is unknown. Various approximations for it have been proposed [41]. The simplest, and still widely used, is the so-called local density approximation (LDA), in which the exchange-correlation energy is cast into the form:

$$E_{\rm xc}[n] = \int d\mathbf{r}\, n(\mathbf{r})\, \varepsilon_{\rm xc}[n](\mathbf{r})\,, \tag{2.13}$$

where $\varepsilon_{\rm xc}[n](\mathbf{r})$ is the exchange-correlation energy density of a homogeneous electron gas with the same density $n(\mathbf{r})$ at every point of space. The exchange energy for a homogeneous electron gas is known analytically, whereas the correlation part can be interpolated from nearly exact Quantum Monte Carlo calculations [44, 45].

If the system was totally homogeneous, the LDA would be exact by definition. A natural way to improve upon the LDA for a real system is to make $\varepsilon_{\rm xc}$ dependent on derivatives of the density, in order to account for its inhomogeneity: $\varepsilon_{\rm xc} = \varepsilon_{\rm xc}[n(\mathbf{r}), \nabla n(\mathbf{r}), \dots]$. The simplest case with $\varepsilon_{\rm xc} = \varepsilon_{\rm xc}[n(\mathbf{r}), \nabla n(\mathbf{r})]$ corresponds to the so-called generalized gradient approximation (GGA). The GGA has become widely used, for example in the form proposed in Ref [46], even if it is not proven that it systematically improves over the LDA results.

2.1.5 Practical calculations: plane waves and pseudopotentials

In this thesis we rely on the DFT implementation of the `Quantum ESPRESSO` suite of *ab initio* computer codes [47], which is based on a plane-wave and pseudopotential representation. Born-von Kármán (BvK) periodic boundary conditions are used (see Appendix B). In the following the spin index is included in the wavevector index for simplicity, and we consider spin-degenerate systems, although the formalism can be generalized to spin-polarized systems [41, 48].

Plane waves

In a crystalline solid all properties are periodic with respect to the unit of repetition of the crystal. Thanks to Bloch's theorem, the wavefunction of an electron in a periodic potential can be written in the form [41]:

$$\psi_{i\mathbf{k}}(\mathbf{r}) = \frac{1}{\sqrt{N_c}} u_{i\mathbf{k}}(\mathbf{r})\, e^{i\mathbf{k}\cdot\mathbf{r}}, \tag{2.14}$$

where N_c is the number of crystal unit cells in the BvK supercell, $\mathbf{k}$ is a wavevector in the first Brillouin zone (see Appendix B) and the Kohn-Sham orbitals are given by $\psi_i(\mathbf{r}) = \sum_{\mathbf{k}} \psi_{i\mathbf{k}}(\mathbf{r})$. The function $u_{i\mathbf{k}}(\mathbf{r})$ has the periodicity of the crystal, $u_{i\mathbf{k}}(\mathbf{r}+\mathbf{R}) = u_{i\mathbf{k}}(\mathbf{r})$, with $\mathbf{R}$ a lattice vector. Since $u_{i\mathbf{k}}(\mathbf{r})$ is periodic, it can be expanded in terms of the Fourier series:

$$u_{i\mathbf{k}}(\mathbf{r}) = \frac{1}{\sqrt{\Omega}} \sum_{\mathbf{G}} c_{i\mathbf{k}}(\mathbf{G})\, e^{i\mathbf{G}\cdot\mathbf{r}}, \tag{2.15}$$

where $\mathbf{G}$ are reciprocal lattice vectors, Ω is the volume of the unit cell and $c_{i\mathbf{k}}(\mathbf{G})$ are complex Fourier coefficients. Putting together Eqs. (2.14) and (2.15), the wavefunctions can be written as a linear combination of plane waves:

$$\psi_{i\mathbf{k}}(\mathbf{r}) = \frac{1}{\sqrt{N_c\Omega}} \sum_{\mathbf{G}} c_{i\mathbf{k}}(\mathbf{G})\, e^{i(\mathbf{k}+\mathbf{G})\cdot\mathbf{r}}. \tag{2.16}$$

We note that in this convention $\psi_{i\mathbf{k}}(\mathbf{r})$ is normalized to one in the BvK supercell, while the periodic function $u_{i\mathbf{k}}(\mathbf{r})$ is normalized to one in the crystal unit cell. The periodicity of $u_{i\mathbf{k}}(\mathbf{r})$ can be exploited to reduce the domain of spatial integrals from the BvK supercell to a single unit cell.

Plane waves constitute a complete orthonormal basis set, but in actual calculations the number of **G** vectors used is truncated, with a cutoff defined by the relation $\hbar^2/(2m_e)|\mathbf{k}+\mathbf{G}|^2 \leq E_{cut}$. The convergence of the calculations with respect to the number of plane waves used (i.e. with respect to E_{cut}) then needs to be checked.

The expansion of the electronic wavefunctions in terms of plane waves allows to rewrite the Kohn-Sham Schrödinger equation (2.7) in a simple form [41]:

$$\sum_{\mathbf{G}'}\left(\frac{\hbar^2}{2m_e}|\mathbf{k}+\mathbf{G}|^2\delta_{\mathbf{G},\mathbf{G}'}+V_{KS}(\mathbf{G}-\mathbf{G}')\right)c_{i\mathbf{k}}(\mathbf{G}')=\epsilon_{i\mathbf{k}}\,c_{i\mathbf{k}}(\mathbf{G}), \tag{2.17}$$

where the Kohn-Sham potential is also expanded in Fourier series. In practice, the terms in Eq. (2.17) involving pairs of $\mathbf{G},\mathbf{G}'$ are most conveniently calculated on a real-space grid, and Fast Fourier Transform (FFT) algorithms are used to help speeding up the self-consistent solution of the Kohn-Sham equations. In general, Eq. (2.17) should be modified to take into account the nonlocality of V_{KS} that can arise from pseudopotential representations (see below) by writing $V_{KS}(\mathbf{k}+\mathbf{G},\mathbf{k}+\mathbf{G}')$.

Pseudopotentials

Even if plane-wave basis sets have many advantages, an all-electron calculation including both core and valence electrons can be very expensive. This is because the wavefunctions oscillate rapidly near the nuclei to maintain orthogonality, and thus a very high number of plane waves is required in order to accurately describe these oscillations. This issue can be overcome by the introduction of pseudopotentials [41, 49], which treat the core electrons and the nuclei together as an ionic core, therefore representing the interaction between valence electrons and ionic cores. This choice is supported by the fact that most of the physical properties are dependent on the valence electrons to a much greater extent than on the core electrons.

An *ab initio* pseudopotential is constructed in such a way that the pseudo wavefunction has no radial nodes within a core region of radius r_c, and that the pseudo wavefunction and potential match the true wavefunction and potential outside that region.

Norm-conserving pseudopotentials [50] also satisfy the condition that for each pseudo orbital, the integrated charge inside r_c agrees with the all-electron one. The smaller the cutoff radius r_c, the more accurate and transferable the pseudopotential is. On the other hand, if r_c is large the pseudofunction is smoother (fewer plane waves are needed to describe it), but transferability from one material to another will worsen. As an additional note, pseudopotentials are also nonlocal in general, meaning that they depend on both $\mathbf{r}$ and $\mathbf{r}'$, $V_{PS}(\mathbf{r},\mathbf{r}')$. This is due to the need of taking into account different angular momentum states for the wavefunctions around the nuclei [41]. In the following we will not consider explicitly the nonlocality of the pseudopotentials when discussing the electron-nuclei interactions in order to keep the formalism simpler.

In general, one must be extremely careful in the construction or choice of suitable pseudopotentials for each calculation needed. In particular, the choice of including so-called semicore states (core electrons in the outermost shells) in the valence configuration can prove to be crucial if there is a large spatial overlap between semicore and valence electrons wavefunctions, or if the energy levels of the semicore states are close to the valence ones. In the following chapters we will specify our choices of pseudopotentials.

2.2 Density-functional perturbation theory

2.2.1 Lattice dynamics

So far we have only been concerned with the electronic properties of crystals. The nuclei were considered fixed in their equilibrium positions during the electronic motion, acting on the electrons through a Coulomb potential V_{ext}. We now move on to study the vibrations of the nuclei.

Within the Born-Oppenheimer approximation introduced in Sec. 2.1.1, the lattice-dynamical properties of the system are determined by the Schrödinger equation:

$$\left(-\sum_I \frac{\hbar^2}{2M_I}\frac{\partial^2}{\partial \mathbf{R}_I^2} + E_N(\{\mathbf{R}_I\}) + E(\{\mathbf{R}_I\})\right)\chi(\{\mathbf{R}_I\}) = \mathcal{E}\chi(\{\mathbf{R}_I\}), \tag{2.18}$$

where $\mathcal{E}$ is the total energy of the system and χ is the nuclear wavefunction. In Eq. (2.18) $E_{\mathrm{N}}(\{\mathbf{R}_I\}) = e^2/2\sum_{I\neq J} Z_I Z_J/|\mathbf{R}_I - \mathbf{R}_J|$ denotes the Coulomb repulsion between different nuclei and $E(\{\mathbf{R}_I\})$ the total electronic energy at clamped nuclei (calculated from DFT). The total potential energy of the nuclei is then $U = E_{\mathrm{N}} + E$, also known as the Born-Oppenheimer energy surface. The equilibrium geometry of the system is given by the condition of vanishing forces for each nucleus I and Cartesian component α: $F_{I\alpha} = -\partial U/\partial R_{I\alpha} = 0$, hence it can be found by minimizing the Born-Oppenheimer energy surface with respect to all nuclear degrees of freedom.

If we consider the nuclear positions as time dependent, we can write them as $\mathbf{R}_I(t) = \mathbf{R}_I^0 + \mathbf{u}_I(t)$ with $\mathbf{R}_I^0$ the fixed equilibrium positions and $\mathbf{u}_I(t)$ the time-dependent displacements. Expanding the potential energy U around the equilibrium positions up to second order in the nuclear displacements $\mathbf{u}_I$ (*harmonic approximation*), we obtain:

$$\begin{aligned} U(\{\mathbf{R}_I\}) &= U(\{\mathbf{R}_I^0\}) + \sum_{I\alpha} \frac{\partial U}{\partial R_{I\alpha}} u_{I\alpha} + \frac{1}{2}\sum_{I\alpha,J\beta} \frac{\partial^2 U}{\partial R_{I\alpha}\partial R_{J\beta}} u_{I\alpha} u_{J\beta} \\ &= U_0 + \frac{1}{2}\sum_{I\alpha,J\beta} C_{I\alpha,J\beta} u_{I\alpha} u_{J\beta}\,. \end{aligned} \tag{2.19}$$

The first-order derivatives correspond to the forces acting on the nuclei which vanish at the equilibrium, and in the last equality we introduced the following definition of the interatomic force constant (IFC) matrix C:

$$C_{I\alpha,J\beta} = \frac{\partial^2 U}{\partial R_{I\alpha}\partial R_{J\beta}}\,. \tag{2.20}$$

The motion of the nuclei can be described classically using Newton's equation:

$$M_I \ddot{u}_{I\alpha} = -\frac{\partial U}{\partial R_{I\alpha}} = -\sum_{J\beta} C_{I\alpha,J\beta} u_{J\beta}\,. \tag{2.21}$$

It is now easy to see that, within the harmonic approximation, the frequencies of vibration ω are determined from the solution of the secular equation:

$$\det\left|\frac{1}{\sqrt{M_I M_J}} C_{I\alpha,J\beta} - \omega^2\right| = 0\,. \tag{2.22}$$

Thanks to the Hellmann-Feynman theorem, the IFCs can be expressed as [51]:

$$C_{I\alpha,J\beta} = -\frac{\partial F_{I\alpha}}{\partial R_{J\beta}} = \int \frac{\partial n(\mathbf{r})}{\partial R_{J\beta}} \frac{\partial V_{\text{ep}}(\mathbf{r};\{\mathbf{R}_I\})}{\partial R_{I\alpha}} d\mathbf{r} + \int n(\mathbf{r}) \frac{\partial^2 V_{\text{ep}}(\mathbf{r};\{\mathbf{R}_I\})}{\partial R_{I\alpha}\partial R_{J\beta}} d\mathbf{r} + \frac{\partial^2 E_{\text{N}}(\{\mathbf{R}_I\})}{\partial R_{I\alpha}\partial R_{J\beta}}, \tag{2.23}$$

where $n(\mathbf{r})$ is the electron density with the nuclei in the position $\{\mathbf{R}_I\}$ and $V_{\text{ep}}(\mathbf{r};\{\mathbf{R}_I\}) = -e^2\sum_I Z_I/|\mathbf{r}-\mathbf{R}_I|$ is the electron-nuclei potential that substitutes the notation $V_{\text{ext}}(\mathbf{r})$ in the Kohn-Sham potential [Eq. (2.9)]. Therefore, in order to evaluate the IFCs – and thus the vibrational frequencies in Eq. (2.22) – one needs a strategy for calculating the linear response of the electronic density after a distortion in the nuclear geometry.

2.2.2 Linear response

The answer to the problem comes from density-functional perturbation theory (DFPT), which is based on the linear response theory of lattice vibrations applied to the DFT framework [52].

In order to keep the notation compact, let us denote by ΔA the variation of a physical quantity A due to a small perturbation, such as a nuclear distortion. Within linear response, we can write the variation of the total electronic density [Eq. (2.8)] as:

$$\Delta n(\mathbf{r}) = 2\,\text{Re}\sum_{i=1}^{N} \psi_i^*(\mathbf{r})\,\Delta\psi_i(\mathbf{r}). \tag{2.24}$$

The variation of the Kohn-Sham orbitals $\Delta\psi_i$ can be obtained through linearization of the Kohn-Sham Schrödinger equation (2.7):

$$(\hat{H}_{\text{KS}} - \varepsilon_i)\,|\Delta\psi_i\rangle = -(\Delta V_{\text{KS}} - \Delta\varepsilon_i)\,|\psi_i\rangle\,, \tag{2.25}$$

which corresponds to standard first-order perturbation theory.[2] In Eq. (2.25) $\hat{H}_{\text{KS}}$ is the self-consistent Kohn-Sham Hamiltonian given by the kinetic term plus V_{KS}, $\Delta\varepsilon_i = \langle\psi_i|\,\Delta V_{\text{KS}}\,|\psi_i\rangle$ is the first-order variation of the Kohn-Sham eigenvalues, and the varia-

[2] Eq. (2.25) is also known as a Sternheimer equation [53].

tion of the Kohn-Sham potential is given by:

$$\Delta V_{\mathrm{KS}}(\mathbf{r}) = \Delta V_{\mathrm{ep}}(\mathbf{r}) + e^2 \int \frac{\Delta n(\mathbf{r}')}{|\mathbf{r}-\mathbf{r}'|}\, d\mathbf{r}' + \left.\frac{dV_{\mathrm{xc}}(n)}{dn}\right|_{n=n(\mathbf{r})} \Delta n(\mathbf{r})\,. \tag{2.26}$$

Eqs. (2.24)–(2.26) are a set of self-consistent equations for the charge-density linear response of the perturbed system analogous to the set of Kohn-Sham equations (2.7)–(2.9) for the unperturbed electronic system. It can be shown that the self-consistent solution of these equations requires knowledge only of the occupied states of the system [54, 51]; thus, the cost of each perturbative step is similar to the one of a ground-state calculation.

2.2.3 Phonons

In the case of vibrations in crystalline solids, one usually denotes the position of each atom in the BvK supercell as:

$$\boldsymbol{\tau}_\kappa(\mathbf{R}) = \mathbf{R} + \boldsymbol{\tau}^0_\kappa + \Delta\boldsymbol{\tau}_\kappa(\mathbf{R})\,, \tag{2.27}$$

where $\mathbf{R}$ is a lattice vector, $\boldsymbol{\tau}^0_\kappa$ is the equilibrium position of atom κ in the primitive unit cell containing M atoms, and $\Delta\boldsymbol{\tau}_\kappa(\mathbf{R})$ is the deviation from the equilibrium. Therefore, the IFCs are defined as:

$$C_{\kappa\alpha,\kappa'\beta}(\mathbf{R},\mathbf{R}') = \frac{\partial^2 U}{\partial\tau_{\kappa\alpha}(\mathbf{R})\,\partial\tau_{\kappa'\beta}(\mathbf{R}')}\,, \tag{2.28}$$

and Newton's equation of motion is:

$$M_\kappa \Delta\ddot{\tau}_{\kappa\alpha}(\mathbf{R}) = -\sum_{\kappa'\beta\,\mathbf{R}'} C_{\kappa\alpha,\kappa'\beta}(\mathbf{R},\mathbf{R}')\Delta\tau_{\kappa'\beta}(\mathbf{R}')\,. \tag{2.29}$$

Analogously to the electronic wavefunctions, the atomic displacement eigenvectors in a crystal follow Bloch's theorem, therefore we can seek solutions of the form [55]:

$$\Delta\tau_{\kappa\alpha}(\mathbf{R},t) = u_{\kappa\alpha}/\sqrt{M_\kappa}\; e^{i(\mathbf{q}\cdot\mathbf{R}-\omega t)}\,, \tag{2.30}$$

with $u_{\kappa\alpha}$ the cell periodic amplitude and $\mathbf{q}$ a Brillouin zone vector. Inserting Eq. (2.30) into Eq. (2.29) we obtain:

$$\omega^2 u_{\kappa\alpha} = \sum_{\kappa'\beta} D_{\kappa\alpha,\kappa'\beta}(\mathbf{q})\, u_{\kappa'\beta}\,, \tag{2.31}$$

where the dynamical matrix is defined as the Fourier transform of the IFC matrix, scaled by the atomic masses:

$$D_{\kappa\alpha,\kappa'\beta}(\mathbf{q}) = \frac{1}{\sqrt{M_\kappa M_{\kappa'}}} \sum_{\mathbf{R}} e^{i\mathbf{q}\cdot\mathbf{R}} C_{\kappa\alpha,\kappa'\beta}(\mathbf{R}), \tag{2.32}$$

and we used the translational invariance property of the IFC, $C(\mathbf{R},\mathbf{R}') = C(\mathbf{R}-\mathbf{R}')$ [55]. The eigenvalues and eigenmodes of the dynamical matrix then correspond to the set of $\omega^2_{\mathbf{q}\nu}$ and $\mathbf{e}_{\kappa\nu}(\mathbf{q})$ ($\nu = 1,\ldots,3M$) that satisfy the equation:

$$\omega^2_{\mathbf{q}\nu} e_{\kappa\alpha\nu}(\mathbf{q}) = \sum_{\kappa'\beta} D_{\kappa\alpha,\kappa'\beta}(\mathbf{q})\, e_{\kappa'\beta\nu}(\mathbf{q}), \tag{2.33}$$

for each value of $\mathbf{q}$. According to Eq. (2.30), the ionic displacement corresponding a normal mode ($\mathbf{q}$, ν) is then:

$$\Delta\boldsymbol{\tau}_\kappa^{\mathbf{q}\nu}(\mathbf{R}) = \mathbf{e}_{\kappa\nu}(\mathbf{q})/\sqrt{M_\kappa}\, e^{i\mathbf{q}\cdot\mathbf{R}}. \tag{2.34}$$

Quantization is easily included by introducing the quanta of atomic oscillations or *phonons*, which are bosonic particles with energy $\hbar\omega_{\mathbf{q}\nu}$ and polarization $\mathbf{e}_{\kappa\nu}(\mathbf{q})$. This will be done in Chapter 3.

In DFPT the dynamical matrix Eq. (2.32) is calculated directly as the second derivative of the potential energy with respect to a static lattice distortion with wavevector $\mathbf{q}$. For the generalization of the linear response formalism of Sec. 2.2.2 to a perturbation with definite wavevector $\mathbf{q}$ we refer the reader to Refs. [54, 51], however we remark that the main advantage of DFPT for the calculation of lattice dynamics in condensed matter systems lies in the fact that perturbations with different wavevectors $\mathbf{q}$ are decoupled, and calculations for any arbitrary $\mathbf{q}$ can be performed within the crystal unit cell. This is in contrast with the direct method or *frozen-phonon* method, where the IFCs are obtained by finite differences after displacing each atom in the unit cell and calculating the resulting forces on every atom in a supercell. Moreover, in these calculations the size of the supercell needed to accurately calculate the force constants may be very large depending on the range of the interatomic forces. In Chapter 8 we will make use of the frozen-phonon method.

Phonon dispersions: Fourier interpolation

In order to calculate the complete phonon dispersion relations $\omega_{\mathbf{q}\nu}$, Fourier interpolation can be efficiently exploited [54, 56]. The dynamical matrices are first calculated for a uniform $N_1 \times N_2 \times N_3$ grid of $\mathbf{q}$ points and are then Fourier transformed to generate the real-space interatomic force constants matrix. This is taken to vanish outside the Wigner-Seitz supercell (SC) made of $N_c = N_1 \times N_2 \times N_3$ unit-cell replicas used to define the BvK supercell (see Appendix B):

$$\begin{aligned} C_{\kappa\alpha,\kappa'\beta}(\mathbf{R}) &= \frac{1}{N_c} \sum_{\mathbf{q}\in(N_1\times N_2\times N_3)} \widetilde{C}_{\kappa\alpha,\kappa'\beta}(\mathbf{q})\, e^{-i\mathbf{q}\cdot\mathbf{R}} \quad && \text{if } \mathbf{R}+\boldsymbol{\tau}^0_\kappa - \boldsymbol{\tau}^0_{\kappa'} \in \text{ SC}\,(N_1\times N_2\times N_3)\,; \\ &= 0 && \text{if } \mathbf{R}+\boldsymbol{\tau}^0_\kappa - \boldsymbol{\tau}^0_{\kappa'} \notin \text{ SC}\,(N_1\times N_2\times N_3)\,, \end{aligned} \tag{2.35}$$

where we denoted as $\widetilde{C}(\mathbf{q})$ the dynamical matrix multiplied by the square root of the masses, $\widetilde{C}_{\kappa\alpha,\kappa'\beta}(\mathbf{q}) = \sqrt{M_\kappa M_{\kappa'}}\, D_{\kappa\alpha,\kappa'\beta}(\mathbf{q})$.[3] Once the IFCs have been calculated following Eq. (2.35), the dynamical matrices for any arbitrary wavevector in reciprocal space can be obtained by Fourier transform, and their diagonalization yields the phonon eigenmodes and eigenvectors. The accuracy of the Fourier interpolation is determined by the range of decay of the force constants in real space, therefore the size of the initial $\mathbf{q}$ grid which defines the BvK supercell needs to be checked *a posteriori*.

2.3 Polar materials

2.3.1 Electric fields and LO-TO splitting

As seen in Sec. 1.1, in polar materials the longitudinal optical (LO) phonons at long wavelength give rise to a macroscopic electric field. The extension of the linear response formalism of DPFT to tackle the response to a homogeneous electric field $\mathbf{E}$ requires some care: in fact, the electrostatic potential $V_{\mathbf{E}} = e\mathbf{E}\cdot\mathbf{r}$ is not compatible with BvK boundary

[3] For brevity, in the following we will refer to either $D(\mathbf{q})$ and $\widetilde{C}(\mathbf{q})$ as the dynamical matrix.

conditions, due to the position operator $\mathbf{r}$ being ill-defined in a periodic system. One can notice, however, that the off-diagonal matrix elements of $\mathbf{r}$ needed in the calculation of the linear response of the electronic density are well defined [57]:

$$\langle\psi_i|\,\mathbf{r}\,|\psi_j\rangle = \frac{\langle\psi_i|\,[\hat{H}_{\mathrm{KS}},\mathbf{r}]\,|\psi_j\rangle}{\varepsilon_i-\varepsilon_j}\,,\quad i\neq j\,, \tag{2.36}$$

with $[\hat{H}_{\mathrm{KS}},\mathbf{r}] = -\hbar^2/(2m_{\mathrm{e}})\,\partial/\partial\mathbf{r} + [V_{\mathrm{KS}},\mathbf{r}]$, and the commutator with the Kohn-Sham potential is nonzero only if nonlocal pseudopotentials are used in the calculation.

The self-consistent (screened) electric field in the crystal satisfies:

$$E_\alpha + 4\pi P_{\mathrm{e},\alpha} = \sum_\beta \epsilon^\infty_{\alpha\beta} E_\beta\,, \tag{2.37}$$

where $\boldsymbol{\epsilon}_\infty$ is the electronic dielectric permittivity tensor and $\mathbf{P}_{\mathrm{e}}$ is the electronic induced polarization:

$$\mathbf{P}_{\mathrm{e}} = -\frac{e}{V}\int_V d\mathbf{r}\,\mathbf{r}\,\Delta^{\mathbf{E}} n(\mathbf{r})\,, \tag{2.38}$$

with $V = N_{\mathrm{c}}\Omega$. The density response $\Delta^{\mathbf{E}} n(\mathbf{r})$ can be calculated as in Eq. (2.24) using the linear variation of the Kohn-Sham orbitals $\Delta\psi_i^{\mathbf{E}}(\mathbf{r})$ induced by the electric field perturbation. It can be readily shown that Eq. (2.38) can be cast in a boundary-insensitive form using Eq. (2.36) [51], while $\Delta\psi_i^{\mathbf{E}}(\mathbf{r})$ satisfies a Sternheimer equation as in Eq. (2.25) including both the macroscopic and the microscopic induced perturbation. We mention for completeness that an alternative approach is given by the elegant *modern theory of polarization*, which reformulates the problem in terms of a Berry phase [58].

As seen in Sec. 1.1, in a polar material the total polarization $\mathbf{P}$ includes a contribution from the ions $\mathbf{P}_{\mathrm{i}}$, as dipoles are created by longitudinal optical vibrations of the atoms. The so-called Born effective charge tensor $\mathbf{Z}^*_\kappa$ gives the proportionality between the dipoles and the atomic displacements [59], so that:

$$P_\alpha = P_{\mathrm{e},\alpha} + P_{\mathrm{i},\alpha} = \frac{1}{4\pi}\left(\sum_\beta \epsilon^\infty_{\alpha\beta} E_\beta - E_\alpha\right) + \frac{e}{\Omega}\sum_{\kappa\beta} Z^{*\kappa}_{\alpha\beta}\Delta\tau_{\kappa\beta}\,, \tag{2.39}$$

where we used Eq. (2.37), and $\Delta\boldsymbol{\tau}_\kappa$ is the amplitude of an atomic displacement cor-

responding to a zone-center optical phonon. From Eq. (2.39) we see that $\boldsymbol{\epsilon}_\infty$ can be calculated from the derivative of the polarization with respect to the macroscopic electric field at clamped nuclei:

$$\epsilon^{\infty}_{\alpha\beta} = \delta_{\alpha\beta} + 4\pi \left.\frac{\partial P_\alpha}{\partial E_\beta}\right|_{\Delta\tau_\kappa=0}, \tag{2.40}$$

whereas the Born effective charges are the derivative of the macroscopic polarization with respect to an ionic displacement corresponding to a zone-center phonon at zero electric field [60]:

$$Z^{*\kappa}_{\alpha\beta} = \frac{\Omega}{e} \left.\frac{\partial P_\alpha}{\partial \tau_{\kappa\beta}}\right|_{\mathbf{E}=0}. \tag{2.41}$$

Both quantities are readily calculated within DFPT, by evaluating the linear response to an electric field as outlined above [54].

The coupling between the phonons and the electric field introduces a nonanalytic term in the dynamical matrix in the long-wavelength limit:

$$\widetilde{C}_{\kappa\alpha,\kappa'\beta}(\mathbf{q}\to 0) = \widetilde{C}^{\mathrm{AN}}_{\kappa\alpha,\kappa'\beta}(\mathbf{q}=0) + \widetilde{C}^{\mathrm{NA}}_{\kappa\alpha,\kappa'\beta}(\mathbf{q}\to 0)\,. \tag{2.42}$$

This result can be understood using a phenomenological model which also allows to derive the form of $\widetilde{C}^{\mathrm{NA}}(\mathbf{q}\to 0)$ [59, 61]. The potential energy in the presence of an electric field $\mathbf{E}$ can be expressed as:

$$U = \frac{1}{2}\sum_{\kappa\alpha,\kappa'\beta} \widetilde{C}^{\mathrm{AN}}_{\kappa\alpha,\kappa'\beta}\Delta\tau_{\kappa\alpha}\Delta\tau_{\kappa'\beta} - \frac{\Omega}{8\pi}\sum_{\alpha\beta} E_\alpha \epsilon^{\infty}_{\alpha\beta} E_\beta - e\sum_{\kappa\alpha\beta} E_\alpha Z^{*\kappa}_{\alpha\beta}\Delta\tau_{\kappa\beta}\,. \tag{2.43}$$

In order to derive $\mathbf{E}$ we first write the electric displacement field $\mathbf{D}$:

$$D_\alpha = E_\alpha + 4\pi P_\alpha = \sum_\beta \epsilon^{\infty}_{\alpha\beta} E_\beta + \frac{4\pi e}{\Omega}\sum_{\kappa\beta} Z^{*\kappa}_{\alpha\beta}\Delta\tau_{\kappa\beta}\,, \tag{2.44}$$

where we used Eq. (2.39). In the absence of external charges, $\mathbf{D}$ satisfies Maxwell's equation $\boldsymbol{\nabla}\cdot\mathbf{D}=0$ (hence $\mathbf{q}\cdot\mathbf{D}=0$), whereas $\mathbf{E}$ satisfies $\boldsymbol{\nabla}\times\mathbf{E}=0$ (hence $\mathbf{q}\times\mathbf{E}=0$). From these relations we find:

$$E_\alpha = -\frac{4\pi e}{\Omega}\sum_\kappa q_\alpha \frac{\sum_{\beta\beta'} q_\beta Z^{*\kappa}_{\beta\beta'}\Delta\tau_{\kappa\beta'}}{\sum_{\gamma\gamma'} q_\gamma \epsilon^{\infty}_{\gamma\gamma'} q_{\gamma'}}, \tag{2.45}$$

and by inserting Eq. (2.45) into Eq. (2.43) we explicitly obtain the expression for the nonanalytic part of the dynamical matrix:

$$\widetilde{C}^{\mathrm{NA}}_{\kappa\alpha,\kappa'\beta}(\mathbf{q}\to 0) = \frac{4\pi e^2}{\Omega}\,\frac{(\sum_\gamma q_\gamma Z^{*\kappa}_{\gamma\alpha})(\sum_{\gamma'} q_{\gamma'} Z^{*\kappa'}_{\gamma'\beta})}{\sum_{\gamma\gamma'} q_\gamma\, \epsilon^{\infty}_{\gamma\gamma'}\, q_{\gamma'}}\,. \tag{2.46}$$

Eq. (2.46) gives rise to the splitting of the transverse optical (TO) and LO frequencies at Γ, of which we will see some examples in the next chapters. This result can be derived equivalently starting from a microscopic treatment of the force constants in terms of the inverse electronic dielectric function $\epsilon^{-1}_{\mathrm{e}}(\mathbf{q}+\mathbf{G},\mathbf{q}+\mathbf{G}')$ [62, 63]. To connect microscopic and macroscopic descriptions, we recall that the macroscopic dielectric function is the inverse of the small-wavelength limit of the $\mathbf{G}=\mathbf{G}'=0$ element of the inverse dielectric function:

$$\epsilon_\infty(\hat{q}) = \lim_{\mathbf{q}\to 0} 1/\epsilon^{-1}_{\mathrm{e}}(\mathbf{q},\mathbf{q})\,, \tag{2.47}$$

and it represents the long-wavelength response of the system for frequencies much higher than the lattice phonon frequencies (but smaller than excitation energies across the gap), hence it is often slightly improperly called the *high-frequency* dielectric constant. The dielectric tensor introduced in Eq. (2.37) is connected to Eq. (2.47) by $\epsilon_\infty(\hat{q}) = \sum_{\alpha\beta}\hat{q}_\alpha\epsilon^{\infty}_{\alpha\beta}\hat{q}_\beta$. In Refs. [62, 63] a microscopic expression for the effective charges is also derived, of which $\boldsymbol{Z}^*_\kappa$ is the $\mathbf{q}\to 0$ limit.

2.3.2 Fourier interpolation

For nonpolar materials, the IFCs are short ranged, and the Fourier interpolation can be performed rather easily. In the case of polar materials instead, the IFCs are long ranged due to the dipole-dipole interactions, and Eq. (2.35) is not a good approximation anymore. The long range of the IFCs in real space is linked to the nonanalytic behavior of the dynamical matrix at long wavelength, as seen in Eq. (2.46).

Fourier interpolation can still be exploited also in the case of polar materials, provided that the strategy devised in Ref. [56] is used. The idea is that if we are able to calculate

the dipole contribution to the dynamical matrix $\widetilde{C}^{\mathrm{DD}}_{\kappa\alpha,\kappa'\beta}(\mathbf{q})$, this can be subtracted from the total dynamical matrix for each $\mathbf{q}$ in the original $N_1 \times N_2 \times N_3$ $\mathbf{q}$ grid:

$$\widetilde{C}^{\mathrm{SR}}_{\kappa\alpha,\kappa'\beta}(\mathbf{q}) = \widetilde{C}_{\kappa\alpha,\kappa'\beta}(\mathbf{q}) - \widetilde{C}^{\mathrm{DD}}_{\kappa\alpha,\kappa'\beta}(\mathbf{q}). \tag{2.48}$$

The real-space force constants $C^{\mathrm{SR}}_{\kappa\alpha,\kappa'\beta}(\mathbf{R})$ that are calculated as in Eq. (2.35) using the set of $\widetilde{C}^{\mathrm{SR}}_{\kappa\alpha,\kappa'\beta}(\mathbf{q})$ from Eq.(2.48) are expected to be short ranged. The dynamical matrix at any wavevector $\mathbf{q}$ can thus be obtained by Fourier transforming $C^{\mathrm{SR}}_{\kappa\alpha,\kappa'\beta}(\mathbf{R})$ and then adding back the dipole contribution $\widetilde{C}^{\mathrm{DD}}_{\kappa\alpha,\kappa'\beta}(\mathbf{q})$:

$$\widetilde{C}_{\kappa\alpha,\kappa'\beta}(\mathbf{q}) = \sum_{\mathbf{R}} C^{\mathrm{SR}}_{\kappa\alpha,\kappa'\beta}(\mathbf{R})\, e^{i\mathbf{q}\cdot\mathbf{R}} + \widetilde{C}^{\mathrm{DD}}_{\kappa\alpha,\kappa'\beta}(\mathbf{q}). \tag{2.49}$$

We refer to Appendix C.2 for the derivation of $\widetilde{C}^{\mathrm{DD}}(\mathbf{q})$ using the Ewald summation technique (Appendix C.1). The result is reported in Eq. (C.14).

CHAPTER 3

Electron-phonon interaction: theory and practical calculations

In this chapter we discuss the electron-phonon interactions. First the general form of the electron-phonon Hamiltonian in second quantization is presented, and how the electron-phonon matrix elements are calculated using density-functional perturbation theory. We also show that an electron-phonon self-energy can be derived within second-order perturbation theory. We then move to the field-theoretic description of the electron-phonon interaction which allows one to rigorously obtain the self-energy of the electrons. We do not present the full derivation which is extremely lengthy, but only describe the main steps. In the last part of the chapter an efficient technique for calculating the electron-phonon matrix elements which makes use of Wannier functions is presented.

3.1 Electron-phonon interaction Hamiltonian

The system of coupled electrons and phonons is described by the following Hamiltonian:

$$\hat{H} = \hat{H}_{\mathrm{e}} + \hat{H}_{\mathrm{p}} + \hat{H}_{\mathrm{ep}} \,. \tag{3.1}$$

In Chapter 2 we dealt with the electronic and lattice part, $\hat{H}_\mathrm{e}$ and $\hat{H}_\mathrm{p}$, within the Born-Oppenheimer and harmonic approximation. In the following we briefly rewrite them using the second quantization formalism, and we then derive the electron-phonon interaction part $\hat{H}_\mathrm{ep}$.

3.1.1 Second quantization

Within the Kohn-Sham formalism, all electron-electron interactions are cast into the one-electron effective Kohn-Sham Hamiltonian $\hat{H}_\mathrm{KS}$. Using Eq. (A.9) it is then easy to write it in second quantization:

$$\hat{H}_\mathrm{e} = \sum_{nm,\mathbf{k}\mathbf{k}'} \langle \psi_{m\mathbf{k}'} | \hat{H}_\mathrm{KS} | \psi_{n\mathbf{k}} \rangle \, \hat{c}^\dagger_{m\mathbf{k}'} \hat{c}_{n\mathbf{k}} = \sum_{n\mathbf{k}} \varepsilon_{n\mathbf{k}} \hat{c}^\dagger_{n\mathbf{k}} \hat{c}_{n\mathbf{k}} \,, \tag{3.2}$$

where we used n, m to label electronic states and $\varepsilon_{n\mathbf{k}}$ are Kohn-Sham eigenenergies.

The nuclear Hamiltonian in the adiabatic (Born-Oppenheimer) and harmonic approximation reads:

$$\hat{H}_\mathrm{p} = -\sum_{\kappa\alpha\mathbf{R}} \frac{\hbar^2}{2M_\kappa} \frac{\partial^2}{\partial \tau_{\kappa\alpha}(\mathbf{R})^2} + \frac{1}{2} \sum_{\mathbf{R}\mathbf{R}'} \sum_{\kappa\alpha,\kappa'\beta} C_{\kappa\alpha,\kappa'\beta}(\mathbf{R},\mathbf{R}') \Delta\tau_{\kappa\alpha}(\mathbf{R}) \Delta\tau_{\kappa'\beta}(\mathbf{R}') \,, \tag{3.3}$$

where we reformulated Eq. (2.19) for a crystalline system, with the constant energy term U_0 omitted and the interatomic force constants matrix defined in Eq. (2.28). $\hat{H}_\mathrm{p}$ can be rewritten in second quantization in terms of the phonon creation and destruction operators $\hat{a}^\dagger_{\mathbf{q}\nu}$ and $\hat{a}_{\mathbf{q}\nu}$ (see Appendix A). It can be shown that by expressing the atomic displacements as [64, 11]:

$$\Delta\tau_{\kappa\alpha}(\mathbf{R}) = \sum_{\mathbf{q}\nu} \Delta\tau^{\mathbf{q}\nu}_{\kappa\alpha}(\mathbf{R}) \, (\hat{a}_{\mathbf{q}\nu} + \hat{a}^\dagger_{-\mathbf{q}\nu}) = \left(\frac{\hbar}{2N_\mathrm{c} M_\kappa \omega_{\mathbf{q}\nu}} \right)^{1/2} \sum_{\mathbf{q}\nu} e^{i\mathbf{q}\cdot\mathbf{R}} e_{\kappa\alpha\nu}(\mathbf{q}) \, (\hat{a}_{\mathbf{q}\nu} + \hat{a}^\dagger_{-\mathbf{q}\nu}) \,, \tag{3.4}$$

the Hamiltonian takes the form:

$$\hat{H}_\mathrm{p} = \sum_{\mathbf{q}\nu} \hbar\omega_{\mathbf{q}\nu} (\hat{a}^\dagger_{\mathbf{q}\nu} \hat{a}_{\mathbf{q}\nu} + 1/2) \,, \tag{3.5}$$

with the sum over ν running from 1 to $3M$ (M is the number of atoms in the unit cell), and the sum over $\mathbf{q}$ running over the N_c wavevectors in the first Brillouin zone. The nuclei are thus described in terms of $3MN_c$ independent harmonic oscillators.

3.1.2 Electron-phonon coupling

Let us now consider the electron-phonon Hamiltonian. The Coulomb interaction between the electrons and the nuclei is given by:[1]

$$V_{ep}(\mathbf{r}, \{\boldsymbol{\tau}_\kappa(\mathbf{R})\}) = -e^2 \sum_{\kappa\mathbf{R}} \frac{Z_\kappa}{|\mathbf{r} - \boldsymbol{\tau}_\kappa(\mathbf{R})|}\,. \tag{3.6}$$

The zero-order term corresponding to the potential calculated with the atoms at their equilibrium positions, $V_{ep}(\mathbf{r}, \{\boldsymbol{\tau}^0_\kappa(\mathbf{R})\})$, is already included in the electronic Hamiltonian $\hat{H}_e$ as the external potential term. The electron-phonon coupling Hamiltonian is obtained from the linear variation of the potential with respect to the atomic displacements. The linear variation of V_{ep}, however, constitutes only the 'bare' electron-phonon coupling potential. In a many-body system one needs to additionally take into account the electronic response that acts to screen the electron-nuclei interaction. The electronic response also has an effect in renormalizing the phonon frequencies, for it enters the interatomic force constant matrix as seen in Eq. (2.23). The full electron-phonon coupling then must be obtained from the linear variation of the self-consistent Kohn-Sham potential that is calculated within DFPT:

$$\Delta V_{KS} = \sum_{\kappa\alpha\mathbf{R}} \partial_{\kappa\alpha,\mathbf{R}} V_{KS}\, \Delta\tau_{\kappa\alpha}(\mathbf{R})\,, \tag{3.7}$$

where we defined $\partial_{\kappa\alpha,\mathbf{R}} V_{KS} = \partial V_{KS}/\partial\tau_{\kappa\alpha}(\mathbf{R})$. Formally, this can be written in terms of an electronic dielectric response function screening the bare electron-ion potential:

$$\Delta V_{KS} = \epsilon^{-1}_{KS}\, \Delta V_{ep}\,. \tag{3.8}$$

[1] In actual calculations V_{ep} is described by a pseudopotential as discussed in Sec. 2.1.5, therefore Eq. (3.6) should in practice be replaced by the corresponding pseudopotential formulation.

In fact, the electronic polarization function can be defined as the density response to a variation of the total effective potential [41]: $P_{\mathrm{KS}} = \delta n / \delta V_{\mathrm{KS}}$. After substituting this in Eq. (2.26), the dielectric screening in Eq. (3.8) is obtained:

$$\epsilon_{\mathrm{KS}} = 1 - (v + f_{\mathrm{xc}})\, P_{\mathrm{KS}}\,, \tag{3.9}$$

where v is the Coulomb potential and f_{xc} is the so-called exchange-correlation kernel, given by $\delta^2 E_{\mathrm{xc}} / \delta n \delta n$.

Substituting the atomic displacements of Eq. (3.4) in Eq. (3.7) yields:

$$\Delta V_{\mathrm{KS}} = \frac{1}{\sqrt{N_{\mathrm{c}}}} \sum_{\mathbf{q}\nu} \partial_{\mathbf{q}\nu} V_{\mathrm{KS}} \left(\hat{a}_{\mathbf{q}\nu} + \hat{a}^{\dagger}_{-\mathbf{q}\nu}\right), \tag{3.10}$$

with:

$$\partial_{\mathbf{q}\nu} V_{\mathrm{KS}} = \sum_{\kappa\alpha} \left(\frac{\hbar}{2M_{\kappa}\omega_{\mathbf{q}\nu}}\right)^{1/2} e_{\kappa\alpha\nu}(\mathbf{q}) \sum_{\mathbf{R}} e^{i\mathbf{q}\cdot\mathbf{R}} \partial_{\kappa\alpha,\mathbf{R}} V_{\mathrm{KS}} \tag{3.11}$$

$$= \sum_{\kappa\alpha} \left(\frac{\hbar}{2M_{\kappa}\omega_{\mathbf{q}\nu}}\right)^{1/2} e_{\kappa\alpha\nu}(\mathbf{q})\, \partial_{\kappa\alpha,\mathbf{q}} V_{\mathrm{KS}}\,. \tag{3.12}$$

The advantage of isolating the quantity $\partial_{\kappa\alpha,\mathbf{q}} V_{\mathrm{KS}} = \sum_{\mathbf{R}} e^{i\mathbf{q}\cdot\mathbf{R}} \partial_{\kappa\alpha,\mathbf{R}} V_{\mathrm{KS}}$ in Eq. (3.12) is that this is precisely the variation of the self-consistent potential with respect to a lattice distortion with wavevector $\mathbf{q}$ that is calculated in DFPT, as seen in Sec. 2.2 [54]. The electron-phonon Hamiltonian in second quantization can now be written following Eq. (A.9) and using Eq. (3.10):

$$\hat{H}_{\mathrm{ep}} = \sum_{mn,\mathbf{k}\mathbf{k}'} \langle \psi_{m\mathbf{k}'} | \Delta V_{\mathrm{KS}} | \psi_{n\mathbf{k}} \rangle\, \hat{c}^{\dagger}_{m\mathbf{k}'} \hat{c}_{n\mathbf{k}} \tag{3.13}$$

$$= \frac{1}{\sqrt{N_{\mathrm{c}}}} \sum_{mn\nu,\,\mathbf{k}\mathbf{q}} g_{mn\nu}(\mathbf{k},\mathbf{q})\, \hat{c}^{\dagger}_{m\mathbf{k}+\mathbf{q}} \hat{c}_{n\mathbf{k}} \left(\hat{a}_{\mathbf{q}\nu} + \hat{a}^{\dagger}_{-\mathbf{q}\nu}\right), \tag{3.14}$$

with the electron-phonon matrix elements $g_{mn\nu}(\mathbf{k},\mathbf{q})$ defined as:

$$g_{mn\nu}(\mathbf{k},\mathbf{q}) = \langle \psi_{m\mathbf{k}+\mathbf{q}} |\, \partial_{\mathbf{q}\nu} V_{\mathrm{KS}} \,| \psi_{n\mathbf{k}} \rangle\,. \tag{3.15}$$

The selection rule $\delta_{\mathbf{k}',\mathbf{k}+\mathbf{q}}$ follows from Bloch's theorem and from the translational invariance of ΔV_{KS}. The so-called *umklapp* processes are included by letting $\mathbf{k}+\mathbf{q}$ fall outside the first Brillouin zone and folding it back with a reciprocal lattice vector $\mathbf{G}$ [65]. For the

case of Fröhlich electron-phonon coupling seen in Sec. 1.1, the matrix element is given by $g_{mn\nu}(\mathbf{k},\mathbf{q}) = g_{\mathrm{F}}(\mathbf{q})\,\delta_{mn}\delta_{\nu,\mathrm{LO}}$ with $g_{\mathrm{F}}(\mathbf{q})$ from Eq. (1.8) and ν corresponding to a LO phonon mode.

3.1.3 Second-order perturbation theory

Starting from the Hamiltonian in Eq. (3.14) we can now derive the renormalization of the electronic energies due to the electron-phonon interaction using standard Rayleigh-Schrödinger perturbation theory. The first-order correction vanishes because the matrix elements of the perturbation in Eq. (3.14) are nonzero only between different initial and final states. For an electron with Bloch energy $\varepsilon_{n\mathbf{k}}$, the correction is then given by second-order perturbation theory [4]:

$$\Delta\varepsilon_{n\mathbf{k}} = \sum_{f\neq i} \frac{|\langle f|\hat{H}_{\mathrm{ep}}|i\rangle|^2}{E_i - E_f}\,. \tag{3.16}$$

The initial and final states $|i\rangle$ and $|f\rangle$ are given by the product of electronic and ionic many-body wavefunctions, that is Slater determinants of Kohn-Sham wavefunctions for the electronic part and products of harmonic oscillators wavefunctions for the ionic one. The calculation of the matrix elements in Eq. (3.16) follows from the action of the ladder operators described in Appendix A on these states. In particular, the only nonzero matrix elements are the ones that couple initial states with phonon number $n_{\mathbf{q}\nu}$ and final states with phonon number $n_{\mathbf{q}\nu}\pm 1$. At finite temperature, $n_{\mathbf{q}\nu}$ represents the Bose-Einstein distribution [Eq. (A.4)], while $f_{n\mathbf{k}}$ is the Fermi-Dirac distribution [Eq. (A.8)]. After considering an initial electronic state containing one added electron in the state $|\psi_{n\mathbf{k}}\rangle$ we obtain:

$$\Delta\varepsilon'_{n\mathbf{k}} = \frac{1}{N_{\mathrm{c}}}\sum_{m\mathbf{q}\nu}|g_{mn\nu}(\mathbf{k},\mathbf{q})|^2\left[\frac{(1-f_{m\mathbf{k}+\mathbf{q}})(n_{\mathbf{q}\nu}+1)}{\varepsilon_{n\mathbf{k}}-\varepsilon_{m\mathbf{k}+\mathbf{q}}-\hbar\omega_{\mathbf{q}\nu}} + \frac{(1-f_{m\mathbf{k}+\mathbf{q}})\,n_{\mathbf{q}\nu}}{\varepsilon_{n\mathbf{k}}-\varepsilon_{m\mathbf{k}+\mathbf{q}}+\hbar\omega_{\mathbf{q}\nu}}\right], \tag{3.17}$$

where the first term in the square brackets corresponds to a phonon emission process, and the second one to a phonon absorption process. There is, however, an additional many-body contribution: indeed, one needs to subtract from Eq. (3.17) a similar expression

that forbids an electron in the initial state $|\psi_{m\mathbf{k}+\mathbf{q}}\rangle$ to scatter via phonon emission or absorption into a final state $|\psi_{n\mathbf{k}}\rangle$, which is already occupied by the added electron [66]:

$$\Delta\varepsilon''_{n\mathbf{k}} = \frac{1}{N_c}\sum_{m\mathbf{q}\nu}|g_{mn\nu}(\mathbf{k},\mathbf{q})|^2\left[\frac{f_{m\mathbf{k}+\mathbf{q}}(n_{\mathbf{q}\nu}+1)}{\varepsilon_{m\mathbf{k}+\mathbf{q}}-\varepsilon_{n\mathbf{k}}-\hbar\omega_{\mathbf{q}\nu}}+\frac{f_{m\mathbf{k}+\mathbf{q}}\,n_{\mathbf{q}\nu}}{\varepsilon_{m\mathbf{k}+\mathbf{q}}-\varepsilon_{n\mathbf{k}}+\hbar\omega_{\mathbf{q}\nu}}\right]. \tag{3.18}$$

The renormalized electron energy is then obtained after subtracting Eq. (3.18) from Eq. (3.17):

$$E_{n\mathbf{k}} = \varepsilon_{n\mathbf{k}} + \frac{1}{N_c}\sum_{m\mathbf{q}\nu}|g_{mn\nu}(\mathbf{k},\mathbf{q})|^2\left[\frac{n_{\mathbf{q}\nu}+f_{m\mathbf{k}+\mathbf{q}}}{\varepsilon_{n\mathbf{k}}-\varepsilon_{m\mathbf{k}+\mathbf{q}}+\hbar\omega_{\mathbf{q}\nu}}+\frac{n_{\mathbf{q}\nu}+1-f_{m\mathbf{k}+\mathbf{q}}}{\varepsilon_{n\mathbf{k}}-\varepsilon_{m\mathbf{k}+\mathbf{q}}-\hbar\omega_{\mathbf{q}\nu}}\right]. \tag{3.19}$$

We conclude this section by noting that the result in Eq. (3.19) is commonly known in the literature of semiconductors and insulators as the Fan self-energy [67], although in the popular Allen-Heine theory of the temperature-dependence of the band structure the phonon energies $\hbar\omega_{\mathbf{q}\nu}$ are generally neglected [68]. An additional contribution to the self-energy, however, emerges if the electron-phonon Hamiltonian expanded up to second order in the atomic displacements is considered. In fact, the second-order term gives a contribution to the renormalized electronic energies that is nonvanishing in first-order perturbation theory, hence of the same order as the Fan term [68]. This is the so-called Debye-Waller self-energy. In this thesis we neglect this term as it is (i) real, hence it does not contribute to the broadening of the electron linewidths, and (ii) static, therefore it does not give rise to additional structure in the one-electron spectral function $A(\mathbf{k},\omega)$. The Debye-Waller term cannot be neglected when studying the zero-point renormalization and the temperature dependence of the electronic band structure [69, 70, 71].

3.2 Many-Body Perturbation Theory

The most rigorous and complete way to derive the electron-phonon self-energy is by using the quantum field theory approach based on Green's functions. The derivation is closely related to the one leading to the *GW* method of Hedin [72], but it is much more elaborate. In fact, the *GW* method corresponds to the theory of electrons in a rigid lattice;

the electron-phonon coupling, on the other hand, is obtained by considering electrons in a vibrating lattice. Such derivation is rarely seen in the literature, and it is nicely presented in Ref. [34]. Only recently a thorough formulation that accurately includes all electron and phonon self-energy terms appeared [73]. In light of this, we find it interesting and useful to describe the main steps that lead to a rigorous derivation of the electron-phonon self-energy, referring to Refs. [34, 73, 74] for a lengthy and detailed treatment.

3.2.1 Self-energy of interacting electrons in a vibrating lattice

The starting point is the complete Hamiltonian of the system written using quantum field operators. The electronic field operators $\hat{\psi}^\dagger(\mathbf{r})$, $\hat{\psi}(\mathbf{r})$ creating or destroying an electron at point $\mathbf{r}$ in space are defined in Appendix A, while for the nuclei we use the operators corresponding to the nuclear displacements from equilibrium $\Delta\hat{\boldsymbol{\tau}}$. The electronic spin variable is ignored for simplicity. In this formalism the Hamiltonian of the system of electrons and nuclei takes the form:

$$\begin{aligned}\hat{H} = &-\frac{\hbar^2}{2m_\mathrm{e}}\int d\mathbf{r}\,\hat{\psi}^\dagger(\mathbf{r})\nabla^2\hat{\psi}(\mathbf{r}) + \frac{1}{2}\int d\mathbf{r}d\mathbf{r}'\hat{\psi}^\dagger(\mathbf{r})\hat{\psi}^\dagger(\mathbf{r}')v(\mathbf{r},\mathbf{r}')\hat{\psi}(\mathbf{r}')\hat{\psi}(\mathbf{r}) \\ &+ \int d\mathbf{r}d\mathbf{r}'\hat{\psi}^\dagger(\mathbf{r})v(\mathbf{r},\mathbf{r}')\hat{n}_\mathrm{n}(\mathbf{r}')\hat{\psi}(\mathbf{r}) + \hat{T}_\mathrm{n} + \hat{V}_\mathrm{nn}\,,\end{aligned} \tag{3.20}$$

where $v(\mathbf{r},\mathbf{r}') = e^2/|\mathbf{r}-\mathbf{r}'|$, $\hat{T}_\mathrm{n}$ and $\hat{V}_\mathrm{nn}$ are the kinetic and potential energy of the nuclei, and we defined the nuclear charge density operator as:

$$\hat{n}_\mathrm{n}(\mathbf{r}) = -\sum_{\kappa\mathbf{R}} Z_\kappa \delta(\mathbf{r}-\boldsymbol{\tau}^0_\kappa-\mathbf{R}-\Delta\hat{\boldsymbol{\tau}}_\kappa(\mathbf{R}))\,. \tag{3.21}$$

It is useful to define also the total charge density operator:

$$\hat{n}(\mathbf{r}) = \hat{n}_\mathrm{e}(\mathbf{r}) + \hat{n}_\mathrm{n}(\mathbf{r})\,, \tag{3.22}$$

where the electronic part is given by:

$$\hat{n}_\mathrm{e}(\mathbf{r}) = \hat{\psi}^\dagger(\mathbf{r})\,\hat{\psi}(\mathbf{r})\,. \tag{3.23}$$

The one-electron Green's function $G(\mathbf{r}t,\mathbf{r}'t')$ at zero temperature is defined in Ap-

pendix D as a time-ordered product of the time-dependent field operators. From the definition in Eq. (D.1) we can see that formally it represents the probability amplitude to find an electron in position $\mathbf{r}$ at time t having added an electron in $\mathbf{r}'$ at time t' (if $t > t'$), or the same for a hole if $t < t'$; hence it is also often called the electronic propagator. From the Heisenberg equation of motion satisfied by the field destruction operator $\hat{\psi}(\mathbf{r}, t)$, Eq. (A.15), the equation of motion for the Green's function can be derived [34]:

$$\left[i\hbar\frac{\partial}{\partial t} + \frac{\hbar^2}{2m_e}\nabla^2 - \phi(\mathbf{r}, t) \right] G(\mathbf{r}t, \mathbf{r}'t') + i/\hbar \int d\mathbf{r}''dt'' v(\mathbf{r}, \mathbf{r}'') \langle \mathcal{T}[\hat{n}(\mathbf{r}'', t'')\hat{\psi}(\mathbf{r}, t)\hat{\psi}^\dagger(\mathbf{r}', t')] \rangle = \delta(\mathbf{r}t, \mathbf{r}'t'), \quad (3.24)$$

where the braket indicates the average over the ground state and $\mathcal{T}$ is the time-ordering operator as in Eq. (D.1). An additional term $\phi(\mathbf{r}, t)$ has been introduced. This is an external perturbing potential that couples with both the electronic and nuclear densities, and it formally allows to exploit Schwinger's functional derivative technique [34]. In order to treat the complicated interaction problem, described by the last term on the left-hand side of Eq. (3.24), it is now customary to introduce a *self-energy* operator, which is nonlocal and time-dependent in general. This is defined from the comparison with Eq. (3.24):

$$i/\hbar \int d\mathbf{r}''dt'' v(\mathbf{r}, \mathbf{r}'') \langle \mathcal{T}[\hat{n}(\mathbf{r}'', t'')\hat{\psi}(\mathbf{r}, t)\hat{\psi}^\dagger(\mathbf{r}', t')] \rangle = - \int d\mathbf{r}''dt''\Sigma(\mathbf{r}t, \mathbf{r}''t'')G(\mathbf{r}''t'', \mathbf{r}'t') + \int d\mathbf{r}' v(\mathbf{r}, \mathbf{r}') \langle \hat{n}(\mathbf{r}', t) \rangle G(\mathbf{r}t, \mathbf{r}'t'). \quad (3.25)$$

It is useful to define the total average potential acting on the electrons and nuclei:

$$V(\mathbf{r}, t) = \int d\mathbf{r}' v(\mathbf{r}, \mathbf{r}') \langle n(\mathbf{r}', t) \rangle + \phi(\mathbf{r}, t), \quad (3.26)$$

so that inserting Eqs. (3.25) and (3.26) in Eq. (3.24), the equation of motion of the Green's function becomes:

$$\left[i\hbar\frac{\partial}{\partial t} + \frac{\hbar^2}{2m_e}\nabla^2 - V(\mathbf{r}, t) \right] G(\mathbf{r}t, \mathbf{r}'t') - \int d\mathbf{r}''dt''\Sigma(\mathbf{r}t, \mathbf{r}''t'')G(\mathbf{r}''t'', \mathbf{r}'t') = \delta(\mathbf{r}t, \mathbf{r}'t'). \quad (3.27)$$

Let us now start using a lighter notation where e.g. $(1) = (\mathbf{r}, t)$ and $v(12) = v(\mathbf{r}, \mathbf{r}')$ $\delta(t - t')$. We define the inverse total dielectric function of the system as the functional derivative of V with respect to the external potential field ϕ:

$$\epsilon^{-1}(12) = \frac{\delta V(1)}{\delta \phi(2)} = \delta(12) + \int d(3) v(13) \frac{\delta \langle \hat{n}(3) \rangle}{\delta \phi(2)}, \tag{3.28}$$

and the screened Coulomb interaction W is:

$$W(12) = \int d(3)\, \epsilon^{-1}(13) v(32). \tag{3.29}$$

Using the definition in Eq. (3.28) and the chain rule for functional derivatives, the latter can also be written as:

$$W(12) = v(12) + \int d(34) v(13) P(34) W(42), \tag{3.30}$$

having defined the polarization propagator:

$$P(12) = \frac{\delta \langle \hat{n}(1) \rangle}{\delta V(2)}, \tag{3.31}$$

which contains the contribution from both the electrons and the nuclei displacements. Correspondingly, it is possible to define an *electronic* polarization as:

$$P_{\mathrm{e}}(12) = \frac{\delta \langle \hat{n}_{\mathrm{e}}(1) \rangle}{\delta V(2)}, \tag{3.32}$$

so that the Coulomb potential screened only by the electrons is:

$$W_{\mathrm{e}}(12) = v(12) + \int d(34) v(13) P_{\mathrm{e}}(34) W_{\mathrm{e}}(42) = \int d(3)\, \epsilon_{\mathrm{e}}^{-1}(13) v(32), \tag{3.33}$$

where the electronic dielectric function is given by:

$$\epsilon_{\mathrm{e}}(12) = \delta(12) - \int d(3) v(13) P_{\mathrm{e}}(32). \tag{3.34}$$

If we now introduce the density-density correlation function for the nuclei, which depends on the nuclear density fluctuations:

$$D(12) = -i/\hbar \, \langle \mathcal{T} [\hat{n}_{\mathrm{n}}(1) - \langle \hat{n}_{\mathrm{n}}(1) \rangle] [\hat{n}_{\mathrm{n}}(2) - \langle \hat{n}_{\mathrm{n}}(2) \rangle] \rangle, \tag{3.35}$$

it is possible to show that the total screened Coulomb potential W can be expressed as:

$$W(12) = W_{\mathrm{e}}(12) + \int d(34) W_{\mathrm{e}}(13) D(34) W_{\mathrm{e}}(24) . \tag{3.36}$$

The derivation is nontrivial and it requires to introduce an additional external perturbation that couples only to the nuclei in order to evaluate the term $\delta \hat{n}_{\mathrm{n}}/\delta\phi$ appearing in Eq. (3.29) after inserting Eq. (3.28) [34].

We are still left with deriving an expression for the self-energy operator Σ. This is done by inserting into Eq. (3.24) the following functional identity [34]:

$$\frac{\delta G(12)}{\delta\phi(3)} = -1/\hbar^2 \left\langle \mathcal{T}[\hat{n}(3) - \langle \hat{n}(3)\rangle] \hat{\psi}(1)\hat{\psi}^{\dagger}(2)\right\rangle , \tag{3.37}$$

which results in:

$$\left[i\hbar \frac{\partial}{\partial t_1} + \frac{\hbar^2}{2m_{\mathrm{e}}}\nabla_1^2 - V(1)\right] G(12) - i\hbar \int d(3) v(1^+3) \frac{\delta G(12)}{\delta\phi(3)} = \delta(12) , \tag{3.38}$$

with $1^+ = 1 + \eta$, η a positive infinitesimal arising from the time ordering. After some manipulations using the chain rule for functional derivatives and inserting the definitions in Eqs. (3.28) and (3.29), the comparison with Eq. (3.27) yields:

$$\Sigma(12) = i\hbar \int d(34) G(13) \Gamma(324) W(41^+) , \tag{3.39}$$

with the so-called *vertex* defined as:

$$\Gamma(123) = -\frac{\delta G^{-1}(12)}{\delta V(3)} . \tag{3.40}$$

Lastly, the electronic polarization is readily written as:

$$P_{\mathrm{e}}(12) = -i\hbar \int d(34) G(13) G(41^+) \Gamma(342) . \tag{3.41}$$

Both the *GW* approximation for the case of rigid nuclei [72] and the Migdal approximation for the case of vibrating nuclei [75] consist of neglecting the vertex corrections: $\Gamma(123) = \delta(12)\delta(13)$. Eqs. (3.27)[2], (3.33), (3.35) (3.36), (3.39) and (3.41) thus constitute a set of nonlinear self-consistent equations that describe an electronic system in a

[2]We now let the perturbing potential ϕ vanish.

vibrating lattice.

For the case of a rigid lattice, that is with the nuclei clamped at their equilibrium positions, $D = 0$ and the popular GW equations are recovered [72]. To avoid ambiguities, we adopt the notation of Ref. [73] and denote as $G_{\rm cn}$ the Green's function calculated at clamped nuclei in Hedin's theory. In this case the equation of motion of $G_{\rm cn}$ reduces to:

$$\left[i\hbar\frac{\partial}{\partial t_1}+\frac{\hbar^2}{2m_{\rm e}}\nabla_1^2-V_{\rm cn}(1)\right]G_{\rm cn}(12)-\int d(3)\Sigma_{\rm e}(13)G_{\rm cn}(32)=\delta(12)\,, \tag{3.42}$$

with $V_{\rm cn}(1)=\int d(2)v(12)[\langle\hat{n}_{\rm e,cn}(2)\rangle+n^0_{\rm n}(1)]$, $n^0_{\rm n}(1)$ the density of the nuclei at the equilibrium positions, and the electronic self-energy is:

$$\Sigma_{\rm e}(12)=i\hbar G_{\rm cn}(12)W_{\rm e}(1^+2)\,. \tag{3.43}$$

To be precise, we should use the subscript 'cn' also for $W_{\rm e}$ and $\Sigma_{\rm e}$, because these quantities are in principle different to the electronic parts of W and Σ calculated in a nonrigid lattice, however we neglect this difference for simplicity.

The full equation of motion of G including the nuclei fluctuations, Eq. (3.27), can be recovered after expressing G in terms of $G_{\rm cn}$ and of an electron-phonon self-energy $\Sigma_{\rm ep}$, in the form of a Dyson's equation:

$$G(12)=G_{\rm cn}(12)+\int d(34)G_{\rm cn}(13)\Sigma_{\rm ep}(34)G(42)\,. \tag{3.44}$$

The comparison between Eqs. (3.27) and (3.42) leads to two main terms for the electron-phonon self-energy $\Sigma_{\rm ep}$ in Eq. (3.44):

$$\begin{aligned}\Sigma_{\rm ep}(12)=i\hbar\,G(12)&\int d(34)W_{\rm e}(1^+3)D(34)W_{\rm e}(24)\\&+\int d(3)v(13)\left[\langle\hat{n}(3)\rangle-\langle\hat{n}_{\rm e,cn}(3)\rangle-n^0_{\rm n}(3)\right]\delta(12)\,.\end{aligned} \tag{3.45}$$

The first term on the right-hand side gives the Fan or Migdal self-energy, while the second one is shown to correspond to the Debye-Waller self-energy that was briefly mentioned in Sec. 3.1.3 [73]. As already discussed, we do not consider the Debye-Waller contribution to the electron-phonon self-energy, and from now on we simply denote the Fan-Migdal

self-energy as Σ.

In passing, we note that some attempts have been made to incorporate the electron-phonon contribution to the renormalization of the band gap arising from the polar Fröhlich coupling by directly modifying the dielectric function that enters W_e in the *GW* self-energy of Eq. (3.43) [76, 77]. This was done by adding the contribution from the dynamic lattice polarization in the long-wavelength limit. In practice, this procedure should be equivalent to separately calculating the Fan-Migdal self-energy by taking into account only the Fröhlich coupling, and leads to a reduction of the band gaps with respect to the values calculated within standard *GW*.

Having established these results, we now look at the form of the Fan-Migdal self-energy which contains the term $W_{ep} = W_e D W_e$ (in symbolic notation). First we rewrite the density-density correlation function of the nuclei D [Eq. (3.35)] by expanding the delta functions in Eq. (3.21) around the equilibrium positions, and we obtain:

$$D(12) = -i/\hbar \sum_{\substack{\kappa\alpha\mathbf{R} \\ \kappa'\beta\mathbf{R}'}} Z_\kappa Z_{\kappa'} \nabla_{1,\alpha} \delta(\mathbf{r}_1 - \boldsymbol{\tau}^0_\kappa - \mathbf{R}) \left\langle \mathcal{T} \Delta\hat{\tau}_{\kappa\alpha}(\mathbf{R}, t_1) \Delta\hat{\tau}_{\kappa'\beta}(\mathbf{R}', t_2) \right\rangle \nabla_{2,\beta} \delta(\mathbf{r}_2 - \boldsymbol{\tau}^0_{\kappa'} - \mathbf{R}') . \tag{3.46}$$

The time-ordered product in Eq. (3.46) can be defined as the displacement-displacement correlation function for the nuclei, or the nuclear Green's function:

$$D_{\kappa\alpha\mathbf{R},\kappa'\beta\mathbf{R}'}(t_1, t_2) = -i/\hbar \left\langle \mathcal{T} \Delta\hat{\tau}_{\kappa\alpha}(\mathbf{R}, t_1) \Delta\hat{\tau}_{\kappa'\beta}(\mathbf{R}', t_2) \right\rangle . \tag{3.47}$$

The screened Coulomb interaction part W_{ep} can now be written as:

$$W_{ep}(12) = \sum_{\substack{\kappa\alpha\mathbf{R} \\ \kappa'\beta\mathbf{R}'}} \int d(34)\, \epsilon_e^{-1}(13) \nabla_{3,\alpha} V_\kappa(\mathbf{r}_3 - \boldsymbol{\tau}^0_\kappa - \mathbf{R}) D_{\kappa\alpha\mathbf{R},\kappa'\beta\mathbf{R}'}(t_3, t_4) \times \epsilon_e^{-1}(24) \nabla_{4,\beta} V_{\kappa'}(\mathbf{r}_4 - \boldsymbol{\tau}^0_{\kappa'} - \mathbf{R}') , \tag{3.48}$$

where we used the relation $W_e = \epsilon_e^{-1} v$ in Eq. (3.33), and $V_\kappa(\mathbf{r}) = -Z_\kappa v(\mathbf{r})$. If we use Eq. (3.4) and rewrite Eq. (3.47) in terms of the phonon ladder operators, we obtain the result (in Fourier space) [34]:

$$D^0_{\kappa\alpha\mathbf{R},\kappa'\beta\mathbf{R}'}(\omega) = \frac{1}{N_\mathbf{q}} \sum_{\mathbf{q}\nu} \left(\frac{\hbar^2}{4 M_\kappa M_{\kappa'} \omega^2_{\mathbf{q}\nu}} \right)^{1/2} e_{\kappa\alpha\nu}(\mathbf{q})\, e^*_{\kappa'\beta\nu}(\mathbf{q})\, e^{i\mathbf{q}\cdot(\mathbf{R}-\mathbf{R}')} D^0_\nu(\mathbf{q}, \omega) , \tag{3.49}$$

where $N_{\mathbf{q}}$ corresponds to a very dense sampling of $\mathbf{q}$ points in the Brillouin zone, and $D^0_\nu(\mathbf{q},\omega)$ is the Fourier transform of the phonon Green's function [4]:

$$D^0_\nu(\mathbf{q},tt') = -i/\hbar\,\langle\mathcal{T}\left[(\hat{a}_{\mathbf{q}\nu}e^{-i\omega_{\mathbf{q}\nu}t}+\hat{a}^\dagger_{-\mathbf{q}\nu}e^{i\omega_{\mathbf{q}\nu}t})(\hat{a}_{-\mathbf{q}\nu}e^{-i\omega_{\mathbf{q}\nu}t'}+\hat{a}^\dagger_{\mathbf{q}\nu}e^{i\omega_{\mathbf{q}\nu}t'})\right]\rangle\,. \tag{3.50}$$

A more complete expression for the nuclear Green's function is found using a rigorous approach that requires to write the equation of motion for the displacement operator $\Delta\hat{\boldsymbol{\tau}}_\kappa(\mathbf{R})$, analogously to the case of the electron Green's function [78, 34, 73]. In this way one can show that the nuclear Green's function is determined by a phonon self-energy, which can be separated into an adiabatic and a nonadiabatic part. The adiabatic part coincides with the interatomic force constant matrix calculated within DFPT, in agreement with the result in Eq. (3.49), while the nonadiabatic part contains the electronic renormalization effects beyond the adiabatic approximation and it is analogous to the electron-phonon self-energy for the electrons. This also justifies the label D^0 used in Eqs. (3.49) and (3.50).

Taken together, Eqs. (3.45) (the first term), (3.48) and (3.49) yield the Fan-Migdal self-energy. We write it in the frequency domain, where it is generally calculated, after taking the matrix elements in the basis of single-particle (Kohn-Sham) electronic states:

$$\Sigma_{nn'\mathbf{k}}(\omega) = \frac{i}{N_{\mathbf{q}}}\sum_{m\mathbf{q}\nu}\int\frac{d\omega'}{2\pi}g^*_{mn\nu}(\mathbf{k},\mathbf{q})g_{mn'\nu}(\mathbf{k},\mathbf{q})D^0_\nu(\mathbf{q},\omega')G_m(\mathbf{k}+\mathbf{q},\omega+\omega')\,, \tag{3.51}$$

where the matrix elements $g_{mn\nu}(\mathbf{k},\mathbf{q})$ coincide with the definition in Eq. (3.15). We need to make an important remark here. In principle, the matrix elements should be frequency dependent, as they are determined by the time-dependent dielectric function in Eq. (3.48). In practice they are taken to be static, following the argument that the phonon frequencies are much smaller than the characteristic frequencies of the electronic response. While this approximation holds well for wide-gap materials, it is not justified for the case of metals or highly doped semiconductors. It is this approximation, however, that allows practical calculations to make use of the matrix elements calculated from

DFPT, which underlies the adiabatic approximation. An additional observation is that the static electronic screening is then the one calculated within the self-consistent DFPT scheme, as discussed in Sec. 3.1.2 [74].

3.2.2 Electron-phonon coupling in *ab initio* calculations

In standard *ab initio* calculations, Eq. (3.51) is evaluated using the unperturbed electron Green's function G^0:

$$G_n^0(\mathbf{k},\omega) = \frac{1}{\omega - \varepsilon_{n\mathbf{k}} + i\eta\,\mathrm{sgn}(\varepsilon_{n\mathbf{k}})}\,, \tag{3.52}$$

which follows from Eq. (D.5), where the single-particle energies are taken to be the Kohn-Sham eigenvalues or the *GW*-corrected ones. The phonon Green's function D^0 is readily calculated by using the definition in Eq. (3.50) and the relations satisfied by the ladder operators, Eqs. (A.1)–(A.3):

$$D_\nu^0(\mathbf{q},\omega) = \frac{1}{\omega - \omega_{\mathbf{q}\nu} + i\eta} - \frac{1}{\omega + \omega_{\mathbf{q}\nu} - i\eta}\,. \tag{3.53}$$

The electron-phonon self-energy is then evaluated after performing a contour integration in the complex frequency plane [65] and neglecting the off-diagonal terms $n \neq n'$. The result is:

$$\Sigma_{n\mathbf{k}}(\omega) = \frac{1}{N_\mathbf{q}} \sum_{m\mathbf{q}\nu} |g_{mn\nu}(\mathbf{k},\mathbf{q})|^2 \left[\frac{f_{m\mathbf{k}+\mathbf{q}}}{\hbar\omega - \varepsilon_{m\mathbf{k}+\mathbf{q}} + \hbar\omega_{\mathbf{q}\nu} - i\eta} + \frac{1 - f_{m\mathbf{k}+\mathbf{q}}}{\hbar\omega - \varepsilon_{m\mathbf{k}+\mathbf{q}} - \hbar\omega_{\mathbf{q}\nu} + i\eta} \right]. \tag{3.54}$$

The generalization of Eq. (3.54) to nonzero temperatures is obtained by using the method of Matsubara Green's functions. We refer to Ref. [4] for the procedure, and only state the result here:

$$\Sigma_{n\mathbf{k}}(\omega) = \frac{1}{N_\mathbf{q}} \sum_{m\mathbf{q}\nu} |g_{mn\nu}(\mathbf{k},\mathbf{q})|^2 \left[\frac{n_{\mathbf{q}\nu} + f_{m\mathbf{k}+\mathbf{q}}}{\hbar\omega - \varepsilon_{m\mathbf{k}+\mathbf{q}} + \hbar\omega_{\mathbf{q}\nu} + i\eta} + \frac{n_{\mathbf{q}\nu} + 1 - f_{m\mathbf{k}+\mathbf{q}}}{\hbar\omega - \varepsilon_{m\mathbf{k}+\mathbf{q}} - \hbar\omega_{\mathbf{q}\nu} + i\eta} \right]. \tag{3.55}$$

A comparison with Eq. (3.19) shows that $\Sigma_{n\mathbf{k}}(\varepsilon_\mathbf{k})$ coincides with the perturbation theory result, if one adds an imaginary part to the denominators. This corresponds to allowing the electronic quasiparticles to have a finite lifetime instead of being sharp excitations.

Dyson's equation [Eq. (3.44)] is used to evaluate the renormalized Green's function, where G_{cn} is given in practice by Eq. (3.52) using the best available approximation for the electronic energies (DFT or *GW*, for example). In frequency domain, and in the basis of Kohn-Sham states, the Dyson's equation is written as:

$$G_n(\mathbf{k},\omega) = \frac{1}{\hbar\omega - \varepsilon_{n\mathbf{k}} + i\eta\,\mathrm{sgn}(\varepsilon_{n\mathbf{k}}) - \Sigma_{n\mathbf{k}}(\omega)}\,. \tag{3.56}$$

The poles of the Green's function in Eq. (3.56) then yield the complex quasiparticle excitation energies:

$$\tilde{E}_{n\mathbf{k}} = \varepsilon_{n\mathbf{k}} + \Sigma_{n\mathbf{k}}(\tilde{E}_{n\mathbf{k}})\,. \tag{3.57}$$

The real and imaginary part of $\tilde{E}_{n\mathbf{k}} = E_{n\mathbf{k}} + i\Gamma_{n\mathbf{k}}$ represent the energy and inverse lifetime of the quasiparticle state. The self-consistent solution of Eq. (3.57), however, requires to know the analytic continuation of $\Sigma_{n\mathbf{k}}(\omega)$ in the complex energy plane [79]. In practice it is customary to neglect the imaginary part of the energies in the argument of the self-energy, so that the quasiparticle equation becomes:

$$E_{n\mathbf{k}} = \varepsilon_{n\mathbf{k}} + \mathrm{Re}\,\Sigma_{n\mathbf{k}}(E_{n\mathbf{k}})\,, \tag{3.58}$$

$$\Gamma_{n\mathbf{k}} = \mathrm{Im}\,\Sigma_{n\mathbf{k}}(E_{n\mathbf{k}})\,. \tag{3.59}$$

A further approximation consists in evaluating Eq. (3.59) on-the-mass-shell, that is using the unperturbed energy $\varepsilon_{n\mathbf{k}}$ instead of $E_{n\mathbf{k}}$, which yields:

$$\begin{aligned}|\mathrm{Im}\Sigma_{n\mathbf{k}}(\varepsilon_{n\mathbf{k}})| = \frac{\pi}{N_{\mathbf{q}}}\sum_{m\,\mathbf{q}\nu} |g_{mn\nu}(\mathbf{k},\mathbf{q})|^2 \Big[&(n_{\mathbf{q}\nu} + f_{m\mathbf{k}+\mathbf{q}})\,\delta(\varepsilon_{n\mathbf{k}} - \varepsilon_{m\mathbf{k}+\mathbf{q}} + \hbar\omega_{\mathbf{q}\nu}) \\ &+ (n_{\mathbf{q}\nu} + 1 - f_{m\mathbf{k}+\mathbf{q}})\,\delta(\varepsilon_{n\mathbf{k}} - \varepsilon_{m\mathbf{k}+\mathbf{q}} - \hbar\omega_{\mathbf{q}\nu})\Big]\,,\end{aligned} \tag{3.60}$$

where we used Eq. (3.55) and the relation $(x \pm i\eta)^{-1} = \mathrm{P}(1/x) \mp i\pi\delta(x)$. Eq. (3.60) corresponds to the Fermi's Golden rule result for the scattering probability. The quasiparticle lifetime is then calculated as:

$$\tau_{n\mathbf{k}} = \frac{\hbar}{2|\Gamma_{n\mathbf{k}}|} = \frac{\hbar}{2\,|\mathrm{Im}\Sigma_{n\mathbf{k}}(\varepsilon_{n\mathbf{k}})|}\,. \tag{3.61}$$

It is useful at this point to also introduce the so-called quasiparticle renormalization factor $Z_{n\mathbf{k}}$:

$$Z_{n\mathbf{k}} = \left(1 - \left. \frac{\partial \mathrm{Re}\,\Sigma_{n\mathbf{k}}(\omega)}{\partial\,\omega} \right|_{\hbar\omega = E_{n\mathbf{k}}} \right)^{-1}, \tag{3.62}$$

and the electron-phonon coupling strength $\lambda_{n\mathbf{k}}$ defined as:

$$\lambda_{n\mathbf{k}} = -\left. \frac{\partial \mathrm{Re}\,\Sigma_{n\mathbf{k}}(\omega)}{\partial\,\omega} \right|_{\hbar\omega = E_{n\mathbf{k}}} = \frac{1}{Z_{n\mathbf{k}}} - 1\,. \tag{3.63}$$

This is also referred to as the mass enhancement parameter or velocity renormalization. In fact, for parabolic bands it follows from Eq. (3.58) that the renormalized effective mass m^* is given by:

$$m^*_{\mathbf{k}} = m_{\mathrm{b},\mathbf{k}}(1 + \lambda_{n\mathbf{k}})\,, \tag{3.64}$$

while the renormalized band velocity $\mathbf{v}_{n\mathbf{k}}$ is:

$$\mathbf{v}_{n\mathbf{k}} = \mathbf{v}^0_{n\mathbf{k}}/(1 + \lambda_{n\mathbf{k}})\,, \tag{3.65}$$

where we retained the wavevector dependence of velocity and effective mass. Eqs. (3.64) and (3.65) hold if the variation of the self-energy with $\mathbf{k}$ can be neglected [4]. We also note that an electron-phonon coupling strength λ averaged over the Fermi surface is often introduced, especially in the case of metals or phonon-mediated superconductors [66].

The quasiparticle properties can be explored further by calculating the one-electron spectral function $A(\mathbf{k}, \omega)$ that was already introduced in Sec. 1.3 for an electron removal process [Eq. (1.15)]. The fact that $A(\mathbf{k}, \omega)$ is related to the imaginary part of the electron Green's function [Eq. (1.16)] follows readily from the Lehmann's representation given in Appendix D. Using Dyson's equation Eq. (3.56) and taking the trace with respect to the band index n, the spectral function can be written as [66]:

$$A(\mathbf{k}, \omega) = \frac{2}{\pi} \sum_n |\mathrm{Im}\, G_n(\mathbf{k}, \omega)| \tag{3.66}$$

$$= \frac{2}{\pi} \sum_n \frac{|\mathrm{Im}\Sigma_{n\mathbf{k}}(\omega)|}{[\hbar\omega - \varepsilon_{n\mathbf{k}} - \mathrm{Re}\Sigma_{n\mathbf{k}}(\omega)]^2 + [\mathrm{Im}\Sigma_{n\mathbf{k}}(\omega)]^2}\,, \tag{3.67}$$

where the factor 2 takes into account the spin degeneracy. The self-consistent solution

of Eq. (3.58) corresponds the main quasiparticle peak in the spectral function, while the imaginary part of the self-energy is responsible for the broadening of the peak. More precisely, the broadening is given approximately by $Z_{n\mathbf{k}}\mathrm{Im}\Sigma_{n\mathbf{k}}$; in fact, if we expand Eq. (3.67) around $E_{n\mathbf{k}}$ we obtain:

$$A(\mathbf{k},\omega) \simeq \frac{2}{\pi}\sum_n Z_{n\mathbf{k}}\frac{Z_{n\mathbf{k}}|\mathrm{Im}\Sigma_{n\mathbf{k}}(E_{n\mathbf{k}})|}{(\hbar\omega - E_{n\mathbf{k}})^2 + [Z_{n\mathbf{k}}\mathrm{Im}\Sigma_{n\mathbf{k}}(E_{n\mathbf{k}})]^2}\,, \tag{3.68}$$

which corresponds to a sum of Lorentzian functions of width $Z_{n\mathbf{k}}\mathrm{Im}\Sigma_{n\mathbf{k}}$ and strength $Z_{n\mathbf{k}}$, hence $Z_{n\mathbf{k}}$ in Eq. (3.62) is named the quasiparticle renormalization factor [66, 73].

3.3 Electron-phonon Wannier

While the main ingredients for investigating the electron-phonon interactions in solids have been presented, we now face the problem of performing practical *ab initio* calculations. The main bottleneck is that the convergence of the Brillouin-zone integral needed to compute the self-energy requires in general a dense sampling with up to millions of points. DFPT calculations for such meshes are in practice prohibitive beyond very simple systems. In the following we present an *ab initio* interpolation strategy based on maximally localized Wannier functions that enables to efficiently calculate Brillouin-zone integrals with high accuracy.

3.3.1 Wannier functions

Wannier functions are an alternative representation for the space spanned by Bloch orbitals. While Bloch functions are labeled by the crystal momentum $\mathbf{k}$ and band index n, Wannier orbitals are characterized by a lattice vector $\mathbf{R}$ and an orbital index m. Wannier functions are obtained from the Fourier transform of Bloch states, hence they are not eigenstates of the Kohn-Sham Hamiltonian, but have the property of being localized in space [80]. Since the Bloch states carry an arbitrary phase, periodic in reciprocal space, Wannier functions are not uniquely defined. A popular choice to fix the gauge freedom

is given by the so-called maximally localized Wannier functions (MLWF):

$$w_{m\mathbf{R}}(\mathbf{r}) = \frac{1}{\sqrt{N_c}} \sum_{n\mathbf{k}} e^{-i\mathbf{k}\cdot\mathbf{R}} U_{nm\mathbf{k}} \psi_{n\mathbf{k}}(\mathbf{r}), \tag{3.69}$$

with $U_{\mathbf{k}}$ a unitary matrix determined from the iterative minimization of a localization functional [81]. Eq. (3.69) strictly holds for a set of bands separated from all other bands by a finite energy gap throughout the Brillouin zone, but can be generalized to the case of 'entangled' energy bands [82]. For convenience we also write explicitly the inverse transformation of Eq. (3.69):

$$\psi_{n\mathbf{k}}(\mathbf{r}) = \frac{1}{\sqrt{N_c}} \sum_{m\mathbf{R}} e^{i\mathbf{k}\cdot\mathbf{R}} U^{\dagger}_{mn\mathbf{k}} w_{m\mathbf{R}}(\mathbf{r}). \tag{3.70}$$

The algorithms to calculate the unitary matrices for the transformation from Bloch to Wannier functions are implemented in the `wannier90` code [83]. In practice one also needs to provide a set of localized functions (projections) used to generate an initial guess. It is easily verified that with the definition of the Bloch states in Eq. (2.14), MLWF are normalized in the BvK supercell. Moreover, from Bloch's theorem it follows that two Wannier functions $w_{m\mathbf{R}}(\mathbf{r})$ and $w_{m\mathbf{R}'}(\mathbf{r})$ transform into each other with a translation of $\mathbf{R}-\mathbf{R}'$; in particular, $w_{m\mathbf{R}}(\mathbf{r}) = w_{m0}(\mathbf{r}-\mathbf{R})$. MLWF have been proven to be a powerful tool in the study of electronic and dielectric properties of materials: their broad range of applications is reviewed for example in Ref. [80]. Here we exploit the localization properties of MLWF for the interpolation of physical quantities onto dense meshes in the Brillouin zone.

In order to interpolate the electronic energies, let us first write the matrix elements of the Kohn-Sham Hamiltonian in Bloch representation:

$$H_{mn}(\mathbf{k}) = \langle \psi_{m\mathbf{k}} | \hat{H}_{\mathrm{KS}} | \psi_{n\mathbf{k}} \rangle = \delta_{mn} \varepsilon_{n\mathbf{k}}. \tag{3.71}$$

Using Eq. (3.69), the Hamiltonian in the basis of the MLWF is then:

$$H_{mn}(\mathbf{R}) = \langle w_{m0} | \hat{H}_{\mathrm{KS}} | w_{n\mathbf{R}} \rangle = \frac{1}{N_c} \sum_{\mathbf{k}} e^{-i\mathbf{k}\cdot\mathbf{R}} U^{\dagger}_{mm'\mathbf{k}} H_{m'n'}(\mathbf{k}) U_{n'n\mathbf{k}}. \tag{3.72}$$

Thanks to the localization of the Wannier functions, $H_{mn}(\mathbf{R})$ decays rapidly with $\mathbf{R}$ and can therefore be assumed to vanish outside the Wigner-Seitz supercell in real space. The energies at any point $\mathbf{k}'$ can thus be obtained by performing the Fourier transform of $H_{mn}(\mathbf{R})$ and diagonalizing the resulting matrix [82, 84]:

$$H_{mn}(\mathbf{k}') = U_{mm'\mathbf{k}'}\left(\sum_{\mathbf{R}} e^{i\mathbf{k}'\cdot\mathbf{R}} H_{m'n'}(\mathbf{R})\right) U^{\dagger}_{n'n\mathbf{k}'}\,. \tag{3.73}$$

The Fourier interpolation procedure for the dynamical matrix presented at the end of Sec. 2.2.3 can also be reformulated in terms of maximally localized 'lattice' Wannier functions corresponding to atomic displacements [85]. In practice the two formulations are equivalent, hence we will not discuss this further.

3.3.2 Electron-phonon matrix elements

The last ingredient needed for the calculation of electron-phonon interaction properties is the matrix element $g_{mn\nu}(\mathbf{k},\mathbf{q})$. This is defined in Eq. (3.15) in terms of the derivative of the self-consistent potential with respect to a collective ionic displacement corresponding to a phonon with branch ν and momentum $\mathbf{q}$, $\partial_{\mathbf{q}\nu} V_{\mathrm{KS}}$. Eq. (3.11) shows that this is readily expressed in terms of the contribution from each ion, $\partial_{\kappa\alpha,\mathbf{R}} V_{\mathrm{KS}}$, which corresponds to the variation of the self-consistent potential due to the displacement of the ion κ in the unit cell $\mathbf{R}$. This quantity may be used in order to define an electron-phonon matrix element in Wannier representation $g_{mn\kappa\alpha}(\mathbf{R},\mathbf{R}')$:

$$g_{mn\kappa\alpha}(\mathbf{R},\mathbf{R}') = \langle w_{m\mathbf{0}} |\, \partial_{\kappa\alpha,\mathbf{R}'} V_{\mathrm{KS}}\, | w_{n\mathbf{R}} \rangle\,. \tag{3.74}$$

By inserting Eqs. (3.70) and (3.11) into Eq. (3.15) we find:

$$g_{mn\nu}(\mathbf{k},\mathbf{q}) = \frac{1}{N_{\mathrm{c}}} \sum_{\mathbf{R}\mathbf{R}'} e^{i(\mathbf{k}\cdot\mathbf{R}+\mathbf{q}\cdot\mathbf{R}')} \sum_{m'n',\kappa\alpha} \left(\frac{\hbar}{2M_\kappa \omega_{\mathbf{q}\nu}}\right)^{1/2} e_{\kappa\alpha\nu}(\mathbf{q})\, U_{mm'\mathbf{k}+\mathbf{q}}\, g_{m'n'\kappa\alpha}(\mathbf{R},\mathbf{R}')\, U^{\dagger}_{n'n\mathbf{k}}\,, \tag{3.75}$$

where the definition in Eq. (3.74) has been used, after noting that:

$$\langle w_{m'\mathbf{R}''} |\, \partial_{\kappa\alpha,\mathbf{R}'} V_{\mathrm{KS}}\, | w_{n'\mathbf{R}} \rangle = \langle w_{m'\mathbf{0}} |\, \partial_{\kappa\alpha,\mathbf{R}'-\mathbf{R}''} V_{\mathrm{KS}}\, | w_{n'\mathbf{R}-\mathbf{R}''} \rangle\,, \tag{3.76}$$

which follows from the translational properties of the Wannier functions, and $\mathbf{R}-\mathbf{R}'$, $\mathbf{R}'-\mathbf{R}''$ are relabeled as $\mathbf{R}$ and $\mathbf{R}'$ respectively.

The electron-phonon matrix element [Eq. (3.15)] is first calculated using DFPT on coarse Brillouin-zone grids with N_c $\mathbf{k}$ points and $N_{\mathrm{c}'}$ $\mathbf{q}$ points, as in general different BvK supercells can be used for the electron and phonon problem. The quantity $g_{mn\kappa\alpha}(\mathbf{R},\mathbf{R}')$ is then computed from the inverse relation of Eq. (3.75), which is obtained by using the unitary property of the $U_\mathbf{k}$ matrices, the orthonormality of the phonon eigenvectors $e_{\kappa\alpha\nu}(\mathbf{q})$ and the identity in Eq. (B.5):

$$g_{mn\kappa\alpha}(\mathbf{R},\mathbf{R}') = \frac{1}{N_{\mathrm{c}'}}\sum_{\mathbf{k},\mathbf{q}} e^{-i(\mathbf{k}\cdot\mathbf{R}+\mathbf{q}\cdot\mathbf{R}')} \sum_{m'n',\nu}\left(\frac{\hbar}{2M_\kappa\omega_{\mathbf{q}\nu}}\right)^{-1/2} e^{*}_{\kappa\alpha\nu}(\mathbf{q})\, U^{\dagger}_{mm'\mathbf{k}+\mathbf{q}}\, g_{m'n'\nu}(\mathbf{k},\mathbf{q})\, U_{n'n\mathbf{k}}\,, \tag{3.77}$$

where the transformation matrices $U_\mathbf{k}$ are obtained from the 'wannierization' of the Bloch wavefunctions, and the phonon eigenmodes and eigenvectors from the diagonalization of the dynamical matrix. Eq. (3.77) is assumed to be vanishing outside the Wigner-Seitz supercells containing N_c and $N_{\mathrm{c}'}$ unit-cell replicas. The matrix elements can then be Fourier interpolated onto fine grids in the Brillouin zone using Eq. (3.75). The $U_\mathbf{k}$ matrices and the phonon eigenmodes and eigenvectors are known for arbitrary $\mathbf{k}$ and $\mathbf{q}$ points from the diagonalization of the Fourier transform of the Hamiltonian in Wannier basis [see Eq. (3.73)] and of the interpolated dynamical matrix.

Eqs. (3.75) and (3.77) complete the Wannier-Fourier interpolation method. Using this technique, all the relevant quantities, that is Kohn-Sham energies and wavefunctions, dynamical matrices and electron-phonon matrix elements, need to be calculated only on coarse $\mathbf{k}$ and $\mathbf{q}$ grids in the Brillouin zone, and are then interpolated onto arbitrary dense meshes in momentum space with high accuracy. This method is implemented in the `EPW` code [86, 87], that is integrated into the `Quantum ESPRESSO` software package, and uses `wannier90` as an internal library. It has been successfully applied to many metals and nonpolar semiconductors, studying for example the electron velocity renormalization and lifetimes [88, 89, 90, 91], phonon softening and lifetimes [92, 93], phonon-

assisted optical absorption [94], band-gap renormalization [69], kinks in photoemission spectra [95, 96], superconducting properties [97, 98, 99] and resistivity [100, 101].

We remark that the method relies on the localization properties of the Wannier functions and of the phonon perturbation, hence it may fail in important cases as discussed in the next chapter.

CHAPTER 4

Fröhlich electron-phonon coupling from first principles

In this chapter we present a general formalism for calculating the electron-phonon matrix elements in polar semiconductors and insulators from first principles. After describing the challenges arising in treating the Fröhlich electron-phonon coupling, we derive the generalization of the Fröhlich matrix element and coupling constant for *ab initio* calculations, and we outline the use of the former specifically in conjunction with Wannier-Fourier interpolation. We demonstrate this method by investigating the electron-phonon interaction in two prototypical polar materials, gallium nitride (GaN) and strontium titanate ($SrTiO_3$).

The formalism introduced in this chapter has been presented in Ref. [102], with a similar formulation also proposed in Ref. [103], and it is fully integrated in the `EPW` package [87]. The method enables the calculation of many properties of polar semiconductors and insulators and has already been used to compute for example electron lifetimes in anatase TiO_2 [102], scattering rates and ultrafast dynamics in GaN [104] and temperature-dependent mobilities in GaAs [105, 106]. We remark that the latter constitute the first fully *ab initio* calculations of carrier mobilities in a polar semiconductor.

4.1 The problem

As mentioned in the first chapter, for the case of polar semiconductors and insulators the progress in the calculation of electron-phonon interaction properties from first principles did not match the advances made for metals and nonpolar materials. Given the fast-growing technological importance of polar semiconductors, from light-emitting devices to transparent electronics, solar cells, and photocatalysts [107, 108, 109], developing accurate and efficient computational methods for studying electron-phonon interactions in these systems is of primary importance.

In polar materials two or more atoms in the unit cell carry nonzero Born effective charge tensors [59]. As a consequence the atomic vibrations corresponding to LO phonons in the long-wavelength limit generate macroscopic electric fields to which electrons and holes can strongly couple, leading to the Fröhlich interaction discussed in Sec. 1.1 [2]. While it is possible in principle to treat this polar electron-phonon coupling within the linear response formalism of DFPT, the two key obstacles towards a description of Fröhlich coupling from first principles are (i) the divergence of the electron-phonon matrix element for small phonon wavevectors ($\mathbf{q} \to 0$) as seen in Eq. (1.8), and (ii) the fact that the Fröhlich model was proposed in order to treat simple isotropic systems with a single electronic band and one dispersionless LO phonon. The second point is related to the fundamental question on how to define the Fröhlich coupling in a more general way, while the first one is responsible for the prohibitive computational cost of *ab initio* electron-phonon calculations in polar materials. Indeed a correct description of the singularity at $\mathbf{q} \to 0$ requires a very fine sampling of the Brillouin zone, and has been carried out accurately only for very simple systems [70, 110].

In general, we saw in Sec. 3.3 how the difficulty of evaluating the electron-phonon matrix elements $g_{mn\nu}(\mathbf{k}, \mathbf{q})$ on extremely dense Brillouin-zone grids can be overcome with the *ab initio* interpolation strategy of `EPW`. This approach, however, relies on the spa-

tial localization of both the phonon scattering potential and the electron wavefunctions when expressed in a real-space Wannier representation. In this way, all the quantities needed can be truncated outside the Wigner-Seitz supercells used to describe the electron and phonon problem. The success of this procedure can be tested for example from Fig. 4.1(a)–(d), where the spatial decays of the largest components of the electronic Hamiltonian, the interatomic force constants and the electron-phonon matrix elements are shown for the case of B-doped diamond. For the technical details of the calculation we refer the reader to Refs. [85, 87]. All quantities decay by almost four orders of magnitude within 12 Å (corresponding to a $6 \times 6 \times 6$ supercell centered in the origin). In particular, we note that the decay of the matrix elements in Wannier representation $g_{mn\kappa\alpha}(\mathbf{R}, \mathbf{R}')$ [Eq. (3.74)] is linked to the decay of the Wannier functions in the limiting case $g_{mn\kappa\alpha}(\mathbf{R}, 0)$, where the phonon perturbation and one Wannier function are located in the same unit cell. In the other limiting case $g_{mn\kappa\alpha}(0, \mathbf{R}')$, where the two Wannier functions belong to the same unit cell, the decay is dictated by the localization of the phonon perturbation instead.

In polar materials the scenario is different: the phonon perturbation is long ranged in real space, as it has the form of a dipole potential which decays as $1/R'^2$. This is reflected in the long-wavelength singularity of the matrix element in reciprocal space. As a consequence, Wannier-Fourier interpolation breaks down in presence of Fröhlich coupling. Analogously, less refined linear interpolation strategies would equally fail. For comparison, in Fig. 4.1(e)–(h) we show the spatial decays in GaN for the same range as in B-doped diamond (the details of this calculation will be presented in Sec. 4.3.1). Here $H_{mn}(\mathbf{R})$ and $g_{mn\kappa\alpha}(\mathbf{R}, 0)$ exhibit a good decay thanks to the localization of the Wannier functions, whereas $C_{\kappa\alpha,\kappa'\beta}(\mathbf{R}')$ and $g_{mn\kappa\alpha}(0, \mathbf{R}')$ decay slowly, thus confirming our point. In the following we present a solution to this problem that addresses the challenges outlined in this section.

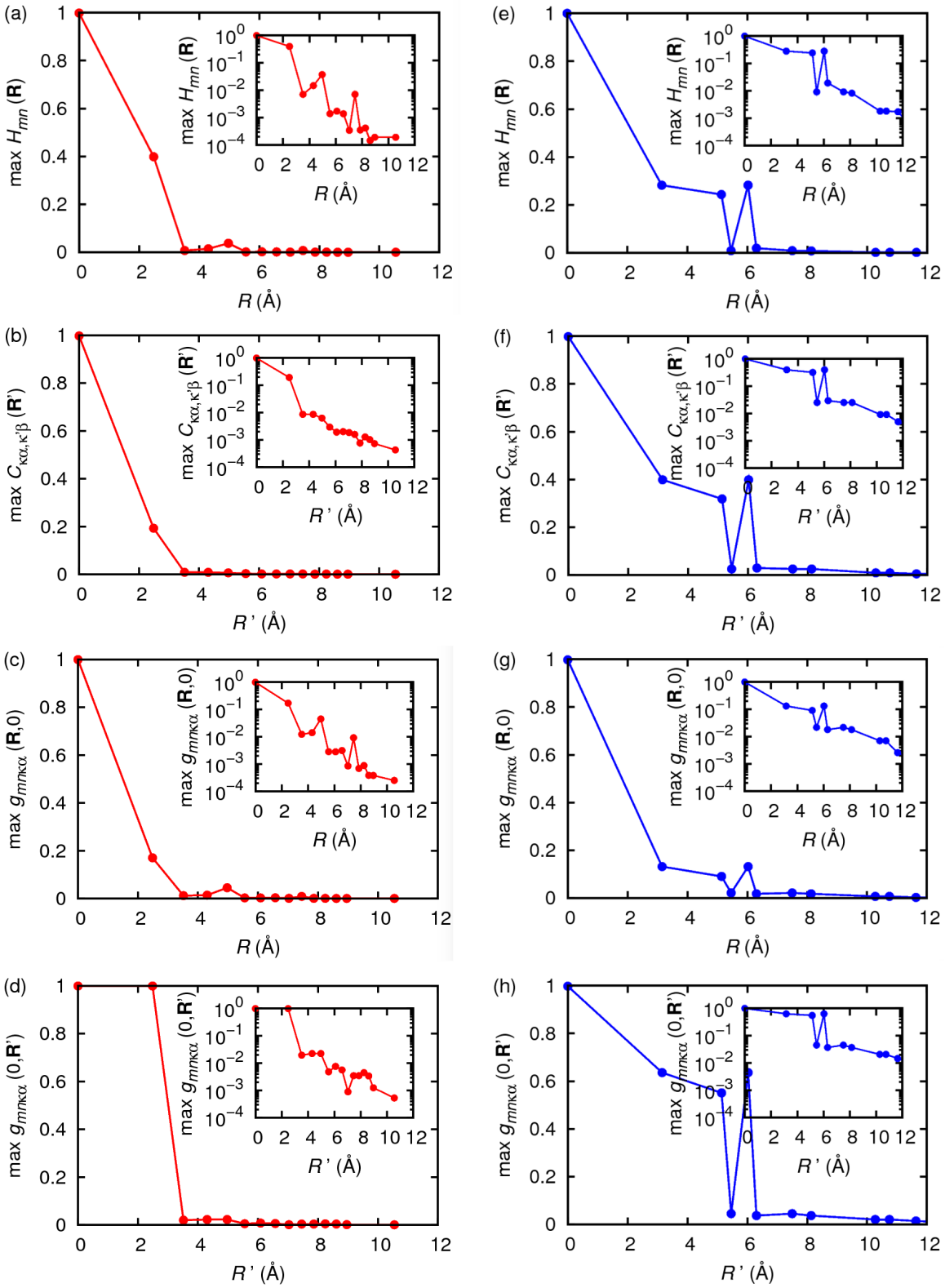

Figure 4.1: Spatial decay of the largest components of the Hamiltonian (a), (e), the interatomic force constants (b), (f) and the electron-phonon matrix elements (c), (d), (g), (h) for B-doped diamond [red, panels (a)–(d)] and GaN [blue, panels (e)–(h)]. R and R' indicate the length of the Wigner-Seitz vectors in the electron and phonon supercells, respectively. All quantities are normalized to the largest value.

4.2 First-principles polar coupling

4.2.1 Generalized Fröhlich matrix element

The first step is to derive a general expression that describes the polar electron-phonon coupling from first principles. This can be achieved by using standard electrostatics if one starts from the ansatz that the macroscopic electric field generated by the nuclei is obtained by associating electric point dipoles $p_\alpha^\kappa = eZ_{\alpha\beta}^{*\kappa}\Delta\tau_{\kappa\beta}$ to each atom κ, where $\Delta\tau_{\kappa\beta}$ is the displacement from equilibrium. This ansatz draws from the actual definition of the Born effective charges as the sources of the macroscopic polarization [see Eqs. (2.39) and (2.41)]. A more formal theory can also be derived within a microscopic many-body treatment [111].

Let us start by deriving the electrostatic potential generated by a point charge Q placed at the position $\boldsymbol{\tau}$, including also a uniform compensating background $-Q/(N_\mathrm{c}\Omega)$ so that the supercell is neutral overall. The medium is an anisotropic dielectric with the permittivity tensor $\boldsymbol{\epsilon}_\infty = \epsilon_{\alpha\beta}^\infty$, as we are assuming that the atomic oscillations take place over much longer time scales than the electron response time, so that the potential is screened by the electronic permittivity. The potential is then obtained as the solution of the Poisson's equation [112]:

$$(\boldsymbol{\nabla}\cdot\boldsymbol{\epsilon}_\infty\cdot\boldsymbol{\nabla})\,\phi(\mathbf{r};\boldsymbol{\tau}) = -4\pi\sum_{\mathbf{T}}\left[Q\,\delta(\mathbf{r}-\boldsymbol{\tau}-\mathbf{T}) - \frac{Q}{N_\mathrm{c}\,\Omega}\right], \tag{4.1}$$

where the compact notation $\mathbf{a}\cdot\mathbf{B}\cdot\mathbf{c} = \sum_{\alpha\beta} a_\alpha B_{\alpha\beta} c_\beta$ is used, and $\mathbf{T}$ are the lattice vectors of the BvK supercell (Appendix B). Since the electrostatic potential $\phi(\mathbf{r};\boldsymbol{\tau})$ is periodic in the supercell, it can be expanded in plane waves as $\phi(\mathbf{r};\boldsymbol{\tau}) = \sum_{\mathbf{q},\mathbf{G}} e^{i(\mathbf{q}+\mathbf{G})\cdot\mathbf{r}}\phi(\mathbf{q}+\mathbf{G};\boldsymbol{\tau})$. By writing Eq. (4.1) in plane-wave components we obtain the solution:

$$\phi(\mathbf{r};\boldsymbol{\tau}) = \frac{4\pi}{\Omega}\frac{Q}{N_\mathrm{c}}\sum_{\mathbf{q}}\sum_{\mathbf{G}\neq-\mathbf{q}}\frac{e^{i(\mathbf{q}+\mathbf{G})\cdot(\mathbf{r}-\boldsymbol{\tau})}}{(\mathbf{q}+\mathbf{G})\cdot\boldsymbol{\epsilon}_\infty\cdot(\mathbf{q}+\mathbf{G})}, \tag{4.2}$$

where the omission of the $\mathbf{G} = -\mathbf{q}$ term guarantees the charge neutrality. The electrostatic

potential generated by a dipole $\mathbf{p} = Q\mathbf{u}$ centered at the origin can be derived as $\phi^{\mathrm{D}}(\mathbf{r}) = \lim_{\mathbf{u}\to 0} \phi(\mathbf{r};\mathbf{u}) - \phi(\mathbf{r};0)$:

$$\phi^{\mathrm{D}}(\mathbf{r}) = -i\frac{4\pi}{\Omega}\frac{1}{N_{\mathrm{c}}}\sum_{\mathbf{q}}\sum_{\mathbf{G}\neq-\mathbf{q}} \mathbf{p}\cdot\frac{(\mathbf{q}+\mathbf{G})\, e^{i(\mathbf{q}+\mathbf{G})\cdot\mathbf{r}}}{(\mathbf{q}+\mathbf{G})\cdot\boldsymbol{\epsilon}_\infty\cdot(\mathbf{q}+\mathbf{G})}\,. \tag{4.3}$$

Following our ansatz we replace the dipole $\mathbf{p}$ with $\sum_{\kappa\mathbf{R}} e\,\mathbf{Z}^*_\kappa\cdot\Delta\boldsymbol{\tau}^{\mathbf{q}\nu}_\kappa(\mathbf{R})$, with $\Delta\boldsymbol{\tau}^{\mathbf{q}\nu}_\kappa(\mathbf{R})$ the displacement of each atom κ in the unit cell $\mathbf{R}$ in the vibrational eigenmode $(\mathbf{q},\nu)$. According to Eq. (3.4), this is given by $\Delta\tau^{\mathbf{q}\nu}_{\kappa\alpha}(\mathbf{R}) = [\hbar/(2N_{\mathrm{c}}M_\kappa\omega_{\mathbf{q}\nu})]^{1/2}\, e^{i\mathbf{q}\cdot\mathbf{R}}\, e_{\kappa\alpha\nu}(\mathbf{q})$. We can now write the electronic potential $V^{\mathcal{L}}_{\mathbf{q}\nu}(\mathbf{r}) = -e\phi^{\mathrm{D}}_{\mathbf{q}\nu}(\mathbf{r};\{\boldsymbol{\tau}^0_\kappa\})$:

$$V^{\mathcal{L}}_{\mathbf{q}\nu}(\mathbf{r}) = i\frac{4\pi e^2}{\Omega}\sum_\kappa\left(\frac{\hbar}{2N_{\mathrm{c}}M_\kappa\omega_{\mathbf{q}\nu}}\right)^{1/2}\sum_{\mathbf{G},\mathbf{q}+\mathbf{G}\neq 0}\frac{(\mathbf{q}+\mathbf{G})\cdot\mathbf{Z}^*_\kappa\cdot\mathbf{e}_{\kappa\nu}(\mathbf{q})\, e^{i(\mathbf{q}+\mathbf{G})\cdot(\mathbf{r}-\boldsymbol{\tau}^0_\kappa)}}{(\mathbf{q}+\mathbf{G})\cdot\boldsymbol{\epsilon}_\infty\cdot(\mathbf{q}+\mathbf{G})}\,, \tag{4.4}$$

where we used the identity in Eq. (B.6). The matrix element $\langle\psi_{m\mathbf{k}+\mathbf{q}}|\, V^{\mathcal{L}}_{\mathbf{q}\nu}\,|\psi_{n\mathbf{k}}\rangle$ finally reads:[1]

$$\begin{aligned} g^{\mathcal{L}}_{mn\nu}(\mathbf{k},\mathbf{q}) = i\,\frac{4\pi e^2}{\Omega}\sum_\kappa\left(\frac{\hbar}{2M_\kappa\omega_{\mathbf{q}\nu}}\right)^{1/2} \\ \times\sum_{\mathbf{G},\mathbf{q}+\mathbf{G}\neq 0}\frac{(\mathbf{q}+\mathbf{G})\cdot\mathbf{Z}^*_\kappa\cdot\mathbf{e}_{\kappa\nu}(\mathbf{q})}{(\mathbf{q}+\mathbf{G})\cdot\boldsymbol{\epsilon}_\infty\cdot(\mathbf{q}+\mathbf{G})}\,\langle\psi_{m\mathbf{k}+\mathbf{q}}|\, e^{i(\mathbf{q}+\mathbf{G})\cdot(\mathbf{r}-\boldsymbol{\tau}^0_\kappa)}\,|\psi_{n\mathbf{k}}\rangle\,, \end{aligned} \tag{4.5}$$

where we left the factor $1/\sqrt{N_{\mathrm{c}}}$ out to be consistent with Eqs. (3.12)–(3.15). An alternative derivation of Eq. (4.5) is presented in Appendix C.3. In principle one could include only one reciprocal lattice vector in the summation over $\mathbf{G}$, namely $\tilde{\mathbf{G}}_{\mathbf{q}}$ such that $|\mathbf{q}+\tilde{\mathbf{G}}_{\mathbf{q}}| = \min_{\mathbf{G}}|\mathbf{q}+\mathbf{G}|$, which would correspond to retaining only the residue of the pole in reciprocal space. In practice this leads to a matrix element with discontinuous $\mathbf{q}$-derivatives at the Brillouin-zone boundaries; instead, in order to preserve a smooth matrix element and the periodicity properties of the lattice, it is sufficient to truncate the sum to the smallest shell of $\mathbf{G}$ vectors surrounding each $\mathbf{q}$.

In the long-wavelength limit our result coincides with the electron-phonon matrix element of Ref. [111], with the difference that in Ref. [111] conduction electrons in a single

[1] To avoid ambiguities we specify that the braket between the Bloch wavefunctions is evaluated within the BvK supercell.

band of a semiconductor or insulator were considered. An advantage of our formulation is that the physics behind the polar singularity becomes completely transparent. Eq. (4.5) represents the generalization of the Fröhlich matrix element for *ab initio* calculations, as we will show in more detail in Sec. 4.2.2. This generalized expression naturally incorporates the coupling to all phonon modes, without the need to make any assumption on the LO mode to be considered. In practice, only the phonons that are infrared active, i.e. the ones carrying nonzero dipole moment, contribute to the polar coupling, with a strength proportional to their dipole moment.

In addition, it follows from the charge-neutrality sum rule on the Born effective charges, that is $\sum_\kappa Z^{*\kappa}_{\alpha\beta} = 0$, that the leading order of Eq. (4.5) vanishes for acoustic modes at long wavelength. In fact, for acoustic modes the relation $\mathbf{e}_{\kappa\nu}(\mathbf{q}=0)/\sqrt{M_\kappa} = \mathbf{u}_\nu$ holds, meaning that the mass-scaled eigenvectors are rigid atomic translations independent of κ [59]. For small $\mathbf{q}$ one can then write [59]:

$$\mathbf{e}_{\kappa\nu}(\mathbf{q})/\sqrt{M_\kappa} \simeq [\mathbf{u}_\nu + i\mathbf{q}u^{(1)}_{\kappa\nu}(\mathbf{q})]e^{i\mathbf{q}\cdot\tau^0_\kappa}, \tag{4.6}$$

and since in Eq. (4.5) a factor $e^{-i\mathbf{q}\cdot\tau^0_\kappa}$ is present, it follows that for acoustic modes the leading order of $g^{\mathcal{L}}$ goes to zero in the long-wavelength limit if $\sum_\kappa Z^{*\kappa}_{\alpha\beta} = 0$. We note that in presence of piezoacoustic coupling, which can be induced by acoustic phonons with small wavevectors in crystals without an inversion center, the matrix elements corresponding to acoustic modes may exhibit a divergence as $q^{-1/2}$ [4]. This behavior is captured by the long-range matrix element $g^{\mathcal{L}}$, as we can see by considering the second term in the expansion in Eq. (4.6). Its contribution to $g^{\mathcal{L}}$ is nonvanishing in general, and leads to a $\mathbf{q}$ dependence as $\omega^{-1/2}_{\mathbf{q}\nu} \sim q^{-1/2}$, since for acoustic phonons at long wavelength $\omega_{\mathbf{q}\nu}$ is linear in $\mathbf{q}$. We also refer to Refs. [59, 111] for thorough discussions.

4.2.2 Generalized Fröhlich coupling constant

Our formalism also allows to generalize the Fröhlich coupling constant α that was defined in Eq. (1.9). First, let us show that the long-range matrix element $g^{\mathcal{L}}$ corresponds to

the well-known Fröhlich one in the limit of long wavelength. In this limit, and under the assumption of having a single electron in the conduction band (the index $m = n$ is omitted), Eq. (4.5) becomes:

$$g_\nu^{\mathcal{L}}(\mathbf{q}) = i\,\frac{4\pi e^2}{\Omega}\sum_\kappa\left(\frac{\hbar}{2M_\kappa\omega_{0\nu}}\right)^{1/2}\frac{\sum_{\alpha\beta} q_\alpha\, Z^{*\kappa}_{\alpha\beta}\, e_{\kappa\beta\nu}(0)}{\sum_{\gamma\gamma'} q_\gamma \epsilon^\infty_{\gamma\gamma'} q_{\gamma'}}\,, \tag{4.7}$$

and after further assuming a single dispersionless LO mode and an isotropic medium, $\epsilon^\infty_{\alpha\beta} = \epsilon_\infty\delta_{\alpha\beta}$:

$$g^{\mathcal{L}}(\mathbf{q}) = i\,\frac{4\pi e^2}{\Omega\,\epsilon_\infty}\left(\frac{\hbar}{2\omega_{\mathrm{LO}}}\right)^{1/2}\sum_{\kappa\alpha\beta}\frac{q_\alpha\, Z^{*\kappa}_{\alpha\beta}\, e_{\kappa\beta}}{\sqrt{M_\kappa}\,q^2}\,, \tag{4.8}$$

where we simply denoted $\mathbf{e}_\kappa = \mathbf{e}_{\kappa(\nu=\mathrm{LO})}(0)$.[2] In order to reduce Eq. (4.8) to the Fröhlich matrix element in Eq. (1.8) we need to connect the total static dielectric tensor and the Born effective charges. Using the relation [113, 56]:

$$\epsilon_{\alpha\beta}(\omega) = \epsilon^\infty_{\alpha\beta} + \frac{4\pi e^2}{\Omega}\sum_{\kappa\kappa'\nu}\frac{\sum_{\alpha'} Z^{*\kappa}_{\alpha\alpha'} e_{\kappa\alpha'\nu}\sum_{\beta'} Z^{*\kappa'}_{\beta\beta'} e_{\kappa'\beta'\nu}}{\sqrt{M_\kappa M_{\kappa'}}\,(\omega^2_{0\nu}-\omega^2)}\,, \tag{4.9}$$

in the static limit $[\epsilon(\omega{=}0) \equiv \epsilon_0]$ we have:

$$\epsilon_0(\hat{q}) = \epsilon_\infty(\hat{q}) + \frac{4\pi e^2}{\Omega}\sum_{\kappa\kappa'\nu}\frac{\sum_{\alpha\alpha'} q_\alpha Z^{*\kappa}_{\alpha\alpha'} e_{\kappa\alpha'\nu}\sum_{\beta\beta'} q_\beta Z^{*\kappa'}_{\beta\beta'} e_{\kappa'\beta'\nu}}{\sqrt{M_\kappa M_{\kappa'}}\;\omega^2_{0\nu}\,q^2}\,, \tag{4.10}$$

where we denoted $\epsilon(\hat{q}) = \sum_{\alpha\beta} q_\alpha \epsilon_{\alpha\beta} q_\beta / q^2$. For an isotropic medium with a single LO mode we can therefore write:

$$\left(\frac{1}{\epsilon_\infty} - \frac{1}{\epsilon_0}\right)^{1/2} = \frac{1}{\epsilon_\infty}\sqrt{\frac{4\pi e^2}{\Omega}}\sum_{\kappa\alpha\alpha'}\frac{q_\alpha Z^{*\kappa}_{\alpha\alpha'}\, e_{\kappa\alpha'}}{\sqrt{M_\kappa}\,\omega_{\mathrm{LO}}\,q}\,. \tag{4.11}$$

Inserting Eq. (4.11) into Eq. (4.8) finally yields the Fröhlich matrix element of Eq. (1.8).

A generalized, mode-resolved Fröhlich coupling constant $\alpha_\nu(\hat{q})$ can now be tentatively defined by combining Eq. (1.10) and the expression for $g_\nu^{\mathcal{L}}(\mathbf{q})$ in Eq. (4.7):

$$\alpha_\nu(\hat{q}) = \frac{4\pi e^4}{\hbar\,\Omega}\,\frac{q^2}{\omega^2_{0\nu}}\left(\frac{m_{\mathrm{b}}}{2\hbar\omega_{0\nu}}\right)^{1/2}\frac{\left[\sum_{\kappa\alpha\beta} q_\alpha\, Z^{*\kappa}_{\alpha\beta}\, e_{\kappa\beta\nu}(0)/\sqrt{M_\kappa}\,\right]^2}{\left[\sum_{\gamma\gamma'} q_\gamma \epsilon^\infty_{\gamma\gamma'} q_{\gamma'}\right]^2}\,. \tag{4.12}$$

[2] Note that the phonon eigenmodes are real for $\mathbf{q} = 0$.

In the next chapters we will encounter cases in which it is crucial to be able to generalize the Fröhlich model from a single LO mode to a system with multiple infrared-active modes that can contribute to the polar electron-phonon coupling. The evaluation of α_ν and, correspondingly, $g^{\mathcal{L}}_\nu$, allows to extract the contribution of such modes from first principles without the need of additional assumptions.

4.2.3 Polar Wannier-Fourier interpolation

In the simplest approach, one could perform calculations of electron-phonon interactions in polar materials using only the long-range matrix element $g^{\mathcal{L}}$. In this case the overlap factors $\langle\psi_{m\mathbf{k}+\mathbf{q}}|\, e^{i(\mathbf{q}+\mathbf{G})\cdot\mathbf{r}}\,|\psi_{n\mathbf{k}}\rangle$ in Eq. (4.5) can safely be replaced by their $\mathbf{q}+\mathbf{G}\to 0$ limit δ_{mn}, as in Ref. [111], so that calculating $g^{\mathcal{L}}$ becomes a trivial post-processing operation.

The formalism of Sec. 4.2.1 can be translated into a more powerful computational scheme by making use of *ab initio* Wannier-Fourier interpolation. In order to cure the breakdown of the standard interpolation scheme in the case of polar materials, our strategy relies on separating the short-range and the long-range contributions to the electron-phonon matrix elements:

$$g_{mn\nu}(\mathbf{k},\mathbf{q}) = g^{\mathcal{S}}_{mn\nu}(\mathbf{k},\mathbf{q}) + g^{\mathcal{L}}_{mn\nu}(\mathbf{k},\mathbf{q}), \tag{4.13}$$

where the long-range component is given by the generalized Fröhlich matrix element in Eq. (4.5). Since all contributions leading to the long-wavelength divergence are collected inside $g^{\mathcal{L}}$, the short-range component is regular and amenable to Wannier-Fourier interpolation. The following steps then need to be performed:

- evaluate the complete matrix elements g on coarse Brillouin-zone grids;
- subtract $g^{\mathcal{L}}$ for each $(\mathbf{k},\mathbf{q})$ point, to be left with the short-ranged part of the matrix elements $g^{\mathcal{S}}$;
- interpolate the short-range matrix elements using Eqs. (3.77) and (3.75);
- add back the long-range part to the short-range one at arbitrary $\mathbf{k}$ and $\mathbf{q}$ points after interpolation.

This strategy is analogous to the calculation of LO-TO splittings and phonon dispersions in polar materials by separating the analytic and nonanalytic contributions to the dynamical matrix seen in Sec. 2.3.2 [56], which we also integrated in EPW accordingly.

The final remark is that in order to exploit this procedure, the interpolation of the overlap factors in Eq. (4.5) is required. In fact, in this case we cannot use the long-wavelength limit $\langle \psi_{m\mathbf{k}+\mathbf{q}} | \, e^{i(\mathbf{q}+\mathbf{G})\cdot\mathbf{r}} \, | \psi_{n\mathbf{k}} \rangle \simeq \delta_{mn}$ [114], since we need to combine the long-range matrix elements with the *ab initio* ones. The latter contain arbitrary phases for the periodic part of the Bloch wavefunctions resulting from the diagonalization procedure. In order to correctly capture the electronic phases, we can use the unitary rotation matrices $U_{\mathbf{k}}$ from the definition of the MLWF in Eq. (3.69). Using this definition and considering small $\mathbf{q}+\mathbf{G}$ we obtain:

$$\langle \psi_{m\mathbf{k}+\mathbf{q}} | \, e^{i(\mathbf{q}+\mathbf{G})\cdot\mathbf{r}} \, | \psi_{n\mathbf{k}} \rangle = \left[U_{\mathbf{k}+\mathbf{q}} \, U_{\mathbf{k}}^{\dagger} \right]_{mn} . \tag{4.14}$$

This result guarantees the smoothness of the matrix elements. As outlined in Sec. 3.3.2, the matrices $U_{\mathbf{k}}$ are known at every point of the coarse grid from the calculation of the MLWF, and they are obtained at any other arbitrary point via the interpolation of the electron Hamiltonian [84].

Taken together, Eqs. (4.5), (4.13) and (4.14) enable the calculation of millions of electron-phonon matrix elements for polar materials with *ab initio* accuracy. The computational cost for each matrix element corresponds to the cost of the standard interpolation of the short-range matrix element, plus a small additional one of the same order as the computation of the nonanalytic dynamical matrix at arbitrary wavevectors.

4.3 Examples of application

In order to validate our method for investigating Fröhlich coupling from first principles we perform calculations on some prototypical and technologically relevant polar materials, GaN and $SrTiO_3$.

4.3.1 GaN

As a first example we choose to study gallium nitride (GaN), which is the subject of intense experimental and theoretical research owing to its applications in many electronic devices such as heterojunction field-effect transistors, light-emitting and laser diodes [108, 115]. GaN is found in the zinc-blend and wurtzite form, the wurtzite one being slightly more stable in ambient conditions. We perform calculations on the wurtzite (hexagonal) structure, *w*-GaN, shown in Fig. 4.2(a), using LDA norm-conserving pseudopotentials from the `Quantum ESPRESSO` library. For Ga the 3*d* semicore states overlap significantly with the valence charge density [116], hence we include them explicitly in the pseudopotential. The kinetic energy cutoff required for convergence is found to be 250 Ry, together with a $6\times6\times6$ **k**-point mesh. The relaxed lattice parameters are $a = 3.16$ Å and $c = 5.15$ Å, 1% lower than the experimental ones ($a = 3.19$ Å and $c = 5.19$ Å [117]). All calculations repeated using ONCV pseudopotentials [118] with a converged kinetic energy cutoff of 160 Ry yield no noticeable difference in the results [87].

Fig. 4.3(a) shows the electronic band structure calculated along the high-symmetry directions in the Brillouin zone of the hexagonal lattice, reported in Fig. 4.2(b). Only the valence bands close to the gap are shown. The bands in this region have a mixed character [119] and they have been wannierized successfully using sp^3 orbitals centered on the

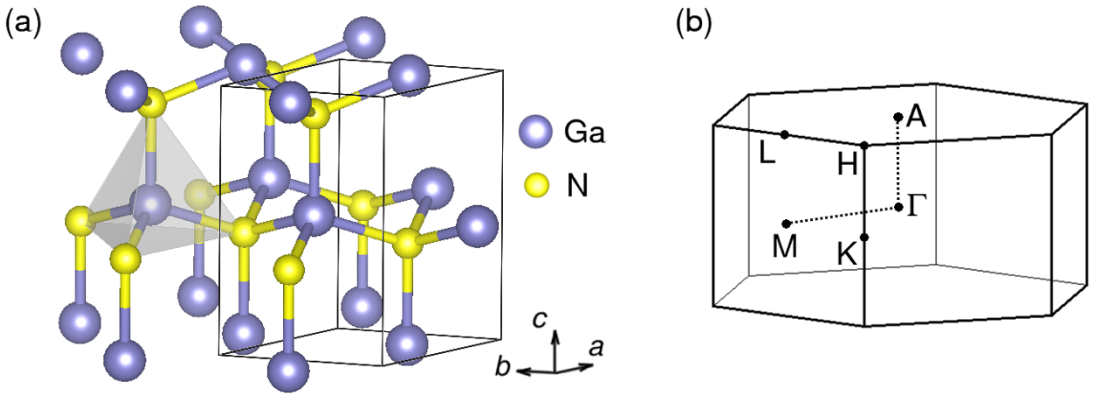

Figure 4.2: (a) Crystal structure of *w*-GaN. (b) Brillouin zone of the hexagonal lattice, with the high-symmetry points labeled.

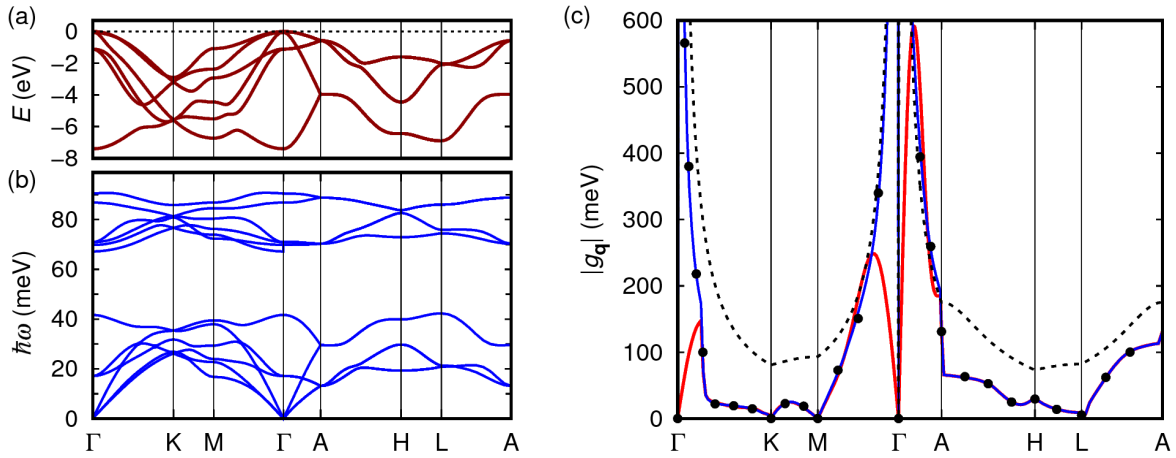

Figure 4.3: (a) Top of the valence band of *w*-GaN. The zero of the energy is set at the valence band maximum. (b) Phonon dispersions along high-symmetry lines in the Brillouin zone. (c) Calculated electron-phonon matrix elements using our method introduced in Sec. 4.2 (blue solid lines) and the standard Wannier-Fourier interpolation (red solid lines), both starting from $6\times6\times6$ electron and phonon Brillouin-zone grids. The simple Fröhlich model is shown as black dashed lines. These are compared with direct DFPT calculations for a subset of wavevectors along the path (filled discs). To obtain $g_{\mathbf{q}}$ we set the initial electronic state $|\psi_{n\mathbf{k}}\rangle$ to the top of the valence band at Γ, the final electronic state $|\psi_{m\mathbf{k}+\mathbf{q}}\rangle$ to the top of the valence band, and the phonon branch to be the highest (LO) optical mode. The gauge-invariant trace of $|g|^2$ over degenerate states is shown.

N atoms together with Ga *d* orbitals (at lower energies) as initial guesses to construct the Wannier functions. In Fig 4.3(b) the phonon dispersion curves calculated starting from a $6\times6\times6$ uniform $\mathbf{q}$ grid are displayed. Our results agree well with previous calculations and experiments [120, 121].

From the linear response to finite electric fields (Sec. 2.3.1) we obtain the high-frequency dielectric constant $\epsilon_\infty = 6.08$ and the Born effective charges (with opposite signs for each Ga and N atom): $Z^*_\perp = 2.63$ and $Z^*_\parallel = 2.74$. For comparison, the experimental values are $\epsilon_\infty = 5.35$ and $Z^*_\perp = 2.65$, $Z^*_\parallel = 2.82$ [122]. The overestimation of the electronic dielectric constant is common in DFT calculations, and it is related to the underestimation of the band gap [123]. These quantities, together with the phonon eigenvectors and eigenmodes, can be used in order to estimate the Fröhlich coupling constant using the generalized formula presented in Eq. (4.12). We also use our calculated electron band effective mass, which is isotropic with a value of $m_\mathrm{b} = 0.20\,m_\mathrm{e}$, in agree-

ment with the literature [124]. We obtain nonzero values of $\alpha_\nu(\hat{q})$ only for the highest phonon branch in each $\mathbf{q}$ direction, with $\alpha_\perp = 0.51$ and $\alpha_\parallel = 0.56$. The calculation of the standard Fröhlich coupling strength α from experimental parameters yields $\alpha_\perp = 0.44$ and $\alpha_\parallel = 0.49$ [122], in good agreement with our estimates.

In Fig. 4.3(c) we demonstrate the method presented in Sec. 4.2 by extracting the electron-phonon matrix elements $g_{mn\nu}(\mathbf{k},\mathbf{q})$ along a path in the Brillouin zone for the highest LO phonon branch (ν=3M=12), initial electronic state at the top of the valence band ($\mathbf{k} = \Gamma$) and final state along the valence band top. We compare (i) direct DFPT calculations, (ii) the Fröhlich model g_F of Eq. (1.8), (iii) the standard Wannier-Fourier interpolation of EPW, and (iv) the polar corrected interpolation using Eqs. (4.5) and (4.13). The matrix element from density-functional perturbation theory goes as $1/|\mathbf{q}|$ for $\mathbf{q} \to 0$ as expected, and vanishes at $\mathbf{q} = 0$ due to the periodic boundary conditions. As a result the 'standard' Wannier-Fourier method attempts to interpolate a strongly fluctuating function, leading to a spurious dip at $\mathbf{q} = 0$ and unphysical behavior elsewhere in the Brillouin zone. The interpolation is accurate only away from the singularity. A similar comparison, but only between the matrix elements calculated using DFPT and the simple Fröhlich model, was also reported in Ref. [125]. At variance with the Fröhlich model, Fig. 4.3(c) demonstrates that our generalized Fröhlich matrix element is able to account for anisotropy in the Brillouin zone, as well as for the band and mode dependence. Most importantly, the generalized interpolation yields accurate matrix elements everywhere in the Brillouin zone and not only near the zone center.

Detailed calculations of electron and hole linewidths in *w*-GaN based on the formalism presented in this chapter have been performed in Ref. [104]. We also mention that a different strategy has been used in Ref. [126] in order to study the band gap renormalization in zinc-blend GaN, combining analytic integration of the Fröhlich matrix element [Eq. (1.8)] near the singularity and numerical evaluation of the full *ab initio* matrix element away from it.

4.3.2 $SrTiO_3$

Despite being an attractive material in the field of oxide electronics for a long time, the interest in $SrTiO_3$ has seen a paradigm shift in recent years after the discovery of the controlled formation of a 2D electron liquid (2DEL) at the bare surface [127] as well as at the interface with $LaAlO_3$ [128]. These 2D electron systems (2DES) offer a playground for a wide range of functional properties such as high-temperature superconductivity and high electron mobility [129]. Many-body interactions, especially electron-phonon coupling, have been found to play an important role in these 2DES and in the bulk system, as we mentioned in Sec. 1.2 [27, 23, 25, 24]. This motivated us to use bulk $SrTiO_3$ as another paradigmatic example to test our method for the study of polar coupling.

$SrTiO_3$ is an oxide with the perovskite structure shown in Fig. 4.4(a). Below 105 K it undergoes a cubic to tetragonal antiferrodistortive phase transition caused by the soft phonon mode at the R point of the Brillouin zone [see Fig. 4.5(a)]. The 'soft' TO mode at Γ, instead, is responsible for a ferroelectric instability that makes $SrTiO_3$ an incipient ferroelectric (or quantum paraelectric) at low temperature with a very high dielectric con-

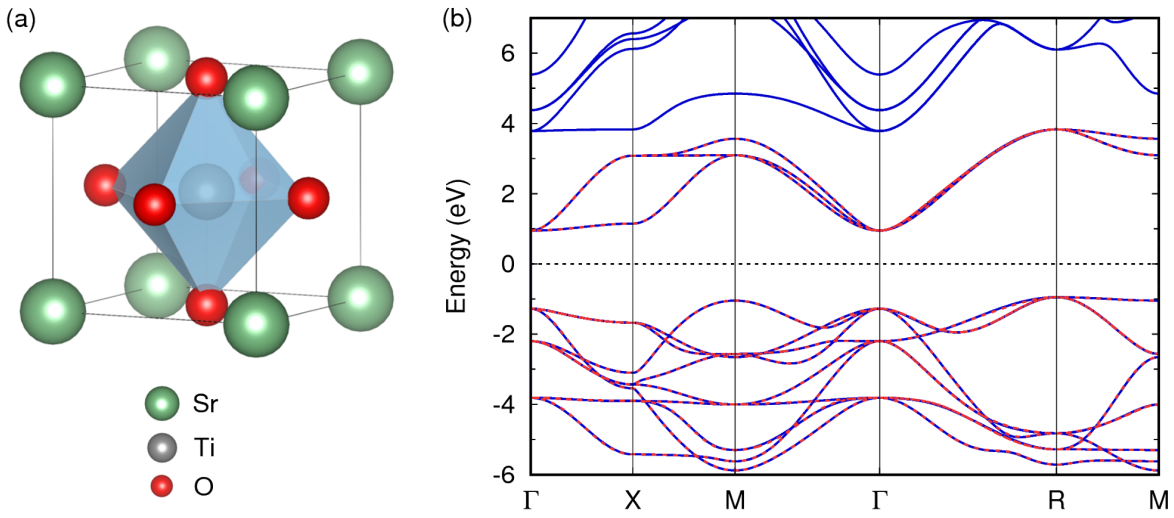

Figure 4.4: (a) Crystal structure of $SrTiO_3$ in the cubic phase. (b) Band structure calculated along high-symmetry directions in the Brillouin zone, with the zero of the energy in the middle of the gap. The dashed red lines on top of the blue solid lines correspond to the band structure obtained with Wannier interpolation: only the highest nine valence bands and lowest three conduction bands have been wannierized.

stant [130]. Our calculations are performed in the cubic phase using norm-conserving pseudopotentials in the LDA approximation generated using the optimized ONCV algorithm [118], with the semicore Ti 3*s* and Ti 3*p* states explicitly taken into account. The LDA was chosen after verifying that it yields phonon frequencies in better agreement with the experiment, especially for the LO phonon branches. The ground-state charge density is converged using a kinetic energy cutoff of 80 Ry and a $8 \times 8 \times 8$ **k**-point mesh. The LDA optimized lattice parameter is $a = 3.855$ Å, which underestimates the experimental one by 1% ($a = 3.900$ Å [131]).

The band gap of $SrTiO_3$ is indirect ($R \rightarrow \Gamma$) as shown in Fig. 4.4(b), with a value of 1.90 eV calculated within the LDA that underestimates the experimental one of 3.25 eV [132]. The band structure in Fig. 4.4(b) is wannierized after calculating the Bloch eigenvalues and wavefunctions on a coarse $4 \times 4 \times 4$ Brillouin-zone grid. We use oxygen *p* orbitals as initial projections for describing the uppermost valence bands and Ti t_{2g} orbitals (d_{xy}, d_{xz}, d_{yz}) for the lowest three conduction bands. The electron effective masses $m = \hbar^2(\partial^2\varepsilon/\partial k^2)^{-1}$ are obtained from finite differences along the ΓX and ΓM directions [see Fig. 4.4(b)], yielding one heavy mass and two light masses for the lowest three conduction bands derived from the Ti t_{2g} orbitals. The results are reported in Tab. 4.1 and are in good agreement with more accurate calculations based on hybrid functionals [133]. The values calculated along the ΓX direction also correspond to the effective masses of each t_{2g} orbital in the three Cartesian directions, each band having light masses along two directions and a heavy mass along the third direction; hence we write $m_l = 0.36$ and $m_h = 5.69$ (in unit of the free electron mass m_e).

The phonon dispersions interpolated from a $4 \times 4 \times 4$ **q** grid are shown in Fig. 4.5(a).

	m_1	m_2	m_3
ΓX	5.69	0.36	0.36
ΓM	0.80	0.58	0.36

Table 4.1: Effective masses calculated along the ΓX and ΓM directions for the three lowest conduction bands, in unit of the free electron mass m_e.

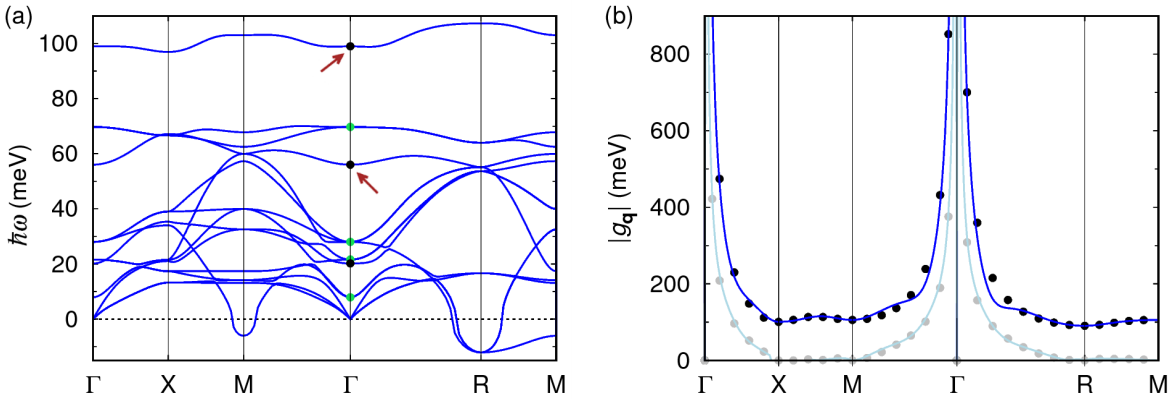

Figure 4.5: (a) Phonon dispersions of cubic $SrTiO_3$, with the LO frequencies at the zone center marked by black filled disks and the TO frequencies marked by green ones. (b) Calculated electron-phonon matrix elements using our polar corrected Wannier-Fourier interpolation starting from $4\times4\times4$ electron and phonon grids, compared with direct DFPT calculations for a set of $\mathbf{q}$ points (filled disks). Analogously to Fig. 4.3(c), $g_{\mathbf{q}}$ is extracted after fixing the initial electronic state $|\psi_{n\mathbf{k}}\rangle$ to the bottom of the conduction band at Γ, the final state $|\psi_{m\mathbf{k}+\mathbf{q}}\rangle$ along the bottom of the conduction band, and the phonon branch to the highest LO mode (LO3, blue line) and to the second highest LO mode (LO2, light blue line). These modes are shown with an arrow in (a).

The zone-center LO and TO modes are highlighted by black and green filled disks, respectively. The calculated LO frequencies, in particular, are in good agreement with the experimental values: $\omega_{\mathrm{LO1}} = 20$ meV, $\omega_{\mathrm{LO2}} = 56$ meV and $\omega_{\mathrm{LO3}} = 99$ meV against the experimental ones $\omega_{\mathrm{LO1}} = 21$ meV, $\omega_{\mathrm{LO2}} = 59$ meV and $\omega_{\mathrm{LO3}} = 99$ meV [134]. We note that the frequency of the 'soft' mode at Γ driving the ferroelectric instability is heavily dependent on the exchange-correlation functional, mainly due to the differences in the theoretical lattice parameter [135]. This mode is generally found to be stable at the LDA relaxed lattice parameter, in agreement with our results, but it becomes unstable upon increasing the lattice volume.

The calculated values for the Born effective charges are $Z^*(\mathrm{Sr}) = 2.56$, $Z^*(\mathrm{Ti}) = 7.26$, $Z_1^*(\mathrm{O}) = -2.055$ and $Z_2^*(\mathrm{O}) = -5.71$, and the high-frequency dielectric constant is $\epsilon_\infty = 6.22$, which is in reasonable agreement with the experimental value $\epsilon_\infty = 5.20$ [136]. The generalized Fröhlich coupling constant $\alpha_\nu(\hat{q})$ can now be calculated from Eq. (4.12). Owing to the cubic structure of $SrTiO_3$, the 'mass-scaled' coupling constant $\alpha_\nu(\hat{q})/\sqrt{m_\mathrm{b}}$ is found to be independent on the $\mathbf{q}$ direction, however it becomes strongly anisotropic

after taking into account the light and heavy electron masses. As in Ref. [137], we choose to use the average band effective mass, $m_b = 0.90\, m_e$. We then obtain isotropic nonzero values for three LO modes: $\alpha_{LO1} = 0.03$, $\alpha_{LO2} = 0.59$ and $\alpha_{LO3} = 1.31$, with the total Fröhlich constant adding up to $\alpha = 1.93$, falling in the intermediate coupling regime.

We now demonstrate that the generalized Wannier-Fourier interpolation [Eqs. (4.5) and (4.13)] is able to correctly reproduce the electron-phonon matrix elements everywhere in the Brillouin zone, including the correct phonon mode dependence. In Fig. 4.5(b) the matrix elements for initial and final electronic states at the bottom of the conduction band are shown, comparing direct calculations from DFPT and the interpolated values using EPW. The black dots and the blue line are for the highest-energy LO mode (LO3), while the gray dots and the light-blue line are for the LO2 mode. These two LO modes are the ones leading to a sizable Fröhlich constant α as discussed above. The agreement of the matrix elements is almost perfect, and the slight discrepancies could be improved by starting from $6 \times 6 \times 6$ coarse Brillouin-zone grids instead of the current $4 \times 4 \times 4$ grids.

Finally we calculate the imaginary part of the electron-phonon self-energy, $\mathrm{Im}\Sigma_{n\mathbf{k}}(\varepsilon_{n\mathbf{k}})$, which represents half of the electron linewidth. We report in Fig. 4.6 calculations per-

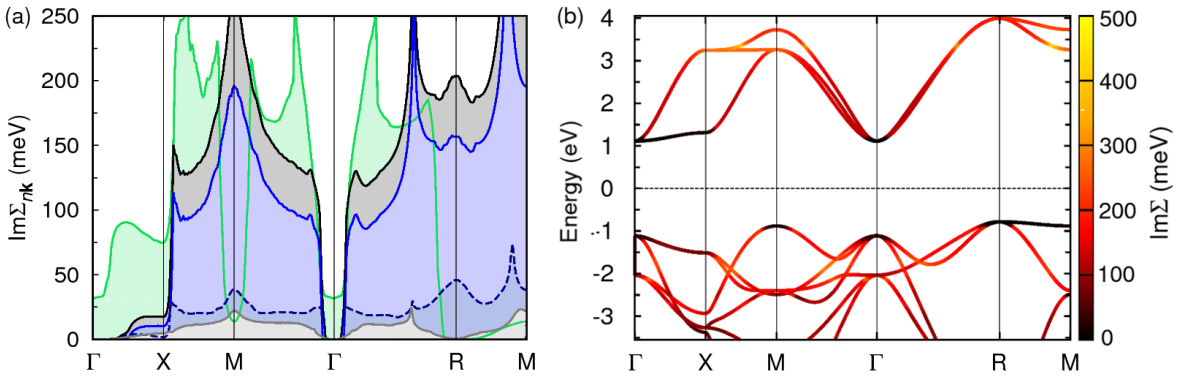

Figure 4.6: (a) Imaginary part of the electron-phonon self energy for the lowest conduction band (black line) and the highest valence band (green line) along the high-symmetry directions. For the conduction band, the total ImΣ is also split into the contributions from different phonon modes: the LO3 mode (solid blue line), the LO2 mode (dashed blue line) and all other phonon modes (gray line). The shades are a guide to the eye. (b) Band structure of $SrTiO_3$ with ImΣ superimposed as a color map.

formed at $T = 20$ K, using 10^6 random $\mathbf{q}$ points to converge the Brillouin-zone integral in Eq. (3.60) and a small Gaussian broadening of 10 meV for the Dirac delta functions. Fig. 4.6(a) shows the linewidths of the lowest conduction band (black line) and of the highest valence band (green line) along the high-symmetry directions in the Brillouin zone. A striking feature is that the imaginary part of the self-energy is zero near the bands edges, that is near Γ for the conduction and R for the valence band. This reflects the fact that the only nonzero contributions to ImΣ come from phonon emission processes, that is the first term in the bracket in Eq. (3.60) for the holes and the second term for the electrons, as no phonon absorption is possible at very low temperature. This means that for initial states within a phonon energy from the conduction band minimum or valence band maximum there are no final states available for scattering. On the other hand, the increase of the linewidths away from the band edges reflects the increase in the density of states in which the electrons (holes) can scatter. This $\mathbf{k}$ dependence can be better understood from the color map shown in Fig. 4.6(b), where the electronic band structure is combined with ImΣ. A more detailed analysis of electron and hole linewidths especially near the band edges will be performed in Chapter 6 for anatase TiO_2.

CHAPTER 5

Polar coupling in the hybrid lead halide perovskite $CH_3NH_3PbI_3$

In this chapter we examine the electron-phonon coupling with polar optical phonons in $CH_3NH_3PbI_3$. After a brief overview of this attractive material and of some questions still open regarding the electron-phonon scattering, we present its fundamental electronic properties including a detailed analysis of the electron and hole effective masses. We then illustrate experimental findings on the temperature-dependent broadening of the emission linewidths that directly motivate our work, and we describe our theoretical results supporting the notion of a strong Fröhlich electron-phonon coupling in this material.

5.1 $CH_3NH_3PbI_3$: an overview

Methylammonium (MA) lead iodide ($CH_3NH_3PbI_3$ or $MAPbI_3$) is an organic-inorganic hybrid lead halide perovskite formed by the two subunits $CH_3NH_3^+$ and PbI_3^-: the former is the organic MA cation while the latter is the inorganic anion. The great interest in halide perovskites is owed to the fact that solar cells based on these materials are some of the most promising photovoltaic technologies and certainly the fastest improving ones, having reached impressive power conversion efficiencies of 22% as compared to 10%

only in 2012 [138, 109, 139]. This is linked to the exceptional capabilities of halide perovskites to operate both as strong light absorbers and as efficient electron and hole conductors. The amount of experimental and theoretical research effort dedicated in the last few years to elucidate the fundamental properties of these materials, as well as to improve the performance of photovoltaic devices, is almost unprecedented. Much research is also currently dedicated to finding suitable lead-free candidates to substitute the traditional lead-based organic-inorganic perovskites, in order to eliminate the issue of toxicity [140].

The most efficient solar cells are based on lead halide perovskites with methylammonium and formamidinium [$CH(NH_2)_2$ or FA] cations [141]. Here we focus on $MAPbI_3$, which can be considered the prototypical material for perovskite photovoltaics. The structure of $MAPbI_3$ is shown in Fig. 5.1, with the lead iodide components forming a network of corner-sharing octahedra and the MA cations located at the center of the cuboctahedral cavities. The crystal structure undergoes two phase transitions, from orthorhombic to tetragonal at 160 K and from tetragonal to cubic at 330 K [142]. While the MA cations have a fixed orientation in the low-temperature orthorhombic phase, an increase of angu-

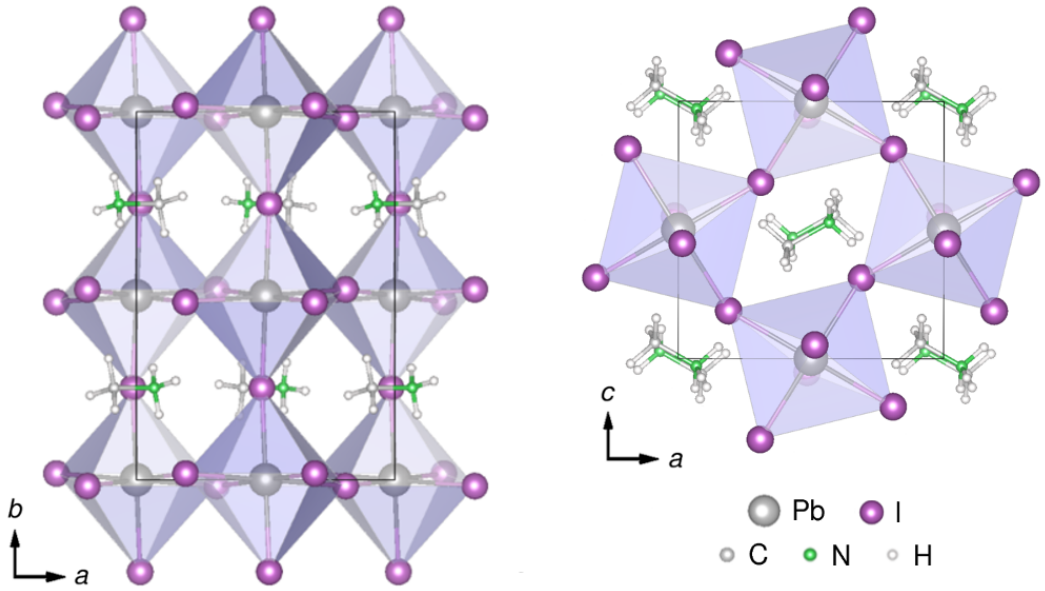

Figure 5.1: Crystal structure of $MAPbI_3$ in the orthorhombic phase: side view (on the left) and top view (on the right).

lar disorder with temperature in the tetragonal and cubic phases is observed [143]. This perovskite compound is a semiconductor with a direct gap of $1.5-1.7$ eV [144], ideal for light absorption in the visible range, and with low carrier effective masses [145]. Moreover, the carrier diffusion length is as high as 1 μm, thus making electron extraction very efficient [146, 147]; however, the fundamental mechanisms causing such a high range of diffusion are still not completely understood [148]. Together with low recombination rates, this requires a high charge-carrier mobility, which has indeed been measured to be of the order of 30 $cm^2\ V^{-1}\ s^{-1}$ at room temperature [149]. The mobility is also found to decrease with temperature via a power law of approximately $T^{-3/2}$ [149, 150]; such temperature dependence indicates that the mobility should be limited mainly by scattering with phonons rather than impurities and imperfections.

The topic of the interaction of charge carriers with lattice vibrations is still a subject of intense debate. In particular, a question to be answered is whether the electron-phonon scattering limiting the mobility is due to acoustic or optical phonons. While the temperature dependence of the mobility is compatible with deformation potential scattering with acoustic phonons, it does not rule out Fröhlich scattering with polar optical phonons, for which it is harder to establish an analytical temperature dependence [151]. In Sec. 5.3 we investigate the Fröhlich coupling in $MAPbI_3$ by focusing on the broadening of emission peaks as seen from photoluminescence experiments.

5.2 Electronic properties

We present calculations of electronic properties of $MAPbI_3$ performed for the orthorhombic phase using the crystallographic data of Ref. [142]. The ground-state electronic structure is computed as in Ref. [152] using norm-conserving pseudopotentials in the LDA approximation, with the semicore *d* states explicitly taken into account for Pb and I, and including spin-orbit coupling. The ground-state calculations are converged with a plane-wave cutoff of 100 Ry and a $6 \times 6 \times 6$ unshifted Brillouin-zone grid.

The band structure obtained within DFT is shown in gray in Fig. 5.2. The corresponding fundamental gap of 0.48 eV heavily underestimates the experimental value of $1.62-1.64$ eV [144]. In order to have a more accurate band structure, we use quasiparticle energies computed by Marina Filip within the *GW* method as in Ref. [153]. These were calculated using the `Yambo` code [154] and a self-consistent scissor scheme which yields a quasiparticle gap of 1.71 eV, in excellent agreement with experiment. To obtain the full *GW* band structure we make use of Wannier interpolation as outlined in Sec. 3.3.1. We construct maximally localized Wannier functions for $MAPbI_3$ starting from iodine and lead *p* states as initial guesses, consistent with the dominant I-*p* character of the valence and the mixed Pb-*p* and I-*p* character of the conduction bands in the vicinity of the gap [155]. In this way we describe the topmost 72 valence bands and the lowest 24 conduction bands; for the empty bands, the disentanglement procedure is used, with an energy window of 5 eV above the conduction band bottom. We checked that the DFT band structure is accurately interpolated starting from a $4\times4\times4$ **k**-point grid. The *GW* eigenvalues calculated on the same $4\times4\times4$ grid are then interpolated using the Wannier functions constructed. The resulting band structure is shown in blue in Fig. 5.2 and it

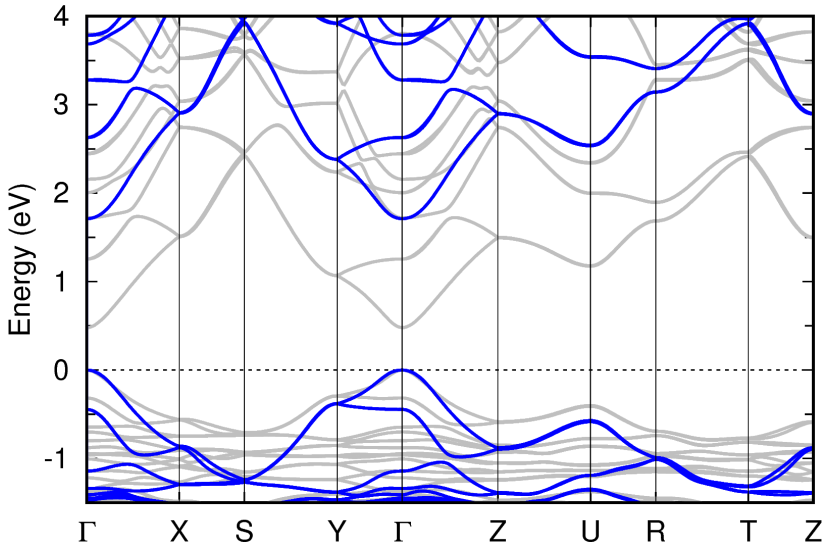

Figure 5.2: Electronic band structure of $MAPbI_3$ in the orthorhombic phase calculated using Wannier interpolation from the DFT (gray) and *GW* (blue) eigenvalues. The bands are aligned to the valence band top, set as the zero of the energy.

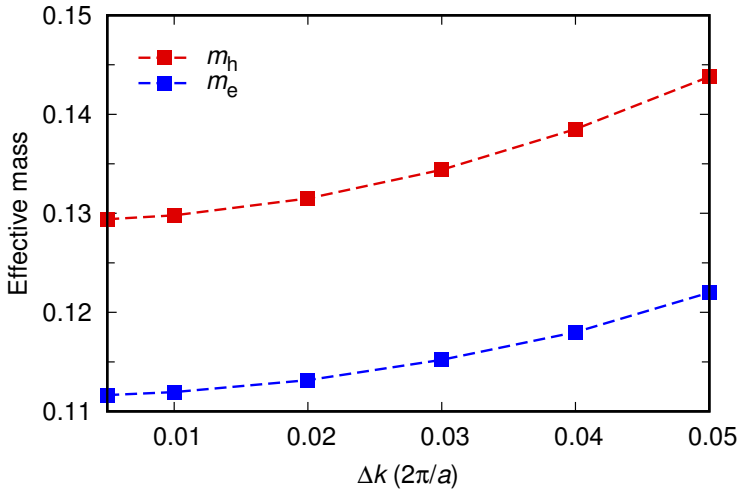

Figure 5.3: Convergence of the electron and hole effective masses, in units of the electron mass, with respect to the distance from the Γ point.

exhibits slightly more dispersive bands than in the DFT case.

We compute the effective mass tensor from the second derivatives of the electronic energies, $m_{\alpha\beta} = \hbar^2\left(\partial^2\varepsilon_{n\mathbf{k}}/\partial k_\alpha \partial k_\beta\right)^{-1}$. The second derivatives are evaluated using finite differences from the eigenvalues calculated at a distance of 1% of $2\pi/a$ from the Γ point, where $a = 8.84$ Å. This ensures a precision of 0.5% in the effective masses, as shown in Fig. 5.3. An isotropic effective mass is obtained by averaging the eigenvalues extracted from the diagonalization of $m_{\alpha\beta}$. In particular, the electron (m_e) and hole (m_h) effective masses at the band edges correspond to $\mathbf{k} = 0$ and n the lowest conduction band or highest valence band index, respectively. The values obtained from the DFT and *GW* Wannier-interpolated eigenvalues are presented in Tab. 5.1. We checked that the ones from the DFT interpolated eigenvalues are accurate up to 2% with respect to direct DFT calculations. We can see that the effective masses are underestimated by almost a factor of two within DFT. The reduced effective mass $\mu = (1/m_h + 1/m_e)^{-1}$ obtained within the *GW* method, $\mu = 0.112$ (in units of the electron mass), is in excellent agreement with the experimental value of 0.104 [145], thus guaranteeing an accurate description of the curvature near the band edges.

	m_h	m_e	μ
DFT	0.130	0.112	0.060
GW	0.230	0.217	0.112

Table 5.1: Isotropic hole (m_h), electron (m_e) and reduced (μ) effective masses of orthorhombic $MAPbI_3$ in unit of the electron mass, calculated from Wannier interpolation of the DFT and *GW* band structures.

5.3 Broadening of emission linewidth

5.3.1 Photoluminescence experiment

A means to investigate the electron-phonon scattering mechanisms in $MAPbI_3$ is by examining the temperature-dependent broadening of the emission lines in photoluminescence experiments. This analysis was carried out by Laura Herz and co-workers and presented in Ref. [156]. Fig. 5.4 displays the full-width at half-maximum (FWHM) extracted from the steady-state photoluminescence peak measured for a broad temperature range. The results for both $FAPbI_3$ and $MAPbI_3$ are reported. In the latter case, the FWHM abruptly increases for temperatures below 150 K: this behavior is observed elsewhere in the literature for $MAPbI_3$, and it is attributed to the presence of some disordered MA domains in the low temperature configuration [149, 156, 157]. This feature complicates the PL spectra and hinders the analysis of the temperature dependence of the linewidth broadening. In the case of $FAPbI_3$, however, such extrinsic features are not present, and this allows to analyze the linewidth broadening using the following model [158, 151]:

$$\begin{aligned}\Gamma(T) &= \Gamma_0 + \Gamma_{imp} + \Gamma_{ac} + \Gamma_{LO} \\ &= \Gamma_0 + \gamma_{imp} e^{-E_b/(k_B T)} + \gamma_{ac} T + \gamma_{LO} n(\omega_{LO}),\end{aligned} \tag{5.1}$$

where Γ_0 is a temperature-independent inhomogeneous broadening term arising from scattering due to disorder and imperfections, while Γ_{imp} accounts for the scattering with ionized impurities with binding energy E_b. The scattering with phonons is described by the last two terms: the first one takes into account deformation potential scattering

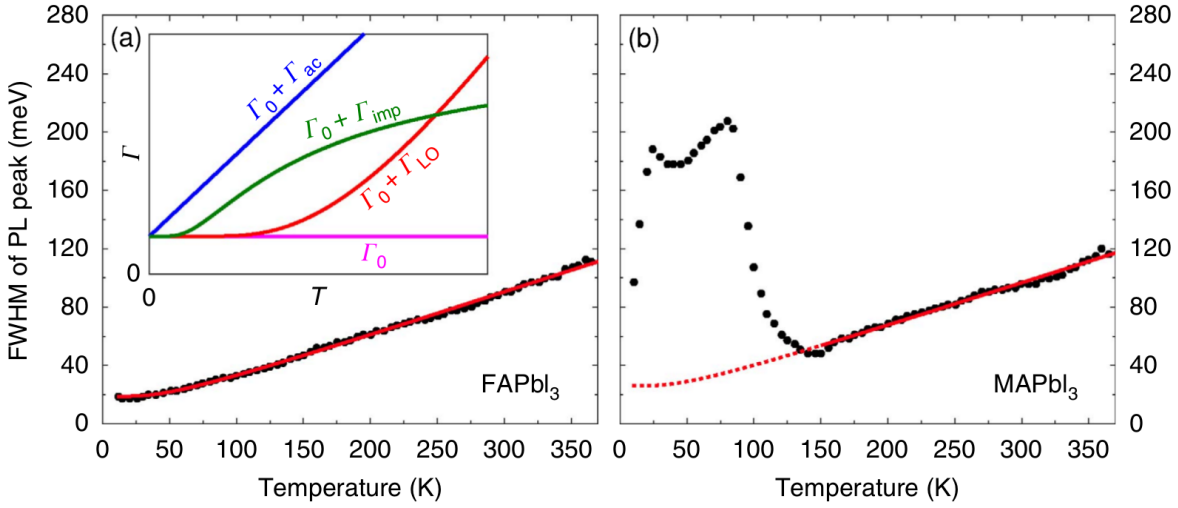

Figure 5.4: FWHM of the PL peak as a function of temperature for $FAPbI_3$ (a) and $MAPbI_3$ (b). The black dots correspond to the experimental data while the red lines are fits of the form $\Gamma(T) = \Gamma_0 + \Gamma_{LO}(T)$. In the case of $MAPbI_3$, the fit is extrapolated in the low temperature region (red dots). The inset in (a) shows the temperature dependence of the various terms in Eq. (5.1) contributing to the broadening of the PL peak. Reproduced from Ref. [156].

with acoustic phonons, and the second one the scattering with LO phonons, taken to have a constant energy ω_{LO}. While both terms are in principle proportional to the Bose-Einstein distribution $n(\omega) = [e^{\hbar\omega/(k_B T)} - 1]^{-1}$, the very low energy of acoustic phonons (up to ~ 2.5 meV in $MAPbI_3$ [156]) allows one to approximate this factor as linear with temperature over the whole experimental range. The functional form of each term in Eq. (5.1) is shown in the inset of Fig. 5.4(a).

The analysis carefully carried out in Ref. [156] reveals that the linewidth broadening of $FAPbI_3$ in Fig. 5.4(a) is dictated by $\Gamma_0 + \Gamma_{LO}$, while Γ_{imp} and Γ_{ac} carry negligible contributions. The resulting fit is shown by the red line. The energy extracted for the LO phonon is $\hbar\omega_{LO} = 11.5$ meV, which is relatively low compared to most polar semiconductors and insulators; correspondingly, the Bose-Einstein factor (and thus the linewidth broadening) starts exhibiting a linear temperature behavior above only ~ 50 K, as compared for example to around 250 K for a LO phonon with an energy of 100 meV.

Having established these results, the same fit can be applied to the case of $MAPbI_3$, and extrapolated for low temperatures as shown in red in Fig. 5.4(b). This corresponds to the broadening expected in the absence of the additional trap-related emission effects.

5.3.2 Calculation details

We now proceed to investigate this interesting problem using first-principles calculations. The electronic band structure is taken from Ref. [153] and corresponds to the *GW* calculations discussed in Sec. 5.2. As seen, this gives effective masses in very good agreement with the experiment, which is crucial for our electron-phonon calculations. The electron-phonon self-energy at the band edges, in fact, is very sensitive to the curvature of the bands. For the lattice dynamical properties, we exploit DFPT calculations performed by M. A. Pérez-Osorio as presented in Ref. [159]. The calculations are carried out for the low-temperature orthorhombic phase of $MAPbI_3$, since the vibrational frequencies are found to be relatively insensitive to the structure; moreover, the measured PL broadening does not change across the orthorhombic to tetragonal phase transition. This avoids the complications due to structural disorder for the higher temperature phases.

As mentioned in Sec. 4.2.3, the long-range electron-phonon matrix element of Eq. (4.5) can be used in first-principles calculations either as a post-processing tool, or in combination with the Wannier-Fourier interpolation technique. Since for the system under study it is computationally prohibitive to perform a full Wannier-Fourier interpolation of the electron-phonon matrix element, we take advantage of the former method. Hence, we calculate only the long-range component $g^{\mathcal{L}}$ corresponding to the generalized Fröhlich matrix element, with $\mathbf{G} = 0$, $\mathbf{q}$ belonging to a Brillouin-zone grid centered in $\mathbf{q} = 0$, and the overlap factors replaced by δ_{mn}. The matrix element then reads:

$$g^{\mathcal{L}}_{mn\nu}(\mathbf{q}) = i\,\frac{4\pi e^2}{\Omega}\sum_{\kappa}\left(\frac{\hbar}{2M_\kappa\omega_{\mathbf{q}\nu}}\right)^{1/2}\frac{\mathbf{q}\cdot\mathbf{Z}^*_\kappa\cdot\mathbf{e}_{\kappa\nu}(\mathbf{q})}{\mathbf{q}\cdot\boldsymbol{\epsilon}_\infty\cdot\mathbf{q}}e^{-i\mathbf{q}\cdot\boldsymbol{\tau}^0_\kappa}\delta_{mn}\,. \tag{5.2}$$

We remark that in this way only the polar interaction with the LO phonons is taken into account.

For our calculations we make use of the software `EPW`, but we create a custom version where only the final step of the interpolation procedure, from Wannier space to arbitrary $(\mathbf{k},\mathbf{q})$ meshes in Bloch space, is performed. The wannierization of the Kohn-

Sham wavefunctions and the transformation of the electronic Hamiltonian in Wannier basis are performed separately using `wannier90` as described in Sec. 5.2, and the resulting real-space Hamiltonian $H_{mn}(\mathbf{R})$ is then read by `EPW`. In order to obtain the phonon frequencies including the LO-TO splittings and the relative phonon eigenmodes, we add to the dynamical matrix calculated at $\mathbf{q} = 0$ the nonanalytic contribution of Eq. (2.46). Finally, the electron-phonon matrix elements are calculated for arbitrary $\mathbf{k}$ and $\mathbf{q}$ points using Eq. (5.2). The imaginary part of the electron-phonon self-energy in Eq. (3.60) is calculated using a broadening for the Dirac delta functions as small as 1 meV, and two million random $\mathbf{q}$ points for the Brillouin-zone integration.

5.3.3 Results

Before calculating the broadening of the electronic quasiparticle states arising from the electron-phonon interactions as described above, we use our first-principles formalism in order to investigate which phonon modes are responsible for the polar coupling without any *a priori* information. The normal modes of vibrations in $MAPbI_3$ are 144 in total, corresponding to the number of degrees of freedom in the unit cell. The polar coupling strength associated to each mode is described by the generalized Fröhlich constant $\alpha_\nu(\hat{q})$ of Eq. (4.12). Fig. 5.5(a) displays this quantity calculated for $\mathbf{q}$ along the $[111]$ direction, showing only the low-energy phonon region (mode numbers $1-72$). These phonon modes correspond mostly to internal vibrations of the PbI_3 network [159]. The higher energy phonons instead correspond to internal vibrations of the MA cations, for which we obtain negligible values of α. The main LO phonon contributing to the polar coupling is found to have an energy of about 13 meV, and it is depicted in Fig. 5.5(b).

We now proceed to calculate the imaginary part of the electron-phonon self-energy. Fig. 5.6(a) shows $\mathrm{Im}\Sigma$ along high-symmetry directions in the Brillouin zone for the highest valence band and the lowest conduction band at $T = 20$ K. In both cases $\mathrm{Im}\Sigma$ vanishes in a narrow region near the band edge at Γ, in accordance with the absence of LO phonon

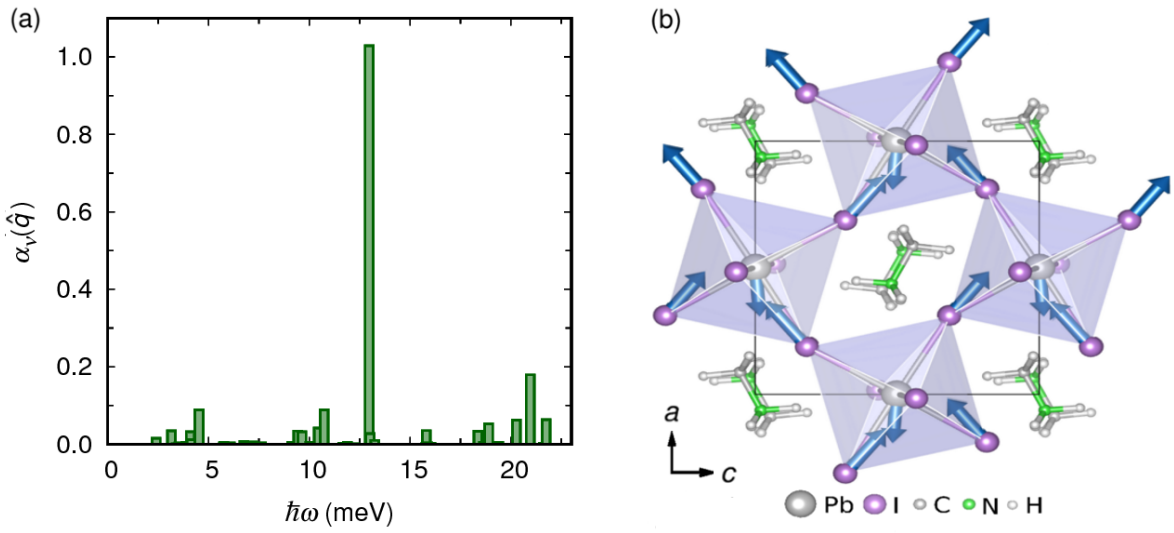

Figure 5.5: (a) Generalized Fröhlich coupling constant $\alpha_\nu(\hat{q})$ calculated for the [111] **q** direction, with the mode number ν going from 1 to 72. (b) Ball-and-stick representation of the LO vibration with the highest coupling constant α (courtesy of M. A. Pérez-Osorio). The blue arrows indicate the stretching of the Pb and I atoms.

absorption processes at low temperature and with the impossibility of scattering to lower energy states through the emission of a LO phonon. The behavior of ImΣ in the rest of the Brillouin zone, instead, is linked to the phase-space availability of final states for scattering. We also remark that in order to resolve the zero linewidth at Γ, a very small delta function broadening (1 meV) is needed. On the other hand, a broadening of 10 meV is accurate in most of the Brillouin zone and gives a smoother trend, but it yields finite linewidths near Γ. This is due to the energy of the main LO phonon being relatively small (13 meV). This observation is important since we are interested primarily in the linewidth broadening of the band edges. In Fig. 5.6(b) the temperature dependence of ImΣ along the same Brillouin-zone path is shown, using a broadening of 10 meV. In particular, we can see an increase at Γ from a few meV at $T = 20$ K to almost 50 meV at $T = 300$ K.

In Fig. 5.7 we present results for a broader energy region at $T = 200$ K. Panel (a) shows a heat map of ImΣ projected on the quasiparticle band structure of $MAPbI_3$, whereas in panel (b) ImΣ is shown as a function of energy together with the electronic density of states (DOS) calculated on a $30 \times 30 \times 30$ uniform **k** grid. This figure shows how the linewidth broadening increases with increasing DOS, as each state can scatter

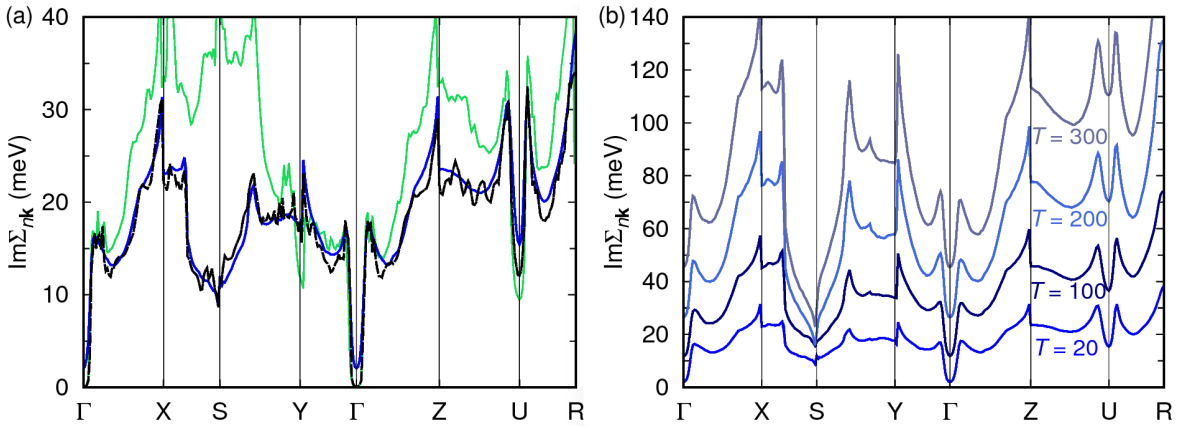

Figure 5.6: (a) Imaginary part of the electron-phonon self-energy for the highest valence band (green) and the lowest conduction band (black) along high-symmetry Brillouin-zone directions, calculated using a delta function broadening of 1 meV. For the lowest conduction band the calculation using a broadening of 10 meV is also shown in blue. (b) ImΣ for the lowest conduction band calculated at the different temperatures indicated in the plot (in K) with a broadening of 10 meV.

into increasingly more states through phonon emission or absorption.

In order to obtain the FWHM of the PL peak, we consider separately the broadening arising from the interaction of conduction-band electrons and valence-band holes with the phonons, namely we sum twice the imaginary part of the electron-phonon self-energy corresponding to the valence and conduction band edges [160]. This is motivated by the fact that even at low temperature, the photoexcited electron-hole pairs are mainly dissociated into free electrons and holes [144, 148, 161, 162]. In addition, the calculated data are rigidly shifted by the FWHM at $T = 0$ K (25.72 meV) to account for the inhomogeneous broadening. The results obtained using this procedure, which we refer to as Fermi's Golden rule as it is based on Eq. (3.60), are shown in Fig. 5.8 as a function of temperature (blue triangles). These are compared with the experimental data obtained from the fit shown in Fig. 5.4(b), which does not take into account the anomalous broadening below 150 K as discussed. The analysis of our data reveals that the temperature dependence is dictated by a characteristic phonon energy scale of 13 meV, in agreement with the results shown in Fig. 5.5(a) and with the experimental analysis [156]. The calculated data, however, appear to overestimate the experimental ones.

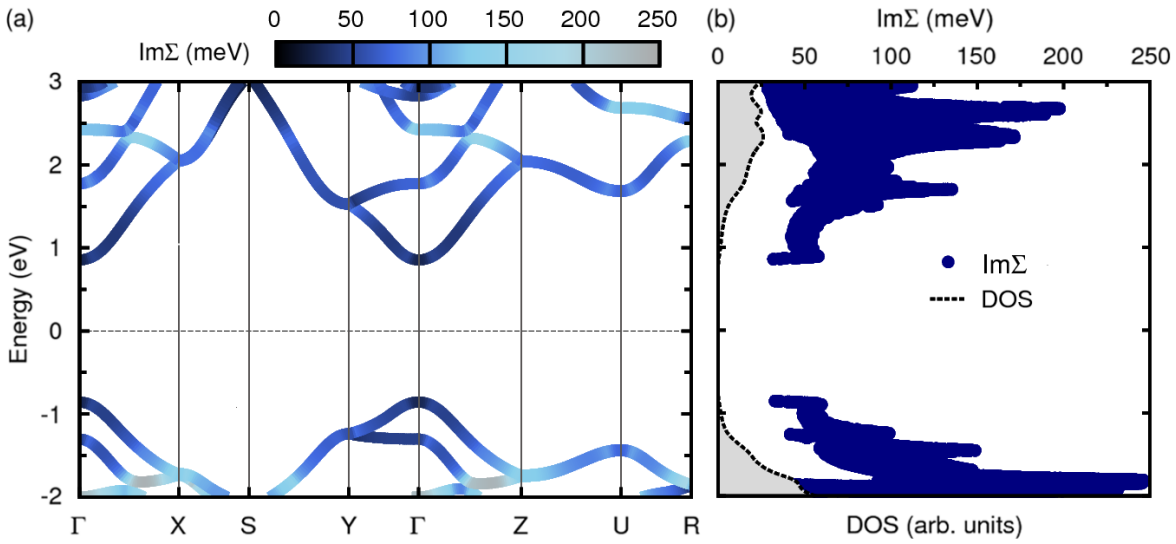

Figure 5.7: (a) *GW* band structure of orthorhombic $MAPbI_3$ combined with a heat map of the imaginary part of the electron-phonon self-energy ImΣ calculated for $T = 200$ K. The zero of the energy is set to the middle of the gap. (b) ImΣ shown as a function of energy, together with the electronic density of states (DOS).

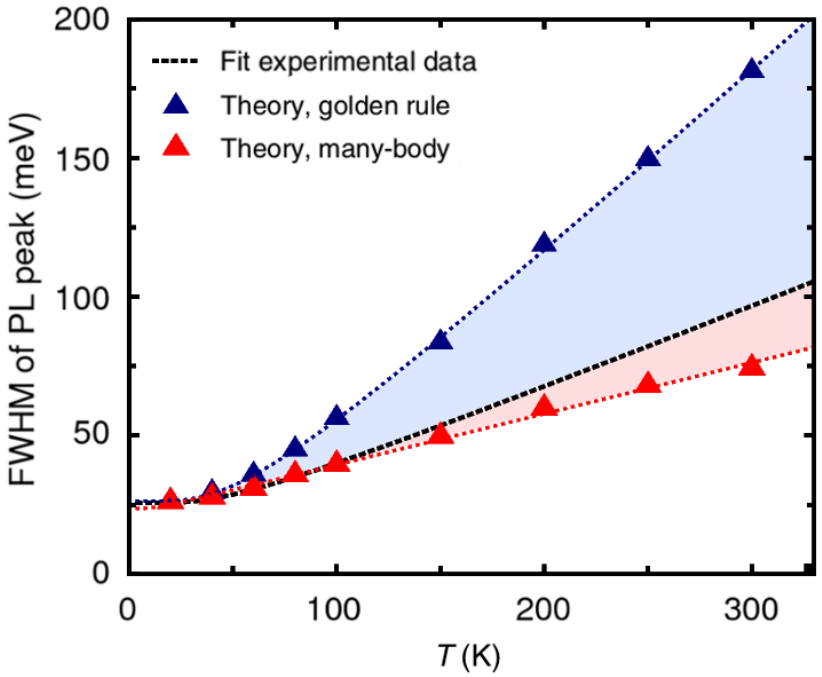

Figure 5.8: Temperature dependence of the FWHM of the PL peak: fit to the experimental data as in Fig. 5.4(b) (black dashed line) compared to the theoretical calculations using Fermi's golden rule (blue triangles) and the many-body renormalization factor (red triangles) as explained in the text. The shades are a guide to the eye.

To provide a better quantitative analysis of the broadening of the PL peak, we need to take into account the quasiparticle renormalization factor Z. Its effect is to rescale the broadening of the Lorentzian quasiparticle peaks as seen from Eq. (3.68); in practice, this corresponds to an improved solution of the quasiparticle equation [79]. We evaluate the many-body renormalization factor $Z_{n\mathbf{k}} = \left(1 - \partial \mathrm{Re}\Sigma_{n\mathbf{k}}(\omega)/\partial\omega\right)^{-1}$ at the band edges. The values obtained for the lowest temperature considered, $T = 20$ K, are $Z = 0.53$ and $Z = 0.54$ for the valence band top and conduction band bottom, respectively. The results are shown as red triangles in Fig. 5.8 and are in good agreement with the experiment.

Our theoretical calculations thus corroborate the experimental analysis, concluding that the broadening of the PL linewidth is driven by the interaction between free carriers and LO phonons. More broadly, it is likely that Fröhlich coupling is the dominant charge-carrier scattering mechanism in $MAPbI_3$, and that this also applies to other hybrid lead halide perovskites. Other subsequent theoretical and experimental studies further support these conclusions [157, 161, 163, 164]. Polaron physics has also been invoked to explain the ease of charge separation in halide perovskites and the charge-carrier mobility [162, 165]. In order to settle some of the remaining questions it would be important to perform full *ab initio* calculations including all electron-phonon scattering mechanisms, and to evaluate the intrinsic temperature-dependent mobilities, however this is extremely demanding computationally, and is yet to be done.

CHAPTER 6

Electron-phonon scattering in anatase TiO_2

In this chapter we investigate the electron-phonon interactions in a polar semiconductor of major technological interest, anatase TiO_2. Following a short introduction, we discuss the electronic and vibrational properties of this material within DFT and DFPT, and we then move to the study of the electron-phonon coupling. Here we focus on the carrier lifetimes, and we show that the polar matrix element significantly reduces them and is responsible for the anisotropy of the coupling.

6.1 Introduction

Titanium dioxide (TiO_2) is found in nature in two main forms, rutile and anatase. Rutile is the most stable phase at high temperatures, and it is by far the most studied thanks to the availability of large single crystals for a long time [166]. On the other hand, only more recently a method to grow large single crystals of anatase by chemical transport reactions has been devised [167], making experimental characterization possible.

Here we are concerned with the properties of pristine bulk TiO_2 in the anatase form, which is the one that presently attracts the most interest and research efforts for its superior properties and performance in technological applications. Some of these are largely

linked to the *n*-type conductivity properties that this material exhibits when doped, as we will see more in detail in the next chapter. In particular, it finds applications in photocatalysis [107, 168] and solar-energy harvesting devices [169, 109], as well as in transparent conductive layers [170].

The crystal structure of anatase is body-centered tetragonal (BCT), and it belongs to the $I4_1/amd$ space group. The basic building blocks are made of slightly distorted TiO_6 octahedra. In Fig. 6.1(a),(b) both the primitive and the conventional unit cells are shown, with the corresponding Brillouin zone of the BCT lattice in Fig. 6.1(c). The lattice parameters are $a = 3.784$ and $c = 9.515$ Å [171]. The electronic band gap of anatase is indirect, with the top of the valence band lying close to the X point and the bottom of the conduction band at the Γ point, as confirmed by recent ARPES studies [172]. The value of the electronic quasiparticle gap was measured very recently by ARPES, and was found to be 3.47 eV [173]. Using *GW* theory the band gap has been estimated to be 3.3−3.8 eV depending on the different flavors of *GW* methods used [174, 175, 176]. This overestimation of the gap likely stems from the neglect of the electron-phonon renormalization effects [77, 173]. The coupling with phonons also manifests itself in the Urbach exponential tail in the measured absorption spectrum [177], making it theoretically challenging to predict the indirect absorption edge. From polarized optical transmission measure-

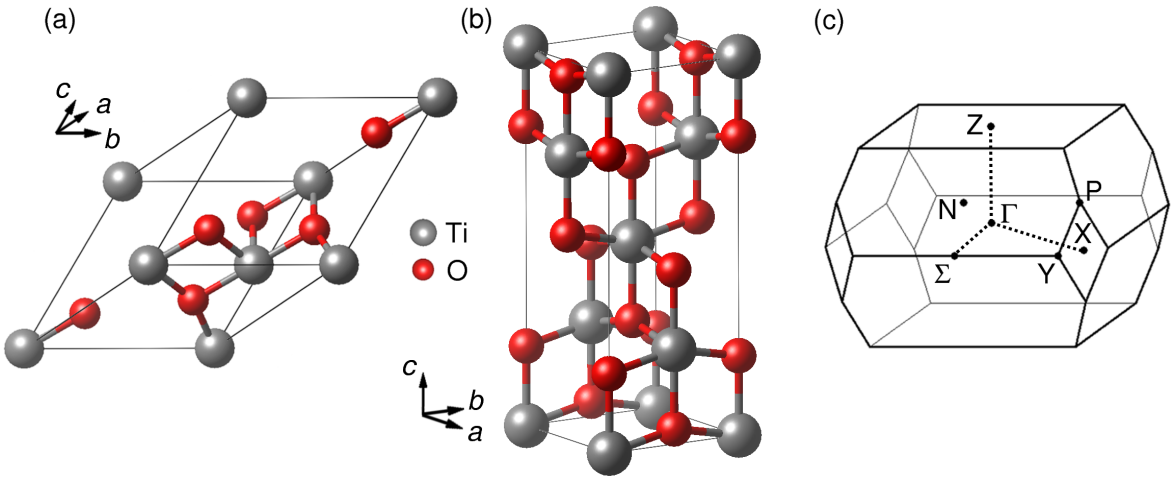

Figure 6.1: Crystal structure of anatase TiO_2: primitive (a) and conventional (b) unit cell. (c) Brillouin zone of the body-centered tetragonal lattice, with the special points labeled.

ments this is found to be 3.2 eV [177]. Calculations using the Bethe-Salpeter equation (BSE) [178] yield direct optical gaps that are in good agreement with experimental data for direct transitions [174, 175]. Exciton physics in anatase has been extensively investigated, and points at the existence of stable bound excitons delocalized in the ab plane [173].

6.2 Electronic and vibrational properties

We perform DFT calculations on anatase TiO_2 using the PBE generalized gradient approximation [46] and allowing the atomic positions to relax. We use norm-conserving pseudopotentials, with the semicore Ti 3s and Ti 3p states explicitly taken into account. Convergence is achieved with a plane-wave kinetic energy cutoff of 200 Ry and a $6\times6\times6$ **k**-point sampling of the Brillouin zone. The calculated band structure is reported in Fig. 6.2, together with the density of electronic states calculated on a $25\times25\times25$ uniform grid. We obtain an indirect band gap of 2.00 eV, in line with DFT results in the literature [174]. The actual quasiparticle gap is underestimated by about 40%, as usual in DFT calculations, however the shape of the bands is found to be accurate within DFT [174, 176]. This point allows us to rely on the DFT electronic states as a good starting point for our study of the electron-phonon interaction effects in anatase.

We compute the electron band effective mass using finite differences around the Γ point. The value is isotropic on the basal plane of the tetragonal lattice (corresponding to the ΓX direction), $m_\perp = 0.40\,m_e$, whereas along the c axis it is $m_\parallel = 4.03\,m_e$, reflecting the smaller curvature seen in the band structure along the ΓZ direction.

The uppermost valence states shown in Fig. 6.2 mainly derive from O 2p orbitals, while the lowest part of the conduction band comes from the strongly localized Ti 3d states. Maximally localized Wannier functions are readily extracted using these orbitals as initial guesses for projecting the Kohn-Sham wavefunctions. The band structure is interpolated accurately starting from a $4\times4\times4$ coarse **k**-point grid; in particular we

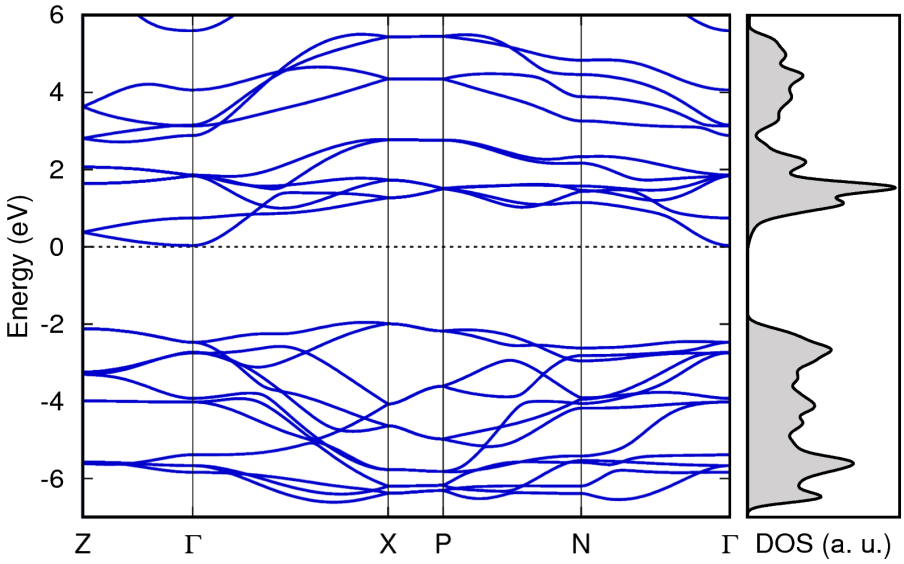

Figure 6.2: Band structure of anatase TiO_2 calculated within DFT along high-symmetry lines of the Brillouin zone of the BCT lattice. The zero of the energy corresponds to the conduction band minimum. The Ti 3*s* and 3*p* states and the O 2*s* states lie at lower energies in the valence bands: the energy region shown corresponds to the wannierized bands. The density of states is displayed in the right panel.

verify that the effective masses coincide with the direct DFT calculation.

The phonon dispersion relations of anatase obtained from DFPT are shown in Fig. 6.3. The interatomic force constants are calculated starting from a $4 \times 4 \times 4$ $\mathbf{q}$ grid and the dynamical matrix is then interpolated onto a fine set of points along the high-symmetry lines to obtain the phonon frequencies. Since the unit cell contains six atoms, there are eighteen modes in total, with three acoustic and fifteen optical modes. For the space group of anatase, the irreducible representations corresponding to the optical modes are $\Gamma_{\text{opt}} = A_{1g} + A_{2u} + 2B_{1g} + B_{2u} + 3E_g + 2E_u$ (the E_g and E_u representations are doubly degenerate) [179]. Among these, the A_{1g}, B_{1g} and E_g modes are Raman active, whereas the A_{2u} and the two E_u modes are infrared (IR) active, and the B_{2u} is silent. Our calculated values are in good agreement with previous calculations [180, 181] and with IR reflectivity and Raman spectroscopy measurements [182, 179].

The polar coupling is manifest in the large LO-TO splittings at Γ for the phonon modes that are infrared active as highlighted in the figure. The LO-TO splittings are calculated through the nonanalytic part of the dynamical matrix in Eq. (2.46), after the Born

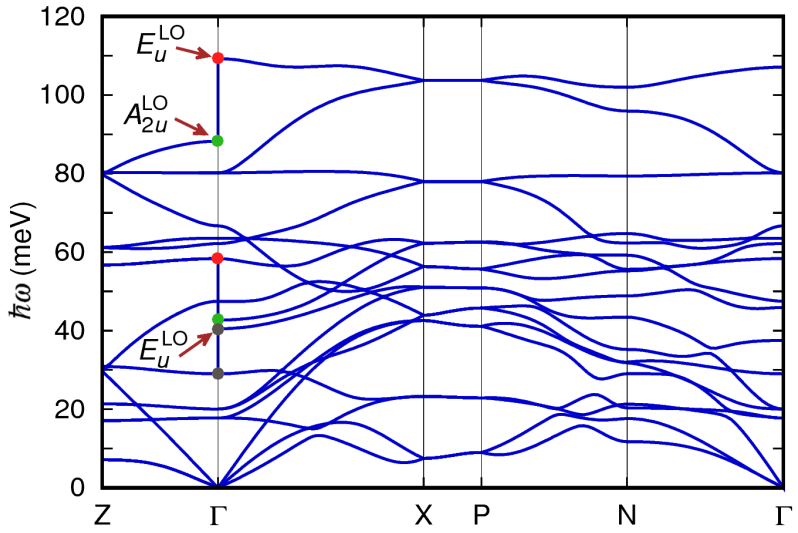

Figure 6.3: Phonon dispersions of anatase TiO_2 from DFPT. The three infrared-active LO modes are explicitly indicated, while the filled circles identify the energies of the split LO and TO modes: the lowest-energy E_u mode (gray), the A_{2u} (green) and the highest-energy E_u (red).

effective charges and high-frequency dielectric constants have been obtained. The latter are $\epsilon_{\perp}^{\infty} = 7.1$ and $\epsilon_{\parallel}^{\infty} = 6.4$, overestimating by about 20% the experimental ones $\epsilon_{\perp}^{\infty} = 5.8$ and $\epsilon_{\parallel}^{\infty} = 5.4$ [182], although there is a degree of uncertainty in the measured data [180]. For the Born effective charges we find two independent values for the Ti atoms, $Z_{\perp}^{*}(\mathrm{Ti}) = 6.76$ and $Z_{\parallel}^{*}(\mathrm{Ti}) = 5.74$, which are both larger than the nominal ionic charge of the Ti ion, $Z(\mathrm{Ti}) = 4$. For the oxygen atoms the anisotropy is stronger and there are three independent components, one of which is smaller (in absolute value) than the nominal ionic charge $Z(O) = -2$: $Z_{xx}^{*}(\mathrm{O}) = -1.15$, $Z_{yy}^{*}(\mathrm{O}) = -5.61$ and $Z_{zz}^{*}(\mathrm{O}) = -2.87$. All oxygen atoms in the unit cell carry the same charge along the parallel direction and two different charges in the perpendicular directions, thus ensuring the total charge neutrality.

We finally comment that the A_{2u} mode is infrared active only for light polarized parallel to the c axis, whereas the E_u modes are active for light polarized perpendicular to the c axis. This is reflected in Fig. 6.3, where the LO-TO frequencies are seen to split along different Brillouin-zone directions for these modes. The two highest-energy LO phonons, which are the ones with the largest LO-TO splittings, are also depicted in Fig. 6.4. The

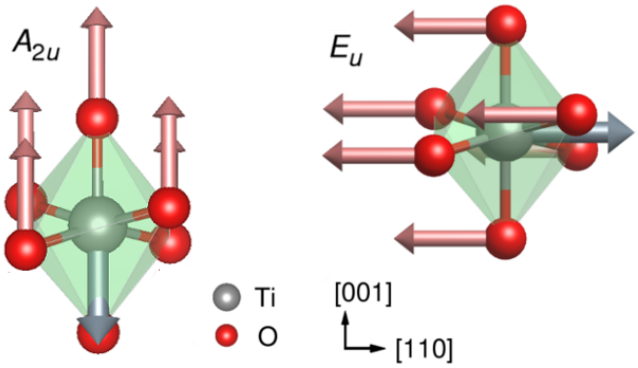

Figure 6.4: Ball-and-stick representation of the LO A_{2u} (left) and E_u (right) phonons, showing for clarity only one of the TiO_6 octahedra.

A_{2u} mode, with energy $\hbar\omega_{\mathrm{LO}} = 88$ meV, corresponds to the stretching of the Ti-O bonds along the c axis, while in the case of the E_u mode, with energy $\hbar\omega_{\mathrm{LO}} = 109$ meV, the stretching is in the ab plane.

6.3 Electron-phonon coupling

6.3.1 Fröhlich matrix element and coupling constant

Fröhlich physics has been long discussed for TiO_2, and it has been recently probed directly in bulk anatase [20, 19]. We are now equipped with the computational tools needed to investigate the electron-phonon coupling. First, we study the electron-phonon matrix elements. In Fig. 6.5(a) we compare representative matrix elements calculated from DFPT with the results of our polar Wannier-Fourier interpolation starting from $4\times4\times4$ $\mathbf{k}$ and $\mathbf{q}$ coarse Brillouin-zone grids (blue line). As in the cases of GaN and $SrTiO_3$ presented in Chapter 4, our method reproduces both the polar singularity at Γ and the behavior of the matrix elements everywhere in the Brillouin zone. For comparison, the nonsingular short-range part $g^{\mathcal{S}}$ is also shown (dashed red line), together with a standard Wannier-Fourier interpolation (solid red line) that does not appropriately take into account the polar coupling. This is seen to fail in reproducing the correct behavior.

In order to better quantify the importance of the polar divergence, it is useful to

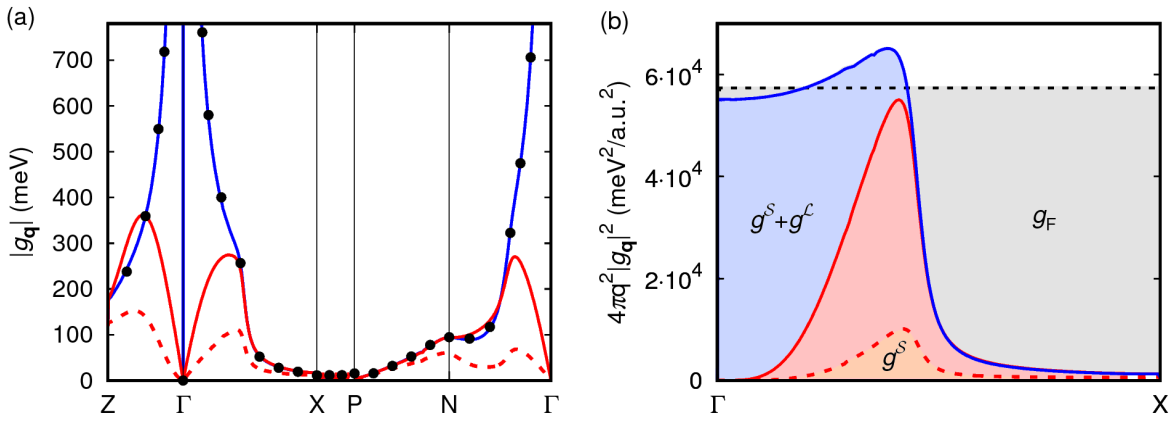

Figure 6.5: (a) Comparison of calculated electron-phonon matrix elements: the blue solid line corresponds to the full matrix element interpolated with the polar corrected method of Chapter 4, while the red solid line is the interpolation using the standard Wannier-Fourier scheme, and the dashed red line is the short-range component g^S in Eq. (4.13). The filled disks correspond to explicit DFPT calculations at each wavevector. The gauge-invariant trace of $|g|^2$ over degenerate states has been taken. The initial electronic state $|\psi_{n\mathbf{k}}\rangle$ is set to the bottom of the conduction band at Γ, the final electronic state $|\psi_{m\mathbf{k}+\mathbf{q}}\rangle$ along the bottom of the conduction band, and the phonon branch is the highest-energy LO mode. (b) Squared modulus of the electron-phonon matrix elements weighed by the spherical volume element, $4\pi q^2|g|^2$, along the ΓX direction. The blue, solid red and dashed red lines have the same meaning as in (a). The result using the simple Fröhlich model is also shown in dashed black. The shades are a guide to the eye.

consider the quantity $4\pi q^2|g|^2$. This quantity is representative of electron-phonon calculations since many physical properties, including the self-energy, involve Brillouin-zone integrations containing $|g_{mn\nu}(\mathbf{k},\mathbf{q})|^2 d\mathbf{q}$ [66]. From Fig. 6.5(b) it is evident that the short-range component (dashed red) only accounts for a small part of the coupling. The Wannier-Fourier interpolation without correcting for the long-range polar interaction (red line) severely underestimates the strength of the coupling, even after the singularity has been lifted by the volume element $4\pi q^2$. On the other hand, when using the simple Fröhlich model of Eq. (1.8), the coupling is significantly overestimated away from the zone center (dashed black). This demonstrates that the incorporation of the *ab initio* long-range coupling using Eq. (4.13) and (4.5) is essential for electron-phonon calculations in anatase and, in general, polar materials.

We evaluate the Fröhlich coupling constant α using the experimental values of ω_{LO}, ϵ_0 and ϵ_∞ from Ref. [182] and our DFT calculations for the effective masses, since no ac-

curate experimental values are available. By using these parameters in Eq. (1.9) we find the experimental Fröhlich constants $\alpha_\perp = 1.0$ and $\alpha_\parallel = 3.4$, and the isotropic average $\alpha = 1.8$. The *ab initio* Fröhlich constant is calculated from Eq. (4.12). In the perpendicular plane the two E_u LO phonons indicated in Fig. 6.3 are infrared active, with the lower energy one giving a contribution of $\alpha_{1,\perp} = 0.14$ and the higher energy one $\alpha_{2,\perp} = 0.76$, hence $\alpha_\perp = 0.9$. In the parallel direction only the A_{2u} LO mode is infrared active, with $\alpha_\parallel = 3.0$. The isotropic average is $\alpha = 1.6$, in excellent agreement with experiment, hence we expect our description of the Fröhlich coupling in anatase to be accurate. We note that the anisotropy of the coupling constant $\alpha_\perp$ and $\alpha_\parallel$ mainly stems from the strong anisotropy in the band masses, which enter α with a square root dependence.

6.3.2 Carrier linewidths and lifetimes

The electron and hole lifetimes $\tau_{n\mathbf{k}}$ are determined by the inverse of the imaginary part of the self-energy $\mathrm{Im}\Sigma_{n\mathbf{k}}$ as in Eq. (3.61). To begin with, we consider electrons in the conduction band along the ΓZ and the ΓX high-symmetry lines (the parallel and perpendicular directions in the Brillouin zone, respectively), with energies up to about 0.3 eV from the band bottom. We evaluate the imaginary part of the self-energy for a temperature $T = 20$ K using a random sampling of the Brillouin zone with 512,000 points and a broadening of 10 meV for the delta functions. This small value is needed in order to converge the linewidth to a fraction of meV near the bottom of the band and to resolve the sharp onsets of phonon emission.

Fig. 6.6(a) and (d) show the calculated linewidths along the ΓZ and ΓX direction, respectively. These are found to be almost negligible below 88 meV, which corresponds to the energy threshold for the emission of the A_{2u} LO phonon at Γ, and to increase more sharply after reaching the high-energy E_u phonon emission threshold. A weaker coupling with a threshold of 40 meV can also be resolved along ΓX, which is associated with the lower energy E_u phonon. Our calculations demonstrate that at low temperature,

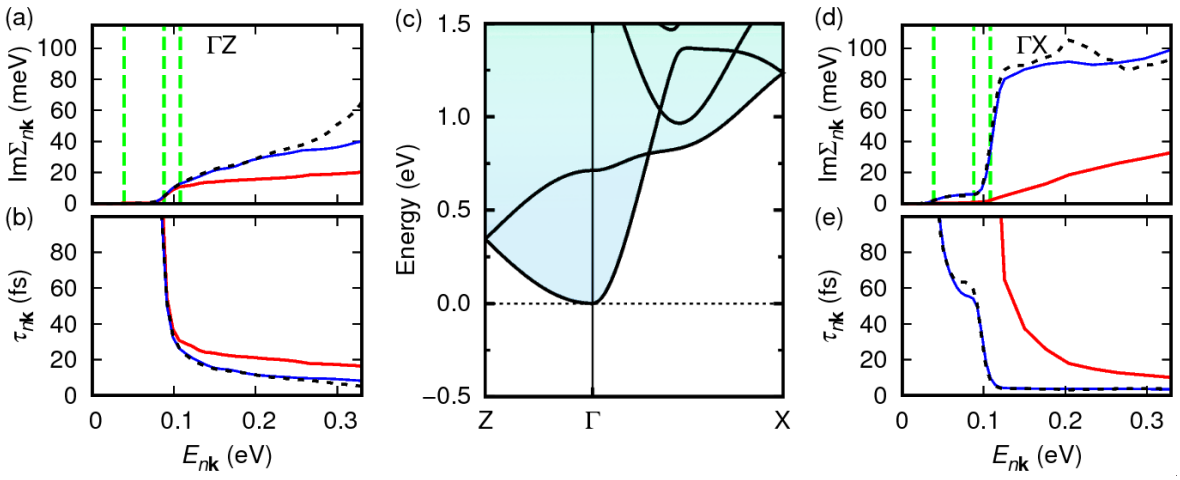

Figure 6.6: (a), (d) Electron linewidths (Im$\Sigma_{n\mathbf{k}}$) in anatase TiO_2 arising from electron-phonon scattering. The band index n corresponds to the lowest conduction band, and $\mathbf{k}$ runs along the ΓZ and the ΓX lines, respectively. The energies of the LO phonons shown in Fig. 6.3 are indicated by the vertical dashed lines. (c) Close-up of the conduction bands near the band bottom at Γ, taken as the zero of the energy. (b), (e) Electron lifetimes corresponding to (a) and (d). In (a), (b), (d) and (e) the blue lines are computed using the polar corrected Wannier-Fourier interpolation, while the red lines are obtained using the standard Wannier interpolation, and the black dashed lines using only the long-range part of the electron-phonon matrix element $g^{\mathcal{L}}$.

for electronic states close to the conduction band bottom the electron-phonon coupling is dominated by the long-range polar interaction with the high-energy A_{2u} and E_u LO modes, in agreement with the experimental conclusions of Refs. [20, 19]. This finding is also supported by the good agreement between the calculations performed using the complete matrix element g (blue lines) and the ones using only the long-range polar part $g^{\mathcal{L}}$ (black dashed lines). In the case of lifetimes, Fig. 6.6(b) and (e) show that these are essentially infinite below the phonon emission threshold, and are reduced to 3–9 fs at higher energies. For comparison, calculations performed with the standard Wannier interpolation technique [85] are also presented (red lines): the lifetimes are incorrectly enhanced by up to an order of magnitude. This comparison demonstrates the importance of the polar singularity in the correct calculation of electron lifetimes. We expect this effect to be important in other properties, as we will show in the next chapter.

The linewidths shown in Fig. 6.6(a) and (d) are highly anisotropic, varying by a factor of three going from the ΓZ direction to the ΓX direction. This interesting feature is

a consequence of the anisotropy of the band structure combined with the fact that the coupling is stronger for small phonon wavevectors. In fact, at vanishing temperature the imaginary part of the self-energy Eq. (3.60) contains the energy-conserving delta function $\delta(\varepsilon_{n\mathbf{k}} - \varepsilon_{m\mathbf{k}+\mathbf{q}} - \hbar\omega_{\mathbf{q}\nu})$. As shown in Fig. 6.6(c), in the direction ΓX the curvature of the band is large, thus making it possible to have electronic transitions with small momentum transfer. In the direction ΓZ instead, the small curvature requires electronic transitions to have larger momentum transfer in order to conserve energy. As the polar matrix element goes as $1/|\mathbf{q}|$, it is clear that the band anisotropy leads to enhanced linewidths for electrons with momentum along ΓX as compared to electrons with momentum along ΓZ. This effect is not captured correctly by using a standard Wannier-Fourier interpolation [red lines in Fig. 6.6(a) and (d)]. In particular, the linewidths are systematically underestimated, with a more significant error for the linewidths along ΓX since they involve a larger degree of coupling to phonons with small wavevectors as seen above.

After discussing in some detail the linewidths and lifetimes of electronic states near the bottom of the conduction band and their anisotropy, together with the role of different phonons in the polar coupling, we now extend the analysis to a broad energy range of a few eV around the band gap. To decrease the computational cost of the calculations, we perform the integration over the phonon momenta by using random $\mathbf{q}$ points sampled from a Lorentzian distribution centered around $\mathbf{q}=0$.[1] In the case where the long-range polar coupling dominates the electron-phonon interactions, as we already demonstrated for anatase TiO_2, this sampling of the Brillouin zone allows to converge the self-energies using fewer $\mathbf{q}$ points, here 1.7×10^5.

Fig. 6.7(a) shows the band structure of anatase along the ZΓX Brillouin-zone directions combined with the imaginary part of the electron-phonon self-energy, thus embedding all the information about the electronic momentum and band dependence. In Fig. 6.7(b) the scattering rate $2\,\mathrm{Im}\Sigma/\hbar$ calculated on a uniform grid of $25 \times 25 \times 25$ $\mathbf{k}$

[1] We thank Samuel Poncé for generating random grids of Lorentzian distributed points with weights determined by Voronoi tessellation [183].

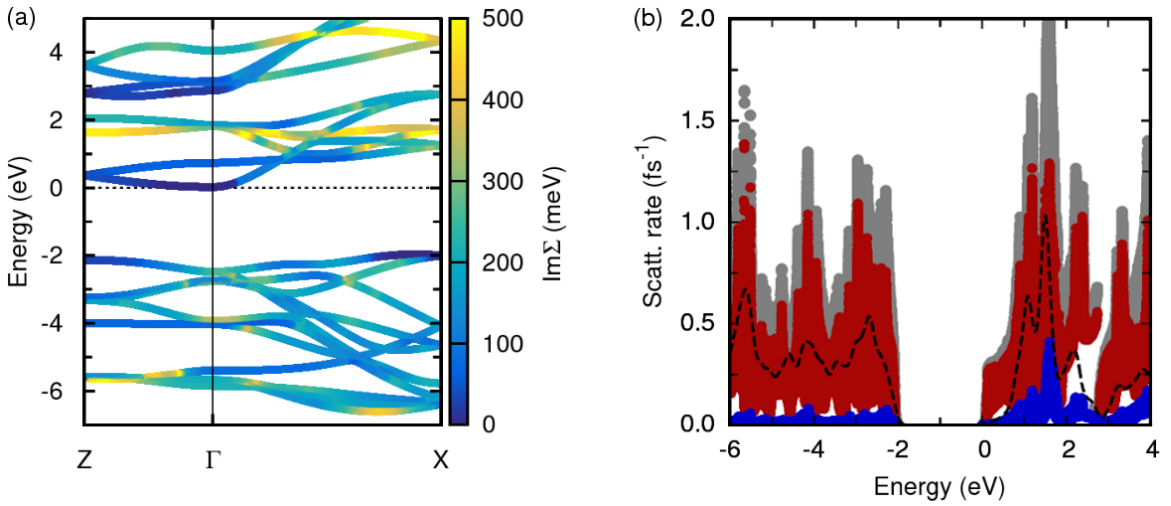

Figure 6.7: (a) Color map of the imaginary part of the electron-phonon self-energy on top of the band structure of anatase TiO_2 along the ZΓX Brillouin-zone directions. (b) Scattering rates as a function of the electronic energy shown as the total scattering rate (gray dots), the scattering from the highest-energy phonon branch (red) and from the second highest one (blue). The electronic density of states (in arbitrary units) is shown as a black dashed line.

points is presented as a function of energy, together with the electronic density of states (black dashed line). This shows that the increase in the scattering rate with energy is linked to the phase-space availability of final states, with a sharp increase near the conduction band bottom due to the strong polar electron-phonon coupling, as seen also in Fig. 6.6. In addition to the total scattering rates (gray dots), the contributions from the highest-energy phonon branch (red dots) and from the second highest-energy one (blue dots) also appear in Fig. 6.7(b). The former represents the main component, which comes from the Fröhlich electron-phonon scattering. The latter, instead, is not linked to infrared-active phonons, and therefore it represents the main short-range component of the scattering. In particular, a close inspection of the conduction band region shows that this becomes non-negligible above 0.3 eV. All other phonon branches give nearly negligible contributions.

In conclusion, we discussed electronic and vibrational properties of bulk anatase TiO_2 and the electron-phonon interactions. In particular, we analyzed properties directly linked to the imaginary part of the electron-phonon self-energy. In the next chapter we will deal with the electron-phonon coupling in *doped* anatase TiO_2.

CHAPTER 7

Polaronic properties of doped anatase TiO_2

In this chapter we examine the electron-phonon interactions in doped anatase TiO_2, and we investigate the origin of the carriers transition from a polaronic liquid to a Fermi liquid regime with increasing doping as revealed by recent ARPES experiments [20]. After some introductory remarks, we first present how the electron-phonon interactions are modified in doped materials, and we show the effect on the electron scattering rates discussed in the previous chapter. Then we introduce the cumulant expansion method for calculating the spectral function, and we report our *ab initio* ARPES spectra. We analyze the results focusing on the crossover between polaronic and Fermi liquid regimes. In particular, we show that the screening of the polar electron-phonon interaction is responsible for this crossover when the plasma energy becomes comparable with the characteristic phonon energy. At the end we also present a calculation of the polaron wavefunction based on first-order perturbation theory. The main results of this chapter can be found in Ref. [184].

7.1 Introduction

Among its broad range of applications, anatase TiO_2 is being targeted in the quest for more affordable and functional transparent conducting oxides (TCOs) [170, 185]. In-

deed, the distinctive features of TCOs, namely transparency in the visible spectrum combined with a low resistivity, can be achieved in insulating oxides following *n*- or *p*-doping. As seen in the previous chapter, anatase TiO_2 is a wide-bandgap semiconductor, transparent in the visible. Notably, it exhibits a tendency for *n*-type conductivity as oxygen vacancies are typically present and create a shallow donor level about 10 meV below the conduction band, as well as an in-gap state 1 eV below [186, 187]. *Ab initio* studies of the energy levels induced by oxygen vacancies in anatase also found a shallow electronic level close in energy to the conduction band bottom and strongly delocalized, together with a deep and localized level [188]. Resistivity measurements indeed show a metallic regime above $50-70$ K and a semiconducting one at lower temperatures [189, 186]. In the metallic regime the resistivity increases with temperature, and it is thought to be compatible with the scattering of large polarons by optical phonons. However, despite the large number of theoretical and experimental studies, the nature of the charge carriers in anatase still appears controversial [190].

Since the conduction properties of doped oxides in general are strongly linked to the nature of the carriers, a detailed understanding is crucial in order to better engineer the materials properties. As discussed in Chapter 1, recently ARPES experiments investigated this aspect in some doped oxides, revealing a crossover between a polaronic regime where the electrons behave as large polarons and a Fermi liquid regime with weaker electron-phonon coupling [20, 24, 28]. Here we perform *ab initio* calculations in order to provide a microscopic understanding of this phenomenon.

7.2 Electron-phonon coupling in doped materials

In order to be able to directly compare our calculations with ARPES data, we focus on the experimental conditions of Ref. [20]. There, the anatase samples contained excess electrons due to the presence of oxygen vacancies which could be tuned by varying the oxygen partial pressure. In particular, all samples presented well-defined three-dimensional

ellipsoidal Fermi surfaces centered at the Γ point and elongated in the k_z direction, in agreement with band structure calculations (Fig. 6.2). From their volumes the density n of excess electrons filling the bottom of the conduction band was estimated to be between 5×10^{18} cm^{-3} and 3.5×10^{20} cm^{-3}.[1] The Mott criterion for the metal-insulator transition [191], $a_0^* n_c^{1/3} \approx 0.25$ [$a_0^* = \hbar^2 \epsilon_0/(e^2 m_b)$ is the effective Bohr radius], gives a value $n_c = 1.3 \times 10^{18}$ cm^{-3} for the critical density, which falls below the smallest doping level considered in Ref. [20]. Since the system is degenerate, we can include doping in our calculations by using the rigid-band approximation and shifting the Fermi level inside the conduction band. This procedure is also supported by recent calculations [173], showing that the electronic bands are substantially unaltered in this range of doping concentrations, and that the effect is just the filling of the conduction band bottom.

In the calculation of the electron-phonon interaction, we need to consider that the electron-phonon self-energy can be strongly altered with respect to the undoped case. Firstly, the presence of a Fermi level near the band edges drastically modifies the Fermi-Dirac occupation factors. This aspect is included by using the rigid-band model as discussed above. Next, the most interesting and delicate effect arising from doping is that an additional source of screening of the electron-phonon interaction potential is present, due to the added carriers in the conduction band. This is critical especially in the case of polar coupling, where the screening of the macroscopic electric field created by the longitudinal optical vibrations can change dramatically the strength of the Fröhlich interaction, as our results will show.

To see how the additional screening affects the electron-phonon interactions, let us write the total electronic dielectric function of the doped system as [192]:

$$\epsilon_e(\mathbf{q}, \omega) = \epsilon_\infty - v_\mathbf{q} P_e(\mathbf{q}, \omega), \tag{7.1}$$

where $v_\mathbf{q} = 4\pi e^2/q^2$ is the Fourier component of the bare Coulomb interaction. Eq. (7.1)

[1] We note that owing to the difficulty in taking into account the elongation of the electron pocket along k_z, the doping levels extracted from the data may underestimate the actual carrier densities in the samples [20].

is valid at long wavelengths and small frequencies, since the relevant frequencies in the problem are much lower than the optical frequencies corresponding to electronic excitations across the band gap. These give rise to the first term ϵ_∞ in Eq. (7.1). The second contribution comes from the polarization of the doped electrons in the conduction band, which is generally evaluated in the random-phase approximation (RPA). The RPA corresponds to calculating the polarization in Eq. (3.41) by neglecting the vertex corrections and using the noninteracting electron Green's function G^0. We can also take the bare Coulomb interaction as renormalized by the optical dielectric constant ϵ_∞, $v_{\mathbf{q}}^\infty = 4\pi e^2/(\epsilon_\infty q^2)$, which corresponds to assuming that the medium has a dielectric permittivity ϵ_∞. The RPA dielectric function for the added carriers, which we simply denote $\epsilon_{\mathrm{RPA}}(\mathbf{q},\omega)$, is then:

$$\epsilon_{\mathrm{RPA}}(\mathbf{q},\omega) = 1 - v_{\mathbf{q}}^\infty P_{\mathrm{e}}(\mathbf{q},\omega)\,. \tag{7.2}$$

As seen in Sec. 3.2.1, the screened Coulomb interaction between the electrons contains the total dielectric response of the system [Eq. (3.29)]. This can be separated into an electron-electron and an electron-phonon part, as in Eq. (3.36). If the renormalization of the phonon propagator due to the added carriers is ignored, then the effect on the electron-phonon interaction is that the electron-phonon matrix element is further screened by the electronic dielectric function in Eq. (7.2) as $g_{mn\nu}(\mathbf{k},\mathbf{q})/\epsilon_{\mathrm{RPA}}(\mathbf{q},\omega)$ [4, 193]. In order to calculate the electron-phonon self-energy, the dielectric function then needs to be evaluated at the phonon frequencies, $g^{\mathrm{NA}}_{mn\nu}(\mathbf{k},\mathbf{q}) = g_{mn\nu}(\mathbf{k},\mathbf{q})/\epsilon_{\mathrm{RPA}}(\mathbf{q},\omega_{\mathbf{q}\nu})$.[2] The superscript NA underlines that the screened matrix element in the doped material is *nonadiabatic*.

The screening arising from the doped carriers can be computed analytically using the RPA dielectric function for a homogeneous electron gas with the same density n, that is the Lindhard dielectric function. We use the compact expression from Ref. [72], after

[2] This result neglects the contribution to the self-energy coming from the poles of the inverse dielectric function.

taking into account the effective mass and dielectric permittivity of anatase:

$$\begin{aligned}\epsilon_{\mathrm{RPA}}(\bar{q},\bar{\omega}) &= 1+\frac{m_{\mathrm{b}}\,e^2}{8\pi k_{\mathrm{F}}\epsilon_\infty}\frac{1}{\bar{q}^3}\left[H(\bar{q}+\bar{\omega}/\bar{q})+H(\bar{q}-\bar{\omega}/\bar{q})\right],\\ H(z) &= 2z+(1-z^2)\log\left(\frac{z+1}{z-1}\right).\end{aligned} \tag{7.3}$$

The momentum and energy variables are rescaled in units of Fermi momentum and Fermi energy, and $\bar{\omega}$ includes an imaginary part: $\bar{q} = q/2k_{\mathrm{F}}$ and $\bar{\omega} = (\omega + i\eta)/4E_{\mathrm{F}}$, with $k_{\mathrm{F}} = (3\pi^2 n)^{1/3}$ and $E_{\mathrm{F}} = k_{\mathrm{F}}^2/(2m_{\mathrm{b}})$. In a self-consistent approach, the imaginary part in the complex energy argument would be the reciprocal electron lifetime $\tau_{n\mathbf{k}}$. Inserting a small value of η in the calculations corresponds to the usual zero-th order step where the quasiparticles are taken as sharp excitations initially. Instead, we include a physical lifetime that takes into account the quasiparticle decay, and has the effect of smearing the poles of the dielectric function. The resulting nonadiabatic matrix element is thus:

$$g^{\mathrm{NA}}_{mn\nu}(\mathbf{k},\mathbf{q}) = g_{mn\nu}(\mathbf{k},\mathbf{q})/\epsilon_{\mathrm{RPA}}(\mathbf{q},\omega_{\mathbf{q}\nu}+i/\tau_{n\mathbf{k}}). \tag{7.4}$$

For simplicity we use a constant value $\hbar/\tau_{n\mathbf{k}} = 55$ meV from Ref. [20], which combines also scattering from impurities and imperfections. We checked that this choice does not affect our conclusions.

The use of an analytical expression is necessary because we need to evaluate the screening for millions of points in the Brillouin zone. Nonetheless, this approximation is well-justified and we expect it to be very accurate in our case. In fact, the systems considered lie in the high-density electron-gas limit: the Wigner-Seitz radius $r_s = (4\pi n a_0^{*3}/3)^{-1/3}$, with a_0^* the effective Bohr radius, is $r_s = 1.6$ for the lowest doping level 5×10^{18} cm^{-3}. This value is comparable or even smaller than what found in simple metals, thus justifying the use of the electron gas model to describe the doped carriers. Moreover, in the energy range considered the electronic bands are parabolic to a good approximation, as we can see from the comparison of the *ab initio* density of states (DOS) and the parabolic band model $\mathrm{DOS}(E) = \Omega/(2\pi^2)\,(2m_{\mathrm{b}}/\hbar^2)^{3/2}\sqrt{E}$ [194] in Fig. 7.1. The *ab initio* DOS is calculated with high accuracy by using Wannier interpolation to compute

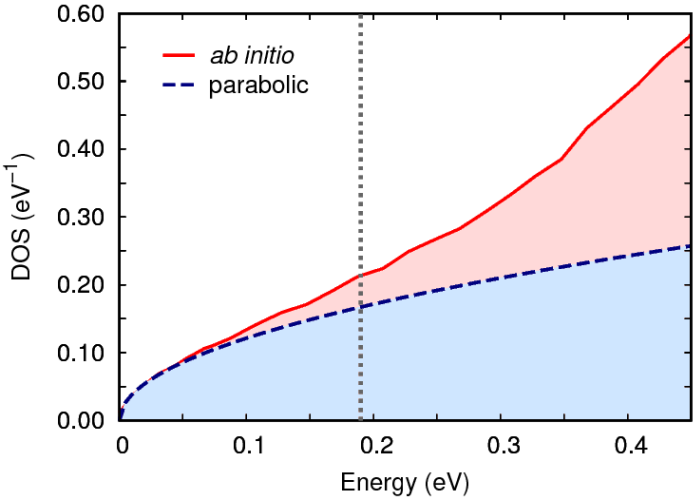

Figure 7.1: Comparison between the density of states (DOS) near the conduction band bottom calculated from first principles (red) and using the parabolic band model (blue). The gray vertical line indicates the energy corresponding to the Fermi level at the highest doping considered, $E_F = 0.19$ eV. The parabolic DOS starts deviating significantly from the calculated one for energies above 0.2 eV.

the electronic energies on a random dense **k**-point grid, and using a Gaussian smearing of 5 meV.

Carrier linewidths and scattering rates

Before investigating the spectral function of doped anatase, we illustrate the effect of screening on the electron linewidths by calculating the imaginary part of the electron-phonon self-energy at three different carrier concentrations. The results are shown in Fig. 7.2 for states within 0.7 eV from the bottom of the conduction band, with momentum **k** taken along the ΓZ (a) and ΓX (b) high-symmetry directions. The results for pristine anatase are also displayed for comparison (black lines). Here we see that for $n = 5 \times 10^{18}$ cm^{-3} (red) the linewidths are virtually unchanged with respect to the undoped case, and they are only slightly smaller for $n = 3 \times 10^{19}$ cm^{-3} (light blue). For the highest doping concentration $n = 3.5 \times 10^{20}$ cm^{-3}, on the other hand, the values of ImΣ are reduced by a factor of the order of two with respect to the values in absence of doping.

Another noticeable effect is that the threshold for phonon emission moves to higher energies, following the shift of the Fermi level inside the conduction band. At the highest

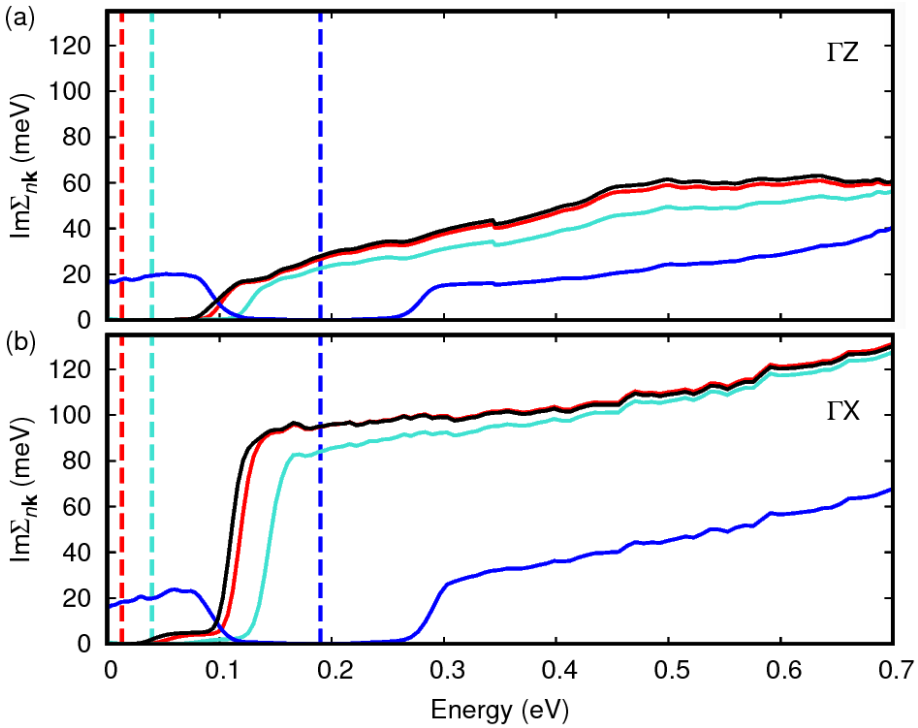

Figure 7.2: Imaginary part of the electron-phonon self-energy calculated for $T = 20$ K, $\mathbf{k}$ along ΓZ (a) and ΓX (b), and electronic energies up to 0.7 eV above the conduction band bottom (set as the zero of the energy). The results are for doping concentrations of 5×10^{18} cm^{-3} (red), 3×10^{19} cm^{-3} (light blue) and 3.5×10^{20} cm^{-3} (blue). The black lines are for the undoped case. The dashed vertical lines indicate the position of the Fermi level for each doping.

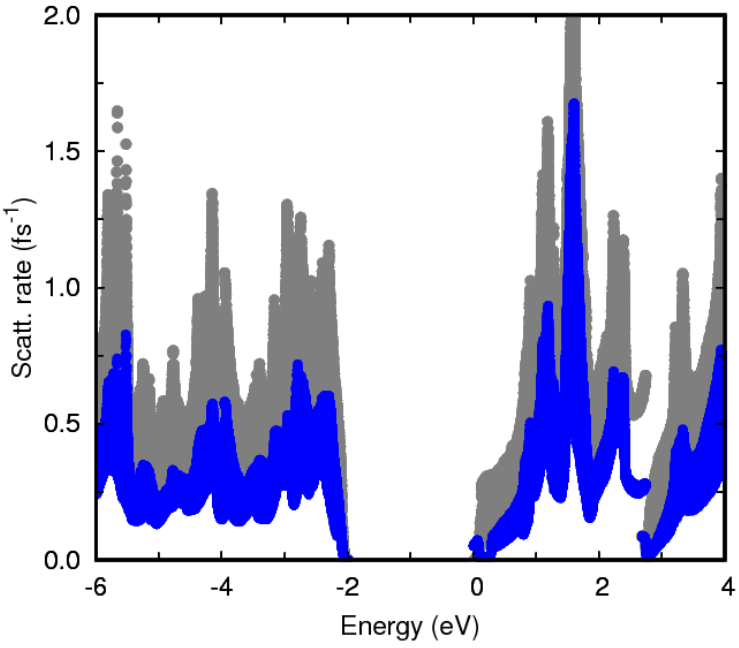

Figure 7.3: Scattering rates as a function of the electronic energy: pristine (gray) and doped ($n = 3.5 \times 10^{20}$ cm^{-3}, blue) anatase TiO_2.

doping level the Fermi energy exceeds the characteristic phonon energy ($\sim$ 100 meV), so that states at the bottom of the band acquire a finite linewidth. We also notice that the modest threshold associated to the emission of the low-energy E_u LO mode for $\mathbf{k}$ along ΓX is only resolved at the smallest doping concentration.

The significant reduction of electron-phonon scattering upon doping is also shown on a larger energy scale in Fig. 7.3, where the results are displayed in the form of scattering rates as a function of energy as in Fig. 6.7(b) in Chapter 6. Here, the undoped and the highly-doped cases are compared. We will analyze the origin of this behavior in more detail in the next section.

7.3 First-principles ARPES spectra

The investigation of polaronic features in ARPES spectra from first principles and their evolution with doping is very challenging and has not been previously reported. In general, the high computational effort needed to accurately calculate the electron-phonon self-energy has hindered the investigation of ARPES spectra from first principles, and practical studies often rely on some models of the electron-phonon interactions [4, 22]. For the case of polar materials, first-principles calculations have been reported only for some simple compounds [110]. Here we perform calculations of ARPES spectra with high accuracy by using Wannier-Fourier interpolation generalized to polar electron-phonon coupling [85, 102] and nonadiabatic screening, combined with the cumulant expansion approach [184].

7.3.1 Beyond Migdal: the cumulant expansion

As discussed in Sec. 1.3 and Sec. 3.2.2, within the sudden approximation ARPES spectra are calculated from first principles using the single-particle spectral function $A(\mathbf{k},\omega) = 2\pi^{-1}\sum_n |\mathrm{Im}G_n(\mathbf{k},\omega)|$. Standard many-body calculations employ Dyson's equation to compute the spectral function following Eq. (3.66). Since this is based on the self-energy

obtained within the Migdal approximation, we refer to this expression for the spectral function as the *one-shot Migdal approximation*. We use the term one-shot in order to remark that the Dyson's equation is not solved self-consistently. This approximation generally fails at describing satellite features accurately, as it is well-known in the field of electron-plasmon coupling [33, 195, 196].

To provide a better description of the spectral function, we use the so-called cumulant expansion method which has been employed recently to successfully describe plasmon satellites [33, 197, 198, 199]. This method can naturally be applied to investigate the spectral properties of a polaronic system since the theory stems from the exact solution of an electron-boson coupling problem of the form of the Fröhlich Hamiltonian [35]. In spite of this, only very recently the cumulant expansion has been applied in this context to investigate the electron-phonon spectral function in simple metals, although a model electron-phonon self-energy was used [200].

Within the cumulant expansion the Green's function is expressed in the time domain as [201]:

$$G_n(\mathbf{k},t) = i\, e^{-i\varepsilon_{n\mathbf{k}}t/\hbar + C_{n\mathbf{k}}(t)}, \tag{7.5}$$

where $C_{n\mathbf{k}}(t)$ is the so-called cumulant function. The spectral function takes the form:

$$A(\mathbf{k},\omega) = \frac{1}{\pi}\sum_n \mathrm{Re}\int_{-\infty}^{+\infty} dt\, e^{i(\omega-\varepsilon_{n\mathbf{k}}/\hbar)t}\, e^{C_{n\mathbf{k}}(t)}. \tag{7.6}$$

Eqs. (7.5) and (7.6) are valid for states below the Fermi level ($\omega < 0$, $t < 0$), and a factor of 2 accounting for spin degeneracy has been included in Eq. (7.6). The cumulant function is obtained from the self-energy as follows:

$$C_{n\mathbf{k}}(t) = \frac{1}{\pi\hbar}\int_{-\infty}^{\infty} d\omega\, \mathrm{Im}\Sigma_{n\mathbf{k}}(\varepsilon_{n\mathbf{k}}/\hbar - \omega)\, \frac{e^{i\omega t} - i\omega t - 1}{\omega^2}\, \theta(\hbar\omega - \varepsilon_{n\mathbf{k}}), \tag{7.7}$$

where θ is the Heaviside function. Rigorous derivations can be found in Refs. [202, 203]. The procedure consists of expanding the exponential in Eq. (7.5) in powers of the cumulant: $G_n(\mathbf{k},t) = G_n^0(\mathbf{k},t)\left[1 + C_{n\mathbf{k}} + C_{n\mathbf{k}}^2/2 + \cdots\right]$, where $G_n^0(\mathbf{k},t) = i\,\exp(-i\varepsilon_{n\mathbf{k}}t/\hbar)$ is the

Green's function without electron-phonon interactions. Using the Dyson's equation, on the other hand, one has $G = G^0 + G^0\Sigma G^0 + G^0\Sigma G^0\Sigma G^0 + \cdots$. Comparing these expansions term-by-term and writing the self-energy in its spectral representation yield Eq. (7.7).

In our calculations the one-shot Migdal self-energy of Eq. (3.55) is used to evaluate the cumulant function. In Ref. [203] it is shown that seeding this first non-crossing self-energy diagram not only constitutes the best available approximation but also guarantees that no overcounting of correlated higher-order contributions is introduced in the theory. Most importantly, the spectral function resulting from the cumulant expansion includes also crossing diagrams which result from the time orderings of the t variables in the cumulant expansion [203, 204]. This allows us to describe the spectral features beyond the one-shot Migdal approximation.

The cumulant expansion is performed as a post-processing of the electron-phonon self-energy calculations. The code was developed by Fabio Caruso [199, 203], and rather than implementing the full expressions Eqs. (7.6) and (7.7) it resorts to the formulation of Ref. [33], extended to the case of multiple satellites (see Appendix E).

7.3.2 Results and discussion

Calculation details

For the nominal carrier concentrations 5×10^{18}, 3×10^{19}, 1×10^{20} and 3.5×10^{20} cm^{-3} measured in Ref. [20] we calculate a Fermi level shift of 13, 40, 88 and 190 meV respectively (measured from the bottom of the conduction band). After interpolating the Hamiltonian, the dynamical matrix and the electron-phonon matrix elements starting from $4 \times 4 \times 4$ coarse $\mathbf{k}$ and $\mathbf{q}$ Brillouin-zone grids, we converge the electron-phonon self-energy in Eq. (3.55) using 2×10^6 random $\mathbf{q}$ points. The positive imaginary part at the denominator is set to $\eta = 10$ meV. The real part of the self-energy is rescaled so that it is zero at the Fermi level, in order to preserve the volume enclosed by the Fermi surface according to Luttinger's theorem [66, 87]. We include the temperature broadening of the

Fermi cutoff by multiplying the calculated spectral function by the Fermi-Dirac occupation factor $f(\omega) = [e^{\hbar\omega/(k_B T)} + 1]^{-1}$ at the experimental temperature $T = 20$ K. Since we investigate a small energy range near the bottom of the conduction band, photon matrix element effects are neglected. The experimental resolution in energy and momentum is taken into account by convoluting the intensity map with two Gaussian distributions G_1 and G_2 of widths 25 meV and 0.015 Å^{-1}, respectively [13]:

$$\tilde{A}(\mathbf{k}, \omega) = \int d\mathbf{k}' d\omega' f(\omega') A(\mathbf{k}', \omega') G_1(\omega - \omega') G_2(\mathbf{k} - \mathbf{k}') . \tag{7.8}$$

ARPES spectra and mass enhancement

The calculated ARPES spectra for the bottom of the conduction band of *n*-doped anatase are shown in Fig. 7.4(e)–(h), and they are directly compared with the measured ones from Ref. [20] for the same four nominal doping concentrations in (a)–(d). All the spectra exhibit a bright parabolic band, whose width increases with doping reflecting the rise of the Fermi energy inside the conduction band. Moreover, for the first three doping levels a satellite is seen at an energy around 0.1 eV below the main peak; a second one another 0.1 eV below is additionally present for the first two doping levels. The appearance of satellites at integer multiples of the optical phonon energy is a signature of polaronic effects, as discussed in Sec. 1.2. At the highest doping, on the other hand, this picture is replaced by band structure kinks near 0.1 eV. Overall, the first-principles ARPES spectra are in remarkable agreement with the experiments of Ref. [20].

From the spectra in Fig. 7.4(e)–(h) we extract the underlying band structures, shown in Fig. 7.5 together with the bare bands from the DFT calculations. The quasiparticle dispersions are calculated from the poles of the electron Green's function following Eq. (3.58), whereas for the satellites we track the maxima in the energy dispersion curves [13]. This yields a set of parabolic bands and polaron satellites in Fig. 7.5(a)–(c), with two satellites in (a), (b) and only one in (c), and a band structure kink in (d) with no satellites (blue curves). From these bands we can extract unambiguously

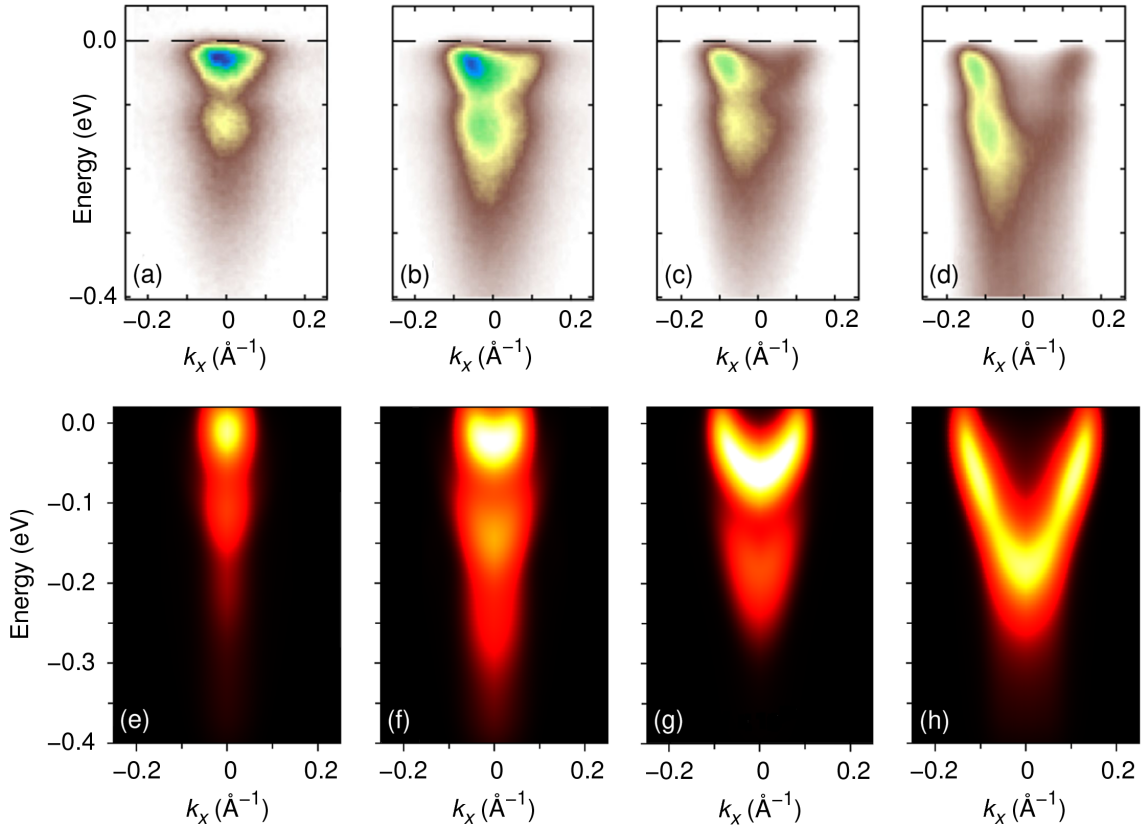

Figure 7.4: (a)–(d) ARPES spectra of anatase TiO_2 measured by Moser *et al.* [20] for samples with doping concentrations of 5×10^{18} cm^{-3} (a), 3×10^{19} cm^{-3} (b), 1×10^{20} cm^{-3} (c) and 3.5×10^{20} cm^{-3} (d). The crystal momentum k_x is along the ΓΣ line of the Brillouin zone. Reproduced with permission from Ref. [20]. Copyright 2013 American Physical Society. (e)–(h) Calculated spectral functions for the same nominal doping levels as in (a)–(d). The spectra are convoluted in both momentum and energy with Gaussian masks to account for the experimental resolution as in Eq. (7.8). The zero of the energy corresponds to the Fermi level.

the mass enhancement parameter or electron-phonon coupling strength λ by calculating the ratio between the Fermi velocity of the bare band, v_{F}^0, and that of the dressed band, v_{F} [see Eqs. (3.64) and (3.65)]. Going from the lowest to the highest doping level we obtain $\lambda_{\mathbf{k}} = 0.73$, 0.70, 0.34 and 0.20, respectively, for $\mathbf{k}$ along the k_x direction on the Fermi surface. Experimentally, the mass enhancement parameter was extracted for $n = 3 \times 10^{19}$ cm^{-3}, yielding $\lambda = 0.7$ in excellent agreement with our value [20].

In Fig. 7.6(a) we show a 3D representation of the spectral function at intermediate doping along the ΓX and ΓZ Brillouin-zone directions. The elongation of the Fermi surface along ΓZ reflects the anisotropy of the band structure and of the relative effective masses,

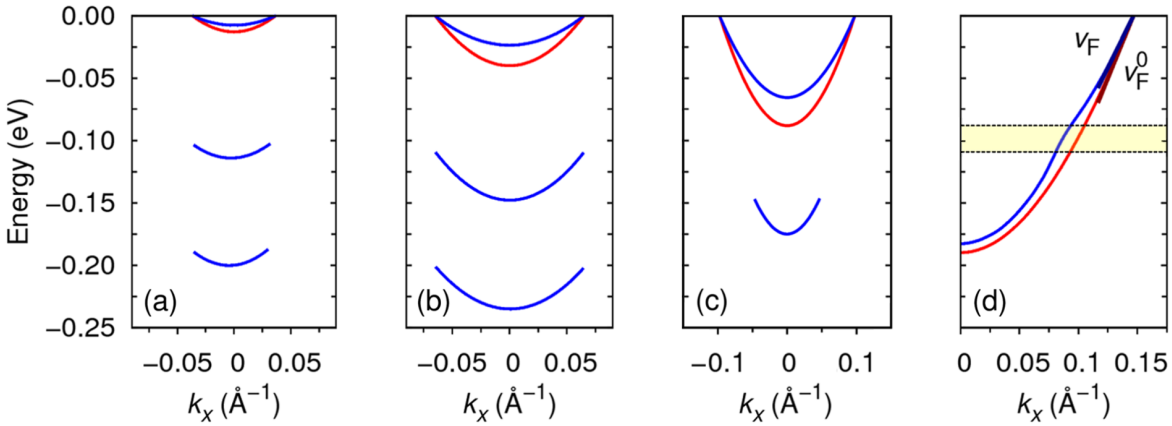

Figure 7.5: Band structures extracted from the calculated spectral functions in Fig. 7.4(e)–(h) for the same doping levels, increasing from (a) to (d). The bare bands are in red and the renormalized ones are in blue. In panel (d) we explicitly indicate the bare and renormalized Fermi velocities, and the region where the kink in the quasiparticle band appears is highlighted in yellow.

as seen in Sec. 6.2. Fig. 7.6(b) shows the corresponding renormalized bands and the satellites. It is interesting to note that the band anisotropy is not reflected in the electron-phonon coupling strength: in fact, our calculations indicate that the mass enhancement $\lambda_{\mathbf{k}}$ varies by less than 10% along the ΓΣ, ΓX and ΓZ Brillouin-zone directions. This conclusion is in line with the findings from resonant inelastic X-ray scattering experiments on anatase [19]. More in detail, along the three directions we obtain $\lambda = 0.73$, 0.73, and 0.74 at the lowest doping; $\lambda = 0.70$, $\lambda = 0.34$ in each direction for the second and third doping, respectively; and $\lambda = 0.20$, 0.20, and 0.18 at the highest doping. The average values over the Fermi surface are $\lambda = 0.73$, 0.70, 0.34 and 0.19 for each doping level.

We also calculate the mass enhancement directly from the energy derivative of the real part of the electron-phonon self-energy at the Fermi level, $\lambda_{n\mathbf{k}} = -\partial \mathrm{Re}\Sigma_{n\mathbf{k}}(\omega)/\partial\omega|_{\omega=0}$ [Eq. (3.63)], with n corresponding to the lowest conduction band. The values thus obtained fall within less than 10% of the ones listed above, the average over the Fermi surface being $\lambda = 0.68$, 0.65, 0.33 and 0.19 for the four values of doping considered.

For weak and intermediate coupling regimes, the polaron effective mass is commonly estimated in the literature from the Fröhlich coupling constant α using Eq. (1.12), $m^* = m_b/(1-\alpha/6)$. As seen in Sec. 6.3.1, the coupling constant in anatase TiO_2 is anisotropic

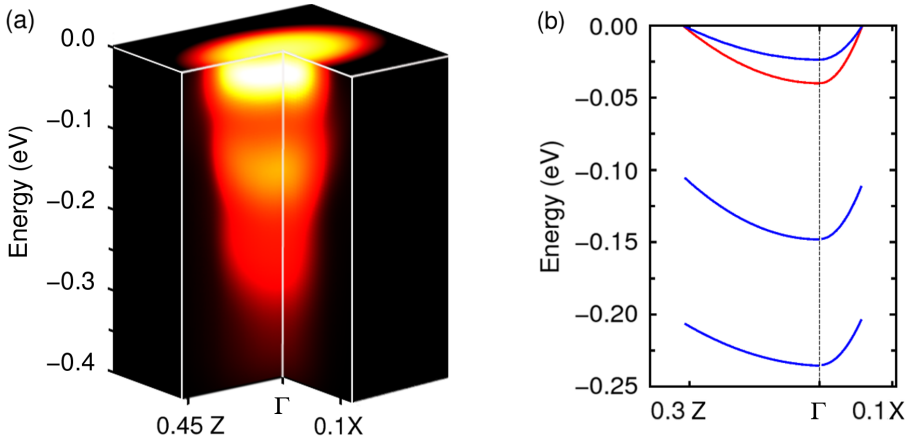

Figure 7.6: (a) Calculated ARPES spectrum for a doping concentration of 3×10^{19} cm^{-3} with the momentum **k** taken along anisotropic Brillouin-zone directions, ΓX (basal plane of the tetragonal lattice) and ΓZ (c axis), as well as the Fermi surface cut. (b) Corresponding band structure extracted from the spectrum (blue) together with the bare band (red).

with $\alpha_\perp = 0.9$ and $\alpha_\parallel = 3.0$, and isotropic average $\alpha = 1.6$. By using the latter, the resulting m^* is underestimated with respect to experiment [20]. On the other hand, if $\alpha_\perp$ and $\alpha_\parallel$ are considered separately, then a strongly anisotropic mass enhancement is obtained, that is not consistent with our many-body calculations. This indicates that, in the case of anisotropic crystals, the Fröhlich constant α cannot be used straightforwardly in order to obtain polaron properties.

From the mass enhancement λ it is also possible to derive the quasiparticle strength $Z = 1/(1+\lambda)$, see Eq. (3.62). Using the average values of λ over the Fermi surface, we obtain $Z = 0.58$, 0.59, 0.75 and 0.83 with increasing doping. The calculated quasiparticle strength at intermediate doping overestimates the value determined experimentally, $Z = 0.36$ [20]. The origin of this difference is not clear at present. It may be attributed to extrinsic losses that are not taken into account within the commonly employed sudden approximation, and that are known to transfer spectral weight to the satellites [32, 33, 205]. Alternatively, the discrepancy may reflect a breakdown of the perturbative approach used to treat the electron-phonon interaction, whereby the quasiparticle renormalization factor is given by Eq. (3.62). This is a delicate point that would require further investigation in order to rigorously establish the importance of extrinsic losses in the spectra, and to

determine whether the values of Z deduced from experiments actually yield the intrinsic quasiparticle renormalization.

At last, we note that using the accurate description of the matrix element including the long-range part as described in Chapter 4 is essential: in fact, we found that calculations performed with standard Wannier-Fourier interpolation, i.e. without including the formalism of Chapter 4, do not show satellite features. Moreover, a poor description of the Fröhlich interaction with the polar optical modes lead to a severe underestimation of the mass enhancement as obtained in Ref. [206].

Origin of satellites and kinks

We now turn to investigating more closely the mechanisms that drive the formation of polaron satellites and kinks. The energy separations between the quasiparticle bands and the first satellite in Fig. 7.5(a)–(c) are 106 meV, 124 meV and 130 meV, respectively, while in Fig. 7.5(d) the kink appears at a binding energy of 100 meV. These energy scales are compatible with the polar Fröhlich coupling to the LO E_u phonon at 109 meV; another candidate, as discussed in Sec. 6.2, is the A_{2u} phonon at 88 meV, although its energy appears too low. To better quantify the importance of the E_u mode, we perform a calculation in which the coupling to phonons with energy above 100 meV is artificially turned off. This is compared with the complete spectrum at intermediate doping (3.5×10^{19} cm^{-3}) in Fig. 7.7(b), while in panel (a) the corresponding intensity profiles at Γ are shown. We see that after removing the highest-energy phonons, the intensity of the first satellite decreases and the second satellite disappears. The effective mass is also lower, yielding a coupling strength $\lambda = 0.3$. We can therefore conclude that the E_u phonon represents the primary mechanism behind the satellites, contributing $\sim 60\%$ of the total coupling.[3]

In Fig. 7.7(c),(d) we analyze the importance of many-body correlations beyond the one-shot Migdal approximation by comparing the spectral function obtained from the cu-

[3] Since λ can be obtained from the energy derivative of $\Sigma_{n\mathbf{k}}(\omega)$ at the Fermi level as discussed previously, the contributions from different phonon modes are additive.

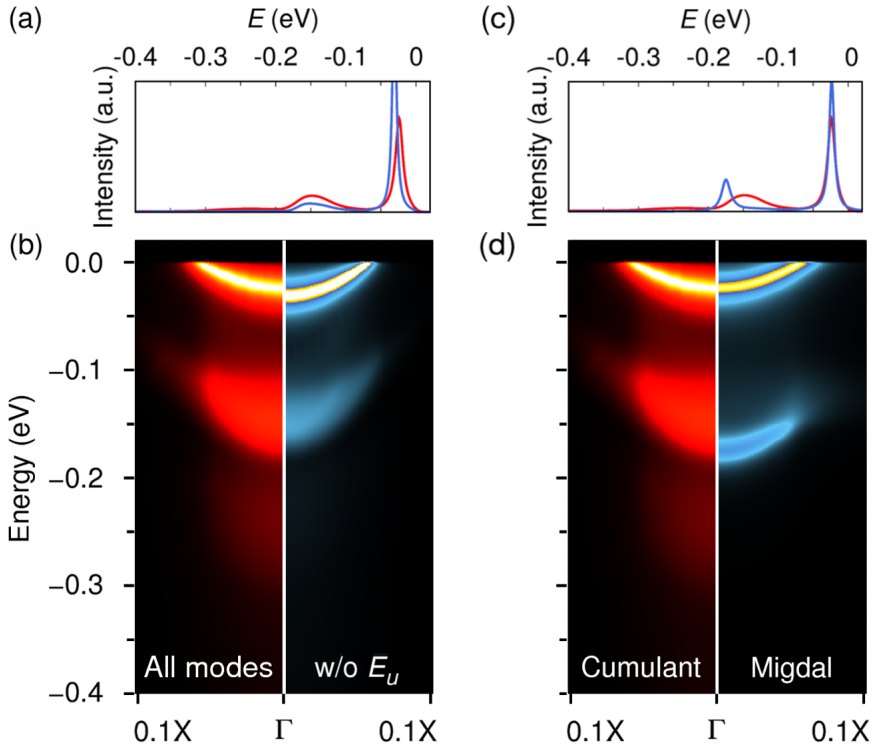

Figure 7.7: Comparison of the intensity profile at Γ (a) and of the energy-momentum intensity map (b) for the intermediate doping level 3×10^{19} cm^{-3} calculated by including all phonon modes (left/red), and by eliminating the phonons with energy above 100 meV (right/blue). (c),(d) Same as in (a),(b) for the spectral function obtained within the cumulant expansion method (left/red) versus the one-shot Migdal approximation (right/blue), for the same doping level. For clarity the spectra are not convoluted with Gaussian masks.

mulant expansion approach used so far, with the one obtained from the one-shot Migdal approximation. From this comparison we notice that the latter has two main shortcomings: (i) the separation between the quasiparticle band and the first satellite is too large with respect to experiment (151 meV instead of ~ 100 meV), and (ii) only one satellite appears in the spectrum. The cumulant expansion formalism, on the other hand, yields multiple phonon satellites, one for each term in the Taylor expansion of $\exp[C_{n\mathbf{k}}(t)]$ in Eq. (7.6) (see also Appendix E). It would be interesting to explore further the effects of self-consistency on the Migdal approximation [207] as compared to the cumulant expansion, however the possibility of going beyond the one-shot Migdal approximation has never been explored in *ab initio* calculations.

We now move to examine a central aspect of our calculations, that is the inclusion of

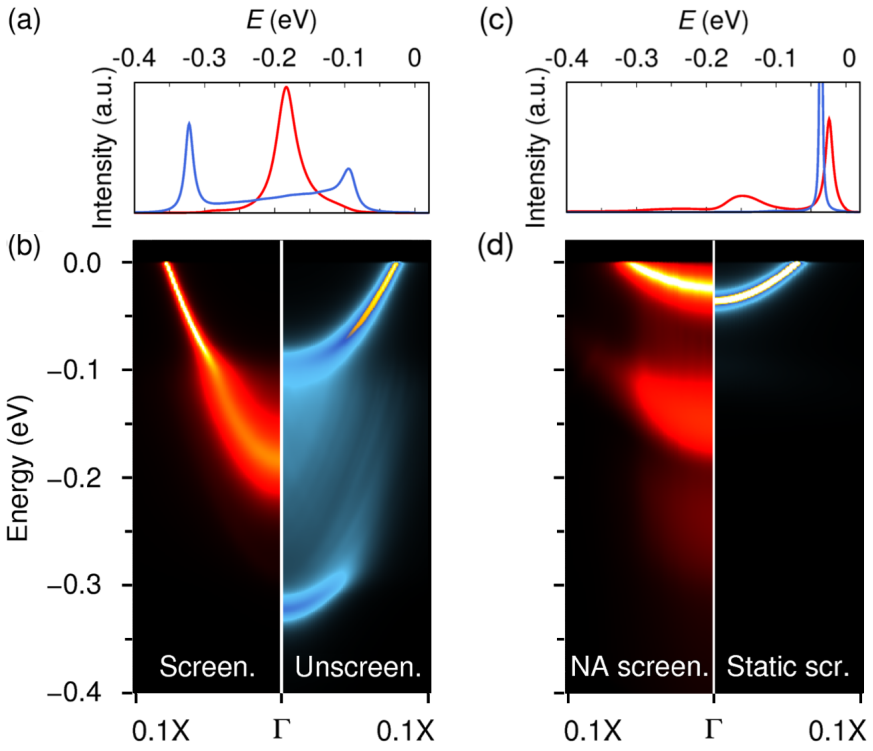

Figure 7.8: Intensity profile at the zone center (a) and full energy-momentum intensity map (b) for the doping concentration 3.5×10^{20} cm^{-3}, comparing a calculation where the screening of the electron-phonon interaction is taken into account (left/red), with one where it is not included (right/blue). (c),(d) Comparison analogous to (a),(b), for the spectral function calculated for the doping 3×10^{19} cm^{-3} including the dynamical Lindhard screening by carriers (left/red), against the static Thomas-Fermi screening (right/blue). As in Fig. 7.8, the spectra are not convoluted with Gaussian masks.

the screening due to the added carriers in the conduction band. As discussed in Sec. 7.2, we treat this issue by screening the electron-phonon matrix elements with the frequency-dependent Lindhard dielectric function for each doping level, including the effective mass and dielectric permittivity of anatase. Fig. 7.8(b) clearly illustrates the importance of carrier screening by comparing the spectrum at high doping (3.5×10^{20} cm^{-3}) calculated with the electronic screening (on the left) and ignoring it (on the right). The corresponding intensity profiles at the zone center are shown in panel (a). In the absence of screening we obtain a sharp polaron satellite, in disagreement with experimental evidence, while when screening is included the satellite disappears and it is replaced by a band structure kink. On the other hand, we find that for the first two doping levels studied the screening does not play any significant role.

This comparison shows that a correct description of the electronic screening is crucial in order to capture the evolution of ARPES spectra with doping, and in particular that this description needs to be *nonadiabatic*. In fact, the use of a static screening is inadequate, as we show in Fig. 7.8(c),(d). Here we compare the spectral function calculated for a carrier concentration of 3×10^{19} cm^{-3} using the Lindhard function as usual, following Eqs. (7.3) and (7.4), and a calculation that uses a Thomas-Fermi static screening. In this case the dielectric function that screens the electron-phonon matrix elements takes the form:

$$\epsilon_{\mathrm{TF}}(q) = 1 + \frac{q_{\mathrm{TF}}^2}{q^2}, \qquad q_{\mathrm{TF}} = \left(\frac{6\pi e^2 n}{\epsilon_\infty E_{\mathrm{F}}}\right)^{1/2}, \tag{7.9}$$

which corresponds to the static limit of the Lindhard function at small wavelength. Fig. 7.8(c) and (d) show that the static screening drastically *overestimates* the effect of weakening of the electron-phonon interactions: the coupling strength is only $\lambda = 0.13$, and the satellites disappear. This dramatic result is not observed, instead, for high carrier concentrations.

We can verify the effect of using a dynamical screening by looking at the dielectric function as a function of frequency for small values of $\mathbf{q}$ (up to 10% of the Brillouin zone), shown in Fig. 7.9(a) at high-doping. The screening is stronger at small wavevectors, thus compensating the divergence of the Fröhlich coupling. In Fig. 7.9(b) the nonadiabatic matrix elements for the same values of $\mathbf{q}$ are shown as a function of carrier density, and we can see that they become weaker at high doping. In conclusion, the investigation of doping levels of the order of the ones considered in this chapter within an adiabatic theory such as DFPT, or including a static screening, can yield an erroneous description of the electron-phonon coupling and should be treated with great care. Conversely, ignoring the screening can also lead to an inaccurate description.

Crossover between polarons and Fermi liquid

The above observations can be rationalized by looking at the timescales of the lattice vibrations as compared to electronic screening. The characteristic response time of the

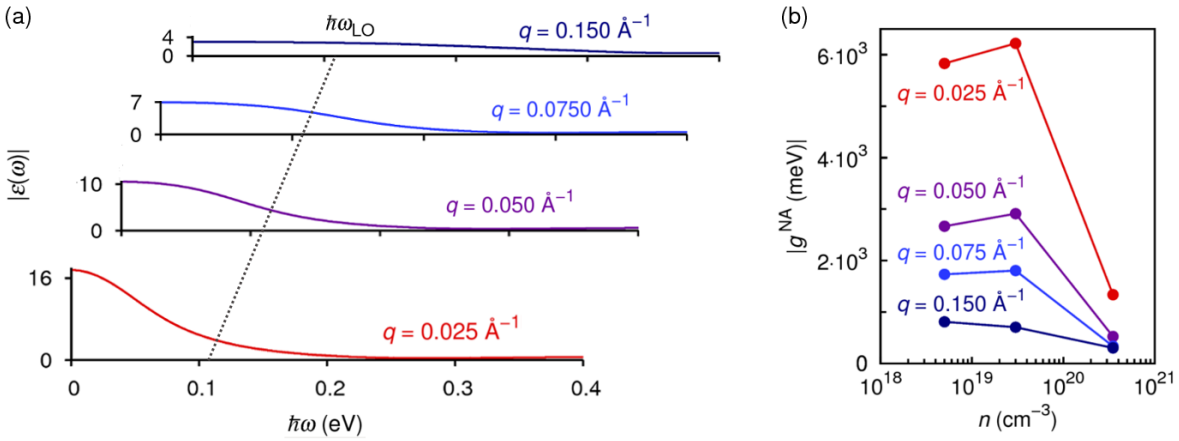

Figure 7.9: (a) Lindhard dielectric function associated with the doped carriers at different values of wavevector **q**, for the highest doping level case 3.5×10^{20} cm^{-3}. (b) Nonadiabatic electron-phonon matrix elements as a function of doping for the same values of **q**. The initial and final electronic states are set to the bottom of the conduction band, and the phonon branch corresponds to the E_u LO phonon.

latter is inversely related to the plasma frequency of doped carriers, given by [4]:

$$\omega_{\mathrm{p}} = \left(\frac{4\pi n e^2}{\epsilon_\infty m_{\mathrm{b}}}\right)^{1/2}. \tag{7.10}$$

If the response time of the electrons is larger than the period of vibration of the LO phonons, we can deduce that the carriers are too slow to screen the long-range electric field generated by the LO phonons. In this case the screening is ineffective and the Fröhlich interaction is similar to the insulating case. On the other hand, if the electrons oscillate faster than the LO phonons, they can screen the electron-phonon coupling. In this regime the strength of the coupling depends critically on the carrier concentration. Ultimately, with increasing doping the coupling to the LO phonons can be completely suppressed, with the ARPES spectra dominated by weaker short-range couplings to nonpolar phonons [24].

In order to quantify and summarize our conclusions, in Fig. 7.10 we compare directly the plasma energy of the carriers $\hbar\omega_{\mathrm{p}}$ with the energy of the main LO phonon, the E_u mode at $\hbar\omega_{\mathrm{LO}} = 109$ meV. In the same plot we also show the evolution of the coupling strength with doping. We can indeed identify two regions: a polaronic regime when $\omega_{\mathrm{p}} < \omega_{\mathrm{LO}}$, and a Fermi liquid regime when $\omega_{\mathrm{p}} > \omega_{\mathrm{LO}}$. In the first region, where the

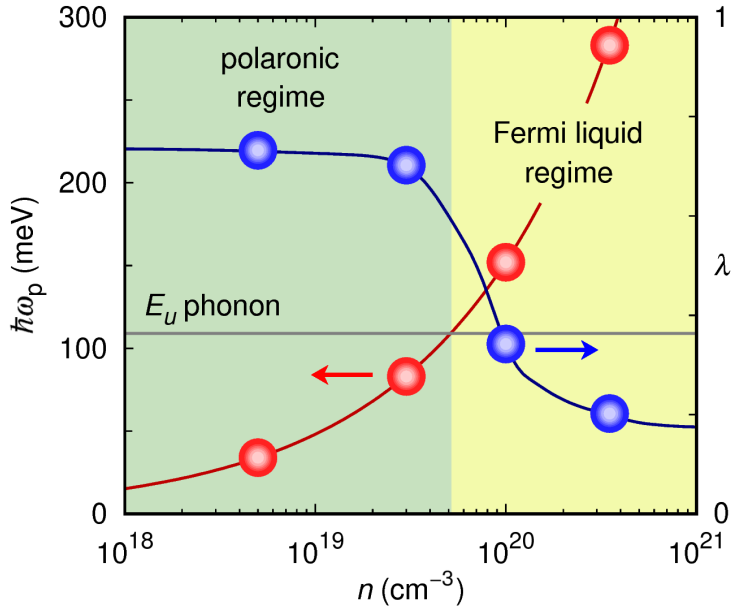

Figure 7.10: Polaronic and Fermi liquid regions in n-doped anatase: the red spheres indicate the plasma energy at each doping level, and the blue ones give the electron-phonon coupling strength λ. The blue line is a guide to the eye, while the red one corresponds to the square root relation between $\hbar\omega_p$ and n. The horizontal line is the energy of the LO E_u phonon (109 meV).

electronic screening is ineffective, satellite features are present in the spectra and the mass enhancement is insensitive to the doping level. In the second region instead, where the electron-phonon coupling is weakened by the screening, the polaron satellites are gradually replaced by photoemission kinks and the coupling strength decreases. This analysis supports the notion that the nonadiabatic Fröhlich interaction is at the origin of the crossover between satellites and kinks in the spectra as a function of doping.

7.4 Polaron wavefunction

Given the qualitative change in the spectral features as a function of doping, and the evolution of the system from a polaronic liquid to a weakly-coupled Fermi liquid, we investigate how this evolution is reflected in the electronic wavefunctions. In order to explore this aspect, we calculate the polaron wavefunctions by using first-order perturbation theory; in particular, we generalize the approach of Ref. [4] to *ab initio* calculations. The choice of using perturbation theory is justified since this theory appears to be valid

in the range $\alpha \lesssim 5$ [4], and the largest Fröhlich coupling constant in anatase is $\alpha_{\parallel} = 3.0$ (see Sec. 6.3.1).

Within standard Rayleigh-Schrödinger perturbation theory, the perturbed wavefunction of the system of electrons and phonons $|i\rangle^{(1)}$ is:

$$|i\rangle^{(1)} = |i\rangle + \sum_{f \neq i} \frac{\langle f | \hat{H}_{\mathrm{ep}} | i \rangle}{E_i - E_f} |f\rangle \,, \tag{7.11}$$

where the terms have the same meaning as in Eq. (3.16). If a system at zero temperature and with a single electron added to the bottom of the conduction band is considered, using Eq. (3.14) the renormalized electron wavefunction $\widetilde{\psi}_{n\mathbf{k}}$ to first order in the perturbation reads:

$$\widetilde{\psi}_{n\mathbf{k}}(\mathbf{r}; \{\boldsymbol{\tau}_\kappa\}) = C \left[\psi_{n\mathbf{k}}(\mathbf{r}) + \frac{1}{\sqrt{N_\mathbf{q}}} \sum_{m\mathbf{q}\nu} \frac{g_{mn\nu}(\mathbf{k}, \mathbf{q}) \psi_{m\mathbf{k}+\mathbf{q}}(\mathbf{r})}{\varepsilon_{n\mathbf{k}} - \varepsilon_{m\mathbf{k}+\mathbf{q}} - \hbar\omega_{\mathbf{q}\nu}} \hat{a}^\dagger_{-\mathbf{q}\nu} \right] |0_\mathrm{p}\rangle \,, \tag{7.12}$$

where C is a normalization constant and $|0_\mathrm{p}\rangle$ is the phonon ground state. Since the atomic displacements are smaller than the characteristic interatomic distances, we can make the approximation of replacing $\hat{a}^\dagger_{-\mathbf{q}\nu}$ by its expectation value over an electron-phonon state [4]. As $\hat{a}^\dagger_{-\mathbf{q}\nu}$ is a function of the phonon normal mode coordinates, this corresponds to describing the average amount of ion displacement around an electron. To determine a lower bound to the polaron radius, we take the electronic state as localized at the center of the reference frame, $\mathbf{r} = 0$. This yields:

$$\hat{a}^\dagger_{-\mathbf{q}\nu} \approx \frac{1}{\sqrt{N_\mathbf{q}}} \sum_{m'} \frac{g^*_{m'n\nu}(\mathbf{k}, \mathbf{q})}{\varepsilon_{n\mathbf{k}} - \varepsilon_{m'\mathbf{k}+\mathbf{q}} - \hbar\omega_{\mathbf{q}\nu}} \,. \tag{7.13}$$

By replacing Eq. (7.13) inside Eq. (7.12) we obtain:

$$\widetilde{\psi}_{n\mathbf{k}}(\mathbf{r}; \{\boldsymbol{\tau}_\kappa\}) = C \left[\psi_{n\mathbf{k}}(\mathbf{r}) + \frac{1}{N_\mathbf{q}} \sum_{m\mathbf{q}\nu} \frac{g_{mn\nu}(\mathbf{k}, \mathbf{q}) \psi_{m\mathbf{k}+\mathbf{q}}(\mathbf{r})}{\varepsilon_{n\mathbf{k}} - \varepsilon_{m\mathbf{k}+\mathbf{q}} - \hbar\omega_{\mathbf{q}\nu}} \sum_{m'} \frac{g^*_{m'n\nu}(\mathbf{k}, \mathbf{q})}{\varepsilon_{n\mathbf{k}} - \varepsilon_{m'\mathbf{k}+\mathbf{q}} - \hbar\omega_{\mathbf{q}\nu}} \right] |0_\mathrm{p}\rangle \,. \tag{7.14}$$

Since the evaluation of Eq. (7.14) is still very cumbersome, we simplify the expression by retaining only the long-wavelength part of the electron-phonon matrix elements. We already saw in Sec. 6.3.2 that this approximation is very accurate for anatase TiO_2. Ad-

ditionally, the effect of the electronic screening is taken into account as in Sec. 7.2 by using the nonadiabatic matrix elements [Eq. (7.4)]: $g_{mn\nu}(\mathbf{k},\mathbf{q}) \to g^{\mathcal{L},\mathrm{NA}}_{mn\nu}(\mathbf{k},\mathbf{q})\,\delta_{mn}$. Since the main contribution to the Fröhlich coupling arises from small phonon wavevectors, we also replace the periodic part of the Kohn-Sham wavefunction $u_{m\mathbf{k}+\mathbf{q}}(\mathbf{r})$ by $u_{m\mathbf{k}}(\mathbf{r})$. The wavefunction is then finally evaluated as:

$$\tilde{\psi}_{n\mathbf{k}}(\mathbf{r};\{\boldsymbol{\tau}_\kappa\}) = C\psi_{n\mathbf{k}}(\mathbf{r})\left[1+\frac{1}{N_\mathbf{q}}\sum_{\mathbf{q}\nu}|g^{\mathcal{L},\mathrm{NA}}_{nn\nu}(\mathbf{k},\mathbf{q})|^2\frac{e^{i\mathbf{q}\cdot\mathbf{r}}}{(\varepsilon_{n\mathbf{k}}-\varepsilon_{n\mathbf{k}+\mathbf{q}}-\hbar\omega_{\mathbf{q}\nu})^2}\right]|0_\mathrm{p}\rangle\,. \quad (7.15)$$

In particular, in our calculations we set $n\mathbf{k}$ to the bottom of the conduction band. We use a random $\mathbf{q}$ grid with 2×10^6 points to converge the Brillouin-zone integration, and a small imaginary part $\eta = 10$ meV is added to the denominator.

The results are displayed in Fig. 7.11, where the square moduli of the polaron wavefunctions at the bottom of the conduction band are shown near the maximum of the wavefunction and a few unit cells away, along the c-axis direction: in blue the intermediate doping level 3×10^{19} cm^{-3}, which is in the polaronic region, and in yellow the high doping level 3.5×10^{20} cm^{-3}, in the Fermi liquid region. The envelope functions, which correspond to the term inside the square brackets in Eq. (7.15), are shown below along

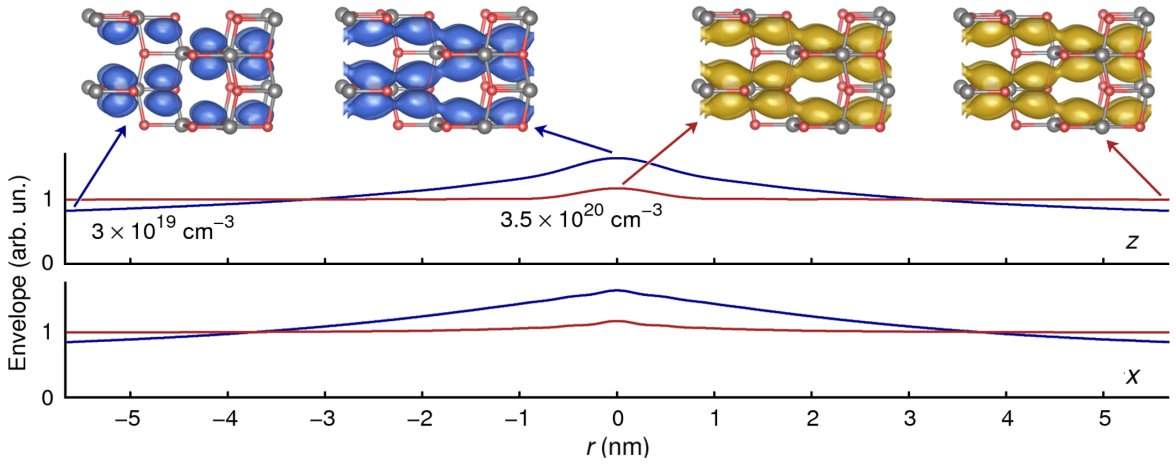

Figure 7.11: Square moduli of the polaron wavefunctions near the origin and further away from the origin along the c-axis direction, in the polaronic region (blue, 3×10^{19} cm^{-3}) and in the Fermi liquid region (yellow, 3.5×10^{20} cm^{-3}). The corresponding envelope functions are shown as the blue and red curves, respectively, both along the c axis (z, upper panel) and along an in-plane direction (x, lower panel).

the z direction (c axis) and the x direction (in-plane). The decays are very similar in the two directions, and are slightly more pronounced along z. From this figure we see that the wavefunction of an electron in the Fermi liquid region is comparable to a periodic Bloch function. On the other hand, in the polaronic region the wavefunction shows spatial localization. In this case, we can quantify the size of the polaron r_p by considering the half-width at half-maximum of the envelope function, and we obtain $r_\mathrm{p} = 5.7$ nm. In passing, we note that the polaron radius is often estimated as $r_\mathrm{p} = \sqrt{\hbar/(2m_\mathrm{b}\omega_\mathrm{LO})}$. As seen in Sec. 1.1, this parameter is an evaluation of the distance that the carrier can travel within the period of an atomic vibration, so it does not rigorously correspond to the polaron radius.

Our results thus indicate that polarons in anatase are large and more delocalized than previously thought [20], and that electrical conduction in principle takes place via standard band-like transport. We remark, however, that although perturbation theory seems to be appropriate for this coupling regime, it is possible that the wavefunctions properties, which have not been explored extensively in the Fröhlich literature, are not described accurately. For example, within the current perturbative approach no self-trapping emerges, regardless of the value of the coupling α. In fact, in the long-range limit the analytical model of Mahan, which is verified by our numerical calculations, shows that the perturbed part of the wavefunction decays as $1/r$ [4]. On the other hand, the solution of the Schrödinger equation for the electron wavefunction including the ionic polarization, which is often referred to as the Pekar instead of Fröhlich model, exhibits exponential localization [4, 8]. Further investigations that go beyond first-order perturbation theory would be useful in order to shed more light on the problem.

CHAPTER 8

Electronic properties and polar coupling in doped EuO

This chapter is concerned with the study of a ferromagnetic ionic semiconductor, europium oxide. Our interest in EuO has been driven by some very recent ARPES experiments on doped samples that probed polaronic physics in this material. An overview of some properties of EuO is given at the beginning of the chapter, followed by the calculation of its electronic and vibrational properties. The electron spectral function including the effects of the polar electron-phonon interaction is then investigated for different doping concentrations, revealing a crossover from a polaronic to a Fermi liquid regime analogous to the case of anatase TiO_2 examined in the previous chapter.

8.1 Europium oxide: an overview

Europium oxide (EuO) is a ferromagnetic semiconductor with rocksalt structure, with a Curie temperature $T_c \sim 69$ K. The half-filled $4f$ shell of Eu is responsible for the magnetic moment of $7\mu_B$. At the origin of the interest in this material is the fact that it was one of the first ferromagnetic semiconductors discovered, and the first rare-earth semiconducting oxide [208]. EuO exhibits a rich variety of exotic physical phenomena such

as a very large magnetoresistance [209]. This compound, as well as other europium calchogenides, has been intensively researched for applications in spintronic devices. In fact, the lower conduction bands are split for spin-up and spin-down electrons, thus making it a good spin-filter to create spin-polarized currents [210]. Although the hopes to raise T_c up to room temperature seem to have faded, this can be increased above 150 K upon doping with rare-earth metals, in particular gadolinium (Gd) [211].

EuO is an indirect gap semiconductor, with ARPES experiments on doped samples revealing a filling of the conduction-band states near the X point [212, 213]. After a small doping EuO indeed becomes metallic, with spin-polarized electron pockets centered at X. The Brillouin zone of the FCC lattice of EuO is shown in Fig. 8.1(a), with a sketch of the six ellipsoidal pockets in Fig. 8.1(b). An example of the Fermi surface measured along the $k_z = 0$ plane from Ref. [212] is reported in Fig. 8.1(c).

The lattice vibrational properties of EuO are less well-known than its electronic properties, with few early Raman and infrared optical studies [214, 215, 216]. Acoustic phonon dispersions have been probed very recently by means of inelastic X-ray scattering [217]. The lack of investigations on the electron-phonon coupling in this material is surprising. Recently, ARPES studies of Gd-doped EuO single crystals have revealed polaronic spectral features, which might be linked to the Fröhlich interaction [218].

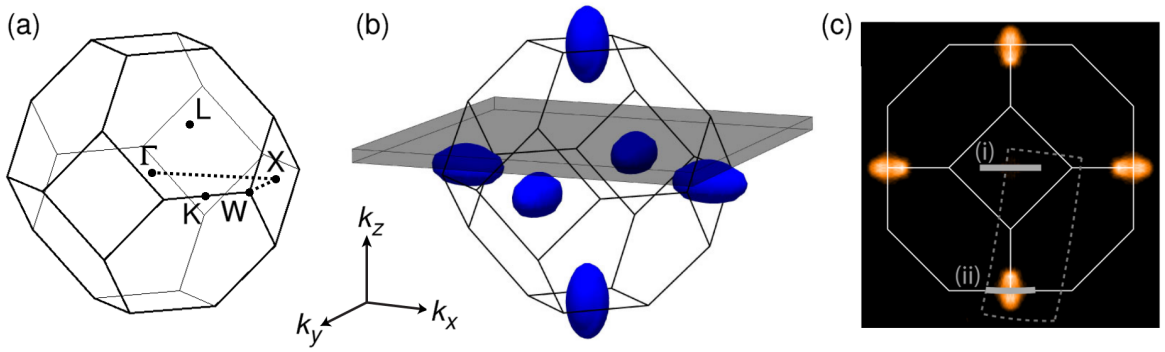

Figure 8.1: (a) Brillouin zone of the FCC lattice, with the special points labeled and the ΓX and XW paths shown explicitly. (b) Electron pockets in doped EuO, centered at X, and (c) Fermi surface corresponding to the $k_z = 0$ plane, shown in gray in (b). Panels (b) and (c) are reproduced with permission from Ref. [212]. Copyright 2012 American Physical Society.

These findings motivate our investigation of the polar coupling in doped EuO presented in Sec. 8.3. A thorough understanding of the electron-phonon coupling in EuO constitutes a key piece of information for a comprehensive description of the exotic properties of this material, and towards the engineering of future spintronic devices based on ferromagnetic semiconductors.

8.2 Electronic and vibrational properties

8.2.1 Electronic structure

We perform spin-polarized calculations on EuO in the low-temperature ferromagnetic state by using the projector augmented wave (PAW) method [219], which provides a better treatment of rare-earth elements with strongly localized states.[1] We adopt the GGA approximation, and include the Eu 5s and 5p semicore states in the valence configuration. Spin-orbit coupling is not considered since it is found to have a negligible effect [222].

DFT calculations predict this material to be metallic; more sophisticated methods need to be used in order to correctly describe the electronic structure in strongly correlated materials. A popular choice is given by the DFT+U scheme [223, 224], which is based on the addition of a corrective term in the DFT total energy functional, inspired from the Hubbard model [225]. This term includes a Coulomb repulsion parameter U^I on specific atomic sites I, usually applied on the localized d states of transition metals or f states of rare-earth elements where the Coulomb repulsion is strong. Here we employ the `Quantum ESPRESSO` implementation of DFT+U based on Ref. [226].

We use an effective on-site Coulomb parameter $U_f = 8.3$ eV for the Eu 4f states, and $U_p = 4.6$ eV for the O p states. This predicts a relaxed lattice constant $a = 5.174$ Å, which overestimates by less than 1% the experimental value $a = 5.144$ Å [209]. Convergence is

[1] The PAW method is a generalization of the pseudopotential method, particularly suitable when strongly localized orbitals are present which make it difficult to construct reliable norm-conserving pseudopotentials. We refer to Refs. [220, 41] for excellent reviews of the theory. The PAW datasets used here are taken from the pseudopotential library of `Quantum ESPRESSO` and from the VLab rare-earth PAW datasets web page [221].

ensured by using a kinetic energy cutoff of 70 Ry and a Brillouin-zone sampling with an $8\times8\times8$ mesh. Our U parameters are in the range of the ones found in the literature [227, 228, 222], and were adjusted to yield an indirect gap of 1.12 eV in agreement with the experiment [209]. The calculated band structure and projected density of states are shown in Fig. 8.2(a). The valence band consists of O $2p$ states between $4-6$ eV and Eu $4f$ states around $1-2$ eV below the conduction band bottom, in excellent agreement with photoemission data [212] and previous calculations [222, 229]. The Hubbard correction applied to the O $2p$ states is necessary in order to shift these states to lower energies. The bottom of the conduction band is derived from Eu $5d$ states. It was found that the addition of a U correction to these empty d orbitals pushes the bands up near X, resulting in a direct band gap at variance with the experiment [230]. Due to the exchange splitting of the conduction bands in the ferromagnetic state, the bottom of the band at X consists of majority spin states, in line with the experimental observations [231]. The effective mass is calculated from finite differences near the conduction band minimum, yielding a light mass $m_\mathrm{l} = 0.26\,m_\mathrm{e}$ along two Cartesian directions and a heavy mass $m_\mathrm{h} = 0.86\,m_\mathrm{e}$ along the third direction, with an average of $0.34\,m_\mathrm{e}$.

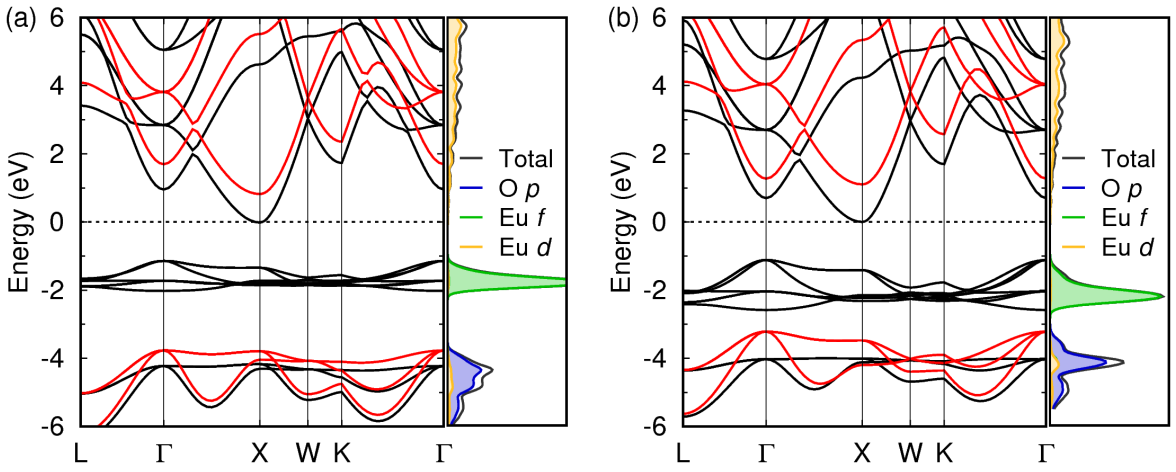

Figure 8.2: Electronic band structure of EuO calculated by DFT+U using the PAW method (a) and norm-conserving pseudopotentials (b). The black and red lines correspond to the majority and minority spin bands, respectively. The projected density of states is shown in the insets on the right (in arbitrary units). The zero of the energy is set to the bottom of the conduction band at X.

Since we need to extract maximally localized Wannier functions for our subsequent electron-phonon calculations, we additionally compute the electronic structure by using standard norm-conserving pseudopotentials. This is dictated by the limitation that the PAW method is not supported by the EPW software. Here we use the Hubbard parameters $U_f = 6.0$ eV and $U_p = 3.0$ eV, which yield the same band gap as previously calculated, and an almost identical effective mass of $0.33\, m_e$. The convergence parameters are 150 Ry for the kinetic energy cutoff, and an $8\times8\times8$ **k** mesh to sample the Brillouin zone. The relaxed lattice constant $a = 5.246$ Å is less accurate, overestimating the experimental one by 2%; moreover, the band structure reported in Fig. 8.2(b) shows more dispersive Eu f bands, and a smaller energy separation between the O p and the Eu f states. Nevertheless, the electronic properties near the conduction band bottom are described correctly.

We construct the MLWF after calculating DFT+U eigenvalues and eigenfunctions as outlined above on a $4 \times 4 \times 4$ **k**-point grid. As a starting guess for the localized functions we use spin-up Eu f orbitals for the highest valence bands, and Eu d and s orbitals of both spin channels for the conduction band region. We checked that the states with O p character can be safely excluded from the wannierization, and that an outer energy window up to 10.5 eV needs to be used for the disentanglement of the conduction band states. With this procedure we are able to accurately reproduce the band structure in proximity of the gap.

8.2.2 Lattice dynamics

To our knowledge the vibrational properties of EuO have been investigated from first principles for the first time only very recently, using a frozen-phonon method [217]. We adopt the same approach here, since the implementation of DFPT including the DFT+U correction (DFPT+U) is not yet available in Quantum ESPRESSO. In particular, we displace the atoms in the unit cell by 0.01 Å and calculate the resulting forces on all atoms in a $6 \times 6 \times 6$ supercell within the PAW method. The corresponding interatomic force

constants obtained by finite differences are then Fourier transformed to generate the dynamical matrix at any **q** wavevector. In order to correctly describe the dipole-dipole interactions and the LO-TO splitting, a strategy analogous to the one presented in Sec. 2.3.2 needs to be used. In fact, the IFCs in a polar material are long ranged and cannot effectively be truncated outside the $6 \times 6 \times 6$ supercell. Since in the frozen-phonon method the IFCs are directly calculated in real space, rather than obtained from the dynamical matrices calculated on a uniform **q** grid as in DFPT, the method of Sec. 2.3.2 needs to be modified. Following Ref. [232], we add to the IFCs $C_{\kappa\alpha,\kappa'\alpha'}(\mathbf{R})$ the contribution from the dipole-dipole interactions between the supercells. This is identical to the result in Eq. (2.46) after replacing the unit-cell volume Ω with the supercell volume $N_c\Omega$. The Fourier transform of these new IFCs gives the correct dynamical matrices, as we verified numerically for the GaN and $SrTiO_3$ examples studied in Chapter 4.

In order to calculate the dipole-dipole contribution to the IFCs, the Born effective charges and the high-frequency dielectric constant are needed. These can be obtained by calculating the change in the total polarization after displacing the atoms in the unit cell or after applying a small electric field, respectively. Within `Quantum ESPRESSO`, however, we cannot calculate successfully the total polarization in the present case of a

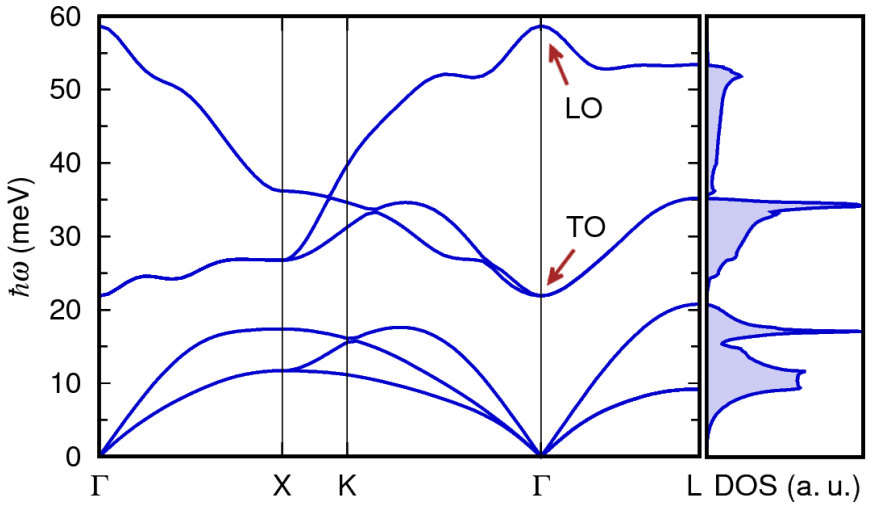

Figure 8.3: Phonon dispersions of EuO, with the split LO and TO modes marked by arrows. The phonon density of states is shown in the inset on the right (in arbitrary units).

spin-polarized system treated with DFT+U. We therefore adopt the results obtained in Ref. [217] using the VASP software. The calculated value of ϵ_∞ is 3.6, as compared to the experimental one of 4.6 [214], and the Born effective charges are $Z^* = 2.65$ for the Eu atoms and $Z^* = -2.65$ for the O atoms.

The phonon dispersion relations finally obtained are shown in Fig. 8.3, together with the phonon density of states. The three optical branches are separated in energy from the acoustic ones. Our calculated LO phonon energy of 58.5 meV is in good agreement with the infrared measurements reporting $\hbar\omega_{\mathrm{LO}} = 54$ meV [214], while the large LO-TO splitting is indicative of a strong polar coupling in this material. Indeed, the generalized Fröhlich coupling constant calculated from Eq. (4.12) using the average effective mass gives $\alpha = 2.3$.

8.3 Evolution of electron-phonon coupling with doping density

8.3.1 Computational details

We now move to analyzing the effects of the electron-phonon coupling in the spectral features of doped EuO, focusing on doping concentrations in the range of the ones investigated in ARPES experiments [218]. Since the implementation of the linear response formalism of DFPT in Quantum ESPRESSO has not been extended to the DFT+U method yet, we adopt a simplified approach where only the polar electron-phonon coupling is taken into account. This is done by computing the long-range matrix elements $g^{\mathcal{L}}$, as we already did in Chapter 5 for the case of $CH_3NH_3PbI_3$. The rationale for this choice is that satellite features have been observed experimentally in doped samples, which seemingly emerge as a consequence of the Fröhlich coupling. The relevant physics should then be fully captured by $g^{\mathcal{L}}$.

We modify the EPW code to implement the Fourier interpolation of the interatomic

n (cm^{-3})	E_F (meV)	n (cm^{-3})	E_F (meV)
6.2×10^{17}	5	2.1×10^{19}	56
2.3×10^{18}	12	3.1×10^{19}	70
2.8×10^{18}	14	4.2×10^{19}	87
7.7×10^{18}	30	1.2×10^{20}	166
1.9×10^{19}	51	1.9×10^{20}	227

Table 8.1: Calculated Fermi level with respect to the bottom of the conduction band for each doping concentration studied.

force constants, including the LO-TO splitting, using the IFCs calculated with the frozen-phonon method, as detailed in Sec. 8.2.2. The electronic Hamiltonian is calculated with norm-conserving pseudopotentials on a $4 \times 4 \times 4$ $\mathbf{k}$ grid and interpolated using Wannier functions following Sec. 8.2.1.

Since for each doping level considered a well-defined Fermi surface has been measured [218], the effect of doping is included using the rigid band model as in Chapter 7. The shift of the Fermi level inside the conduction band, following the addition of a small charge in the unit cell, is calculated by Wannier-interpolating the Kohn-Sham eigenvalues onto a very fine Brillouin-zone grid with 10^6 random $\mathbf{k}$ points. The ten values of doping considered and their Fermi level shifts relative to the conduction band minimum are reported in Tab. 8.1. We further take into account the dynamical screening arising from the added carriers by using the nonadiabatic matrix elements of Eq. (7.4). The Lindhard dielectric function is calculated taking into account the number of X valleys (six) and their spin-polarized nature. A constant electron lifetime $\hbar/\tau_{n\mathbf{k}} = 50$ meV [218] is included.

The Brillouin-zone integral needed to evaluate the electron-phonon self-energy in Eq. (3.55) is converged using 10^5 random $\mathbf{q}$ points sampled from a Lorentzian distribution centered around $\mathbf{q} = 0$.[2] The positive imaginary part at the denominator is set to $\eta = 10$ meV, and the temperature to $T = 20$ K. The electronic spectral function including electron-phonon coupling effects is then calculated both using the one-shot Migdal

[2]We checked the convergence of the self-energy using random grids of Lorentzian distributed $\mathbf{q}$ points that were generated by Samuel Poncé, with weights determined by Voronoi tessellation [183].

approximation and the cumulant expansion method as in Chapter 7. The temperature broadening of the Fermi cutoff is included by multiplying the spectral function by the Fermi distribution at $T = 20$ K.

8.3.2 Results

The spectral functions calculated within the one-shot Migdal approximation [Eq. (3.66)] are shown in Fig. 8.4 for six doping concentrations ranging from 6.2×10^{17} cm^{-3} to 1.2×10^{20} cm^{-3}. For the lowest three dopings in panels (a)–(c) a parabolic band followed by a satellite are clearly distinguished, whereas in panels (d) and (e) the satellites disappear and the bottom of the quasiparticle band acquires a large broadening. For the highest doping level in (f) the scenario evolves into a weak band structure kink visible near the LO phonon energy, below which the broadening of the band is enhanced. This remarkable

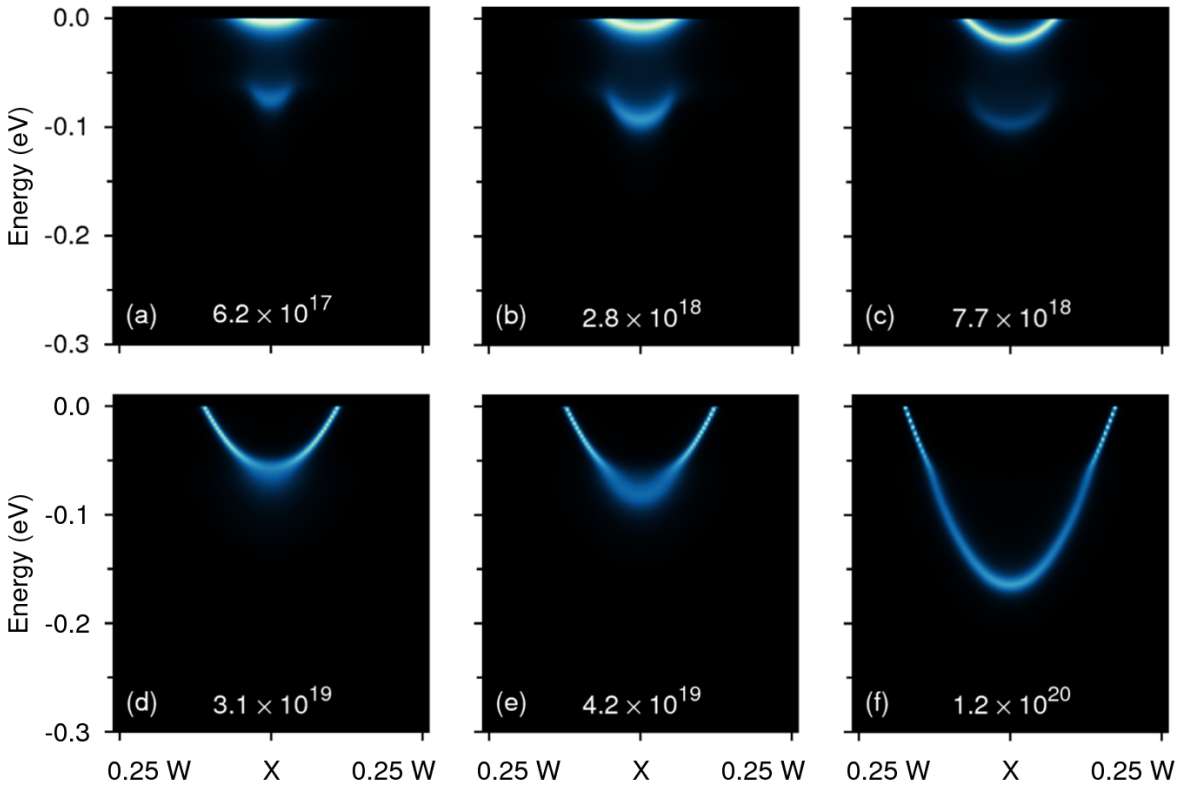

Figure 8.4: Spectral functions of EuO calculated for different doping concentrations as indicated in each panel (in cm^{-3}) using the one-shot Migdal approximation. The crystal momentum is taken along the WX Brillouin-zone direction, and the zero of the energy corresponds to the Fermi level.

evolution of the spectral features with doping concentration appears to be similar to the case of anatase TiO_2 analyzed in Chapter 7.

The energy separation between the main quasiparticle peak and the satellite in Fig. 8.4(a)–(c) goes from 72 to 88 meV, whereas the LO phonon energy is only 58.5 meV. The cumulant expansion method, however, reduces this energy separation to $53-60$ meV, compatible with the characteristic LO phonon energy. The spectra calculated with the cumulant expansion are presented in Fig. 8.5(e)–(h), together with the experimental data for the same doping concentrations in panels (a)–(d) [218]. In order to compare directly our results with the experimental ARPES measurements, two additional steps are performed: (i) the intensity map is integrated over the out-of-plane direction k_z, and (ii) the results are convoluted with two Gaussian masks of width 20 meV and 0.015 Å^{-1} accounting for the experimental energy and momentum resolution, respectively.

We see that at variance with the one-shot Migdal approximation, the cumulant expansion yields two satellites for the spectra in Fig. 8.5(e)–(f), the second one being very dim especially for the lowest doping concentration. On the other hand, no additional features are present below the bottom of the band for the last two doping levels, apart from some broadening due to the small lifetime of these electronic states. The theoretical and experimental spectra are in nice agreement, with some minor discrepancies related to the energy of the bottom of the quasiparticle band. In particular, the main feature in the experimental maps seems to extend to slightly lower energies than in our calculations. We can formulate the hyphothesis that the difference in the position of the band bottom is due to a mismatch in the Fermi level of the system. This hyphothesis is related to inaccuracies in the curvature of the lowest conduction band given by our calculations. Due to the unavailability of reliable experimental effective masses, it is arduous to establish the correctness of this hypothesis.

In order to analyze more in detail the strength of the electron-phonon coupling and its evolution with doping, we proceed by extracting the quasiparticle bands from the calculated spectra for each doping concentration listed in Tab. 8.1. From the electron

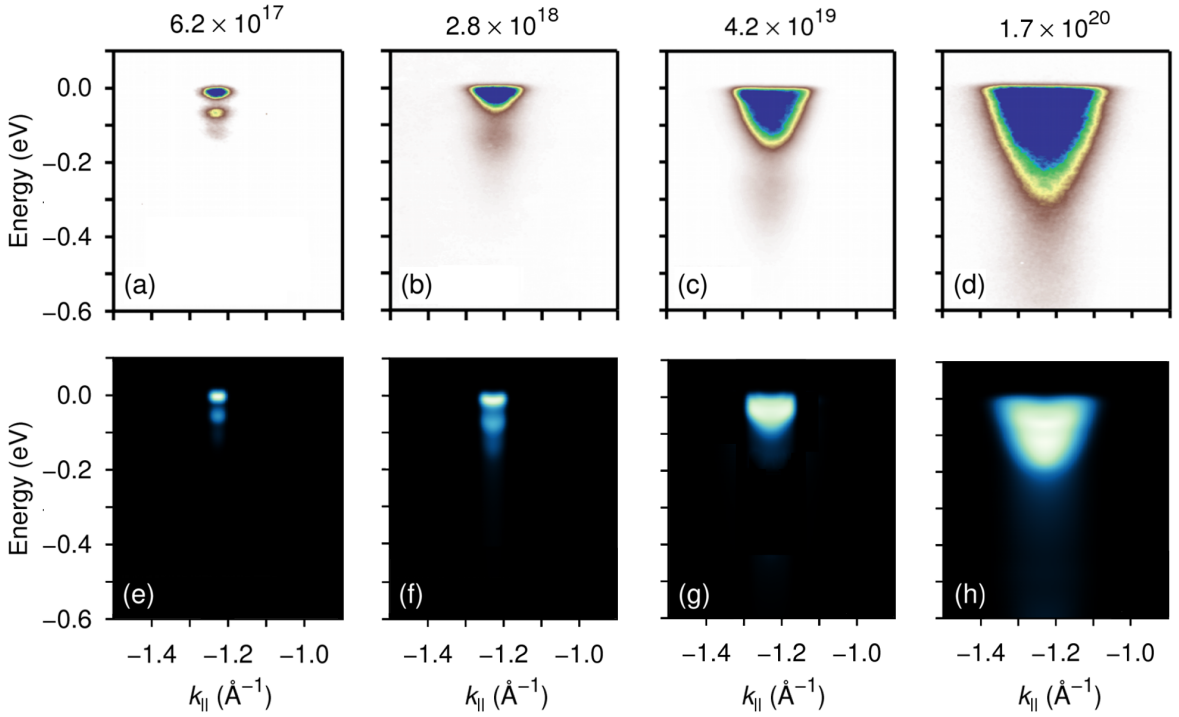

Figure 8.5: (a)–(d) ARPES spectra measured by King *et al.* [218] for samples with varying doping concentrations as indicated on top of each panel (in cm^{-3}). The crystal momentum $k_{||}$ is along the WX line of the Brillouin zone as in Fig. 8.4, with the X point corresponding to the Cartesian coordinates $(0, -2\pi/a, 0)$. (e)–(h) *Ab initio* spectral functions for the same nominal doping levels as in (a)–(d) and Brillouin-zone line, calculated using the cumulant expansion method. The spectra are convoluted in both momentum and energy with Gaussian masks and are integrated on different k_z planes.

velocity renormalization [Eq. (3.65)], that is from the slope of the bare and renormalized bands near the Fermi level, we obtain the coupling strength λ. The results are reported in Fig. 8.6 (blue disks). We can identify a polaronic region at low doping where λ is approximately constant, with a value of nearly 1.0; a transition region at intermediate doping where λ decreases by about a half and the polaronic satellite features become less prominent; and a Fermi liquid region where λ is gradually reduced to about 0.16, and the satellites are replaced by band structure kinks. To further establish the effect of the anisotropy of the bands, we perform additional calculations along the ΓX Brillouin-zone direction. The corresponding electron-phonon coupling strength is given by the blue triangles in Fig. 8.6. From these results we see that the coupling is isotropic, differing by no more than 5% along different directions.

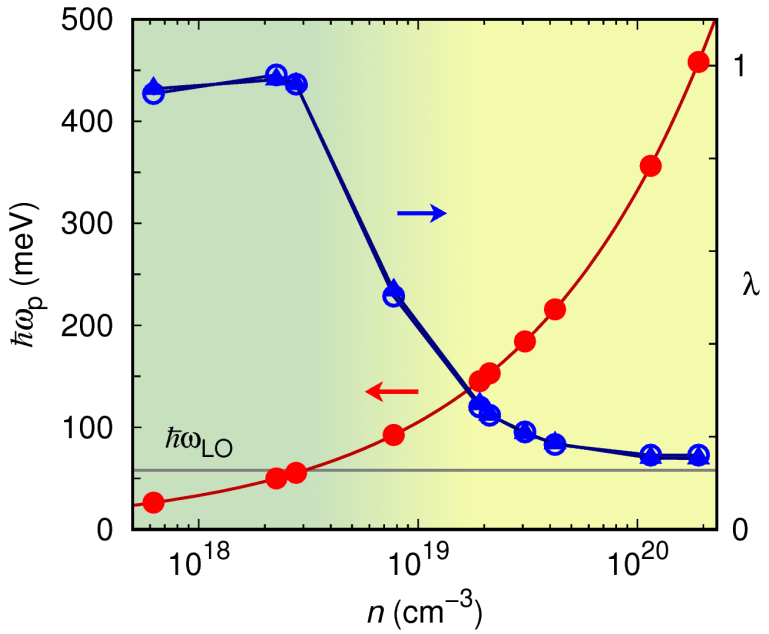

Figure 8.6: Polaronic and Fermi liquid regions in n-doped EuO: the blue disks indicate the electron-phonon coupling strength λ calculated along the WX Brillouin-zone direction, while the blue triangles are for the ΓX direction. The blue line is a guide to the eye. The red disks give the plasma energy at each doping level, with the red line corresponding to the square root relation between $\hbar\omega_p$ and n. The horizontal line identifies the energy of the LO phonon mode.

The evolution of the electron-phonon coupling with carrier concentration presented in Fig. 8.6 can be attributed to the dynamical screening of the Fröhlich interaction, analogously to the case of anatase TiO_2. In fact, if we apply the same reasoning as in Chapter 7 and we compare the energy scale of the LO phonon (gray line) with the plasma energy (red disks) at each carrier concentration, we see that the electron-phonon coupling is weakened when the timescale of the electronic response becomes smaller than that of the longitudinal optical vibrations.

While the current investigation establishes the presence of a strong Fröhlich electron-phonon coupling in EuO, that is progressively suppressed with increasing doping concentration, it does not rule out the additional presence of other forms of electron-boson coupling. In particular, a preliminary analysis of the experimental data showed that the coupling with plasmons may contribute to the observed spectral features [218]. This is not surprising since the energy scale of the plasmon excitations can be compatible with these features for low and intermediate carrier densities. At variance with the coupling

with polar phonons, the characteristic energies of the electron-plasmon coupling present a strong dependence on the doping concentration (the plasma energy goes as the square root of the carrier density). A careful analysis of the experimental data, combined with advanced *ab initio* calculations of the electron-plasmon coupling [233], will shed more light on this aspect.

CHAPTER 9

Conclusions

9.1 Summary

In this thesis we investigated the polar Fröhlich electron-phonon coupling from first principles, focusing both on establishing a solid approach to tackle the problem, and on applying it to calculate selected properties of some technologically relevant materials. In addition, we elaborated a novel framework for calculating ARPES spectra from first principles, in order to study the polaronic character of the charge carriers in doped oxides.

The new method developed to accurately compute the electron-phonon matrix elements in polar materials from first principles was presented in Chapter 4. The formalism allowed us to define a generalized Fröhlich matrix element and coupling constant, which easily account for the coupling to multiple infrared-active phonon modes and for anisotropy in the crystal. Moreover, we devised an efficient implementation of this method in conjunction with the *ab initio* Wannier-Fourier interpolation of `EPW`, which was successfully tested on GaN and $SrTiO_3$. We also presented a simplified approach where only the polar electron-phonon coupling is calculated, by approximating the full electron-phonon matrix element with the long-range component. This was adopted for

the case of $CH_3NH_3PbI_3$ illustrated in Chapter 5. There, we reached conclusions in line with the analysis of experimental data regarding the temperature dependence of the broadening of the photoluminescence peak. Moreover, the energy of the representative LO mode contributing the most to the polar coupling was determined without resorting to any additional information, which would have not been possible within the simple Fröhlich model.

In Chapter 6 we used our method to study the electron linewidths and lifetimes in anatase TiO_2, establishing that the polar coupling is the main electron-phonon scattering mechanism near the band edges. In Chapter 7 and 8 we presented a first-principles analysis of the evolution of ARPES spectra with varying doping concentrations for two doped oxides, anatase TiO_2 and EuO, by calculating the electron spectral function including the electron-phonon self-energy. Our calculations were directly compared to experimental data, demonstrating a good agreement. We showed that it is paramount to include the effect of the dynamical screening of the electron-phonon interaction from the doped carriers, and that the cumulant expansion method gives an improved description of the satellite structures. Most importantly, our first-principles calculations allowed us to clarify the origin of the transition from a polaronic liquid to a Fermi liquid regime without making any *a priori* assumption about the underlying mechanism. This transition was identified in the interplay between the screening of the electron plasma and the Fröhlich coupling.

9.2 Outlook

We trust that the work presented in this thesis provided new insight into the Fröhlich electron-phonon interaction, and will spark future *ab initio* investigations. In particular, the theory and methodology presented in Chapter 4 enable to explore several properties of polar semiconductors and insulators which were previously out of reach within *ab initio* calculations, e.g. carrier lifetimes and mobilities in transparent oxides, dynamics of

photoexcited carriers in light-emitting devices and polaron physics in wide-gap semiconductors and oxides. Using this approach, routine calculations that are truly predictive become possible.

The generalized Fröhlich matrix element of Eq. (4.5) can be used to assess the role of polar electron-phonon coupling in relevant materials for which full *ab initio* calculations are too expensive, following the example of $CH_3NH_3PbI_3$. On the other hand, the use of the polar corrected Wannier interpolation allows to investigate the interplay of long and short-range electron-phonon interactions on the same footing.

The investigation of the polaronic character of charge carriers in conducting oxides and the evolution with doping is a stimulating topic that ought to be explored further in future research. We expect that the work presented in this thesis conveys a powerful technique to investigate polaron formation in these materials. Notably, the nonadiabatic Fröhlich coupling that we identified could be the unifying mechanism behind the transition from polarons to Fermi liquids. Further to the materials studied at present, anatase TiO_2 and EuO, it would be timely to extend the investigation to other compounds, in particular $SrTiO_3$. In this case, the 2D electron gas formed at the surface constitutes a fascinating system, and one that presents additional issues, for example due to dimensionality effects [22, 234]. As an additional note, it would also be interesting to include the effects of electron-plasmon coupling in the calculation of the spectral function [233].

A rigorous treatment of the electron-phonon coupling in doped materials from first principles poses major challenges. In our approach presented in Chapter 7 we take into account the *dynamical* screening of the electron-phonon coupling due to doped carriers using a homogeneous electron gas model, however it would be important to describe this effect employing a more rigorous *ab initio* theory. This could be achieved for example within a time-dependent linear response formalism, however it would be computationally prohibitive [235]. The mutual renormalization of the plasmon and phonon modes, which has been neglected in our approach, is also an interesting aspect that calls for further investigation [192, 193]. We anticipate that this intricate scenario could be explored

by calculating the renormalization of the phonon Green's function due to the added carriers through a nonadiabatic phonon self-energy [236, 73]. The poles of the renormalized Green's function would yield the bosonic excitations of the coupled electron-phonon system [193].

Another question still open concerns the accurate description of the size of the polarons formed as a consequence of electron-phonon coupling. DFT calculations of excess electrons using large supercells are extremely sensitive to the size of the supercell and to the exchange and correlation functional [187, 237]. In our work we attempted to address the problem by using first-order perturbation theory in order to calculate the electron wavefunction, however we anticipate that the development of a more elaborate approach for the variation of the electron wavefunctions and the nuclear displacements would be desirable.

To conclude, we would like to emphasize that the investigation of ARPES spectra from first principles is a topic of considerable interest not only for theorists, but also for many experimentalists who are keen to have access to accurate *ab initio* calculations that can help disclose the physical mechanisms behind their results. We hope that the work carried out in this thesis will stimulate new efforts in order to bridge the gap between the growing abundance of experimental data and the complexity of *ab initio* many-body calculations.

APPENDIX A

Second quantization and field operators

In this Appendix we briefly summarize the basic formalism of second quantization; at the end the electronic field operators are also defined. In second quantization ladder operators are introduced with the property of creating or destroying particles in each quantized state [238].

For a system of identical particles obeying the Bose-Einstein statistics (bosons) such as phonons, the creation and destruction operators $\hat{a}^{\dagger}_{\mathbf{q}\nu}$ and $\hat{a}_{\mathbf{q}\nu}$, respectively, are defined so that they create or destroy a phonon of energy $\hbar\omega_{\mathbf{q}\nu}$ and polarization $\mathbf{e}_{\kappa\nu}(\mathbf{q})$. These operators obey the following commutation relations:

$$[\hat{a}_{\mathbf{q}\nu}, \hat{a}^{\dagger}_{\mathbf{q}'\nu'}] = \delta_{\mathbf{q}\mathbf{q}'}\delta_{\nu\nu'}\,; \tag{A.1}$$

$$[\hat{a}_{\mathbf{q}\nu}, \hat{a}_{\mathbf{q}'\nu'}] = [\hat{a}^{\dagger}_{\mathbf{q}\nu}, \hat{a}^{\dagger}_{\mathbf{q}'\nu'}] = 0. \tag{A.2}$$

If we denote by $|n_{\mathbf{q}\nu}\rangle$ a state with n phonons with momentum $\mathbf{q}$ and branch ν, then the action of the ladder operators on this state gives:

$$\begin{aligned} \hat{a}^{\dagger}_{\mathbf{q}\nu}\,|n_{\mathbf{q}\nu}\rangle &= \sqrt{n_{\mathbf{q}\nu}+1}\;|n_{\mathbf{q}\nu}+1\rangle\,; \\ \hat{a}_{\mathbf{q}\nu}\,|n_{\mathbf{q}\nu}\rangle &= \sqrt{n_{\mathbf{q}\nu}}\;|n_{\mathbf{q}\nu}-1\rangle\,, \end{aligned} \tag{A.3}$$

and at finite temperature we take $n_{\mathbf{q}\nu}$ to represent the thermal average of the phonon

occupation number $\hat{a}^\dagger_{\mathbf{q}\nu}\hat{a}_{\mathbf{q}\nu}$:

$$n_{\mathbf{q}\nu} = n(\omega_{\mathbf{q}\nu}) = \frac{1}{e^{\omega_{\mathbf{q}\nu}/(k_\mathrm{B}T)} - 1}\,, \tag{A.4}$$

which is the Bose-Einstein distribution.

For identical particles following the Fermi-Dirac statistics (fermions) such as electrons, the operators that create or destroy electrons in a state n with momentum $\mathbf{k}$ are defined as $\hat{c}^\dagger_{n\mathbf{k}}$ and $\hat{c}_{n\mathbf{k}}$, respectively. In this case they obey anti-commutation relations:

$$\{\hat{c}_{n\mathbf{k}}, \hat{c}^\dagger_{m\mathbf{k}'}\} = \delta_{\mathbf{k}\mathbf{k}'}\delta_{nm}\,; \tag{A.5}$$

$$\{\hat{c}_{n\mathbf{k}}, \hat{c}_{m\mathbf{k}'}\} = \{\hat{c}^\dagger_{n\mathbf{k}}, \hat{c}^\dagger_{m\mathbf{k}'}\} = 0. \tag{A.6}$$

The action of these operators on the many-body electronic wavefunction needs to take into account the signs given by the antisymmetrization, and it is well summarized in Ref. [238]. We recall that:

$$\hat{c}^\dagger_{n\mathbf{k}}\hat{c}_{n\mathbf{k}}\,|\cdots n\mathbf{k}\cdots\rangle = f_{n\mathbf{k}}\,|\cdots n\mathbf{k}\cdots\rangle\,, \tag{A.7}$$

where the ket contains a Slater determinant, and the thermal occupation factor is given by the Fermi-Dirac distribution:

$$f_{n\mathbf{k}} = f(\varepsilon_{n\mathbf{k}}) = \frac{1}{e^{\varepsilon_{n\mathbf{k}}/(k_\mathrm{B}T)} + 1}\,. \tag{A.8}$$

A one-body electron operator $\hat{A}$ can be rewritten in second quantization notation as [238]:

$$\hat{A}_\mathrm{e} = \sum_{nm,\mathbf{k}\mathbf{k}'} \langle\psi_{m\mathbf{k}'}|\hat{A}|\psi_{n\mathbf{k}}\rangle\,\hat{c}^\dagger_{m\mathbf{k}'}\hat{c}_{n\mathbf{k}} = \sum_{nm,\mathbf{k}\mathbf{k}'} \hat{A}_{m\mathbf{k}'n\mathbf{k}}\hat{c}^\dagger_{m\mathbf{k}'}\hat{c}_{n\mathbf{k}}\,. \tag{A.9}$$

The quantum field operators for electrons are defined as a linear combination of the creation and destruction operators:

$$\hat{\psi}^\dagger(\mathbf{r}) = \sum_{n\mathbf{k}} \psi^*_{n\mathbf{k}}(\mathbf{r})\,\hat{c}^\dagger_{n\mathbf{k}}\,; \tag{A.10}$$

$$\hat{\psi}(\mathbf{r}) = \sum_{n\mathbf{k}} \psi_{n\mathbf{k}}(\mathbf{r})\,\hat{c}_{n\mathbf{k}}\,, \tag{A.11}$$

where $\psi_{n\mathbf{k}}(\mathbf{r})$ are single-particle wavefunctions. The meaning of these operators is to create ($\hat{\psi}^\dagger$) and destroy ($\hat{\psi}$) a particle at point $\mathbf{r}$. Following Eqs. (A.5)–(A.6), they obey the anticommutation relations:

$$\{\hat{\psi}(\mathbf{r}), \hat{\psi}^\dagger(\mathbf{r}')\} = \delta(\mathbf{r}-\mathbf{r}')\,; \tag{A.12}$$

$$\{\hat{\psi}(\mathbf{r}), \hat{\psi}(\mathbf{r}')\} = \{\hat{\psi}^\dagger(\mathbf{r}), \hat{\psi}^\dagger(\mathbf{r}')\} = 0\,. \tag{A.13}$$

The time-dependent field operators in the Heisenberg picture are defined as:

$$\hat{\psi}(\mathbf{r}, t) = e^{i\hat{H}t/\hbar}\,\hat{\psi}(\mathbf{r})\,e^{-i\hat{H}t/\hbar}\,, \tag{A.14}$$

where $\hat{H}$ is the Hamiltonian of the system. An analogous definition holds for the creation operator. It can be readily seen that $\hat{\psi}(\mathbf{r}, t)$ satisfies the Heisenberg equation of motion:

$$\begin{aligned} i\hbar\frac{\partial}{\partial t}\hat{\psi}(\mathbf{r}, t) &= \left[\hat{\psi}(\mathbf{r}, t), \hat{H}\right] \\ &= \left[-\frac{\hbar^2}{2m_\mathrm{e}}\nabla^2 + \int d\mathbf{r}'\, v(\mathbf{r}, \mathbf{r}')\,\hat{n}(\mathbf{r}', t)\right]\hat{\psi}(\mathbf{r}, t)\,, \end{aligned} \tag{A.15}$$

where we used Eqs. (3.20) and (3.22) in the main text and the anticommutation relations in Eqs. (A.12)–(A.13).

APPENDIX B

Born-von Kármán supercell

Here we summarize some useful details related to the Born-von Kármán boundary conditions introduced in Chapter 2.

The unit cell of a crystal is defined by the primitive lattice vectors $\mathbf{a}_1$, $\mathbf{a}_2$ and $\mathbf{a}_3$, and has a volume $\Omega = |\mathbf{a}_1 \cdot \mathbf{a}_2 \times \mathbf{a}_3|$. The direct lattice vectors $\mathbf{R}$ defining the whole crystal are:

$$\mathbf{R} = n_1\mathbf{a}_1 + n_2\mathbf{a}_2 + n_3\mathbf{a}_3\,, \qquad n_1, n_2, n_3 \in \mathbb{Z}\,. \tag{B.1}$$

The primitive vectors of the reciprocal lattice are defined as:

$$\mathbf{b}_1 = 2\pi\,\frac{\mathbf{a}_2 \times \mathbf{a}_3}{\mathbf{a}_1 \cdot \mathbf{a}_2 \times \mathbf{a}_3}\,, \tag{B.2}$$

and similarly for $\mathbf{b}_2$ and $\mathbf{b}_3$ using permutations of the indices [194]. The reciprocal lattice is defined by the vectors $\mathbf{G}$:

$$\mathbf{G} = m_1\mathbf{b}_1 + m_2\mathbf{b}_2 + m_3\mathbf{b}_3\,, \qquad m_1, m_2, m_3 \in \mathbb{Z}\,. \tag{B.3}$$

It is customary to define the region in reciprocal space enclosing all $\mathbf{k}$ vectors with a distance from $\mathbf{G} = 0$ smaller than the distance from the other $\mathbf{G}$ vectors as the *first Brillouin zone*. The corresponding definition in real space forms the *Wigner-Seitz cell*. The volume

of the first Brillouin zone is the same as the volume of the unit cell in reciprocal space, $\Omega_{\mathrm{BZ}} = |\mathbf{b}_1 \cdot \mathbf{b}_2 \times \mathbf{b}_3| = (2\pi)^3/\Omega$. Since $\mathbf{a}_i$ and $\mathbf{b}_j$ satisfy the relation $\mathbf{a}_i \cdot \mathbf{b}_j = 2\pi\delta_{ij}$, it is straightforward to verify that $e^{i\mathbf{G}\cdot\mathbf{R}} = 1$.

The Born-von Kármán (BvK) supercell consists of $N_\mathrm{c} = N_1 \times N_2 \times N_3$ crystal unit cells, hence it has a volume $V = N_\mathrm{c}\Omega$. Following the BvK boundary conditions, the wavefunctions $\psi_{m\mathbf{k}}(\mathbf{r})$ are taken to be periodic over the BvK supercell, $\psi_{m\mathbf{k}}(\mathbf{r}+\mathbf{T}) = \psi_{m\mathbf{k}}(\mathbf{r})$ where $\mathbf{T}$ is a lattice vector of the BvK supercell. The integers n_i defining the lattice vectors $\mathbf{R}$ in Eq. (B.1) now assume the values $0 \le n_i \le N_i - 1, i = 1,2,3$. A uniform grid in the reciprocal unit cell is defined by:

$$\mathbf{q} = \frac{m_1}{N_1}\mathbf{b}_1 + \frac{m_2}{N_2}\mathbf{b}_2 + \frac{m_3}{N_3}\mathbf{b}_3\,, \qquad 0 \le m_j \le N_j - 1 \;\; (j = 1,2,3) \tag{B.4}$$

and it contains the same number of vectors as the number of unit cells N_c in the BvK supercell. It is easily verified that the following identities hold:

$$\sum_{\mathbf{q}} e^{i\mathbf{q}\cdot\mathbf{R}} = N_\mathrm{c}\sum_{\mathbf{T}}\delta_{\mathbf{R},\mathbf{T}}\,; \;\; \int d\mathbf{q}\, e^{i\mathbf{q}\cdot\mathbf{R}} = \frac{(2\pi)^3}{\Omega}\sum_{\mathbf{T}}\delta_{\mathbf{R},\mathbf{T}}\,; \tag{B.5}$$

$$\sum_{\mathbf{R}} e^{i\mathbf{q}\cdot\mathbf{R}} = N_\mathrm{c}\sum_{\mathbf{G}}\delta_{\mathbf{q},\mathbf{G}} = \frac{(2\pi)^3}{\Omega}\sum_{\mathbf{G}}\delta(\mathbf{q}-\mathbf{G})\,. \tag{B.6}$$

APPENDIX C

Derivations using Ewald sums

The Ewald summation technique constitutes a convenient numerical method to evaluate slowly converging expressions for lattice sums such as the potential due to an infinite periodic array of charges. In the following we show the main steps to derive the Ewald sum and how to use it to obtain the total energy of the ionic charges, the dipole-dipole contribution to the interatomic force constants and the long-range polar coupling of Chapter 4.

C.1 Ewald method

The potential due to periodic array of charges can be rewritten equivalently as a summation over the lattice vectors **R** or over the reciprocal lattice vectors **G** [239]:

$$\sum_{\mathbf{R}} \frac{1}{|\mathbf{r}-\mathbf{R}|} = \int_0^\infty d\rho \, \frac{2}{\sqrt{\pi}} \sum_{\mathbf{R}} e^{-\rho^2 |\mathbf{r}-\mathbf{R}|^2} \tag{C.1}$$

$$= \int_0^\infty d\rho \, \frac{2}{\sqrt{\pi}} \int d\mathbf{k} \frac{1}{\rho^3 \sqrt{\pi^3}} \sum_{\mathbf{R}} e^{-k^2/\rho^2 + 2i\mathbf{k}\cdot(\mathbf{r}-\mathbf{R})} \tag{C.2}$$

$$= \int_0^\infty d\rho \, \frac{2}{\sqrt{\pi}} \int d\mathbf{k} \frac{1}{\rho^3 \sqrt{\pi^3}} \left(\sum_{\mathbf{G}} \frac{(2\pi)^3}{\Omega} \delta(2\mathbf{k}-\mathbf{G}) \right) e^{-k^2/\rho^2 + 2i\mathbf{k}\cdot\mathbf{r}} \tag{C.3}$$

$$= \frac{2\pi}{\Omega} \int_0^\infty d\rho \, \frac{1}{\rho^3} \sum_{\mathbf{G}} e^{-G^2/4\rho^2} e^{i\mathbf{G}\cdot\mathbf{r}}, \tag{C.4}$$

where to obtain Eq. (C.3) we used the relation in Eq. (B.6). It can be noted that the sum over **R** in Eq. (C.1) converges rapidly when ρ is large, whereas the sum over **G** converges rapidly when ρ is small. Therefore, it is convenient to express the left-hand term of Eqs. (C.1)–(C.4) as the sum of two integrals:

$$\sum_{\mathbf{R}} \frac{1}{|\mathbf{r}-\mathbf{R}|} = \int_{\eta}^{\infty} d\rho \, \frac{2}{\sqrt{\pi}} \sum_{\mathbf{R}} e^{-\rho^2|\mathbf{r}-\mathbf{R}|^2} + \frac{2\pi}{\Omega} \int_{0}^{\eta} d\rho \, \frac{1}{\rho^3} \sum_{\mathbf{G}} e^{-G^2/4\rho^2} e^{i\mathbf{G}\cdot\mathbf{r}}, \tag{C.5}$$

where we introduced the so-called Ewald parameter η. We remark that Eq. (C.5) holds for any choice of η. We rewrite the equation by (i) expressing the first integral using the complementary error function $\mathrm{erfc}(x) = 1 - \mathrm{erf}(x) = \frac{2}{\sqrt{\pi}} \int_x^{\infty} dt \, e^{-t^2}$, (ii) performing the second integral analytically, and (iii) introducing a compensating background which corresponds to the omission of the $\mathbf{G} = 0$ term:

$$\sum_{\mathbf{R}} \frac{1}{|\mathbf{r}-\mathbf{R}|} \to \sum_{\mathbf{R}} \frac{\mathrm{erfc}(\eta|\mathbf{r}-\mathbf{R}|)}{|\mathbf{r}-\mathbf{R}|} + \frac{4\pi}{\Omega} \sum_{\mathbf{G}\neq 0} \frac{1}{G^2} e^{-\frac{G^2}{4\eta^2}} e^{i\mathbf{G}\cdot\mathbf{r}} - \frac{\pi}{\eta^2\Omega}, \tag{C.6}$$

where the last term is the analytic limit for $\mathbf{G} \to 0$ of the second integral in Eq. (C.5).

The total Coulomb energy per unit cell of the ionic charges plus the compensating background (E_{Ew}) can then be obtained by using Eq. (C.6) and omitting the self-interaction term for each ion [41]:

$$E_{\mathrm{Ew}} = \frac{e^2}{2} \sum_{\kappa,\kappa'} Z_\kappa Z_{\kappa'} {\sum_{\mathbf{R}}}' \frac{1}{|\boldsymbol{\tau}_\kappa - \boldsymbol{\tau}_{\kappa'} - \mathbf{R}|} \tag{C.7}$$

$$\begin{aligned} &= \frac{e^2}{2} \sum_{\kappa,\kappa'} Z_\kappa Z_{\kappa'} \left({\sum_{\mathbf{R}}}' \frac{\mathrm{erfc}(\eta|\boldsymbol{\tau}_\kappa - \boldsymbol{\tau}_{\kappa'} - \mathbf{R}|)}{|\boldsymbol{\tau}_\kappa - \boldsymbol{\tau}_{\kappa'} - \mathbf{R}|} + \frac{4\pi}{\Omega} \sum_{\mathbf{G}\neq 0} \frac{1}{G^2} e^{-\frac{G^2}{4\eta^2}} e^{i\mathbf{G}\cdot(\boldsymbol{\tau}_\kappa - \boldsymbol{\tau}_{\kappa'})} \right) \\ &\quad - \frac{e^2}{2} \left(\sum_\kappa Z_\kappa \right)^2 \frac{\pi}{\eta^2\Omega} - \frac{e^2}{2} \sum_\kappa Z_\kappa^2 \frac{2\eta}{\sqrt{\pi}}, \end{aligned} \tag{C.8}$$

where the prime on the sum over **R** indicates that the divergent terms with $\mathbf{R} = 0$ for $\kappa = \kappa'$ are excluded. The last term arises from the omission of the self-interaction term included in the reciprocal space sum.[1] We remark that in practical calculations the Ewald parameter η is often chosen large enough to allow to neglect the real-space contribution.

[1] It can be calculated from Eqs. (C.1) and (C.5) if the term with $\mathbf{R} = 0$ is omitted for $\mathbf{r} = 0$.

C.2 Dipole-dipole force constants

The dipole-dipole contribution to the dynamical matrix at arbitrary wavevector $\widetilde{C}^{\mathrm{DD}}(\mathbf{q})$ introduced in Sec. 2.3.2 can be obtained from the second derivatives with respect to the atomic displacements of the ionic interaction energy of Eq. (C.7), after replacing the bare nuclear charges eZ_κ with $eZ^*_\kappa/(\epsilon_\infty)^{1/2}$ [54, 56] (correspondingly, we call the expression $E^{\mathrm{d}}_{\mathrm{Ew}}$). As in deriving Eq. (C.8), the Ewald summation provides a useful technique in order to compute the final result.

Let us first consider an isotropic system with dielectric permittivity $\epsilon^{\infty}_{\alpha\beta} = \epsilon_\infty \delta_{\alpha\beta}$ and Born effective charges Z^*_κ. We only calculate explicitly the contribution coming from the sum over $\mathbf{G}$ vectors, as we assume that the contribution from the real-space sum can be neglected with a suitable choice of the Ewald parameter η. We also notice that the limiting contribution [the term proportional to $(\sum_\kappa Z_\kappa)^2/(\eta^2\Omega)$ in Eq. (C.8)] vanishes in this case, as it contains the Born effective charges which obey the sum rule $\sum_\kappa Z^*_\kappa = 0$. The contribution arising from the omission of the self-interaction term in reciprocal space, instead, does not vanish but it is eliminated after applying the acoustic sum rule to the dynamical matrix [see Eq. (C.13)]. The first and second derivatives of the effective ionic energy with respect to an atomic displacement then read:

$$\frac{\partial E^{\mathrm{d}}_{\mathrm{Ew}}}{\partial \tau_{\kappa\alpha}} = \frac{4\pi e^2}{\Omega\epsilon_\infty} Z^*_\kappa \sum_{\kappa'} Z^*_{\kappa'} \sum_{\mathbf{G}\neq 0} i \frac{G_\alpha}{G^2} e^{-\frac{G^2}{4\eta^2}} e^{i\mathbf{G}\cdot(\tau^0_\kappa - \tau^0_{\kappa'})}; \tag{C.9}$$

$$\frac{\partial^2 E^{\mathrm{d}}_{\mathrm{Ew}}}{\partial \tau_{\kappa\alpha}\partial \tau_{\kappa'\beta}} = \frac{4\pi e^2}{\Omega} \frac{Z^*_\kappa Z^*_{\kappa'}}{\epsilon_\infty} \sum_{\mathbf{G}\neq 0} \frac{G_\alpha G_\beta}{G^2} e^{-\frac{G^2}{4\eta^2}} e^{i\mathbf{G}\cdot(\tau^0_\kappa - \tau^0_{\kappa'})}. \tag{C.10}$$

From Eq. (C.10) the dipole contribution to the dynamical matrix $\widetilde{C}^{\mathrm{DD}}(\mathbf{q})$ is obtained as:

$$\widetilde{C}^{\mathrm{DD}}_{\kappa\alpha,\kappa'\beta}(\mathbf{q}) = \frac{1}{N_{\mathrm{c}}} \sum_{\mathbf{R}} \frac{\partial^2 E^{\mathrm{d}}_{\mathrm{Ew}}}{\partial \tau_{\kappa\alpha}\partial \tau_{\kappa'\beta}} e^{i\mathbf{q}\cdot\mathbf{R}} \tag{C.11}$$

$$\begin{aligned} &= \frac{4\pi e^2}{\Omega} \frac{Z^*_\kappa Z^*_{\kappa'}}{\epsilon^\infty} \sum_{\mathbf{G},\,\mathbf{q}+\mathbf{G}\neq 0} \frac{(\mathbf{q}+\mathbf{G})_\alpha (\mathbf{q}+\mathbf{G})_\beta}{|\mathbf{q}+\mathbf{G}|^2} e^{-|\mathbf{q}+\mathbf{G}|^2/4\eta^2} e^{i(\mathbf{q}+\mathbf{G})\cdot(\tau^0_\kappa - \tau^0_{\kappa'})} \\ &\quad - \delta_{\kappa\kappa'} \sum_{\kappa''} \frac{4\pi e^2}{\Omega} \frac{Z_\kappa Z_{\kappa''}}{\epsilon^\infty} \sum_{\mathbf{G}\neq 0} \frac{G_\alpha G_\beta}{G^2} e^{-G^2/4\eta^2} e^{i\mathbf{G}\cdot(\tau^0_\kappa - \tau^0_{\kappa''})}, \end{aligned} \tag{C.12}$$

where we used the first identity in Eq. (B.6) and we imposed the acoustic sum rule:

$$\widetilde{C}^{\mathrm{DD}}_{\kappa\alpha,\kappa'\beta}(\mathbf{q}) = \widetilde{C}^{\mathrm{'DD}}_{\kappa\alpha,\kappa'\beta}(\mathbf{q}) - \delta_{\kappa\kappa'} \sum_{\kappa''} \widetilde{C}^{\mathrm{'DD}}_{\kappa\alpha,\kappa''\beta}(\mathbf{q}) \,. \tag{C.13}$$

The result in Eq. (C.12) is easily generalized to materials with anisotropic dielectric permittivity and Born effective charge tensors (the Ewald exponential factor has been dropped by assuming large η):

$$\begin{aligned} \widetilde{C}^{\mathrm{DD}}_{\kappa\alpha,\kappa'\beta}(\mathbf{q}) = \frac{4\pi e^2}{\Omega} \sum_{\mathbf{G},\,\mathbf{q}+\mathbf{G}\neq 0} \frac{\sum_\gamma (\mathbf{q}+\mathbf{G})_\gamma Z^{*\kappa}_{\gamma\alpha} \sum_{\gamma'} (\mathbf{q}+\mathbf{G})_{\gamma'} Z^{*\kappa'}_{\gamma'\beta}}{\sum_{\gamma\gamma'} (\mathbf{q}+\mathbf{G})_\gamma \, \epsilon^{\infty}_{\gamma\gamma'} \, (\mathbf{q}+\mathbf{G})_{\gamma'}} \, e^{i(\mathbf{q}+\mathbf{G})\cdot(\boldsymbol{\tau}^0_\kappa - \boldsymbol{\tau}^0_{\kappa'})} \\ - \delta_{\kappa\kappa'} \sum_{\kappa''} \frac{4\pi e^2}{\Omega} \sum_{\mathbf{G}\neq 0} \frac{\sum_\gamma G_\gamma Z^{*\kappa}_{\gamma\alpha} \sum_{\gamma'} G_{\gamma'} Z^{*\kappa''}_{\gamma'\beta}}{\sum_{\gamma\gamma'} G_\gamma \, \epsilon^{\infty}_{\gamma\gamma'} \, G_{\gamma'}} \, e^{i\mathbf{G}\cdot(\boldsymbol{\tau}^0_\kappa - \boldsymbol{\tau}^0_{\kappa''})} \,. \end{aligned} \tag{C.14}$$

The limit of small wavevector of $\widetilde{C}^{\mathrm{DD}}(\mathbf{q})$ corresponds to the nonanalytic contribution to the dynamical matrix presented in Eq. (2.46).

C.3 Long-range polar matrix element

In order to calculate the long-range contribution to the electron-phonon matrix element as in Chapter 4, we can equivalently start from the expression for the potential energy arising from the dipoles created by the atomic displacements at a generic point $\mathbf{r}$:

$$V^{\mathrm{D}}(\mathbf{r}) = -e^2 \sum_\kappa \frac{Z^*_\kappa}{\epsilon_\infty} \sum_{\mathbf{R}} \frac{1}{|\mathbf{r} - \boldsymbol{\tau}_\kappa - \mathbf{R}|} \,, \tag{C.15}$$

where again we substituted the bare nuclear charges eZ_κ with the Born effective charges, and the medium has a dielectric permittivity tensor $\epsilon^{\infty}_{\alpha\beta} = \epsilon_\infty \delta_{\alpha\beta}$. By exploiting the Ewald summation technique we can rewrite Eq. (C.15) as:

$$V^{\mathrm{D}}(\mathbf{r}) = -e^2 \sum_\kappa \frac{Z^*_\kappa}{\epsilon_\infty} \left(\sum_{\mathbf{R}} \frac{\mathrm{erfc}(\eta\,|\mathbf{r} - \boldsymbol{\tau}_\kappa - \mathbf{R}|)}{|\mathbf{r} - \boldsymbol{\tau}_\kappa - \mathbf{R}|} + \frac{4\pi}{\Omega} \sum_{\mathbf{G}\neq 0} \frac{1}{G^2} e^{-\frac{G^2}{4\eta^2}} e^{i\mathbf{G}\cdot(\mathbf{r} - \boldsymbol{\tau}_\kappa)} \right) + \sum_\kappa \frac{e^2 Z^*_\kappa}{\epsilon_\infty} \frac{\pi}{\eta^2 \Omega} \,, \tag{C.16}$$

where there is no term arising from the omission of the self-interaction, and the last term is the analytic limit for $\mathbf{G} \to 0$, which vanishes because of the sum rule obeyed by the

Born effective charges. The variation of $V^{\mathrm{D}}(\mathbf{r})$ with respect to the displacement of ion κ in the unit cell $\mathbf{R}$ is:

$$\partial_{\kappa\alpha,\mathbf{R}} V^{\mathrm{D}}(\mathbf{r}) = \frac{e^2 Z^*_\kappa}{\epsilon_\infty} \sum_{\mathbf{R}} \frac{(\mathbf{r}-\boldsymbol{\tau}^0_\kappa-\mathbf{R})_\alpha \left[\eta\,\mathrm{erfc}'(\eta|\mathbf{r}-\boldsymbol{\tau}^0_\kappa-\mathbf{R}|) - \mathrm{erfc}(\eta|\mathbf{r}-\boldsymbol{\tau}^0_\kappa-\mathbf{R}|)/|\mathbf{r}-\boldsymbol{\tau}^0_\kappa-\mathbf{R}|\right]}{|\mathbf{r}-\boldsymbol{\tau}^0_\kappa-\mathbf{R}|^2} + i\,\frac{4\pi e^2}{\Omega}\frac{Z^*_\kappa}{\epsilon_\infty}\sum_{\mathbf{G}\neq 0}\frac{G_\alpha}{G^2}\,e^{-G^2/4\eta^2}e^{i\mathbf{G}\cdot(\mathbf{r}-\boldsymbol{\tau}^0_\kappa)}, \tag{C.17}$$

with $\mathrm{erfc}'(x) = -2/\sqrt{\pi}\,e^{-x^2}$. We can choose again η large enough to retain only the $\mathbf{G}$ vectors sum. The variation of the potential with respect to a phonon with branch ν and wavevector $\mathbf{q}$ is then:

$$\begin{aligned}\partial_{\mathbf{q}\nu} V^{\mathrm{D}}(\mathbf{r}) &= \frac{1}{N_{\mathrm{c}}}\sum_{\kappa\alpha,\mathbf{R}} \Delta\tau^{\mathbf{q}\nu}_{\kappa\alpha}(\mathbf{R})\,\partial_{\kappa\alpha,\mathbf{R}} V^{\mathrm{D}}(\mathbf{r}) \\ &= i\,\frac{4\pi e^2}{\Omega}\sum_{\kappa\alpha}\left(\frac{\hbar}{2N_{\mathrm{c}}M_\kappa\omega_{\mathbf{q}\nu}}\right)^{1/2}\frac{Z^*_\kappa}{\epsilon_\infty}\sum_{\mathbf{G},\mathbf{q}+\mathbf{G}\neq 0}\frac{(\mathbf{q}+\mathbf{G})_\alpha}{|\mathbf{q}+\mathbf{G}|^2}\,e_{\kappa\alpha\nu}(\mathbf{q})\,e^{i(\mathbf{q}+\mathbf{G})\cdot(\mathbf{r}-\boldsymbol{\tau}^0_\kappa)},\end{aligned} \tag{C.18}$$

where we inserted the expression in Eq. (3.4) for the displacement of each atom in the vibrational eigenmode $(\mathbf{q},\nu)$, $\Delta\tau^{\mathbf{q}\nu}_{\kappa\alpha}(\mathbf{R})$. The long-range contribution to the electron-phonon matrix element $g^{\mathcal{L}}_{mn\nu}(\mathbf{k},\mathbf{q})$ finally is the braket of Eq. (C.18) between the initial and final Bloch states. The final expression, generalized to anisotropic systems, is identical to the result in Eq. (4.5):

$$\begin{aligned}g^{\mathcal{L}}_{mn\nu}(\mathbf{k},\mathbf{q}) = i\,\frac{4\pi e^2}{\Omega}\sum_{\kappa}\left(\frac{\hbar}{2M_\kappa\omega_{\mathbf{q}\nu}}\right)^{1/2} \\ \times\sum_{\mathbf{G},\mathbf{q}+\mathbf{G}\neq 0}\frac{(\mathbf{q}+\mathbf{G})\cdot\mathbf{Z}^*_\kappa\cdot\mathbf{e}_{\kappa\nu}(\mathbf{q})}{(\mathbf{q}+\mathbf{G})\cdot\boldsymbol{\epsilon}_\infty\cdot(\mathbf{q}+\mathbf{G})}\,\langle\psi_{m\mathbf{k}+\mathbf{q}}|\,e^{i(\mathbf{q}+\mathbf{G})\cdot(\mathbf{r}-\boldsymbol{\tau}^0_\kappa)}\,|\psi_{n\mathbf{k}}\rangle\,,\end{aligned} \tag{C.19}$$

where we used the compact notation $\mathbf{a}\cdot\mathbf{B}\cdot\mathbf{c} = \sum_{\alpha\beta} a_\alpha B_{\alpha\beta} c_\beta$, and we left the factor $1/\sqrt{N_{\mathrm{c}}}$ out to be consistent with Eqs. (3.12)–(3.15).

APPENDIX D

Electron Green's function

The single-particle Green's function for a system of N interacting electrons with ground state $\Psi_0(N)$ at zero temperature is defined as:

$$\begin{aligned} G(\mathbf{r}t,\mathbf{r}'t') &= -i/\hbar \left\langle \Psi_0(N)\right| \mathcal{T}\left[\hat{\psi}(\mathbf{r},t)\hat{\psi}^\dagger(\mathbf{r}',t')\right] \left|\Psi_0(N)\right\rangle \\ &= \begin{cases} -i/\hbar \left\langle \Psi_0(N)\right| \hat{\psi}(\mathbf{r},t)\hat{\psi}^\dagger(\mathbf{r}',t') \left|\Psi_0(N)\right\rangle & t > t'\,; \\ i/\hbar \left\langle \Psi_0(N)\right| \hat{\psi}^\dagger(\mathbf{r}',t')\hat{\psi}(\mathbf{r},t) \left|\Psi_0(N)\right\rangle & t < t'\,, \end{cases} \end{aligned} \tag{D.1}$$

where $\mathcal{T}$ is the time-ordering operator and $\hat{\psi}(\mathbf{r},t)$, $\hat{\psi}^\dagger(\mathbf{r}',t')$ are the time-dependent field operators in the Heisenberg picture defined in Eq. (A.14). $G(\mathbf{r}t,\mathbf{r}'t')$ contains all the fundamental information about many properties of the electronic system, namely the expectation value of all single-particle operators, the ground-state energy and the quasiparticle excitation spectrum [238]. In particular, the electronic ground-state density corresponds to $\langle \hat{n}_\mathrm{e}\rangle = -i\hbar\, G(\mathbf{r}t,\mathbf{r}t^+)$, with $t^+ = t+\delta$ (δ is a positive infinitesimal) and the braket a short notation for the expectation value on the ground state.

If we insert in Eq. (D.1) complete sets of $(N+1)$ and $(N-1)$-particle states and use Eq. (A.14), we obtain the expression:

$$G(\mathbf{r}t,\mathbf{r}'t') = -i/\hbar \sum_i \Big[\theta(t-t')\theta(E_i-E_\mathrm{F}) - \theta(t'-t)\theta(E_\mathrm{F}-E_i)\Big] f_i(\mathbf{r}) f_i^*(\mathbf{r}') e^{-iE_i/\hbar(t-t')}\,, \tag{D.2}$$

where the so-called Lehmann's or quasiparticle amplitudes $f_i(\mathbf{r})$ are defined as follows:

$$f_i(\mathbf{r}) = \begin{cases} \langle \Psi_0(N)| \hat{\psi}(\mathbf{r}) |\Psi_i(N+1)\rangle & E_i > E_\mathrm{F}\,; \\ \langle \Psi_i(N-1)| \hat{\psi}(\mathbf{r}) |\Psi_0(N)\rangle & E_i < E_\mathrm{F}\,, \end{cases} \tag{D.3}$$

and the one-particle excitation energies E_i are:

$$E_i = \begin{cases} E^{N+1,i} - E^{N,0} & E_i > E_\mathrm{F}\,; \\ E^{N,0} - E^{N-1,i} & E_i < E_\mathrm{F}\,. \end{cases} \tag{D.4}$$

The Fourier transform of Eq. (D.2) gives the *Lehmann's representation* for the Green's function:

$$G(\mathbf{r}, \mathbf{r}', \omega) = \sum_i \frac{f_i(\mathbf{r}) f_i^*(\mathbf{r}')}{\hbar\omega - E_i + i\eta\,\mathrm{sgn}(E_i - E_\mathrm{F})}\,, \tag{D.5}$$

where η is a small positive quantity introduced to perform the Fourier transform. From Eqs. (D.4) and (D.5) it is clear that the quasiparticle excitation energies correspond to the poles of $G(\omega)$. Moreover, they are exactly the electron addition/removal energies, i.e. they coincide with the electron energies measured in photoemission experiments.

APPENDIX E

Cumulant expansion

Here we present briefly the expressions used in the implementation of the cumulant expansion method [184]. The formalism is based on the convenient formulation of Ref. [33], here extended to the case of multiple bosonic satellites. Following Ref. [33], we rewrite the spectral function as:

$$A(\mathbf{k},\omega) = \sum_n \left[A_n^{\mathrm{QP}}(\mathbf{k},\omega) + A_n^{\mathrm{QP}}(\mathbf{k},\omega) * A_n^{\mathrm{S1}}(\mathbf{k},\omega) + A_n^{\mathrm{QP}}(\mathbf{k},\omega) * A_n^{\mathrm{S2}}(\mathbf{k},\omega) + \cdots \right], \quad \text{(E.1)}$$

where $*$ denotes a convolution, and $A_n^{\mathrm{QP}}(\mathbf{k},\omega)$ is the quasiparticle contribution:

$$A_n^{\mathrm{QP}}(\mathbf{k},\omega) = \frac{2}{\pi} Z_{n\mathbf{k}} \frac{|\mathrm{Im}\Sigma_{n\mathbf{k}}(\varepsilon_{n\mathbf{k}})|}{[\hbar\omega - \varepsilon_{n\mathbf{k}} - \mathrm{Re}\Sigma_{n\mathbf{k}}(\varepsilon_{n\mathbf{k}})]^2 + [\mathrm{Im}\Sigma_{n\mathbf{k}}(\varepsilon_{n\mathbf{k}})]^2}\,. \quad \text{(E.2)}$$

The satellite contributions are calculated in terms of a new cumulant function C^{S} derived from Eq. (7.7) after separating the 'quasiparticle' and 'satellite' components. For the one-phonon and two-phonon processes they are:

$$A_n^{\mathrm{S1}}(\mathbf{k},\omega) = \int_{-\infty}^{\infty} dt\, e^{i\omega t} C_{n\mathbf{k}}^{\mathrm{S}}(t), \quad \text{(E.3)}$$

$$A_n^{\mathrm{S2}}(\mathbf{k},\omega) = \int_{-\infty}^{\infty} dt\, e^{i\omega t} \frac{1}{2} C_{n\mathbf{k}}^{\mathrm{S}}(t) C_{n\mathbf{k}}^{\mathrm{S}}(t)\,, \quad \text{(E.4)}$$

with:

$$C^{\mathrm{S}}_{n\mathbf{k}}(t) = \frac{1}{\pi\hbar}\int_{-\infty}^{\infty} d\omega\, \frac{\mathrm{Im}\,\Sigma_{n\mathbf{k}}(\varepsilon_{n\mathbf{k}}/\hbar-\omega)}{(\omega-i\eta)^2}\, e^{(i\omega+\eta)t}\,\theta(\hbar\omega-\varepsilon_{n\mathbf{k}})\,. \tag{E.5}$$

By inserting Eq. (E.5) in Eq. (E.3), A^{S1}_n can be obtained analytically:

$$A^{\mathrm{S1}}_n(\mathbf{k},\omega) = \frac{\beta_{n\mathbf{k}}(\omega)-\beta_{n\mathbf{k}}(\varepsilon_{n\mathbf{k}}/\hbar)-(\hbar\omega-\varepsilon_{n\mathbf{k}})\left.\frac{\partial\beta_{n\mathbf{k}}}{\partial\omega}\right|_{\varepsilon_{n\mathbf{k}}/\hbar}}{(\hbar\omega-\varepsilon_{n\mathbf{k}})^2}\,, \tag{E.6}$$

with:

$$\beta_{n\mathbf{k}}(\omega) = \frac{1}{\pi}\mathrm{Im}\Sigma_{n\mathbf{k}}(\omega)\,\theta(-\omega)\,. \tag{E.7}$$

After noting that $A^{\mathrm{S1}}_n(\mathbf{k},\omega)$ is the Fourier transform of $C_{n\mathbf{k}}(t)$, the two-phonon contribution $A^{\mathrm{S2}}_n(\mathbf{k},\omega)$ can be rewritten using the convolution theorem, $A^{\mathrm{S2}}_n(\mathbf{k},\omega) = 1/2\; A^{\mathrm{S1}}_n(\mathbf{k},\omega) * A^{\mathrm{S1}}_n(\mathbf{k},\omega)$. The general expression for the case of many satellites can thus be cast into the form:

$$\begin{aligned} A(\mathbf{k},\omega) &= \sum_n \left[1 + A^{\mathrm{S1}}_n(\mathbf{k},\omega) * + \frac{1}{2}A^{\mathrm{S1}}_n(\mathbf{k},\omega) * A^{\mathrm{S1}}_n(\mathbf{k},\omega) * + \cdots\right] A^{\mathrm{QP}}_n(\mathbf{k},\omega) \\ &= \sum_n e^{A^{\mathrm{S1}}_n(\mathbf{k},\omega)*} A^{\mathrm{QP}}_n(\mathbf{k},\omega)\,. \end{aligned} \tag{E.8}$$

Eq. (E.8) is evaluated up to the two-phonon satellite term for the spectra presented in Chapter 7 and 8.

If a simplified model system with dispersionless electrons and an Einstein phonon ω_0 is considered, Eq. (E.8) reduces to the well-known Lang-Firsov series of polaron satellites [35, 240]. In fact, by setting $A^{\mathrm{QP}} = Z\,\delta(\omega)$ and $A^{\mathrm{S1}} = \lambda\delta(\omega-\omega_0)$, Eq. (E.8) gives $A(\omega) = Z\sum_{m=0}^{\infty}(\lambda^m/m!)\,\delta(\omega-m\omega_0)$. By requiring the normalization of the spectral function, that is $\int A(\omega)\,\mathrm{d}\omega = 1$, we obtain $Z = e^{-\lambda}$ and the Lang-Firsov expression is recovered.

Bibliography

[1] Landau, L. D. & Pekar, S. I. Effective mass of a polaron. *Zh. Eksp. Teor. Fiz.* **18**, 419 (1948).

[2] Fröhlich, H. Electrons in lattice fields. *Adv. Phys.* **3**, 325 (1954).

[3] Mitra, T. K., Chatterjee, A. & Mukhopadhyay, S. Polarons. *Phys. Rep.* **153**, 91 (1987).

[4] Mahan, G. D. *Many-Particle Physics* (Plenum, New York, 1981).

[5] Lee, T. D., Low, F. E. & Pines, D. The motion of slow electrons in a polar crystal. *Phys. Rev.* **90**, 297 (1953).

[6] Dunn, D. Electron–phonon interactions in an insulator. *Can. J. Phys.* **53**, 321 (1975).

[7] Feynman, R. P. Slow electrons in a polar crystal. *Phys. Rev.* **97**, 660 (1955).

[8] Devreese, J. T. & Alexandrov, A. S. Fröhlich polaron and bipolaron: recent developments. *Rep. Prog. Phys.* **72**, 066501 (2009).

[9] Landau, L. D. On the motion of electrons in a crystal lattice. *Phys. Z. Sowjet.* **3**, 664 (1933).

[10] Langreth, D. C. Polaron mobility at finite temperature. *Phys. Rev.* **159**, 717 (1967).

[11] Ziman, J. M. *Electrons and Phonons* (Oxford University Press, Oxford, 1960).

[12] Austin, I. G. & Mott, N. F. Polarons in crystalline and non-crystalline materials. *Adv. Phys.* **18**, 41 (1969).

[13] Damascelli, A., Hussain, Z. & Shen, Z.-X. Angle-resolved photoemission studies of the cuprate superconductors. *Rev. Mod. Phys.* **75**, 473 (2003).

[14] Ament, L. J. P., van Veenendaal, M., Devereaux, T. P., Hill, J. P. & van den Brink, J. Resonant inelastic X-ray scattering studies of elementary excitations. *Rev. Mod. Phys.* **83**, 705 (2011).

[15] Lanzara, A. *et al.* Evidence for ubiquitous strong electron-phonon coupling in high-temperature superconductors. *Nature* **412**, 510 (2001).

[16] Cuk, T. *et al.* A review of electron–phonon coupling seen in the high-T_c superconductors by angle-resolved photoemission studies (ARPES). *Phys. Stat. Sol. B* **242**, 11 (2005).

[17] Mannella, N. *et al.* Nodal quasiparticle in pseudogapped colossal magnetoresistive manganites. *Nature* **438**, 474 (2005).

[18] Bostwick, A., Ohta, T., Seyller, T., Horn, K. & Rotenberg, E. Quasiparticle dynamics in graphene. *Nat. Phys.* **3**, 36 (2007).

[19] Moser, S. *et al.* Electron-phonon coupling in the bulk of anatase TiO_2 measured by resonant inelastic X-ray spectroscopy. *Phys. Rev. Lett.* **115**, 096404 (2015).

[20] Moser, S. *et al.* Tunable polaronic conduction in anatase TiO_2. *Phys. Rev. Lett.* **110**, 196403 (2013).

[21] McKeown Walker, S., Bruno, F. Y. & Baumberger, F. ARPES studies of two-dimensional electron gases at transition metal oxide surfaces. In Cancellieri, C. & Strocov, V. N. (eds.) *Spectroscopy of Transition Metal Oxide Interfaces* (Springer, 2017). In press. Preprint at arxiv.org/abs/1612.03571.

[22] King, P. D. C. *et al.* Quasiparticle dynamics and spin-orbital texture of the $SrTiO_3$ two-dimensional electron gas. *Nat. Commun* **5**, 3414 (2014).

[23] Chen, C., Avila, J., Frantzeskakis, E., Levy, A. & Asensio, M. C. Observation of a two-dimensional liquid of Fröhlich polarons at the bare $SrTiO_3$ surface. *Nat. Commun.* **6**, 8585 (2015).

[24] Wang, Z. *et al.* Tailoring the nature and strength of electron-phonon interactions in the $SrTiO_3$(001) two-dimensional electron liquid. *Nat. Mater.* **15**, 835 (2016).

[25] Cancellieri, C. *et al.* Polaronic metal state at the $LaAlO_3/SrTiO_3$ interface. *Nat. Commun* **7**, 10386 (2016).

[26] Chang, Y. J., Bostwick, A., Kim, Y. S., Horn, K. & Rotenberg, E. Structure and correlation effects in semiconducting $SrTiO_3$. *Phys. Rev. B* **81**, 235109 (2010).

[27] Meevasana, W. *et al.* Strong energy-momentum dispersion of phonon-dressed carriers in the lightly doped band insulator $SrTiO_3$. *New J. Phys.* **12**, 023004 (2010).

[28] Yukawa, R. *et al.* Phonon-dressed two-dimensional carriers on the ZnO surface. *Phys. Rev. B* **94**, 165313 (2016).

[29] Rödel, T. C. *et al.* Engineering two-dimensional electron gases at the (001) and (101) surfaces of TiO_2 anatase using light. *Phys. Rev. B* **92**, 041106(R) (2015).

[30] Strocov, V. N. *et al.* High-resolution soft X-ray beamline ADRESS at the Swiss Light Source for resonant inelastic X-ray scattering and angle-resolved photoelectron spectroscopies. *J. Synchrotron Radiat.* **17**, 631 (2010).

[31] Hüfner, S. *Photoelectron Spectroscopy* (Springer, 2003), 3 edn.

[32] Bardyszewski, W. & Hedin, L. A new approach to the theory of photoemission from solids. *Phys. Scr.* **32**, 439 (1985).

[33] Aryasetiawan, F., Hedin, L. & Karlsson, K. Multiple plasmon satellites in Na and Al spectral functions from *ab initio* cumulant expansion. *Phys. Rev. Lett.* **77**, 2268 (1996).

[34] Hedin, L. & Lundqvist, S. Effects of electron-electron and electron-phonon interactions on the one-electron states of solids. In Seitz, F., Turnbull, D. & Ehrenreich, H. (eds.) *Solid State Physics*, vol. 23, 1–181 (Academic Press, New York, 1969).

[35] Langreth, D. C. Singularities in the X-ray spectra of metals. *Phys. Rev. B* **1**, 471 (1970).

[36] Born, M. & Oppenheimer, J. M. Zur quantentheorie der molekeln. *Ann. Physik* **84**, 457 (1927).

[37] Thomas, L. H. The calculation of atomic fields. *Proc. Cambridge Phyl. Soc.* **23**, 542 (1927).

[38] Fermi, E. Un metodo statistico per la determinazione di alcune proprietà dell'atomo. *Rend. Accad. Naz. Lincei* **6**, 602 (1927).

[39] Hohenberg, P. & Kohn, W. Inhomogeneous electron gas. *Phys. Rev.* **136**, B864 (1964).

[40] Kohn, W. & Sham, L. J. Self-consistent equations including exchange and correlation effects. *Phys. Rev.* **140**, A1133 (1965).

[41] Martin, R. M. *Electronic Structure: Basic Theory and Practical Methods* (Cambridge University Press, Cambridge, United Kingdom, 2004).

[42] Sham, L. J. & Schlüter, M. Density-functional theory of the energy gap. *Phys. Rev. Lett.* **51**, 1888 (1983).

[43] Perdew, J. P. & Levy, M. Physical content of the exact Kohn-Sham orbital energies: Band gaps and derivative discontinuities. *Phys. Rev. Lett.* **51**, 1884 (1983).

[44] Ceperley, D. M. & Alder, B. J. Ground state of the electron gas by a stochastic method. *Phys. Rev. Lett.* **45**, 566 (1980).

[45] Perdew, J. P. & Zunger, A. Self-interaction correction to density-functional approximations for many-electron systems. *Phys. Rev. B* **23**, 5048 (1981).

[46] Perdew, J. P., Burke, K. & Ernzerhof, M. Generalized gradient approximation made simple. *Phys. Rev. Lett.* **77**, 3865 (1996).

[47] Giannozzi, P. *et al.* QUANTUM ESPRESSO: a modular and open-source software project for quantum simulations of materials. *J. Phys. Condens. Matter* **21**, 395502 (2009).

[48] Giustino, F. *Materials Modelling using Density Functional Theory* (Oxford University Press, 2014).

[49] Fuchs, M. & Scheffler, M. *Ab initio* pseudopotentials for electronic structure calculations of poly-atomic systems using density-functional theory. *Comput. Phys. Commun.* **119**, 67 (1999).

[50] Hamann, D. R., Schlüter, M. & Chiang, C. Norm-conserving pseudopotentials. *Phys. Rev. Lett.* **43**, 1494 (1979).

[51] Baroni, S., de Gironcoli, S., Dal Corso, A. & Giannozzi, P. Phonons and related crystal properties from density-functional perturbation theory. *Rev. Mod. Phys.* **73**, 515 (2001).

[52] Baroni, S., Giannozzi, P. & Testa, A. Green's-function approach to linear response in solids. *Phys. Rev. Lett.* **58**, 1861 (1987).

[53] Sternheimer, R. M. Electronic polarizabilities of ions from the Hartree-Fock wave functions. *Phys. Rev.* **96**, 951 (1954).

[54] Giannozzi, P., de Gironcoli, S., Pavone, P. & Baroni, S. *Ab initio* calculation of phonon dispersions in semiconductors. *Phys. Rev. B* **43**, 7231 (1991).

[55] Maradudin, A. A. & Vosko, S. H. Symmetry properties of the normal vibrations of a crystal. *Rev. Mod. Phys.* **40**, 1 (1968).

[56] Gonze, X. & Lee, C. Dynamical matrices, Born effective charges, dielectric permittivity tensors, and interatomic force constants from density-functional perturbation theory. *Phys. Rev. B* **55**, 10355 (1997).

[57] Baroni, S. & Resta, R. *Ab initio* calculation of the macroscopic dielectric constant in silicon. *Phys. Rev. B* **33**, 7017 (1986).

[58] Resta, R. Macroscopic polarization in crystalline dielectrics: the geometric phase approach. *Rev. Mod. Phys.* **66**, 899 (1994).

[59] Born, M. & Huang, K. *Dynamical Theory of Crystal Lattices* (Oxford University Press, Oxford, 1954).

[60] Ghosez, P., Michenaud, J.-P. & Gonze, X. Dynamical atomic charges: The case of ABO_3 compounds. *Phys. Rev. B* **58**, 6224 (1998).

[61] Cochran, W. & Cowley, R. A. Dielectric constants and lattice vibrations. *J. Phys. Chem. Solids* **23**, 447 (1962).

[62] Sham, L. J. Electronic contribution to lattice dynamics in insulating crystals. *Phys. Rev.* **188**, 1431 (1969).

[63] Pick, R. M., Cohen, M. H. & Martin, R. M. Microscopic theory of force constants in the adiabatic approximation. *Phys. Rev. B* **1**, 910 (1970).

[64] Peierls, R. E. *Quantum Theory of Solids* (Oxford University Press, Oxford, 1955).

[65] Schrieffer, J. R. *Theory of Superconductivity* (Advanced Book Program, Perseus Books, London, 1983).

[66] Grimvall, G. *The Electron-Phonon Interaction in Metals* (North-Holland, New York, 1981).

[67] Fan, H. Y. Temperature dependence of the energy gap in semiconductors. *Phys. Rev.* **82**, 900 (1951).

[68] Allen, P. B. & Heine, V. Theory of the temperature dependence of electronic band structures. *J. Phys. C* **9**, 2305 (1976).

[69] Giustino, F., Louie, S. G. & Cohen, M. L. Electron-phonon renormalization of the direct band gap of diamond. *Phys. Rev. Lett.* **105**, 265501 (2010).

[70] Poncé, S. *et al.* Temperature dependence of the electronic structure of semiconductors and insulators. *J. Chem. Phys.* **143**, 102813 (2015).

[71] Zacharias, M. & Giustino, F. One-shot calculation of temperature-dependent optical spectra and phonon-induced band-gap renormalization. *Phys. Rev. B* **94**, 075125 (2016).

[72] Hedin, L. New method for calculating the one-particle Green's function with application to the electron-gas problem. *Phys. Rev.* **139**, A796 (1965).

[73] Giustino, F. Electron-phonon interactions from first principles. *Rev. Mod. Phys.* **89**, 015003 (2017).

[74] Marini, A., Poncé, S. & Gonze, X. Many-body perturbation theory approach to the electron-phonon interaction with density-functional theory as a starting point. *Phys. Rev. B* **91**, 224310 (2015).

[75] Migdal, A. B. Interaction between electrons and lattice vibrations in a normal metal. *Sov. Phys. JETP* **34**, 996 (1958).

[76] Bechstedt, F., Seino, K., Hahn, P. H. & Schmidt, W. G. Quasiparticle bands and optical spectra of highly ionic crystals: AlN and NaCl. *Phys. Rev. B* **72**, 245114 (2005).

[77] Botti, S. & Marques, M. A. L. Strong renormalization of the electronic band gap due to lattice polarization in the *GW* formalism. *Phys. Rev. Lett.* **110**, 226404 (2013).

[78] Engelsberg, S. & Schrieffer, J. R. Coupled electron-phonon system. *Phys. Rev.* **131**, 993 (1963).

[79] Eiguren, A., Ambrosch-Draxl, C. & Echenique, P. M. Self-consistently renormalized quasiparticles under the electron-phonon interaction. *Phys. Rev. B* **79**, 245103 (2009).

[80] Marzari, N., Mostofi, A. A., Yates, J. R., Souza, I. & Vanderbilt, D. Maximally localized Wannier functions: Theory and applications. *Rev. Mod. Phys.* **84**, 1419 (2012).

[81] Marzari, N. & Vanderbilt, D. Maximally localized generalized Wannier functions for composite energy bands. *Phys. Rev. B* **56**, 12847 (1997).

[82] Souza, I., Marzari, N. & Vanderbilt, D. Maximally localized Wannier functions for entangled energy bands. *Phys. Rev. B* **65**, 035109 (2001).

[83] Mostofi, A. A. *et al.* wannier90: A tool for obtaining maximally-localised Wannier functions. *Comput. Phys. Commun.* **178**, 685 (2008).

[84] Yates, J. R., Wang, X., Vanderbilt, D. & Souza, I. Spectral and Fermi surface properties from Wannier interpolation. *Phys. Rev. B* **75**, 195121 (2007).

[85] Giustino, F., Cohen, M. L. & Louie, S. G. Electron-phonon interaction using Wannier functions. *Phys. Rev. B* **76**, 165108 (2007).

[86] Noffsinger, J. *et al.* EPW: A program for calculating the electron-phonon coupling using maximally localized Wannier functions. *Comput. Phys. Commun.* **181**, 2140 (2010).

[87] Poncé, S., Margine, R., Verdi, C. & Giustino, F. EPW: Electron-phonon coupling, transport and superconducting properties using maximally localized Wannier functions. *Comput. Phys. Commun.* **209**, 116 (2016).

[88] Park, C.-H., Giustino, F., Cohen, M. L. & Louie, S. G. Velocity renormalization and carrier lifetime in graphene from the electron-phonon interaction. *Phys. Rev. Lett.* **99**, 086804 (2007).

[89] Park, C.-H., Giustino, F., Spataru, C. D., Cohen, M. L. & Louie, S. G. First-principles study of electron linewidths in graphene. *Phys. Rev. Lett.* **102**, 076803 (2009).

[90] Bernardi, M., Vigil-Fowler, D., Lischner, J., Neaton, J. B. & Louie, S. G. *Ab initio* study of hot carriers in the first picosecond after sunlight absorption in silicon. *Phys. Rev. Lett.* **112**, 257402 (2014).

[91] Mustafa, J. I., Bernardi, M., Neaton, J. B. & Louie, S. G. *Ab initio* electronic relaxation times and transport in noble metals. *Phys. Rev. B* **94**, 155105 (2016).

[92] Giustino, F., Yates, J. R., Souza, I., Cohen, M. L. & Louie, S. G. Electron-phonon interaction via electronic and lattice Wannier functions: Superconductivity in boron-doped diamond reexamined. *Phys. Rev. Lett.* **98**, 047005 (2007).

[93] Liao, B. *et al.* Significant reduction of lattice thermal conductivity by the electron-phonon interaction in silicon with high carrier concentrations: A first-principles study. *Phys. Rev. Lett.* **114**, 115901 (2015).

[94] Noffsinger, J., Kioupakis, E., Van de Walle, C. G., Louie, S. G. & Cohen, M. L. Phonon-assisted optical absorption in silicon from first principles. *Phys. Rev. Lett.* **108**, 167402 (2012).

[95] Giustino, F., Cohen, M. L. & Louie, S. G. Small phonon contribution to the photoemission kink in the copper oxide superconductors. *Nature* **452**, 975 (2008).

[96] Park, C.-H., Giustino, F., Spataru, C. D., Cohen, M. L. & Louie, S. G. Angle-resolved photoemission spectra of graphene from first-principles calculations. *Nano Lett.* **9**, 4234 (2009).

[97] Margine, E. R. & Giustino, F. Anisotropic Migdal-Eliashberg theory using Wannier functions. *Phys. Rev. B* **87**, 024505 (2013).

[98] Margine, E. R. & Giustino, F. Two-gap superconductivity in heavily *n*-doped graphene: *Ab initio* Migdal-Eliashberg theory. *Phys. Rev. B* **90**, 014518 (2014).

[99] Zhang, X.-L. & Liu, W.-M. Electron-phonon coupling and its implication for the superconducting topological insulators. *Sci. Rep.* **5**, 8964 (2015).

[100] Park, C.-H. *et al.* Electron-phonon interactions and the intrinsic electrical resistivity of graphene. *Nano Lett.* **14**, 1113 (2014).

[101] Fiorentini, M. & Bonini, N. Thermoelectric coefficients of *n*-doped silicon from first principles via the solution of the Boltzmann transport equation. *Phys. Rev. B* **94**, 085204 (2016).

[102] Verdi, C. & Giustino, F. Fröhlich electron-phonon vertex from first principles. *Phys. Rev. Lett.* **115**, 176401 (2015).

[103] Sjakste, J., Vast, N., Calandra, M. & Mauri, F. Wannier interpolation of the electron-phonon matrix elements in polar semiconductors: Polar-optical coupling in GaAs. *Phys. Rev. B* **92**, 054307 (2015).

[104] Jhalani, V. A., Zhou, J.-J. & Bernardi, M. Ultrafast hot carrier dynamics in GaN and its impact on the efficiency droop. *Nano Lett.* **17**, 5012 (2017).

[105] Zhou, J.-J. & Bernardi, M. *Ab initio* electron mobility and polar phonon scattering in GaAs. *Phys. Rev. B* **94**, 201201(R) (2016).

[106] Liu, T.-H., Zhou, J., Liao, B., Singh, D. J. & Chen, G. First-principles mode-by-mode analysis for electron-phonon scattering channels and mean free path spectra in GaAs. *Phys. Rev. B* **95**, 075206 (2017).

[107] Fujishima, A. & Honda, K. Electrochemical photolysis of water at a semiconductor electrode. *Nature (London)* **238**, 37 (1972).

[108] Pimputkar, S., Speck, J. S., DenBaars, S. P. & Nakamura, S. Prospects for LED lighting. *Nat. Photon.* **3**, 180 (2009).

[109] Green, M. A., Ho-Baillie, A. & Snaith, H. The emergence of perovskite solar cells. *Nat. Photon.* **8**, 506 (2014).

[110] Antonius, G. *et al.* Dynamical and anharmonic effects on the electron-phonon coupling and the zero-point renormalization of the electronic structure. *Phys. Rev. B* **92**, 085137 (2015).

[111] Vogl, P. Microscopic theory of electron-phonon interaction in insulators or semiconductors. *Phys. Rev. B* **13**, 694 (1976).

[112] Landau, L. D. & Lifshits, E. M. *Electrodynamics of Continuous Media* (Pergamon, Oxford, 1960).

[113] Dolgov, O. V. & Maksimov, E. G. The dielectric function of crystalline systems. In Keldysh, L. V., Kirzhnitz, D. A. & Maradudin, A. A. (eds.) *The Dielectric Function of Condensed Systems* (Elsevier Science Publishers, 1989).

[114] Antoncík, E. & Landsberg, P. T. Overlap integrals for Bloch electrons. *Proc. Phys. Soc.* **82**, 337 (1963).

[115] Okumura, H. A roadmap for future wide bandgap semiconductor power electronics. *MRS Bull.* **40**, 439 (2015).

[116] Stampfl, C. & Van de Walle, C. G. Density-functional calculations for III-V nitrides using the local-density approximation and the generalized gradient approximation. *Phys. Rev. B* **59**, 5521 (1999).

[117] Maruska, H. P. & Tietjen, J. J. The preparation and properties of vapor-deposited single-crystalline GaN. *Appl. Phys. Lett.* **15**, 327 (1969).

[118] Schlipf, M. & Gygi, F. Optimization algorithm for the generation of ONCV pseudopotentials. *Comput. Phys. Commun.* **196**, 36 (2015).

[119] Magnuson, M., Mattesini, M., Höglund, C., Birch, J. & Hultman, L. Electronic structure of GaN and Ga investigated by soft X-ray spectroscopy and first-principles methods. *Phys. Rev. B* **81**, 085125 (2010).

[120] Karch, K., Wagner, J.-M. & Bechstedt, F. *Ab initio* study of structural, dielectric, and dynamical properties of GaN. *Phys. Rev. B* **57**, 7043 (1998).

[121] Ruf, T. *et al.* Phonon dispersion curves in wurtzite-structure GaN determined by inelastic X-ray scattering. *Phys. Rev. Lett.* **86**, 906–909 (2001).

[122] Barker, A. S. & Ilegems, M. Infrared lattice vibrations and free-electron dispersion in GaN. *Phys. Rev. B* **7**, 743 (1973).

[123] Del Sole, R. & Girlanda, R. Optical properties of semiconductors within the independent-quasiparticle approximation. *Phys. Rev. B* **48**, 11789 (1993).

[124] Rinke, P. *et al.* Consistent set of band parameters for the group-III nitrides AlN, GaN, and InN. *Phys. Rev. B* **77**, 075202 (2008).

[125] Kioupakis, E., Rinke, P., Schleife, A., Bechstedt, F. & Van de Walle, C. G. Free-carrier absorption in nitrides from first principles. *Phys. Rev. B* **81**, 241201(R) (2010).

[126] Nery, J. & Allen, P. B. Influence of Fröhlich polaron coupling on renormalized electron bands in polar semiconductors. Results for zinc-blende GaN. *Phys. Rev. B* **94**, 115135 (2016).

[127] Meevasana, W. *et al.* Creation and control of a two-dimensional electron liquid at the bare $SrTiO_3$ surface. *Nat. Mater.* **10**, 114 (2011).

[128] Ohtomo, A. & Hwang, H. A high-mobility electron gas at the $LaAlO_3/SrTiO_3$ heterointerface. *Nature* **427**, 423 (2004).

[129] Frantzeskakis, E., Rödel, T. C., Fortuna, F. & Santander-Syro, A. F. 2D surprises at the surface of 3D materials: Confined electron systems in transition metal oxides. *J. Electron Spectrosc. Relat. Phenom.* (2016). dx.doi.org/10.1016/j.elspec.2016.10.001.

[130] Sai, N. & Vanderbilt, D. First-principles study of ferroelectric and antiferrodistortive instabilities in tetragonal $SrTiO_3$. *Phys. Rev. B* **62**, 13942 (2000).

[131] Cao, L., Sozontov, E. & Zegenhagen, J. Cubic to tetragonal phase transition of $SrTiO_3$ under epitaxial stress: An X-ray backscattering study. *Phys. Stat. Sol. A* **181**, 387 (2000).

[132] van Benthem, K., Elsässer, C. & French, R. H. Bulk electronic structure of $SrTiO_3$: Experiment and theory. *J. Appl. Phys.* **90**, 6156 (2001).

[133] Himmetoglu, B., Janotti, A., Peelaers, H., Alskauskas, A. & Van de Walle, C. G. First-principles study of the mobility of $SrTiO_3$. *Phys. Rev. B* **90**, 241204(R) (2014).

[134] Servoin, J. L., Luspin, Y. & Gervais, F. Infrared dispersion in $SrTiO_3$ at high temperature. *Phys. Rev. B* **22**, 5501 (1980).

[135] Wahl, R., Vogtenhuber, D. & Kresse, G. $SrTiO_3$ and $BaTiO_3$ revisited using the projector augmented wave method: Performance of hybrid and semilocal functionals. *Phys. Rev. B* **78**, 104116 (2008).

[136] Spitzer, W. G., Miller, R. C., Kleinman, D. A. & Howarth, L. E. Far infrared dielectric dispersion in $BaTiO_3$, $SrTiO_3$, and TiO_2. *Phys. Rev.* **126**, 1710 (1962).

[137] Devreese, J. T., Klimin, S. N., van Mechelen, J. L. M. & van der Marel, D. Many-body large polaron optical conductivity in $SrTi_{1-x}Nb_xO_3$. *Phys. Rev. B* **81**, 125119 (2010).

[138] Lee, M. M., Teuscher, J., Miyasaka, T., Myrakami, T. N. & Snaith, H. J. Efficient hybrid solar cells based on meso-superstructured organometal halide perovskites. *Science* **338**, 643 (2012).

[139] Green, M. A., Emery, K., Hishikawa, Y., Warta, W. & Dunlop, E. D. Solar cell efficiency tables (version 48). *Prog. Photovoltaics* **24**, 905 (2016).

[140] Giustino, F. & Snaith, H. Towards lead-free perovskite solar cells. *ACS Energy Lett.* **1**, 1233 (2016).

[141] Eperon, G. E. *et al.* Formamidinium lead trihalide: A broadly tunable perovskite for efficient planar heterojunction solar cells. *Energy Environ. Sci.* **7**, 982 (2014).

[142] Baikie, T. *et al.* Synthesis and crystal chemistry of the hybrid perovskite $CH_3NH_3PbI_3$ for solid-state sensitized solar applications. *J. Mater. Chem. A* **1**, 5628 (2013).

[143] Weller, M. T., Weber, O. J., Henry, P. F., Di Pumpo, A. M. & Hansen, H. C. Complete structure and cation orientation in the perovskite photovoltaic methylammonium lead iodide between 100 and 352 K. *Chem. Commun.* **51**, 4180 (2015).

[144] D'Innocenzo, V. *et al.* Excitons versus free charges in organo-lead tri-halide perovskites. *Nat. Commun.* **5**, 3586 (2014).

[145] Miyata, A. *et al.* Direct measurement of the exciton binding energy and effective masses for charge carriers in an organic-inorganic tri-halide perovskite. *Nat. Phys.* **11**, 582 (2015).

[146] Stranks, S. D. *et al.* Electron-hole diffusion lengths exceeding 1 micrometer in an organometal trihalide perovskite absorber. *Science* **342**, 341 (2013).

[147] Wehrenfennig, C., Eperon, G. E., Johnston, M. B., Snaith, H. J. & Herz, L. M. High charge carrier mobilities and lifetimes in organolead trihalide perovskites. *Adv. Mater.* **26**, 1584 (2014).

[148] Herz, L. M. Charge-carrier dynamics in organic-inorganic metal halide perovskites. *Annu. Rev. Phys. Chem.* **67**, 65 (2016).

[149] Milot, R. L., Eperon, G. E., Snaith, H. J., Johnston, M. B. & Herz, L. M. Temperature-dependent charge-carrier dynamics in $CH_3NH_3PbI_3$ perovskite thin films. *Adv. Funct. Mater.* **25**, 6218 (2015).

[150] Karakus, M. *et al.* Phonon-electron scattering limits free charge mobility in methylammonium lead iodide perovskites. *J. Phys. Chem. Lett.* **6**, 4991 (2015).

[151] Yu, P. Y. & Cardona, M. *Fundamental of Semiconductors* (Springer, 2010).

[152] Filip, M. R. & Giustino, F. *GW* quasiparticle band gap of the hybrid organic-inorganic perovskite $CH_3NH_3PbI_3$: Effect of spin-orbit interaction, semicore electrons, and self-consistency. *Phys. Rev. B* **90**, 245145 (2014).

[153] Filip, M. R., Verdi, C. & Giustino, F. *GW* band structures and carrier effective masses of $CH_3NH_3PbI_3$ and hypothetical perovskites of the type $APbI_3$: A = NH_4, PH_4, AsH_4, and SbH_4. *J. Phys. Chem. C* **119**, 25209 (2015).

[154] Marini, A., Hogan, C., Grüning, M. & Varsano, D. Yambo: An *ab initio* tool for excited state calculations. *Comput. Phys. Commun.* **180**, 1392 (2009).

[155] Filip, M. R., Eperon, G., Snaith, H. J. & Giustino, F. Steric engineering of metal-halide perovskites with tunable optical band gaps. *Nat. Commun.* **5**, 5757 (2014).

[156] Wright, A. D. *et al.* Electron–phonon coupling in hybrid lead halide perovskites. *Nat. Commun.* **7**, 11755 (2016).

[157] Dar, M. I. *et al.* Origin of unusual bandgap shift and dual emission in organic-inorganic lead halide perovskites. *Sci. Adv.* **2**, e1601156 (2016).

[158] Rudin, S., Reinecke, T. L. & Segall, B. Temperature-dependent exciton linewidths in semiconductors. *Phys. Rev. B* **42**, 11218 (1990).

[159] Pérez-Osorio, M. A. *et al.* Vibrational properties of the organic-inorganic halide perovskite $CH_3NH_3PbI_3$ from theory and experiment: Factor group analysis, first-principles calculations, and low-temperature infrared spectra. *J. Phys. Chem. C* **119**, 25703 (2015).

[160] Gopalan, S., Lautenschlager, P. & Cardona, M. Temperature dependence of the shifts and broadenings of the critical points in GaAs. *Phys. Rev. B* **35**, 5577 (1987).

[161] Phuong, L. Q., Nakaike, Y., Wakamiya, A. & Kanemitsu, Y. Free excitons and exciton-phonon coupling in $CH_3NH_3PbI_3$ single crystals revealed by photocurrent and photoluminescence measurements at low temperatures. *J. Phys. Chem. Lett.* **7**, 4905 (2016).

[162] Bokdam, M. *et al.* Role of polar phonons in the photo excited state of metal halide perovskites. *Sci. Rep.* **6**, 28618 (2016).

[163] Filippetti, A., Mattoni, A., Caddeo, C., Saba, M. I. & Delugas, P. Low electron-polar optical phonon scattering as a fundamental aspect of carrier mobility in methylammonium lead halide $CH_3NH_3PbI_3$ perovskites. *Phys. Chem. Chem. Phys.* **18**, 15352 (2016).

[164] Sendner, M. *et al.* Optical phonons in methylammonium lead halide perovskites and implications for charge transport. *Mater. Horiz.* **3**, 613 (2016).

[165] Zhu, X.-Y. & Podzorov, V. Charge carriers in hybrid organic-inorganic lead halide perovskites might be protected as large polarons. *J. Phys. Chem. Lett.* **6**, 4758 (2015).

[166] Grant, F. A. Properties of rutile (titanium dioxide). *Rev. Mod. Phys.* **31**, 646 (1959).

[167] Berger, H., Tang, H. & Lévy, F. Growth and raman spectroscopic characterization of TiO_2 anatase single crystals. *J. Cryst. Growth* **130**, 108 (1993).

[168] Fujishima, A., Rao, T. N. & Tryk, D. A. Titanium dioxide photocatalysis. *J. Photochem. Photobiol. C* **1**, 1 (2000).

[169] Hardin, B. E., Snaith, H. J. & McGehee, M. D. The renaissance of dye-sensitized solar cells. *Nat. Photon.* **6**, 162 (2012).

[170] Furubayashi, Y. *et al.* A transparent metal: Nb-doped anatase TiO_2. *Appl. Phys. Lett.* **86**, 252101 (2005).

[171] Horn, M., Schwerdtfeger, C. F. & Meagher, E. P. Refinement of the structure of anatase at several temperatures. *Z. Kristallogr.* **136**, 273 (1972).

[172] Emori, M., Sugita, M., Ozawa, K. & Sakama, H. Electronic structure of epitaxial anatase TiO_2 films: Angle-resolved photoelectron spectroscopy study. *Phys. Rev. B* **85**, 035129 (2012).

[173] Baldini, E. *et al.* Strongly bound excitons in anatase TiO_2 single crystals and nanoparticles. *Nat. Commun.* **8**, 13 (2017).

[174] Chiodo, L. *et al.* Self-energy and excitonic effects in the electronic and optical properties of TiO_2 crystalline phases. *Phys. Rev. B* **82**, 045207 (2010).

[175] Kang, W. & Hybertsen, M. S. Quasiparticle and optical properties of rutile and anatase TiO_2. *Phys. Rev. B* **82**, 085203 (2010).

[176] Patrick, C. E. & Giustino, F. *GW* quasiparticle bandgaps of anatase TiO_2 starting from DFT+U. *J. Phys.: Condens. Matter* **24**, 202201 (2012).

[177] Tang, H., Lévy, F., Berger, H. & Schmid, P. E. Urbach tail of anatase TiO_2. *Phys. Rev. B* **52**, 7771 (1995).

[178] Rohlfing, M. & Louie, S. G. Electron-hole excitations and optical spectra from first principles. *Phys. Rev. B* **62**, 4927 (2000).

[179] Ohsaka, T., Izumi, F. & Fujiki, Y. Raman spectrum of anatase, TiO_2. *J. Raman Spectrosc.* **7**, 321 (1978).

[180] Mikami, M., Nakamura, S., Kitao, O. & Arakawa, H. Lattice dynamics and dielectric properties of TiO_2 anatase: A first-principles study. *Phys. Rev. B* **66**, 155213 (2002).

[181] Dou, M. & Persson, C. Comparative study of rutile and anatase SnO_2 and TiO_2: Band-edge structures, dielectric functions, and polaron effects. *J. Appl. Phys.* **113**, 083703 (2013).

[182] Gonzalez, R. J., Zallen, R. & Berger, H. Infrared reflectivity and lattice fundamentals in anatase TiO_2. *Phys. Rev. B* **55**, 7014 (1997).

[183] Aurenhammer, F. Voronoi diagrams – a survey of a fundamental data structure. *ACM Comput. Surv.* **23**, 345 (1991).

[184] Verdi, C., Caruso, F. & Giustino, F. Origin of the crossover from polarons to Fermi liquids in transition metal oxides. *Nat. Commun.* **8**, 15769 (2017).

[185] Ellmer, K. Past achievements and future challenges in the development of optically transparent electrodes. *Nat. Photon.* **6**, 809 (2012).

[186] Jácimović, J. *et al.* Pressure dependence of the large-polaron transport in anatase TiO_2 single crystals. *Europhys. Lett.* **99**, 57005 (2012).

[187] Setvin, M. *et al.* Direct view at excess electrons in TiO_2 rutile and anatase. *Phys. Rev. Lett.* **113**, 086402 (2014).

[188] Mattioli, G., Filippone, F., Alippi, P. & Amore Bonapasta, A. *Ab initio* study of the electronic states induced by oxygen vacancies in rutile and anatase TiO_2. *Phys. Rev. B* **78**, 241201(R) (2008).

[189] Forro, L. *et al.* High mobility *n*-type charge carriers in large single crystals of anatase (TiO_2). *J. Appl. Phys.* **75**, 633 (1994).

[190] De Angelis, F., Di Valentin, C., Fantacci, S., Vittadini, A. & Selloni, A. Theoretical studies on anatase and less common TiO_2 phases: Bulk, surfaces, and nanomaterials. *Chem. Rev.* **114**, 9708 (2014).

[191] Mott, N. F. *Metal-insulator transitions* (Taylor&Francis, London, 1990).

[192] Varga, B. B. Coupling of plasmons to polar phonons in degenerate semiconductors. *Phys. Rev.* **137**, A1896 (1965).

[193] Mahan, G. D. In Devreese, J. D. (ed.) *Polarons in Ionic Crystals and Polar Semiconductors* (North-Holland, New York, 1972).

[194] Kittel, C. *Introduction to Solid State Physics* (Wiley, New York, 1976), 5 edn.

[195] Hedin, L. On correlation effects in electron spectroscopies and the *GW* approximation. *J. Phys.: Condens. Matter* **11**, R489 (1999).

[196] Onida, G., Reining, L. & Rubio, A. Electronic excitations: density-functional versus many-body Green's-function approaches. *Rev. Mod. Phys.* **74**, 601 (2002).

[197] Guzzo, M. *et al.* Valence electron photoemission spectrum of semiconductors: *Ab initio* description of multiple satellites. *Phys. Rev. Lett.* **107**, 166401 (2011).

[198] Lischner, J., Vigil-Fowler, D. & Louie, S. G. Physical origin of satellites in photoemission of doped graphene: An *ab initio GW* plus cumulant study. *Phys. Rev. Lett.* **110**, 146801 (2013).

[199] Caruso, F., Lambert, H. & Giustino, F. Band structure of plasmonic polarons. *Phys. Rev. Lett.* **114**, 146404 (2015).

[200] Story, S. M., Kas, J. J., Vila, F. D., Verstraete, M. J. & Rehr, J. J. Cumulant expansion for phonon contributions to the electron spectral function. *Phys. Rev. B* **90**, 195135 (2014).

[201] Hedin, L. Effects of recoil on shake-up spectra in metals. *Phys. Scr.* **21**, 477 (1980).

[202] Zhou, J. S. *et al.* Dynamical effects in electron spectroscopy. *J. Chem. Phys.* **143**, 184109 (2015).

[203] Gumhalter, B., Kovač, V., Caruso, F., Lambert, H. & Giustino, F. On the combined use of *GW* approximation and cumulant expansion in the calculations of quasiparticle spectra: The paradigm of Si valence bands. *Phys. Rev. B* **94**, 035103 (2016).

[204] Holm, B. & Aryasetiawan, F. Self-consistent cumulant expansion for the electron gas. *Phys. Rev. B* **56**, 12825 (1997).

[205] Kas, J. J., Rehr, J. J. & Curtis, J. B. Particle-hole cumulant approach for inelastic losses in X-ray spectra. *Phys. Rev. B* **94**, 035156 (2016).

[206] Zhukov, V. P. & Chulkov, E. V. *Ab initio* calculations of the electron-phonon interaction and characteristics of large polarons in rutile and anatase. *Phys. Solid State* **56**, 1302 (2014).

[207] Marsiglio, F. Pairing and charge-density-wave correlations in the Holstein model at half-filling. *Phys. Rev. B* **42**, 2416 (1990).

[208] Matthias, B. T., Bozorth, R. M. & Van Vleck, J. H. Ferromagnetic interaction in EuO. *Phys. Rev. Lett.* **7**, 160 (1961).

[209] Mauger, A. & Godart, C. The magnetic, optical, and transport properties of representatives of a class of magnetic semiconductors: the europium chalcogenides. *Phys. Rep.* **141**, 51 (1986).

[210] Santos, T. S. & Moodera, J. S. Observation of spin filtering with a ferromagnetic EuO tunnel barrier. *Phys. Rev. B* **69**, 241203 (2004).

[211] Ott, H. *et al.* Soft X-ray magnetic circular dichroism study on Gd-doped EuO thin films. *Phys. Rev. B* **73**, 094407 (2006).

[212] Shai, D. E. *et al.* Temperature dependence of the electronic structure and Fermi-surface reconstruction of $Eu_{1-x}Gd_xO$ through the ferromagnetic metal-insulator transition. *Phys. Rev. Lett.* **108**, 267003 (2012).

[213] Coloón Santana, J. A. *et al.* Effect of gadolinium doping on the electronic band structure of europium oxide. *Phys. Rev. B* **85**, 014406 (2012).

[214] Güntherodt, G. Optical properties and electronic structure of europium chalchogenides. *Phys. Cond. Matter* **18**, 37 (1974).

[215] Tsang, J. C., Dresselhaus, M. S., Aggarwal, R. L. & Reed, T. B. Inelastic light scattering in the europium chalcogenides. *Phys. Rev. B* **9**, 984 (1974).

[216] Grünberg, P., Güntherodt, G., Frey, A. & Kress, W. Raman scattering and phonon dispersion of europium monochalcogenides. *Physica B* **89**, 225 (1977).

[217] Pradip, R. *et al.* Lattice dynamics of EuO: Evidence for giant spin-phonon coupling. *Phys. Rev. Lett.* **116**, 185501 (2016).

[218] King, P. D. C. *et al.* Private communication and to be published.

[219] Blöchl, P. E. Projector augmented-wave method. *Phys. Rev. B* **50**, 17953 (1994).

[220] Kresse, G. & Joubert, D. From ultrasoft pseudopotentials to the projector augmented-wave method. *Phys. Rev. B* **59**, 1758 (1999).

[221] `http://www.vlab.msi.umn.edu/resources/repaw/index`.

[222] An, J. M., Barabash, S. V., Ozolins, V., van Schilfgaarde, M. & Belashchenko, K. D. First-principles study of phase stability of Gd-doped EuO and EuS. *Phys. Rev. B* **83**, 064105 (2011).

[223] Anisimov, V. I., Zaanen, J. & Andersen, O. K. Band theory and Mott insulators: Hubbard U instead of Stoner I. *Phys. Rev. B* **44**, 943 (1991).

[224] Liechtenstein, A. I., Anisimov, V. I. & Zaanen, J. Density-functional theory and strong interactions: Orbital ordering in Mott-Hubbard insulators. *Phys. Rev. B* **52**, R5467 (1995).

[225] Hubbard, J. Electron correlations in narrow energy bands. *Proc. R. Soc. Lond. A* **276**, 237 (1963).

[226] Cococcioni, M. & de Gironcoli, S. Linear response approach to the calculation of the effective interaction parameters in the LDA+U method. *Phys. Rev. B* **71**, 035105 (2005).

[227] Wan, X., Dong, J. & Savrasov, S. Y. Mechanism of magnetic exchange interactions in europium monochalcogenides. *Phys. Rev. B* **83**, 205201 (2011).

[228] Ingle, N. J. C. & Elfimov, I. S. Influence of epitaxial strain on the ferromagnetic semiconductor EuO: First-principles calculations. *Phys. Rev. B* **77**, 121202(R) (2008).

[229] Schlipf, M., Betzinger, M., Ležaić, M., Friedrich, C. & Blügel, S. Structural, electronic, and magnetic properties of the europium chalcogenides: A hybrid-functional DFT study. *Phys. Rev. B* **88**, 094433 (2013).

[230] Larson, P. & Lambrecht, W. R. L. Electronic structure and magnetism of europium chalcogenides in comparison with gadolinium nitride. *J. Phys.: Condens. Matter* **18**, 11333 (2006).

[231] Steeneken, P. G. *et al.* Exchange splitting and charge carrier spin polarization in EuO. *Phys. Rev. Lett.* **88**, 047201 (2002).

[232] Wang, Y., Shang, S., Liu, Z.-K. & Chen, L.-Q. Mixed-space approach for calculation of vibration-induced dipole-dipole interactions. *Phys. Rev. B* **85**, 224303 (2012).

[233] Caruso, F. & Giustino, F. Theory of electron-plasmon coupling in semiconductors. *Phys. Rev. B* **94**, 115208 (2016).

[234] Sohier, T., Calandra, M. & Mauri, F. Two-dimensional Fröhlich interaction in transition-metal dichalcogenide monolayers: Theoretical modeling and first-principles calculations. *Phys. Rev. B* **94**, 085415 (2016).

[235] Timrov, I., Vast, N., Gebauer, R. & Baroni, S. Electron energy loss and inelastic X-ray scattering cross sections from time-dependent density-functional perturbation theory. *Phys. Rev. B* **88**, 064301 (2013).

[236] Calandra, M., Profeta, G. & Mauri, F. Adiabatic and nonadiabatic phonon dispersion in a Wannier function approach. *Phys. Rev. B* **82**, 165111 (2010).

[237] Spreafico, C. & VandeVondele, J. The nature of excess electrons in anatase and rutile from hybrid DFT and RPA. *Phys. Chem. Chem. Phys.* **16**, 26144 (2014).

[238] Fetter, A. L. & Walecka, J. D. *Quantum Theory of Many-Particle Systems* (McGraw-Hill, New York, 1971).

[239] Marder, M. P. *Condensed Matter Physics* (Wiley, New York, 2010), 2 edn.

[240] Berciu, M. Green's function of a dressed particle. *Phys. Rev. Lett.* **97**, 036402 (2006).

Acknowledgements

My most sincere gratitude goes to Feliciano Giustino for being an incredible supervisor, who besides teaching me countless things, supporting my research and helping me progress during these years, has been a great mentor. His enthusiasm for many fields of research is contagious, and his knowledge and wisdom something to truly look at.

A huge thank you to all the people I had the privilege to collaborate with for sharing some exciting work and for contributing to my growth as a researcher. A special mention goes to Marios, my 'DPhil brother', and to everyone in the (MML) group, past and present, for sharing many lunches, housewarmings, coffees, beers (and tequilas): Marina, Samuel, George, Miguel-Angel, Fabio, Martin, Nourdine, Kun, Christoph, Tim, Natalie, Alex, Weng-Hong, Tim, Henry, Harry, Chris, Keian, Hannes – I shared these years with the best research group I could ask for!

During my time in Oxford I met some of my best friends, who contributed so much to making me enjoy my life here. A special thought goes to Lizzie, Lexie, Delphine and Ruby, and of course to Julian, who has been beside me for most of my DPhil journey.

I haven't forgotten all my friends from Italy – the old ones and slightly-less-old ones. It has been precious to be able to count on you and catch up with you whenever possible when travelling around.

I am so grateful to have a family who has always supported me in full with my decisions and activities, and that I can bother with my little or big troubles if I need to. I am lucky to have a big wise brother and two even wiser and caring parents to count on!

List of publications

1. C. Verdi, F. Caruso and F. Giustino. Origin of the crossover from polarons to Fermi liquids in transition metal oxides. *Nature Communications* **8**, 15769 (2017).

2. S. Poncé, R. Margine, C. Verdi and F. Giustino. Superconducting properties using maximally localized Wannier functions. *Computer Physics Communications* **209**, 116 (2016).

3. A. D. Wright, C. Verdi, R. L. Milot, G. E. Eperon, M. A. Pérez-Osorio, H. J. Snaith, F. Giustino, M. Johnston and L. M. Herz. Electron-phonon coupling in hybrid lead halide perovskites. *Nature Communications* **7**, 11755 (2016).

4. M. Filip, C. Verdi and F. Giustino. *GW* band structures and carrier effective masses of $CH_3NH_3PbI_3$ and hypothetical perovskites of the type $APbI_3$: A = NH_4, PH_4, AsH_4, and SbH_4. *The Journal of Physical Chemistry C* **119**, 25209 (2015).

5. C. Verdi and F. Giustino. Fröhlich electron-phonon vertex from first principles. *Physical Review Letters* **115**, 176401 (2015).

6. C. Verdi, E. Mosconi, F. De Angelis, M. Marsili, and P. Umari. Alignment of energy levels in dye/semiconductor interfaces by *GW* calculations. *Physical Review B* **90**, 155410 (2014).